



**HAL**  
open science

# Ferroelectric polymers for organic electronic applications

Nicoletta Spampinato

► **To cite this version:**

Nicoletta Spampinato. Ferroelectric polymers for organic electronic applications. Polymers. Université de Bordeaux, 2018. English. NNT : 2018BORD0392 . tel-02115772

**HAL Id: tel-02115772**

**<https://theses.hal.science/tel-02115772>**

Submitted on 30 Apr 2019

**HAL** is a multi-disciplinary open access archive for the deposit and dissemination of scientific research documents, whether they are published or not. The documents may come from teaching and research institutions in France or abroad, or from public or private research centers.

L'archive ouverte pluridisciplinaire **HAL**, est destinée au dépôt et à la diffusion de documents scientifiques de niveau recherche, publiés ou non, émanant des établissements d'enseignement et de recherche français ou étrangers, des laboratoires publics ou privés.

THÈSE PRÉSENTÉE  
POUR OBTENIR LE GRADE DE  
**DOCTEUR DE**  
**L'UNIVERSITÉ DE BORDEAUX**

École Doctorale des Sciences Chimiques

Spécialité : Polymères

Par Nicoletta SPAMPINATO

**FERROELECTRIC POLYMERS**  
**FOR ORGANIC ELECTRONIC APPLICATIONS**

Sous la direction de : Pr. Georges HADZIIOANNOU  
Co-directeur : Dr. Mario MAGLIONE

Soutenue le 18 Décembre 2018

Membres du jury :

**M. POULIN Philippe**, Directeur de Recherche, CRPP - CNRS  
**M. GEOGHEGAN Mark**, Professeur, University of Sheffield  
**Mme NOGALES RUIZ Aurora**, Directrice de Recherche, IEM - CSIC  
**M. AMEDURI Bruno**, Directeur de Recherche, ICGM - CNRS  
**M. PORTALE Giuseppe**, Maître de Conférences, University of Groningen  
**Mme PAVLOPOULOU Eleni**, Maître de Conférences, Bordeaux INP  
**M. MAGLIONE Mario**, Directeur de Recherche, ICMCB - CNRS  
**M. HADZIIOANNOU Georges**, Professeur, Université de Bordeaux

Président du Jury  
Rapporteur  
Rapporteuse  
Examineur  
Examineur  
Invité  
Co-directeur de Thèse  
Directeur de Thèse



**“All the effort in the world won't matter if you're not inspired.”**

C. Palahniuk



# Ferroelectric Polymers for Organic Electronic Applications

## Abstract

Organic electronics represent a realistic alternative to conventional silicon-based technologies through the design, synthesis and implementation of functional organic materials into light and flexible devices. Organic materials, such as small molecules or organic polymers, are advantageous for their low-cost, flexibility and easy processing. Thanks to the economical and timesaving advantages, organic electronics have emerged as an innovative field with application in energy, environment, health, information and communication technologies.

Organic electronics originates from the discovery of polymers with semiconducting functionalities. However, one should not neglect another class of outstanding polymers, the ferroelectric polymers. The electroactive nature of ferroelectric polymers, which are also pyroelectric and piezoelectric, combined with the intrinsic advantages of polymers have designated them as constituent elements of a widespread range of organic electronic devices. The most well-known family of ferroelectric polymers is that of poly(vinylidene fluoride), P(VDF), and its copolymers with trifluoroethylene, P(VDF-co-TrFE). Energy harvesting, data storage and sensing, main applications of organic electronics, can potentially all be realised using these exceptional functional materials.

Since ferroelectricity is a structure-dependent property an insight into the interrelations between structure and final ferroelectric properties is indispensable in order to improve existing applications of ferroelectric polymers in organic electronics and to promote the introduction of P(VDF-co-TrFE) in new application fields.

P(VDF-*co*-TrFE) as semi-crystalline polymer possess crystalline properties which are sensitive to thermal treatment. Since only the crystalline regions contribute to ferroelectric switching and not the amorphous ones, the degree of crystallinity is a key factor to modulate the ferroelectric properties. Moreover, crystallites orientation as well as the presence of defects within the crystallites are crucial parameters playing an important role in defining the final performance of the devices in which P(VDF-*co*-TrFE) is incorporated.

Herein stands the aim of this thesis: reach an exhaustive understanding of processing-structure-function relationships that will serve as tool to modulate ferroelectric devices performances.

Going one step further, the potential applications of P(VDF-*co*-TrFE) in organic electronics are explored by investigating it in: (1) medical piezoelectric catheter sensors for measuring cardiac function and eventually for detecting cardiac disease and (2) electronic devices in which P(VDF-*co*-TrFE) is blended with the semiconducting polymer poly(3-hexylthiophene), P3HT. The latter has already been applied in non-volatile ferroelectric memory diodes and the potential use in organic photovoltaics is explored.

## Keywords

Polymers, Ferroelectric, Organic Device, Structure-Function, Piezoelectric

---

# Polymères Ferroélectriques pour Applications Electroniques Organiques

## Résumé

L'électronique organique représente une alternative réaliste aux technologies conventionnelles à base de silicium par le design, la synthèse et la mise en œuvre des matériaux organiques fonctionnels dans des dispositifs légers et flexibles. Les matériaux organiques, tels que les petites molécules ou les polymères organiques, sont avantageux pour leur faible coût, leur flexibilité et leur facilité de traitement. Grâce aux avantages liés à l'utilisation de matériaux organiques, en termes économiques et de gain de temps, l'électronique organique est devenue un domaine innovant qui s'applique aux technologies de l'énergie, de l'environnement, de la santé, de l'information et de la communication.

L'électronique organique est issue de la découverte de polymères dotés de fonctionnalités semi-conductrices. Cependant, il ne faut pas négliger une autre classe de polymères exceptionnels, les polymères ferroélectriques. La nature électroactive des polymères ferroélectriques, qui sont également pyroélectriques et piézoélectriques, combinés aux avantages intrinsèques des polymères, les a désignés comme éléments constitutifs d'une gamme étendue de dispositifs électroniques organiques.

La famille de polymères ferroélectriques la plus connue est celle du poly(fluorure de vinylidène) P(VDF) et de son copolymère avec le trifluoroéthylène, P(VDF-co-TrFE). La récupération d'énergie, le stockage et la détection de données, principales applications de l'électronique organique, peuvent potentiellement tous être réalisés avec ces matériaux fonctionnels exceptionnels.

La ferroélectricité étant une propriété dépendant de la structure, il est indispensable de mieux comprendre les relations réciproques entre la structure et les propriétés ferroélectriques finales afin d'améliorer les applications existantes des polymères ferroélectriques en électronique organique et de promouvoir l'introduction du P(VDF-*co*-TrFE) dans de nouvelles applications.

P(VDF-*co*-TrFE) en tant que polymère semi-cristallin possède des propriétés cristallines sensibles au traitement thermique. Puisque seules les régions cristallines contribuent à la commutation électronique de la polarisation et non les amorphes, le degré de cristallinité est un facteur clé pour moduler les propriétés ferroélectriques. En outre, l'orientation des cristallites ainsi que la présence de défauts dans les cristallites sont des paramètres cruciaux qui jouent un rôle important dans la définition des performances finales des dispositifs dans lesquels P(VDF-*co*-TrFE) est incorporé. Tel est l'objectif de cette thèse: atteindre une compréhension exhaustive des relations traitement-structure-fonction qui serviront d'outil pour moduler les performances des dispositifs ferroélectriques.

De plus, les applications potentielles de P(VDF-*co*-TrFE) en électronique organique sont explorées en examinant sa mise en œuvre dans: (1) des capteurs médicaux à cathéter piézoélectrique destinés à mesurer la fonction cardiaque et éventuellement à détecter maladies cardiaques et (2) dispositifs électroniques dans lesquels P(VDF-*co*-TrFE) est mélangé avec le polymère poly(3-hexylthiophène) semi-conducteur, P3HT. Ce dernier a déjà été appliqué dans les diodes à mémoire ferroélectrique non volatile et l'utilisation potentielle dans le champ de l'organique photovoltaïque est explorée.

## Mots clés

Polymères, Ferroélectrique, Dispositifs organiques, Structure-Fonction, Piézoélectrique

---

# **Unité de recherche**

Laboratoire de Chimie des Polymères Organiques (LCPO) - UMR5629

Group 4: " Polymer Electronic Materials and Devices"

16 Avenue Pey-Berland

33607 Pessac Cedex

France



# Table of contents

<b>Abstract</b> .....	5
<b>Résumé</b> .....	7
<b>List of abbreviations</b> .....	15
<b>1 General introduction and Thesis outline</b> .....	21
1.1 Ferroelectric polymers in organic electronics .....	21
1.2 Basic dielectric definitions.....	24
1.3 Ferroelectric polarisation .....	26
1.4 Ferroelectric polymers: state-of-the-art .....	28
1.4.1 PVDF and its polymorphs .....	28
1.4.2 P(VDF- <i>co</i> -TrFE) and its polymorphs.....	31
1.4.3 Challenges and Thesis objectives .....	37
1.5 Thesis Outline .....	40
References.....	42
<b>2 Optimisation of the ferroelectric properties of cold-crystallised P(VDF-<i>co</i>-TrFE) films</b> .....	49
2.1 Introduction.....	49
2.2 Samples preparation .....	50
2.3 Results and discussion.....	52
2.4 Conclusion .....	67
References.....	69
<b>3 Unravelling the P(VDF-<i>co</i>-TrFE) polymorphism by investigating its crystallisation from the melt</b> 75	
3.1 Introduction.....	75
3.2 Sample preparation.....	79
3.3 Results and discussion.....	80
3.3.1 ① First heating ramp: Curie transition and melting.....	81
3.3.2 ②First cooling ramp: isothermal crystallisation and Curie transition .....	83
3.3.3 ③Second heating ramp: Curie transition of the melt-crystallised samples .....	98
3.3.4 Impact on the ferroelectric properties.....	102
3.4 Conclusions.....	105
References.....	108
<b>4 The effect of crystallites orientation on the ferroelectric performance of P(VDF-<i>co</i>-TrFE).....</b>	<b>113</b>
4.1 Introduction.....	113
4.2 Sample preparation.....	116

4.3	Results and discussion.....	117
4.3.1	Structural characterisation: crystallites orientation distribution.....	117
4.3.2	Ferroelectric properties.....	129
4.3.3	Dielectric properties.....	130
4.3.4	Structure – Function relationships in ferroelectric polymers .....	136
4.4	Conclusions.....	138
	References.....	140
<b>5</b>	<b>P(VDF-co-TrFE) a sensor for ventricular laparoscopic surgery simulation.....</b>	<b>145</b>
5.1	P(VDF-co-TrFE) for biomedical sensing .....	145
5.1.1	First system: organic device on Polyethylene terephthalate (PET).....	147
5.1.2	Second system: organic flexible device on PDMS .....	150
5.1.3	Third system: free standing sensors.....	152
5.2	Conclusion .....	159
	References.....	161
<b>6</b>	<b>Phase separated P(VDF-co-TrFE):rr-P3HT blend: an alternative to organic photovoltaics? ....</b>	<b>165</b>
6.1	An introduction to the P(VDF-co-TrFE):P3HT blend.....	165
6.2	Phase separated structure: a morphological characterisation .....	173
6.2.1	Samples preparation .....	173
6.2.2	Structural characterisation.....	174
6.3	Application in organic photovoltaics.....	180
6.3.1	Device fabrication.....	182
6.3.2	J vs V characterisation .....	183
6.4	Conclusions.....	189
	References.....	191
<b>7</b>	<b>General conclusions .....</b>	<b>197</b>
<b>8</b>	<b>Annex.....</b>	<b>203</b>
8.1	Materials.....	203
8.1.1	P(VDF-co-TrFE).....	203
8.1.2	P3HT .....	204
8.2	Thin films preparation .....	204
8.2.1	P(VDF-co-TrFE) thin films.....	204
8.2.2	P(VDF-co-TrFE):P3HT thin films .....	205
8.3	Capacitor fabrication .....	205
8.4	Thermal treatment .....	206

8.5	Techniques .....	206
8.5.1	Spin-coating deposition technique.....	206
8.5.2	Profilometer .....	208
8.5.3	Differential Scanning Calorimetry (DSC) .....	208
8.5.4	Grazing incidence Wide Angle X-ray scattering (GIWAXS) .....	209
8.5.5	Scanning Probe Microscopies: AFM, PFM, KPFM and CFM .....	211
8.5.6	Ferroelectric characterisation .....	213
8.5.7	Dielectric spectroscopy .....	214
8.5.8	Photovoltaic characterisation .....	216
	References.....	217



## List of abbreviations

- 1D: One dimension
- 2D: Two dimensions
- 3D: Three dimensions
- A: Area
- AC: alternating current
- $A_{F1}$ : integrated area of the fit peak of the  $F_1$  phase
- $A_{F1-2}$ : integrated area of the fit peak of the  $F_{1-2}$  phase
- $A_{F2}$ : integrated area of the fit peak of the  $F_2$  phase
- AFM: Atomic Force Microscopy
- $A_{TOT}$ : integrated area of the scattering peak centred at  $1,4 \text{ \AA}^{-1}$
- BHJ: bulk heterojunction
- C: capacitance
- CFM: Conductive Force Microscopy
- CL: CoolLed phase
- D: Displacement
- d: thickness
- DC: direct current
- DFE: Defective Ferroelectric Phase
- DSC: Differential Scanning Calorimetry
- d-spacing: inter-planar spacing
- E: Electric Field
- $e^-$ : electron
- $E_a$ : activation energy
- $E_c$ : coercive electric field
- $F_1$ : most ordered ferroelectric phase
- $F_{1-2}$ : intermediately disordered ferroelectric phase
- $F_2$ : disordered ferroelectric phase
- FE: ferroelectric phase
- FeFET: Ferroelectric Field Effect Transistor

- $f_m$ : maximum frequency
- FRAM: Ferroelectric Random Access Memory
- FWHM: Full Width at Half Maximum
- G: Gauche
- GIWAXS: Grazing Incident Wide Angle X-ray Scattering
- $h^+$ : hole
- HOMO: highest occupied molecular orbital
- HT: High Temperature phase
- I: intensity
- IoT: Internet of Things
- J: current density
- $k_B$ : Boltzmann constant  $8.6 \cdot 10^{-5}$  eV K<sup>-1</sup>
- KPFM: Kelvin Probe Force Microscopy
- $L_{\text{coherence}}$ : structural coherence size
- Liryc: l'insitut de rythmologie et modélisation cardiaque
- LT: Low Temperature phase
- LUMO: lowest unoccupied molecular orbital
- OPV: Organic Photovoltaic
- P(VDF-co-TrFE): poly(vinylidene fluoride-co-trifluoroethylene) copolymer
- P: Polarisation
- P3HT: Poly(3-hexylthiophene)
- PCBM: [6,6]-phenyl-C<sub>61</sub>-butyric acid methyl ester
- PCE: Power Conversion Efficiency
- PDMS: poly(dimethylsiloxane)
- PE: paraelectric phase
- PEDOT: poly(3,4-ethylenedioxythiophene)
- PET: poly(ethylene terephthalate)
- PFM Piezoresponse Force Microscopy
- $P_r$ : Remnant Polarisation
- $P_{\text{sat}}$ : Saturated Polarisation
- PSTFSI: poly(4-styrene trifluoromethyl (bissulfonylimide))

- PVDF: Poly(vinylidene fluoride)
- $q$ : scattering vector
- $Q$ : stored charges
- $R$ : gas constant,  $1.987 \cdot 10^{-3} \text{ kcal mol}^{-1} \text{ K}^{-1}$
- rpm: revolutions per minute
- SAXS: Small Angle X-ray Scattering
- SC: semiconducting phase
- SPM: Scanning Probe Microscopy
- $t$ : Film thickness
- $T$ : Temperature
- $T_0$ : crystallisation onset
- $T_c$ : crystallisation temperature
- $T_{\text{Curie}}$ : Curie transition temperature
- $T_g$ : Glass transition temperature
- THF: Tetrahydrofuran
- $T_m$ : Melting temperature
- TrFE: trifluoroethylene
- TTT: trans sequence
- $V$ : voltage
- $V_{\text{CPD}}$ : contact potential difference
- VCPD: Contact potential difference
- VDF: vinylidene fluoride
- WAXD: Wide Angle X-Ray Diffusion
- WAXS: Wide Angle X-ray Scattering
- $\alpha$ : alpha phase
- $\beta$ : beta phase
- $\gamma$ : gamma phase
- $\Delta H_{\text{iso}}$ : enthalpy of the isothermal crystallisation
- $\Delta H_{\text{post-iso}}$ : enthalpy of the post-isothermal crystallisation
- $\Delta H_{\text{pre-iso}}$ : enthalpy of the pre-isothermal crystallisation
- $\epsilon$ : dielectric permittivity

- $\epsilon_0$ : vacuum permittivity
- $\epsilon_r$ : relative permittivity
- $\epsilon_r'$ : real dielectric permittivity
- $\epsilon_r''$ : imaginary dielectric permittivity
- $\mu$ : dipole moment
- $\tau$ : relaxation time
- $\phi$ : Work function
- $\chi$ : susceptibility
- $\chi_{\text{ferro}}$ : degree of ferroelectric crystallinity

# Chapter 1

*General introduction and*

*Thesis outline*



# 1 General introduction and Thesis outline

## 1.1 Ferroelectric polymers in organic electronics

Organic electronics gave birth to a realistic alternative to conventional silicon-based technologies through the design, synthesis and implementation of functional organic materials into light and flexible devices. Organic materials are low cost materials that require low pressure and low temperature in order to be processed. Therefore, the economical and timesaving advantages, provided by organic materials, promote organic electronics as an innovative field that meets challenges in energy, environment, health, information and communication technologies.

Thinking about organic electronics, our mind goes spontaneously to semiconducting polymers, neglecting the significance of organic dielectrics: ferroelectric polymers constitute one of those. The most well-known family of ferroelectric polymers is that of poly(vinylidene fluoride), P(VDF), and its copolymers with trifluoroethylene, the P(VDF-co-TrFE). Their electroactive nature, given by their ferroelectric, pyroelectric and piezoelectric functionalities, combined with the intrinsic advantages of polymers have promoted them as constituent elements for a widespread range of organic electronic devices.

Ferroelectric fluorinated polymers have been used for decades in acoustics to develop for example audio-frequency microphones, headphone, speakers, and in electromechanical applications to develop sensors such as pressure switches. The operation of such devices is based on the piezoelectric effect. Acoustic devices are made up of a flexible polymeric film that vibrates upon application of a voltage, generating sound (Figure 1.1a). On the other hand, electromechanical transducers are low-frequency piezoelectric switches whose operation depends on the deformation of the film, induced by the pressure applied onto a push button (Figure 1.1b).<sup>1,2</sup>

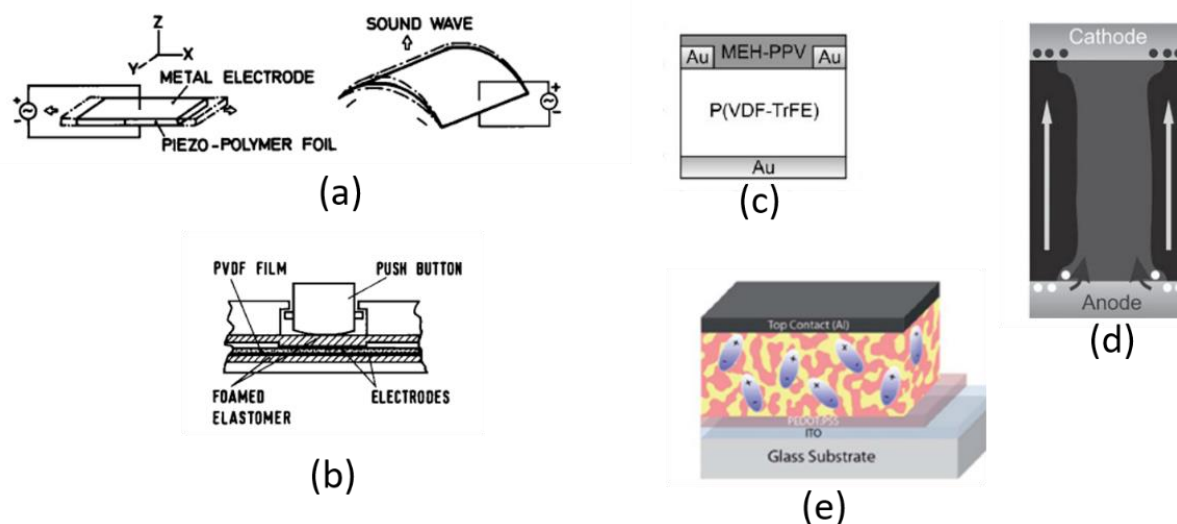


**Figure 1.1** (a) Example of acoustic generator operation: when a voltage is applied the plane piezoelectric element bends. This transverse motion represents a pulsed motion that generates sound. Reproduced from reference <sup>2</sup>. (b) Schematic cross section of an electromechanical switch. Reproduced from reference <sup>2</sup>. (c) A polymer-based FeFET device where the p-semiconducting polymer used is poly(2-methoxy,5-(20-ethylhexyloxy)-p-phenylenevinylene), MEH-PPV. Reproduced from reference <sup>3</sup>. (d) A schematic representation of the cross-section of a non-volatile diode memory made by a phase-separated blend of P3HT and P(VDF-co-TrFE). Reproduced from reference <sup>4</sup>. (e) Schematic draw of a BHJ photovoltaic device that incorporates P(VDF-co-TrFE) domains in the active layer. Reproduced from reference <sup>5</sup>.

In the last 10-15 years PVDF and its copolymers expanded their field of use in memory applications and photovoltaics. Concerning memory devices, ferroelectric Field effect transistors, FeFET, in which the ferroelectric insulator P(VDF-co-TrFE) acts as the gate dielectric have been fabricated (Figure 1.1c). The gate voltage can tune the ferroelectric polarisation of the gate insulator inducing either high or low semiconductor channel conductance. In this way, FeFETs provide a non-volatile memory that can be non-destructively read-out.<sup>3,4,6,7</sup>

Another kind of ferroelectric non-volatile memory has been achieved by blending P(VDF-co-TrFE) with the semiconducting polymer poly(3-hexylthiophene), P3HT (Figure 1.1d). These non-volatile resistive memories use the polarisation field of the ferroelectric matrix to modulate the injection barrier at the semiconductor–metal interface: through variation of the

polarisation direction a lowering (increase) of the injection barrier occurs and with it an increase (reduction) of the device current: the device is in the on-state (off-state).

In organic photovoltaics, OPVs, one of the main issues that need to be overcome in order to achieve high efficiency devices concerns the electron-hole,  $e^-h^+$ , recombination. Bulk-heterojunction OPVs that incorporate ferroelectric polymers are reported to exhibit an improved efficiency (Figure 1.1e)<sup>5</sup> thanks to the fact that ferroelectric polymers act as promoters of the dissociation of the photo generated  $e^-h^+$  pairs (singlet excitons) thanks to their polarisation potential that hinders exciton recombination.

Nowadays ferroelectric polymers are increasingly seizing attention for applications related to the realization of the Internet of Things (IoT), a technological challenge based on networks of environmentally-friendly and auto-sustainable sensors and energy sources. An example of recent achievements in energy harvesting that can be seen as a knot of the IoT network is the implementation of ferroelectric polymers in piezoelectric nanogenerators, in which, ferroelectrics (being piezoelectrics that exhibit a large electromechanical response) are able to harvest and efficiently convert mechanical energy into electrical power.<sup>8-10</sup> Energy harvesting, data storage and sensing, main applications of organic electronics, can potentially all be realised using ferroelectric polymers (Figure 1.2). This Thesis is centred on the study of these exceptional functional materials.

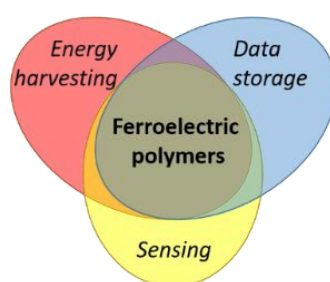


**Figure 1.2** The main organic applications of ferroelectric polymers.

## 1.2 Basic dielectric definitions

A ferroelectric material is first of all a dielectric material, which acts as a barrier for the free charges to flow when an electric field is applied. When a dielectric of thickness  $d$  and surface area  $A$  is placed between two metallic electrodes, in a parallel plate capacitor geometry (Figure 1.3.a) and a voltage  $V$  is applied charges,  $Q$ , are stored at the surface:

$$Q = C V \quad (1.1)$$

$C$  is the capacitance that is defined as:

$$C = \frac{\epsilon A}{d} = \frac{\epsilon_0 \epsilon_r A}{d} \quad (1.2)$$

Where  $\epsilon_0$  is a constant, the vacuum permittivity ( $8.854 \cdot 10^{-12} \text{ F m}^{-1}$ ), and  $\epsilon_r$  is the relative dielectric permittivity of the material:

$$\epsilon_r = (1 + \chi) \quad (1.3)$$

Where  $\chi$  is the susceptibility, the same as  $\epsilon_r$  after the  $\epsilon_0$  contribution subtraction:

$$\epsilon_0 \chi = \epsilon_0 \epsilon_r - \epsilon_0 = \epsilon_0 (\epsilon_r - 1) \quad (1.4)$$

Dielectric permittivity,  $\epsilon$  and susceptibility,  $\chi$ , essentially represent the same phenomena. When an electric field is applied to a material, the response of the materials depends on the frequency of the field. Indeed, the dielectric permittivity,  $\epsilon$  is function of the frequency of the applied electric field and is defined as a complex function:

$$\epsilon_r = \epsilon'_r + i\epsilon''_r \quad (1.5)$$

where  $\epsilon'_r$  represents the real part of the relative permittivity and is related to the energy stored in the dielectric and  $\epsilon''_r$  represents the imaginary part of the relative permittivity and relates to the energy loss in the material.

The applied electric field  $\vec{E}$  induces a spatial displacement of charges,  $\vec{D}$ :

$$\vec{D} = \epsilon_0 \vec{E} + \vec{P} \quad (1.6)$$

The overall macroscopic polarisation  $\vec{P}$  is the density of charges created at the surface, namely the total amount of charges per unit area ( $P = Q A^{-1}$ ) and is defined as:

$$\vec{P} = \epsilon_0 \chi \vec{E} \quad (1.7)$$

In the limit of small fields, the dielectric polarisation varies in a linear way with the electric field as shown in Figure 1.3.b where the polarisation  $\vec{P}$  dependence to the  $\vec{E}$  for a classical dielectric material is represented.<sup>11</sup>

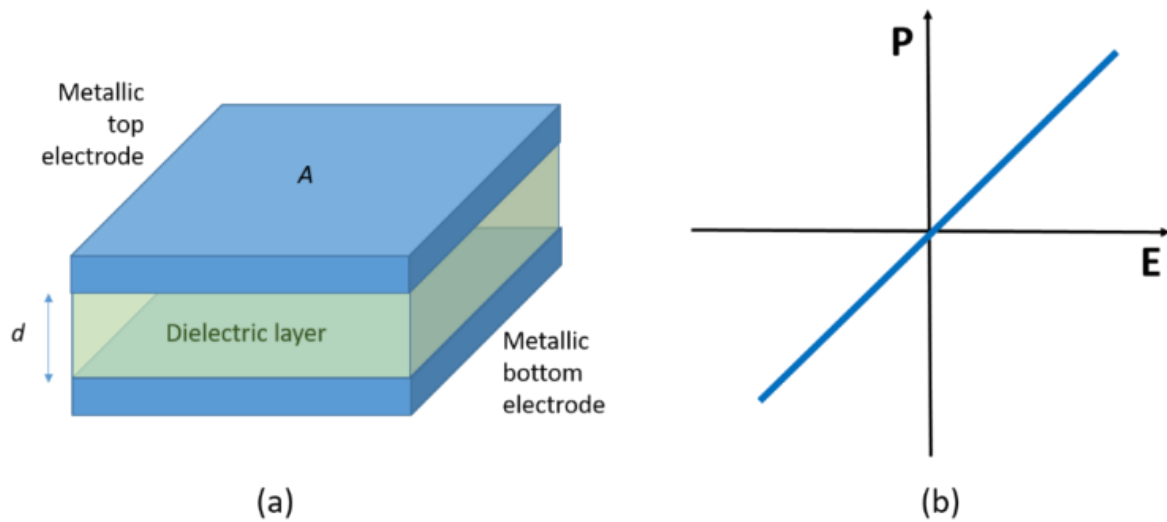


**Figure 1.3** (a) Schematic representation of a capacitor device where a dielectric material of area  $A$  and thickness  $d$  is placed between two parallel metallic plates; (b) the typical linear dependence of the polarisation of a dielectric material versus the electric field applied.

### 1.3 Ferroelectric polarisation

A crystalline dielectric material with non-centrosymmetric structure is called polar dielectric and its net polarisation can be modified by an applied field, giving rise to high permittivity. Certain crystalline polar dielectrics exhibit high permittivity and bear, even in absence of electric field, a spontaneous and reversible electric polarisation. Such materials are called ferroelectrics. The ferroelectric polarisation originates from the alignment of dipoles inside the crystallites through the application of an electric field. The ferroelectric polarisation is bi-stable, i.e. when the direction of the electric field is reversed, inversion of dipoles moment orientation occurs giving rise to a ferroelectric hysteresis loop, electrical analogue of the hysteresis loops exhibited by ferromagnetic materials (Figure 1.4.a).

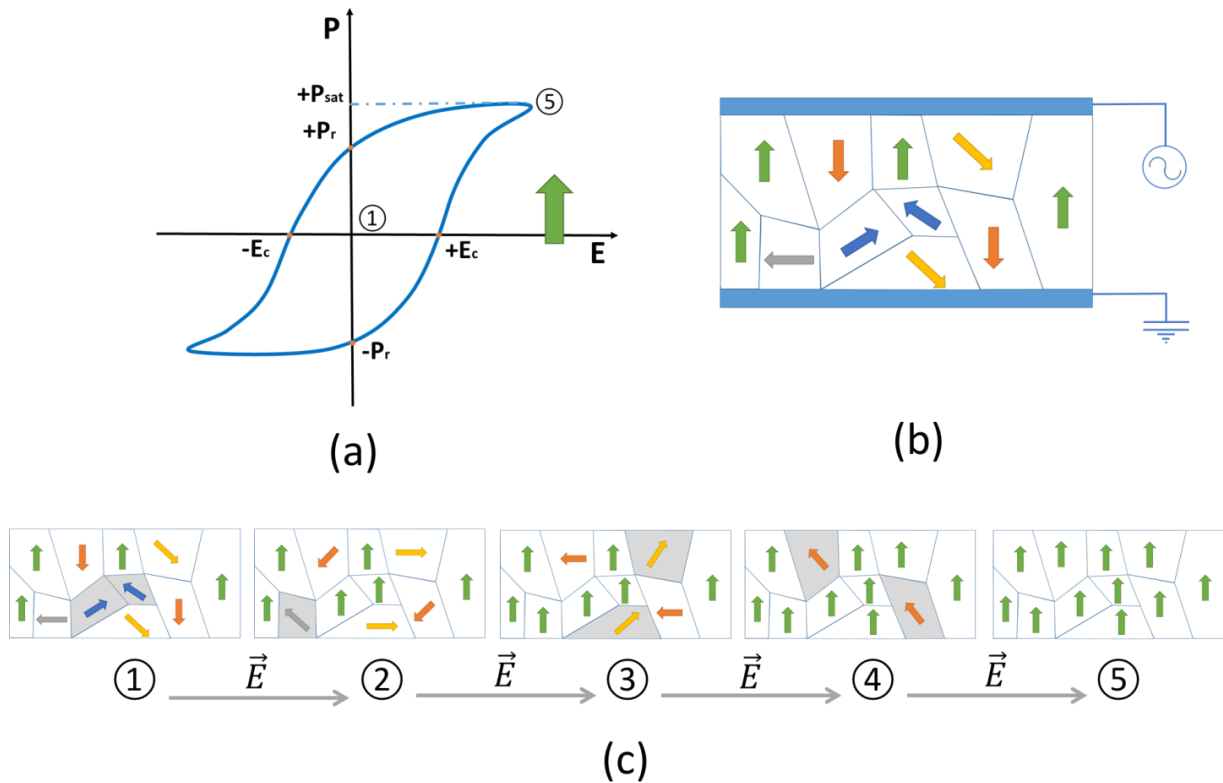


**Figure 1.4** (a) A representative ferroelectric hysteresis loop, which arises from the electrical switching; polarisation  $P$  is measured as function of the applied electric field  $E$ . (b) Simple schema of a capacitor in which the active layer is a ferroelectric crystalline material: the crystallites are depicted as polygons with a defined orientation of the ferroelectric domain. (c) Steps to induce a polarised state: ①, all dipoles are randomly oriented, ⑤ all dipoles are aligned.

As it emerges, the ferroelectric polarisation does not vary with the electric field in a linear way as classical dielectrics do. A crystalline ferroelectric material can be schematised by crystallites that can form ferroelectric domains with a certain polarisation axis. The intrinsic polarisation of the ferroelectric domains is represented by arrows oriented in different directions, namely different dipoles orientation in Figure 1.4b. When the ferroelectric is placed between two electrodes and a voltage is applied, an orientation of the dipoles within the crystallites will be induced.

In Figure 1.4.c the transition of a material from the non-polarized to the polarized state under application of an electric field  $\vec{E}$  is depicted. Ferroelectric domains, initially randomly oriented with respect to each other (Figure 1.4c, ①), tend to align (Figure 1.4.c from ② to

④) until reaching saturation of  $\vec{P}$  at high  $\vec{E}$  (Figure 1.4.c ⑤): the material is finally polarised and its polarisation can be inverted by applying an opposite equal electric field.

From the recorded hysteresis loop the ferroelectric parameters characterising the material can be determined. The saturation polarisation,  $P_{sat}$ , is the maximum polarisation obtainable at a specific value of electric field and is related to the total amount of dipoles responding to the  $\vec{E}$ . At the intersections with the  $P$ -axis and  $E$ -axis respectively we can determine the remnant polarisation,  $\pm P_r$ , which is the retained polarisation in absence of electric field, and the coercive field,  $\pm E_c$ , which is the value of the electric field that must be applied in order to switch the full saturated polarisation (Figure 1.4a). On this polarisation reversal are based the non-volatile ferroelectric random access memories, FRAMs, where the binary logic states “1” and “0” are associated with the bi-stable polarisation states  $+P_r$  and  $-P_r$ .

The comprehension of this electrical switching process and the evaluation of the parameters that come out from it are of fundamental importance to target the final application of the device. For example, in case of capacitors, normally the goal is to induce the highest amount of charges per surface area by applying the lowest effort to switch the dipoles, namely the lowest electric field. Therefore, a good ferroelectric performance in that case corresponds to a high  $P_r$  (high amount of information stored in the write process) and a low  $E_c$  (read-out requires low voltages).

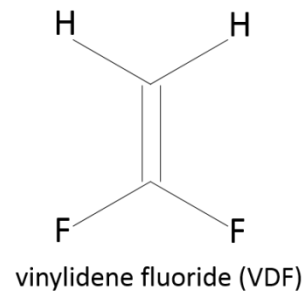
Another important parameter that is characteristic of ferroelectric materials is the Curie temperature,  $T_{Curie}$ , that marks the transition from the ferroelectric to the paraelectric state and vice versa. Above  $T_{Curie}$  the crystallites are in a paraelectric state, i.e. the dipoles are randomly oriented, the spontaneous polarisation vanishes and the ferroelectricity is lost.

## 1.4 Ferroelectric polymers: state-of-the-art

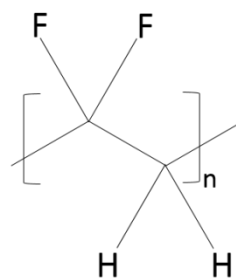
### 1.4.1 PVDF and its polymorphs

PVDF is the most well-known organic ferroelectric polymer, whose the repeating unit is  $(CH_2-CF_2)_n$ . The chemical structures of monomer and polymer are shown in Figure 1.5. The

PVDF ferroelectricity arises from the presence of the small highly electronegative fluorine atom (its effective ionic radius is 1.35 Å) which forms a polar bond with carbon (with a dipolar moment  $\mu$  of  $6.4-7 \times 10^{-30}$  C m) (Figure 1.5a).<sup>1,12,13</sup>



**(a)**



PVDF

**(b)**

**Figure 1.5** Chemical structures of the monomer VDF and of the polymer PVDF.

Nevertheless, the presence of dipoles is not sufficient to make PVDF a ferroelectric polymer: molecular conformation and crystalline packing play an important role in the final polymeric electroactivity. Some requirements need to be encountered concerning both conformation and packing of the chains inside a crystallite to obtain a ferroelectric material (Figure 1.6).

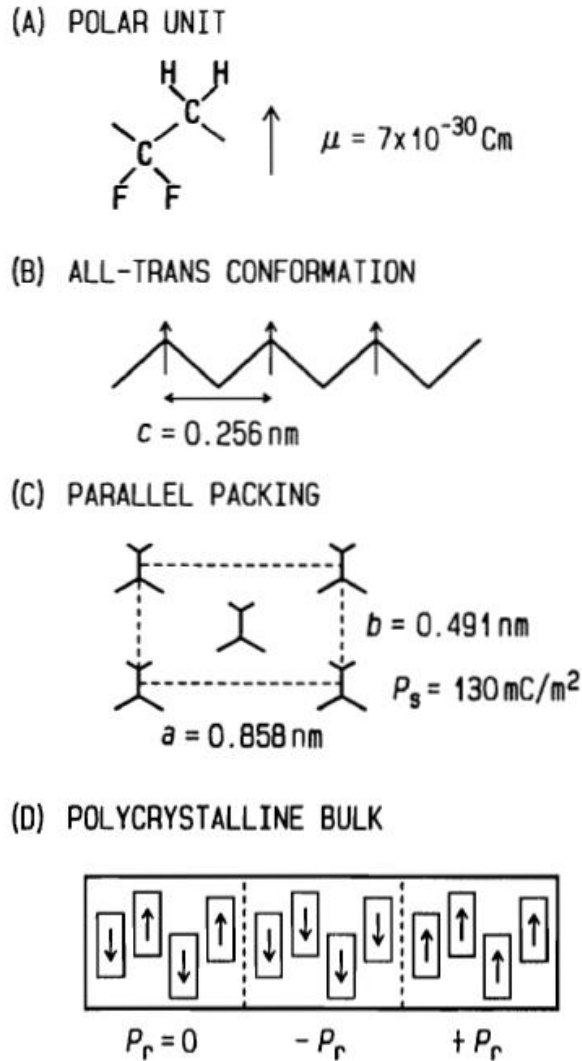


**Figure 1.6** Unit (a), molecular (b), crystalline (c) and bulk structure (d) of PVDF.

PVDF is semi-crystalline and exists in several crystalline polymorphs: the most common crystalline phases are  $\alpha$  or II,  $\beta$  or I,  $\gamma$  or III (Figure 1.7).<sup>1,14,15</sup> The difference between  $\alpha$ ,  $\beta$ ,  $\gamma$  polymorphic forms relies on the polarity of their chain conformation and on the polarity of the crystals that consequently determine a non-, highly- or slightly-ferroelectric phase. The most ferroelectric phase of PVDF is the  $\beta$ , obtained by a parallel packing of polymeric chains with an all-trans stereo-chemical conformation (TTT) where F and H substituents are at  $180^\circ$  to each other (Figure 1.6b and Figure 1.7a). In the all-trans conformation, the dipoles are all aligned in the same direction, perpendicular to the main chain. The parallel packing of these all-trans chains within a crystalline unit cell (Figure 1.6c) leads to a crystalline ferroelectric phase. However, this highly polar phase ( $\mu = 7 \times 10^{-30} \text{ C m}$  per repeating unit), is energetically

unfavourable and in order to achieve it a uniaxial mechanical stretching of the stable  $\alpha$ -phase is required.<sup>16-18</sup>

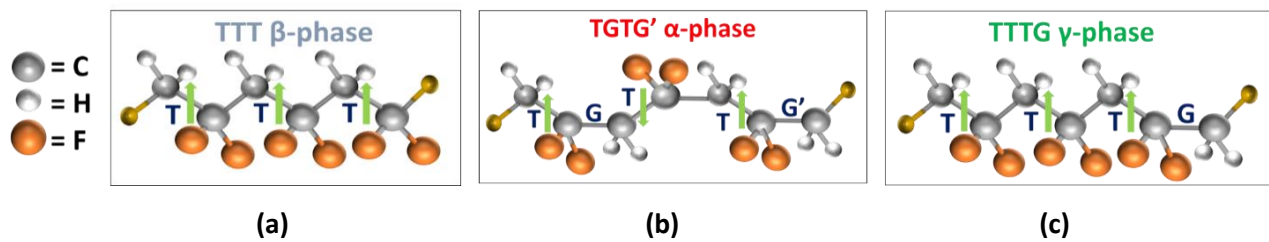


**Figure 1.7** Chain conformations of the  $\beta$ - (a),  $\alpha$ - (b) and  $\gamma$ -PVDF phases (c).

The  $\alpha$ -phase is obtained by the packing of two trans-gauche ( $TG^+TG^-$ ) chains, in which the F and H substituents are at  $180^\circ$  and at  $\pm 60^\circ$  alternatively (Figure 1.7b). The absence of steric strains between fluorine atoms makes the  $TG^+TG^-$  the lowest potential energy conformation.<sup>19</sup> Nevertheless the antiparallel arrangement of the dipole moments within the  $\alpha$ -unit cell, in which every dipole is neutralized by a neighbouring one that is oriented in the opposite direction, makes the  $\alpha$ -PVDF a non ferroelectric crystalline phase.<sup>16</sup>

Another common and polar crystalline phase of PVDF is the  $\gamma$ -phase that, with respect to the  $\beta$ -, exhibits weaker piezo- and ferroelectric properties because of the presence of gauche defects ( $\mu = 4-3.4 \times 10^{-30}$  C m per repeating unit). This polar  $\gamma$ -phase made by a parallel packing of  $TTT^+TTT^-$  chains (Figure 1.7c), is achieved by isothermal crystallisation at high temperature or by a solid-state transition from  $\alpha$ - or  $\beta$ - to  $\gamma$ -phase by annealing at temperatures close to the melting point,  $T_m$ , or by adding nucleating agents.<sup>20-23</sup>

As it arises obtaining the polar phases,  $\beta$  and  $\gamma$ , is not trivial so easy to obtain but it is in any case required in order to exploit the ferroelectric functionality of PVDF.

#### 1.4.2 P(VDF-co-TrFE) and its polymorphs

When trifluoroethylene, TrFE, ( $CF_2-CFH$ ), monomer is added in the PVDF chain, the P(VDF-co-TrFE), statistical copolymer is obtained.<sup>24,25</sup> The repeating unit is  $(CH_2-CF_2)_n-stat-(CHF-CF_2)_m$ . The monomers and the copolymer's chemical structures are shown in Figure 1.8.

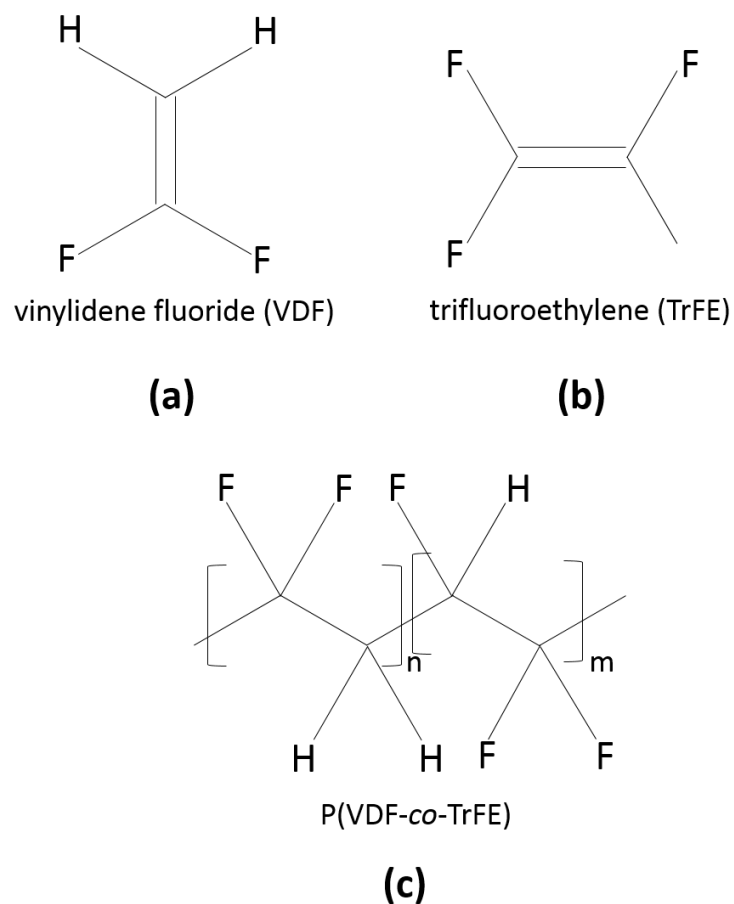


**Figure 1.8** Chemical structures of the monomers VDF and TrFE and of the copolymer P(VDF-co-TrFE).

The copolymer of PVDF with trifluoro ethylene exhibits a polymorphism which is reported to be molar ratio dependent. In literature many studies have investigated the crystalline structures of P(VDF-co-TrFE) with different molar ratios.

Lovinger's and Furukawa's works constitute the milestone for PVDF and its copolymers with TrFE. In the 80<sup>ies</sup>, by means of X-rays diffraction analysis they have shown the crystalline structure difference between copolymers with a VDF molar content less or higher than 54%. The melt solidified copolymer with a VDF/TrFE 52/48 molar ratio was found to crystallize into a mixture of two rather disordered crystalline phases: one well-organized trans planar zig-zag phase arranged in a hexagonal packing, and another 3/1 helical structure arranged in pseudo-hexagonal packing. It was proposed that both these conformations give rise to an overall chain

structure of irregular succession of TT, TG<sup>+/-</sup> sequences that appear in the diffractogram as a single peak because of the superposition of two independent peaks.<sup>26</sup>

For higher VDF content, at room temperature, the copolymer was found to co-crystallize directly into a well-ordered trans zig-zag packing, resulting in a ferroelectric polar phase analogous to that of  $\beta$ -PVDF. This low-temperature state of P(VDF-co-TrFE) with 54 mol%  $\leq$  VDF  $\leq$  82 mol% has a polar trans conformation of molecular chains whose order increases with the VDF content, leading to a decrease of the dimension of the pseudo-hexagonal unit cells.<sup>16</sup>

In 1986, Tashiro and Kobayashi studied the copolymer with a content of VDF of 55 mol% and reported the appearance of a defective phase when cooled down after annealing. In particular, three crystal forms were defined: a low-temperature (LT) phase, essentially the  $\beta$ -PVDF, where VDF monomeric units are replaced statistically by TrFE units in the crystal structure; a high temperature (HT) phase, statistical combination of TT and TG<sup>+/-</sup> rotational isomers in a nonpolar unit cell and a cooled (CL) phase (Figure 1.9). When LT is annealed above the  $T_{\text{Curie}}$ , molecular chains experience a violent rotational motion around the chain axis through a trans-gauche conformational exchange and the HT paraelectric phase is obtained, which, upon cooling, generates a defective CL. For copolymers with VDF content higher than 55% Tashiro et al. did not find any CL phase but they described an almost reversible transition between LT and HT.<sup>15,27</sup>

The CL phase of Tashiro is an individual disordered ferroelectric phase that should correspond to the one described by Lovinger as the mixture of two individual phases whose diffraction peaks overlap at RT.

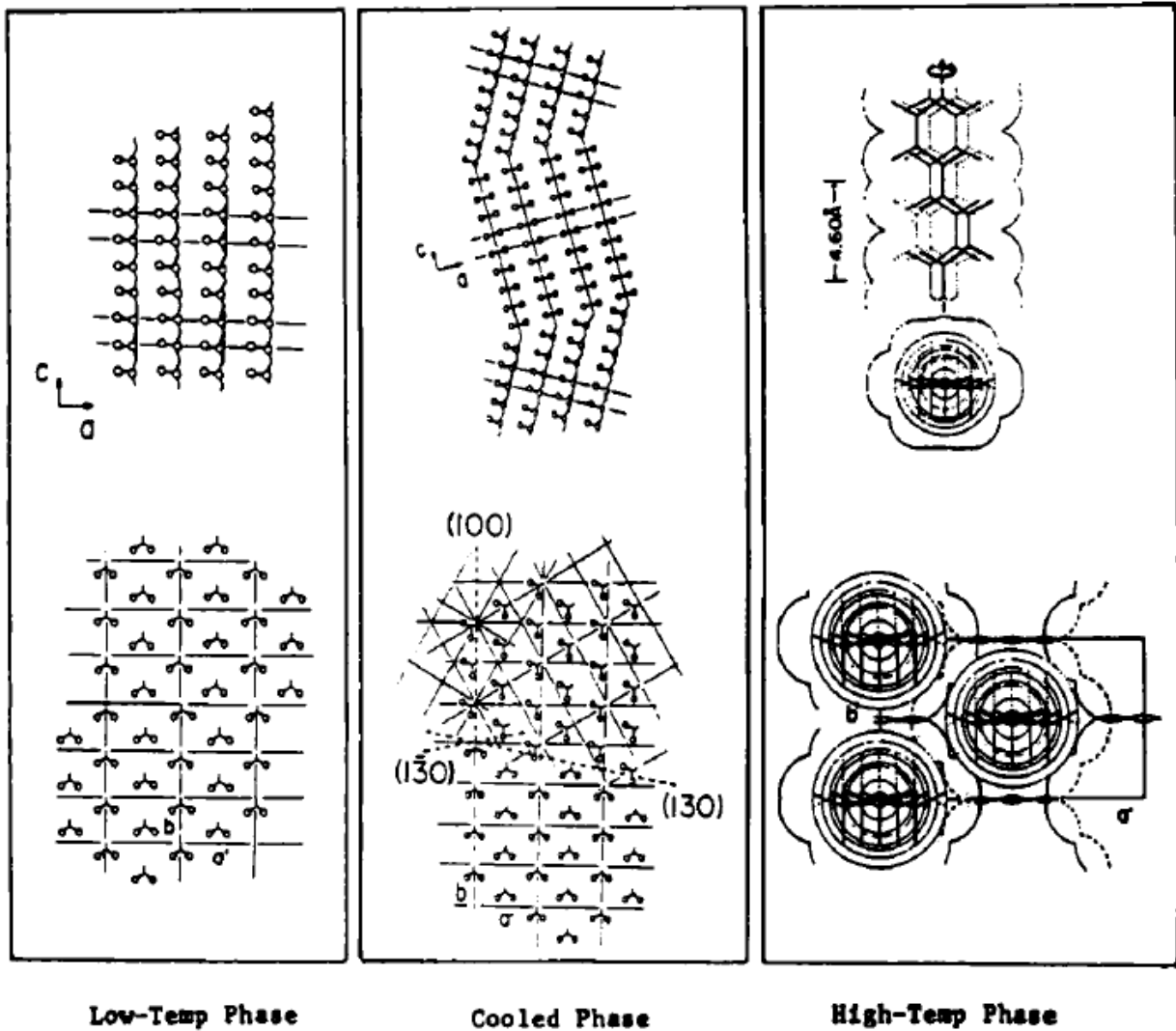


**Figure 1.9** The Low temperature phase, LT, the Cooled phase, CL, and the High temperature phase, HT, described by Tashiro et al. for P(VDF-co-TrFE) copolymers with a VDF content lower than 55 mol%. The c-axis represents the chain axis, the a-axis and b-axis being perpendicular to the c-axis.<sup>15</sup>

Even though both Lovinger and Tashiro described just one ordered ferroelectric phase for the low temperature state of copolymers with high VDF content (>55%), Koga et al. have proposed the existence of three different ferroelectric phases for copolymers of  $60 \text{ mol}\% \leq \text{VDF} \leq 90 \text{ mol}\%$  based on the multiple-peak Curie transition shape recorded with DSC. It was suggested that copolymers belonging to this weight ratio group crystallize into a mixture of  $\alpha$ -phase,  $(\text{TG}^+\text{TG}^-)$ ,  $\beta$ -phase  $(\text{TTT})$ , and  $\gamma$ -phase  $(\text{T}_3\text{G}^+\text{T}_3\text{G}^-)$ . This mixture of phases has been shown to convert into the same ordered regular all-trans phase through poling with a strong electric

field: the multiple DSC peaks of the Curie transition merge into a single sharp peak, shifted towards higher  $T_{\text{Curie}}$ .<sup>28,29</sup>

Towards the same direction, Kim *et al.* succeed in separating the multiple Curie peaks into isolated ones confirming (by IR spectroscopy) that upon heating, the peak at higher temperature corresponds to a ferroelectric phase with more trans sequences (the TTT,  $\beta$ -phase of Koga) and less gauche defects which in order to convert into a paraelectric phase requires higher thermal energy.<sup>30</sup>

In 1998, Gregorio completed the studies of Kim demonstrating the effect of annealing below or above the crystallization onset,  $T_0$ .<sup>31</sup> Annealing at a crystallization temperature,  $T_c$ , which is below  $T_0$  results in ordering the ferroelectric phase:  $T_{\text{Curie}}$  upon heating shifts towards higher temperatures but the melting temperature,  $T_m$ , remains the same, i.e. there is no change in the crystallite size. When annealing is performed at a temperature above  $T_0$  both paraelectric and ferroelectric phases are modified: a shift of  $T_{\text{Curie}}$  towards lower temperatures and of  $T_m$  towards higher temperatures is recorded (Figure 1.10). These phenomena have been explained by the appearance of one paraelectric and one ferroelectric phases (named  $F_{\alpha 2}$  and  $F_{\beta 1}$  respectively) at  $T_c < T_0$  or two paraelectric and ferroelectric phases (named  $F_{\alpha 1}$ ,  $F_{\alpha 2}$  and  $F_{\beta 1}$ ,  $F_{\beta 2}$ ) at  $T_c > T_0$ , a hypothesis that was corroborated by means of Wide Angle X-Ray Diffusion (WAXD).<sup>29</sup> The importance of ordering within the paraelectric phase had already been arisen with the work of Stack *et al.* who have demonstrated that higher isothermal crystallization temperatures form crystallites with greater thermodynamic stability (lower free energy,  $G$ ) and greater structural order, whose melting point  $T_m$  increases (due to the low  $G$ ). Such paraelectric crystallites of greater stability must be cooled to lower temperature before undergoing the Curie transition and analogously they reform sooner (at lower temperatures) on subsequent heating.<sup>32</sup>

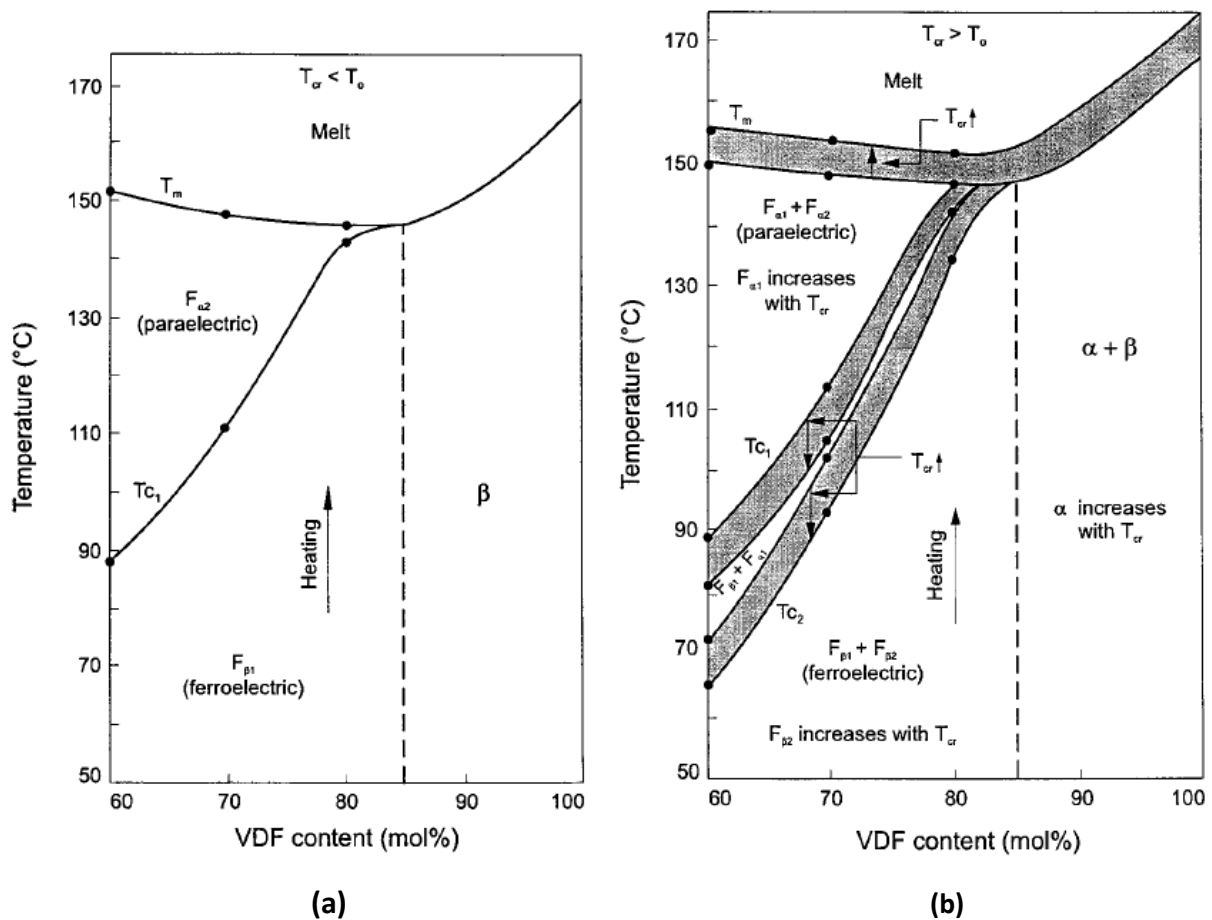


**Figure 1.10** Phase diagram of P(VDF-co-TrFE) annealed at temperatures below the crystallization onset,  $T_0$ , on the left (a) and annealed at temperatures above the  $T_0$  on the right (b). Reproduced from reference <sup>31</sup>.

The most recent study of the structural transition of P(VDF-co-TrFE) has been reported by Bargain et al. <sup>33</sup> They investigated isotropic films investigated by means of simultaneous SAXS/WAXS and DSC experiments. By following the structural changes during heating and cooling they concluded that the orthorhombic defective ferroelectric phase, called *DFE*, arises from the crystallization of chain segments containing chemical conformational defects in the hexagonal paraelectric phase during a first heating above the Curie transition. This *DFE* is probably the same phase as the CL, or the  $F\beta_2$  phases already described in literature.

From this summary of studies on P(VDF-co-TrFE) structure it arises an absence of a common terminology and of a convergent theory that described the structure of P(VDF-co-TrFE). Even though it is clear the enhanced complexity of the copolymer polymorphism with respect to that of PVDF, few groups still refer to copolymer phases using the homopolymer terminology

(i.e.  $\alpha$ -,  $\beta$ -,  $\gamma$ -phases), while others keep the Tashiro definitions of LT, HT and CL or introduce new ones, such as DFE, based on the different origins found for those phases. Despite the huge amount of studies, there is still confusion regarding the polymorphism of P(VDF-co-TrFE).

### 1.4.3 Challenges and Thesis objectives

Since ferroelectricity is a structure-dependent property, a complete understanding of existing interrelations between resulting structure and final ferroelectric properties is indispensable in order to improve existing applications of ferroelectric polymers in organic electronics and to promote the introduction of P(VDF-co-TrFE) in new fields of applications.

As already highlighted, despite the multiplicity of studies that have investigated the structural properties of P(VDF-co-TrFE) a unified theory is still missing. Moreover, just few studies correlate the functional ferroelectric properties of P(VDF-co-TrFE), such as the  $P_r$  and the  $E_c$ , to its structural characteristics in terms of degree of crystallinity, polymorphism and crystallites orientation.<sup>13,17,34-38</sup>

The degree of crystallinity is a key factor to modulate the ferroelectric properties since only the crystalline regions are involved in the ferroelectric switching of P(VDF-co-TrFE) and contribute to ferroelectricity. Note that as a semi crystalline polymer, P(VDF-co-TrFE) can be viewed as an intrinsic composite where ferroelectric crystallites are embedded in an amorphous, and thus non-ferroelectric, matrix (Figure 1.11).<sup>39</sup> In order to enhance the degree of crystallinity, crystallisation of polymers can be carried out either by melt crystallisation, i.e. crystallising from the molten state, or by cold crystallisation, i.e. crystallising from the glassy state.<sup>40-42</sup> Even though various protocols can be found in literature, normally the P(VDF-co-TrFE) films are annealed at a temperature between the Curie transition ( $T_{Curie}$ ) and melting ( $T_m$ ), through a “cold crystallisation” process, for typically 2 hours. However, the choice of conditions seems mainly arbitrary.

The first challenge of this Thesis will be to define the “cold crystallisation” annealing conditions that lead to best ferroelectric properties. The role of crystallinity and polymorphism will be examined.

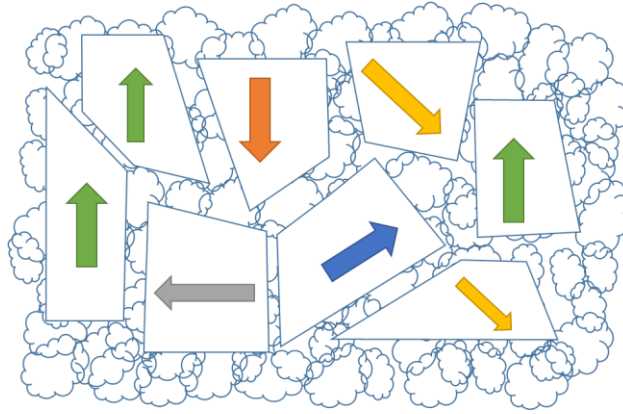


**Figure 1.11** Schematic representation of a ferroelectric semi-crystalline material: the crystallites are illustrated as quadrilaterals with a defined orientation of the ferroelectric domain; the curved features correspond to the amorphous regions.

Concerning polymorphism, the lack of a unified terminology and theory for the P(VDF-co-TrFE) polymorphs leads to confusion in defining the possible crystalline phases in which the copolymer can crystallise into. Especially comprehending the origin of the polymorphs is of fundamental importance to predict the formation or not of such phases, more or less ordered, more or less ferroelectric. It has been highlighted above (Chapter 1.4.2) that the appearance of defects in P(VDF-co-TrFE) cannot be neglected when we consider the crystalline phases. Since it is not possible to get rid of these imperfections, the way to control it should be investigated.

Therefore, polymorphism needs to be defined in terms of type of generated phases, the way they originate and how they affect the functional properties. In order to reply to these questions, in this Thesis we seek to reveal the structural changes at which the ferroelectric polymer P(VDF-co-TrFE) undergoes during typical processing steps in order to define how the different polymorphs are generated and how they are related to defects. To the best of our knowledge, the way that the different polymorphs affect the ferroelectric functionality has never been studied before. Herein we intent to address this issue. We will try to shine light on the role of defects on polarization switching.

Another important parameter is crystallites orientation. The intrinsic link between polarisation and dipoles orientation within the crystallites (note that the C-F dipoles are perpendicular to the polymer backbone) points out that the crystallites orientation with

respect to the applied electric field is fundamental to help the alignment and get after poling the maximum density of charges at the surface. In literature, it has been demonstrated that crystallites orientation can be varied by surface modification of the substrate or by specific processing protocols. These studies have stressed the need for a perpendicular orientation of the dipoles with respect to the substrate plane in order to achieve a high value of  $P_r$ .<sup>43,44</sup> Herein we will attempt to quantify the impact of crystallite orientation on the ferroelectric properties. To address this challenge we induce by appropriate processing various crystallite orientations and we investigate how these respond to the electric field.

Addressing the challenges described above will provide the tool to modulate the ferroelectric performance of P(VDF-*co*-TrFE) in organic electronic devices through tuning its structure. This Thesis will shine light in the processing-structure-function relations of P(VDF-*co*-TrFE).

Finally, two applications of P(VDF-*co*-TrFE) in organic electronics will be explored in this Thesis. The first one concerns the implementation of P(VDF-*co*-TrFE) in medical piezoelectric sensors for laparoscopic simulation.

The goal is to design and optimise flexible piezoelectric catheter sensors that that allows mapping different regions of a 3D plastic heart used in training sessions by students to simulate surgery investigation. The second application is based on a more complex structure than that of a simple capacitor. Electronic devices in which P(VDF-*co*-TrFE) is blended with the semiconducting polymer P3HT will be studied. P(VDF-*co*-TrFE):P3HT blends form a phase separated active layer whose morphology at the nanoscale is critical for the operation of the devices made thereafter.<sup>45</sup> This blend has been already used in non-volatile ferroelectric diodes. Herein the potential of employing it in order to build un-conventional organic photovoltaics devices is explored.

## 1.5 Thesis Outline

After having highlighted the main objectives and challenges of this Thesis entitled “Ferroelectric polymers for organic electronic applications”, we conclude this introductory Chapter with the Thesis outlook.

In **Chapter 2** the thermal processing conditions that lead to an optimised ferroelectric function in terms of high  $P_r$  and low  $E_c$  will be defined. Since cold crystallisation is the post-deposition treatment normally used for organic electronic devices, a study of the effect of thermal annealing at various temperatures between the crystallisation onset and the melting temperature of P(VDF-co-trFE) is performed for various annealing times. The crystallization properties induced by applied these thermal protocols are investigated by means of grazing incidence wide angle x-ray scattering, GIWAXS, while the effect of processing on the ferroelectric properties is investigated by means of polarisation hysteresis loops.

**Chapter 3** is focused on exploring the polymorphism of P(VDF-co-TrFE). In order to identify the various crystalline phases generated in P(VDF-co-TrFE) during thermal annealing, the phase transitions that the polymer undergoes have been followed by means of time-resolved WAXS and DSC employing an isothermal melt crystallisation protocol. Starting from the molten state, we study how different isothermal crystallization temperatures,  $T_c$ , affect the appearance of defective ferroelectric crystalline phases, as well as the ferroelectric performance. A thorough investigation of the ferroelectric and paraelectric crystalline phases that appear during the Curie transition is presented. The combination of time resolved WAXS and DSC employed herein allows following these structural transitions with a unique precision and to unveil the P(VDF-co-TrFE)'s polymorphism in an unprecedented way.

In **Chapter 4** the effect of crystallites orientation is studied. Huge differences on structure, including a crystallites orientation change, have been generated by applying disruptive thermal protocols. It is discussed and quantified how the inversion of crystallites orientation with respect to the substrate play an important role on the device response to the applied electric field and on the shape of the ferroelectric hysteresis loops, thus on device function.

In **Chapter 5** an application of P(VDF-co-TrFE) is demonstrated. Thick films are used to build a pressure sensor for medical catheter applications. In this Chapter the achievements of the

work carried out for a project named “sweet heart” conducted in collaboration with the research centre *Liryc (L’Institut de Rythmologie et modélisation Cardiaque)* are presented. Flexible piezoelectric devices have been fabricated and characterised. A flexible sensor that can map different regions of a 3D-printed heart that will serve for laparoscopic simulation has been developed.

Finally, in **Chapter 6** thin films made of a ferroelectric: semiconducting polymer blend are investigated. P(VDF-*co*-TrFE) is blended with the semiconducting P3HT and the phase separated morphology that results for different weight ratios (95:5, 90:10, 80:20) is studied by means of several scanning probe microscopy techniques such as AFM, PFM, KPFM, CFM. The performance of devices that incorporate this blend is then investigated in order to evaluate the potential application of this blend in un-conventional photovoltaic devices.

## References

- 1 Lovinger, A. J. Ferroelectric polymers. *Science* **220**, 1115-1121 (1983).
- 2 Sessler, G. M. Piezoelectricity in polyvinylidene fluoride. *The Journal of the Acoustical Society of America* **70**, 1596-1608, doi:10.1121/1.387225 (1981).
- 3 Naber, R. C. G., Asadi, K., Blom, P. W. M., de Leeuw, D. M. & de Boer, B. Organic Nonvolatile Memory Devices Based on Ferroelectricity. *Advanced Materials* **22**, 933-945, doi:10.1002/adma.200900759 (2010).
- 4 Asadi, K. *et al.* Spinodal Decomposition of Blends of Semiconducting and Ferroelectric Polymers. *Advanced Functional Materials* **21**, 1887-1894, doi:10.1002/adfm.201001505 (2011).
- 5 Nalwa, K. S. *et al.* Enhanced charge separation in organic photovoltaic films doped with ferroelectric dipoles. *Energy Environ. Sci.* **5**, 7042-7049, doi:10.1039/c2ee03478f (2012).
- 6 Naber, R. C. G. *et al.* High-performance solution-processed polymer ferroelectric field-effect transistors. *Nature Materials* **4**, 243-248, doi:10.1038/nmat1329 (2005).
- 7 Asadi, K., De Leeuw, D. M., De Boer, B. & Blom, P. W. M. Organic non-volatile memories from ferroelectric phase-separated blends. *Nature Materials* **7**, 547-550, doi:10.1038/nmat2207 (2008).
- 8 Lee, J.-H. *et al.* Highly sensitive stretchable transparent piezoelectric nanogenerators. *Energy Environ. Sci.* **6**, 169-175, doi:10.1039/c2ee23530g (2013).
- 9 Pi, Z., Zhang, J., Wen, C., Zhang, Z.-b. & Wu, D. Flexible piezoelectric nanogenerator made of poly(vinylidene fluoride-co-trifluoroethylene) (PVDF-TrFE) thin film. *Nano Energy* **7**, 33-41, doi:http://dx.doi.org/10.1016/j.nanoen.2014.04.016 (2014).
- 10 Lee, J.-H. *et al.* Micropatterned P(VDF-TrFE) Film-Based Piezoelectric Nanogenerators for Highly Sensitive Self-Powered Pressure Sensors. *Adv. Funct. Mater.* **25**, 3203-3209, doi:10.1002/adfm.201500856 (2015).
- 11 West, A. R. *Solid state chemistry and its applications.* (Wiley, 2014).
- 12 Kim, K. J. & Kim, G. B. Curie transition, ferroelectric crystal structure and ferroelectricity of a VDF/TrFE (75/25) copolymer: 2. The effect of poling on curie transition and ferroelectric crystal structure. *Polymer* **38**, 4881-4889 (1997).

- 13 Xia, W., Wang, Z., Xing, J., Cao, C. & Xu, Z. The Dependence of Dielectric and Ferroelectric Properties on Crystal Phase Structures of the Hydrogenized P(VDF-TrFE) Films With Different Thermal Processing. *IEEE Transactions on Ultrasonics, Ferroelectrics, and Frequency Control* **63**, 1674-1680, doi:10.1109/tuffc.2016.2594140 (2016).
- 14 Hasegawa, R., Takahashi, Y., Chatani, Y. & Tadokoro, H. Crystal Structures of Three Crystalline Forms of Poly(vinylidene fluoride). *Polym J* **3**, 600-610, doi:10.1295/polymj.3.600 (1972).
- 15 Tashiro, K. & Kobayashi, M. Structural phase transition in ferroelectric fluorine polymers: X-ray diffraction and infrared/Raman spectroscopic study. *Phase Transit.* **18**, 213-246, doi:10.1080/01411598908206864 (1989).
- 16 Lovinger, A. J., Furukawa, T., Davis, G. T. & Broadhurst, M. G. Crystallographic changes characterizing the Curie transition in three ferroelectric copolymers of vinylidene fluoride and trifluoroethylene: 1. As-crystallized samples. *Polymer* **24**, 1225-1232, doi:http://dx.doi.org/10.1016/0032-3861(83)90050-2 (1983).
- 17 Furukawa, T. Ferroelectric properties of vinylidene fluoride copolymers. *Phase Transit.* **18**, 143-211, doi:10.1080/01411598908206863 (1989).
- 18 Martins, P., Lopes, A. C. & Lanceros-Mendez, S. Electroactive phases of poly(vinylidene fluoride): Determination, processing and applications. *Progress in Polymer Science* **39**, 683-706, doi:https://doi.org/10.1016/j.progpolymsci.2013.07.006 (2014).
- 19 Lovinger, A. J. in *Developments in Crystalline Polymers—1* (ed D. C. Bassett) 195-273 (Springer Netherlands, 1982).
- 20 Gregorio Jr, R. Determination of the  $\alpha$ ,  $\beta$ , and  $\gamma$  crystalline phases of poly(vinylidene fluoride) films prepared at different conditions. *Journal of Applied Polymer Science* **100**, 3272-3279, doi:10.1002/app.23137 (2006).
- 21 Kobayashi, M., Tashiro, K. & Tadokoro, H. Molecular Vibrations of Three Crystal Forms of Poly(vinylidene fluoride). *Macromolecules* **8**, 158-171, doi:10.1021/ma60044a013 (1975).
- 22 Miyazaki, T., Takeda, Y., Akasaka, M., Sakai, M. & Hoshiko, A. Preparation of Isothermally Crystallized  $\gamma$ -Form Poly(vinylidene fluoride) Films by Adding a KBr Powder as a Nucleating Agent. *Macromolecules* **41**, 2749-2753, doi:10.1021/ma702691c (2008).

- 23 Gregorio, J. R. & Cestari, M. Effect of crystallization temperature on the crystalline phase content and morphology of poly(vinylidene fluoride). *Journal of Polymer Science Part B: Polymer Physics* **32**, 859-870, doi:10.1002/polb.1994.090320509 (1994).
- 24 Soulestin, T., Ladmiral, V., Dos Santos, F.D., Améduri, B. Vinylidene fluoride- and trifluoroethylene-containing fluorinated electroactive copolymers. How does chemistry impact properties? *Progress in Polymer Science* **72**, 16-60, (2017).
- 25 Ameduri, B., From Vinylidene Fluoride (VDF) to the Applications of VDF-Containing Polymers and Copolymers: Recent Developments and Future Trends, *Chemical Reviews* **109 (12)**, 6632-6686, (2009).
- 26 Lovinger, A. J., Davis, G. T., Furukawa, T. & Broadhurst, M. G. Crystalline forms in a copolymer of vinylidene fluoride and trifluoroethylene (52/48 mol %). *Macromolecules* **15**, 323-328, doi:10.1021/ma00230a024 (1982).
- 27 Tashiro, K., Takano, K., Kobayashi, M., Chatani, Y. & Tadokoro, H. Structural study on ferroelectric phase transition of vinylidene fluoride-trifluoroethylene copolymers (III) dependence of transitional behavior on VDF molar content. *Ferroelectrics* **57**, 297-326, doi:10.1080/00150198408012770 (1984).
- 28 Koga, K. & Ohigashi, H. Piezoelectricity and related properties of vinylidene fluoride and trifluoroethylene copolymers. *Journal of Applied Physics* **59**, 2142-2150, doi:10.1063/1.336351 (1986).
- 29 Koga, K., Nakano, N., Hattori, T. & Ohigashi, H. Crystallization, field-induced phase transformation, thermally induced phase transition, and piezoelectric activity in P(vinylidene fluoride-TrFE) copolymers with high molar content of vinylidene fluoride. *Journal of Applied Physics* **67**, 965-974, doi:10.1063/1.345706 (1990).
- 30 Kim, K. J., Kim, G. B., Vanlencia, C. L. & Rabolt, J. F. Curie transition, ferroelectric crystal structure, and ferroelectricity of a VDF/TrFE(75/25) copolymer 1. The effect of the consecutive annealing in the ferroelectric state on curie transition and ferroelectric crystal structure. *Journal of Polymer Science Part B: Polymer Physics* **32**, 2435-2444, doi:10.1002/polb.1994.090321501 (1994).
- 31 Gregorio, R. & Botta, M. M. Effect of crystallization temperature on the phase transitions of P(VDF/TrFE) copolymers. *Journal of Polymer Science Part B: Polymer Physics* **36**, 403-414, doi:10.1002/(sici)1099-0488(199802)36:3<403::aid-polb2>3.0.co;2-s (1998).

- 32 Stack, G. M. & Ting, R. Y. Thermodynamic and morphological studies of the solid-state transition in copolymers of vinylidene fluoride and trifluoroethylene. *J. Polym. Sci. B Polym. Phys.* **26**, 55-64, doi:10.1002/polb.1988.090260102 (1988).
- 33 Bargain, F., Panine, P., Domingues Dos Santos, F. & Tencé-Girault, S. From solvent-cast to annealed and poled poly(VDF-co-TrFE) films: New insights on the defective ferroelectric phase. *Polymer* **105**, 144-156, doi:http://doi.org/10.1016/j.polymer.2016.10.010 (2016).
- 34 Mao, D., Quevedo-Lopez, M. A., Stiegler, H., Gnade, B. E. & Alshareef, H. N. Optimization of poly(vinylidene fluoride-trifluoroethylene) films as non-volatile memory for flexible electronics. *Org. Electron.* **11**, 925-932, doi:https://doi.org/10.1016/j.orgel.2010.02.012 (2010).
- 35 Guo, D., Stolichnov, I. & Setter, N. Thermally Induced Cooperative Molecular Reorientation and Nanoscale Polarization Switching Behaviors of Ultrathin Poly(vinylidene fluoride-trifluoroethylene) Films. *The Journal of Physical Chemistry B* **115**, 13455-13466, doi:10.1021/jp2061442 (2011).
- 36 Mahdi, R., Gan, W. & Majid, W. Hot Plate Annealing at a Low Temperature of a Thin Ferroelectric P(VDF-TrFE) Film with an Improved Crystalline Structure for Sensors and Actuators. *Sensors* **14**, 19115 (2014).
- 37 Aliane, A. *et al.* Impact of crystallization on ferro-, piezo- and pyro-electric characteristics in thin film P(VDF-TrFE). *Org. Electron.: phys. mater. appl.* **25**, 92-98, doi:10.1016/j.orgel.2015.06.007 (2015).
- 38 Kim, J. *et al.* High-Performance Piezoelectric, Pyroelectric, and Triboelectric Nanogenerators Based on P(VDF-TrFE) with Controlled Crystallinity and Dipole Alignment. *Adv. Funct. Mater.* **27**, 1700702-n/a, doi:10.1002/adfm.201700702 (2017).
- 39 Bellet-Amalric, E. & Legrand, J. F. Crystalline structures and phase transition of the ferroelectric P(VDF-TrFE) copolymers, a neutron diffraction study. *Eur Phys J B* **3**, 225-236 (1998).
- 40 Qiu, Z., Ikehara, T. & Nishi, T. Crystallization behaviour of biodegradable poly(ethylene succinate) from the amorphous state. *Polymer* **44**, 5429-5437, doi:https://doi.org/10.1016/S0032-3861(03)00577-9 (2003).
- 41 Supaphol, P. & Spruiell, J. E. Isothermal melt- and cold-crystallization kinetics and subsequent melting behavior in syndiotactic polypropylene: a differential scanning

- calorimetry study. *Polymer* **42**, 699-712, doi:[https://doi.org/10.1016/S0032-3861\(00\)00399-2](https://doi.org/10.1016/S0032-3861(00)00399-2) (2001).
- 42 Vasanthan, N., Manne, N. J. & Krishnama, A. Effect of Molecular Orientation on the Cold Crystallization of Amorphous–Crystallizable Polymers: The Case of Poly(trimethylene terephthalate). *Industrial & Engineering Chemistry Research* **52**, 17920-17926, doi:10.1021/ie402860t (2013).
- 43 Park, Y. J. *et al.* Molecular and Crystalline Microstructure of Ferroelectric Poly(vinylidene fluoride-co-trifluoroethylene) Ultrathin Films on Bare and Self-Assembled Monolayer-Modified Au Substrates. *Macromolecules* **41**, 109-119, doi:10.1021/ma0718705 (2008).
- 44 Park, Y. J. *et al.* Irreversible extinction of ferroelectric polarization in P(VDF-TrFE) thin films upon melting and recrystallization. *Applied Physics Letters* **88**, 242908, doi:10.1063/1.2207831 (2006).
- 45 Lacroix, C. *Etude des mélanges de polymères semi-conducteur / ferroélectrique en films minces : application en électronique organique.*, Université de Bordeaux, (2014).

# Chapter 2

*Optimisation  
of the ferroelectric properties  
of cold-crystallised  
P(VDF-co-TrFE) films*



## 2 Optimisation of the ferroelectric properties of cold-crystallised P(VDF-co-TrFE) films

### 2.1 Introduction

In order to enhance device performance in view of the use of P(VDF-co-TrFE) in organic electronic applications, the functionality brought by the ferroelectric film should be maximised. In particular, the ferroelectric performance of P(VDF-co-TrFE) is known to depend on its structure, which in turns can be tuned through film processing. Given the intrinsic link between polarisation and dipoles orientation within the P(VDF-co-TrFE) crystallites,<sup>1</sup> triggering the crystalline structure of the polymer is expected to affect ferroelectric properties.

In organic electronics, devices are mainly layered structures that are complemented by the deposition of electrodes on both surfaces of this multilayer. The organic films are commonly formed by doctor blading, dip-coating, spray-coating, etc. Among film disposition techniques, spin coating is maybe the most used one for lab-scale device fabrication (i.e. before passing to industrial-scale production) thanks to its simplicity, low cost, and possibility to modulate the thickness of uniform films through variation of the deposition parameters. After deposition, organic thin films are usually subjected to a thermal treatment in order to eliminate solvent that is eventually trapped in the film, or improve surface smoothness, or, most commonly, to enhance crystallinity. In this latter case, one can consider that “cold-crystallisation” takes place. Therefore, to comply with the procedures followed for organic electronic devices fabrication, in this Chapter we study the “cold-crystallisation” of spun-cast P(VDF-co-TrFE) films and we correlate annealing conditions to ferroelectric properties.

Semi-crystalline polymers are able to crystallise between their glass transition temperature,  $T_g$ , and melting,  $T_m$ . Depending on the initial state, the crystallisation process can be classified as: i) melt crystallisation, when the initial state is the molten one. In this case the polymer should be annealed at  $T > T_m$  for few minutes to assure that all crystallites have

melted, and then cool down and let crystallise at a crystallisation temperature  $T_c < T_m$ . ii) cold crystallisation, when the initial state is the amorphous or a partially crystalline one. After spin-coating at room temperature, P(VDF-co-TrFE) is already in a partially crystalline state. Note that at room temperature P(VDF-co-TrFE) is already above its glass transition ( $T_g \approx -50$  °C). Annealing its films at  $T_g < T_c < T_m$  will result in an increase of crystallinity, since this is energetically favourable for the polymer chains that during spin-coating have been “trapped” in the amorphous state. Therefore, the thermal treatment at  $T_c < T_m$  that is applied after spin-coating can be indeed considered as “cold-crystallisation”.

By modulating the thermal processing conditions, i.e. annealing temperature and annealing time, crystallinity can be enhanced and, subsequently, the ferroelectric performance can be improved. Although investigations of the bulk crystalline structure of bulk P(VDF-co-TrFE) have been attempted in literature since the 80's, <sup>2-12</sup> studies that relate film processing conditions to the final ferroelectric properties are rare <sup>13-20</sup> and concern only the effect of annealing temperature or solvent casting. In literature several annealing conditions for the processing of P(VDF-co-TrFE) can be found. Just to mention a few, annealing temperatures of 120 °C,<sup>21</sup> 130 °C,<sup>18</sup> 135 °C,<sup>8,10,22</sup> 140 °C,<sup>23,24</sup> have been applied during various annealing times such as 30 minutes,<sup>18</sup> 1 hour,<sup>17,25</sup> 2 h,<sup>23,26,27</sup> 5 h,<sup>28</sup> 8 h,<sup>14</sup> 12 h,<sup>8,9,27</sup> or even 24 hours.<sup>21</sup> However, no justification is provided. The choice of annealing conditions seems arbitrary and mostly depends on empirical observations.

In this Chapter, a study of the effect of cold crystallisation conditions on the structural properties dictating the ferroelectric performance of P(VDF-co-TrFE) is conducted in order to find the processing conditions that result in optimum ferroelectric performance of P(VDF-co-TrFE) thin films. The work presented herein has been published in *Polymer* (Spampinato *et al.*)

## 2.2 Samples preparation

A 10<sub>wt</sub>% solution of P(VDF-co-TrFE) (75-25 VDF/TrFE molar ratio) in cyclopentanone has been spin-coated onto Si substrates (for GIWAXS) or on Al/glass substrates (for capacitors). The films were annealed on a precision hot plate with a rate of 5 °C min<sup>-1</sup> from room temperature until the temperature of choice (130 °C, 133 °C, 135 °C, 137 °C, 140 °C). The

temperature range explored is set between the crystallisation onset temperature,  $T_c$ , and the melting temperature,  $T_m$ , because in this range an enhanced degree of crystallinity, driven by the rearrangement of molecular chains, is induced.<sup>23</sup>  $T_c$  and  $T_m$  were determined by DSC scans performed on P(VDF-co-TrFE) powder from room temperature to 200 °C at a heating/cooling rate of 10 °C min<sup>-1</sup> (Figure 2.1a where the first cooling and the second heating ramps are shown). Already during this heating ramp the cold-crystallisation of the films is initiated, as proven by the DSC exothermic peak in Figure 2.1b which shows a zoom of the first DSC cycle of a drop-casted self-standing P(VDF-co-TrFE) film. The heating ramp applied mimics the preparation conditions used for the films under study.

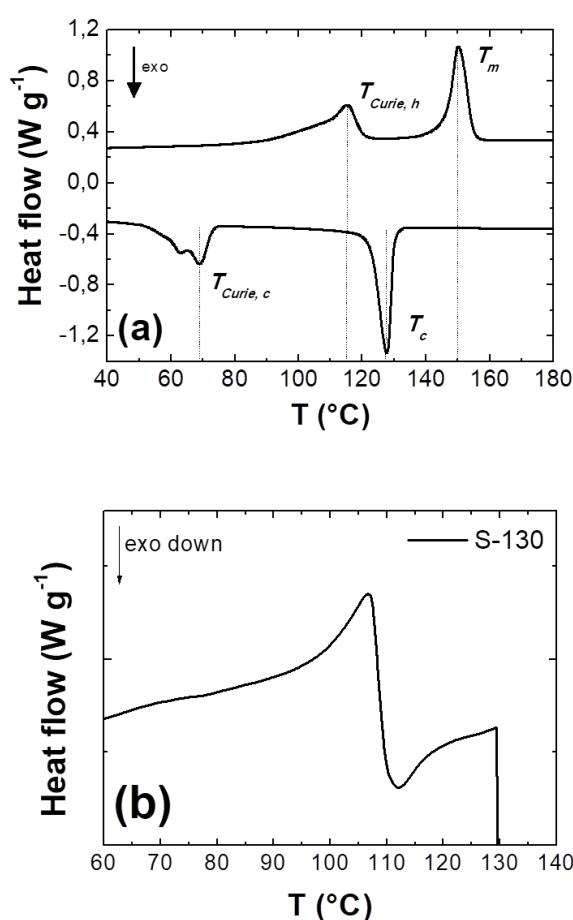


**Figure 2.1** (a) DSC curve of P(VDF-co-TrFE) 75/25 powder. A first heating ramp was used to erase thermal history, herein we present the first cooling and the second heating ramps, in consistence with common practice. (b) DSC curves of P(VDF-co-TrFE) self-standing film. A zoom of the first heating ramp that mimics the thermal treatment of the sample S-130 is displayed. The exothermic peak after the Curie transition suggests that no previous treatment has been performed.

Then an isothermal annealing step is performed at the selected temperature for 5 min, 15 min, 30 min, 1 h or 2 h, during which cold-crystallisation continues. Finally, the films were let to cool down to room temperature slowly, with a cooling rate of  $1.6\text{ }^{\circ}\text{C min}^{-1}$  on the same hot stage.

Additionally, a pristine film (i.e. not thermally treated) has been studied and used as a reference sample. Among all different combinations of annealing temperatures and times tested, we present herein two series of samples that are representative of the effect of temperature and of the effect of annealing time.

Capacitors were fabricated for the ferroelectric characterizations. 100 nm thick aluminium electrodes were thermally evaporated onto clean glass substrates and P(VDF-co-TrFE) films of  $1\text{ }\mu\text{m}$  were spin-coated on top. 100 nm thick Al films were finally thermally evaporated to form the top electrode. The temperature inside the evaporator was kept below  $70\text{ }^{\circ}\text{C}$ , i.e. below the Curie transition temperature, to avoid undergoing the ferroelectric-to-paraelectric transition. The thermal treatment of P(VDF-co-TrFE) has been performed on the devices (i.e. after top electrode deposition) following the procedure described above.

## 2.3 Results and discussion

Depending on thermal processing conditions, the ferroelectric properties of P(VDF-co-TrFE) films change significantly. Figure 2.2a presents the polarisation vs electric field ( $P$  vs  $E$ ) hysteresis loops recorded by applying an external oscillating electric field of amplitude  $150\text{ MV m}^{-1}$  under a frequency of  $0.1\text{ Hz}$  for the P(VDF-co-TrFE) films isothermally annealed at various crystallisation temperatures during a fixed time of 15 min. Hereinafter these samples will be called T-130, T-133, T-135, T-137, T-140, where the number denoted the isothermal crystallization temperature.

The response of the not annealed (pristine) film with respect to the annealed ones clearly shows the drastic overall effect of thermal treatment: an enhanced ferroelectric response is achieved after annealing. The remnant polarisation,  $P_r$ , almost doubles (from  $38\text{ mC m}^{-2}$  for the not annealed to  $70\text{ mC m}^{-2}$  for T-130) while the coercive field,  $E_c$ , reduces to half (from  $96\text{ MV m}^{-1}$  for the not annealed to  $56\text{ MV m}^{-1}$  for T-130). Concerning the annealed devices,

samples T-130 and T-140 exhibit lower  $P_r$  compared to samples T-133, T-135 and T-137 that were annealed at temperatures close to the crystallisation onset (Figure 2.2a). That latter exhibits a very high  $P_r$ , almost  $90 \text{ mC m}^{-2}$ .  $E_c$  is only mildly dependent on annealing temperature, it is lower than  $57 \text{ MV m}^{-1}$  for all annealed samples and it exhibits a minimum of  $50 \text{ MV m}^{-1}$  for sample T-135. Figure 2.2b presents the corresponding electric current vs electric field ( $I$  vs  $E$ ) curves. Sharper switching current peaks are recorded for T-133 and T-135, which suggest a faster ferroelectric switching. We thus conclude that T-135 exhibits the best ferroelectric response in terms of faster switching rate, lower  $E_c$  ( $50 \text{ MV m}^{-1}$ ), higher  $P_r$  ( $89 \text{ mC m}^{-2}$ ). Hence, this temperature has been chosen to show the effect of annealing time on ferroelectric properties.

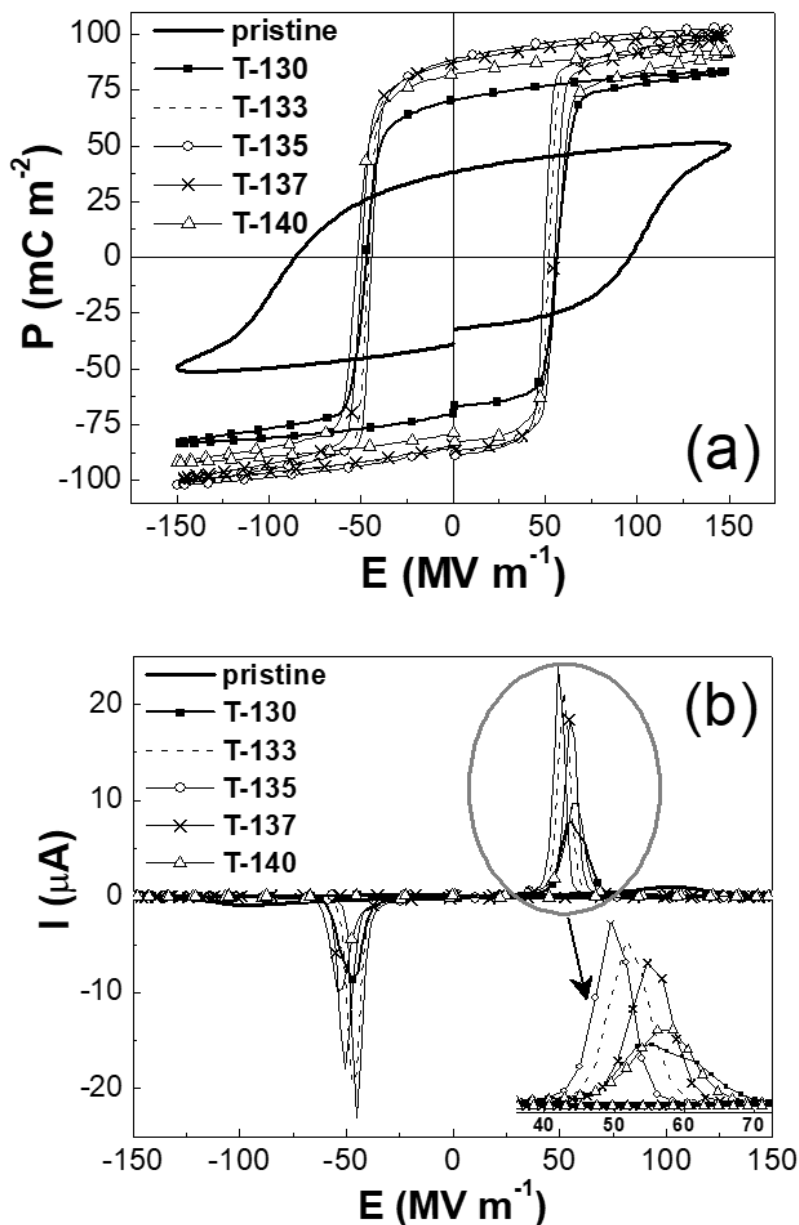


**Figure 2.2** (a) Polarisation vs electric field hysteresis loops for the pristine sample and for those annealed at 130 °C, 133 °C, 135 °C, 137 °C and 140 °C for 15 min, and (b) the corresponding current vs electric field data. The height of the symbols on the polarisation curves corresponds to the error bar associated with the remnant polarisation.

Figure 2.3a presents the hysteresis loops obtained for the samples isothermally crystallised at 135 °C during various annealing times. Hereinafter these samples will be called t-5, t-15, t-30, t-60, t-120, where the number denotes the annealing time in minutes. Annealing for just 5 min already results in a decrease of  $E_c$  from 96  $\text{MV m}^{-1}$  for the pristine film to 78  $\text{MV m}^{-1}$ , which further decreases to 50  $\text{MV m}^{-1}$  for samples annealed for 15 min (t-15) and 30 min (t-

30) (Figure 2.3a). This is the lowest electric field for the ferroelectric switching process. However, increasing annealing time above 30 min results in an increased  $E_c$ . In consistence with this observation, the corresponding switching current peaks are significantly shifted along the electric field axis (Figure 2.3b). The sharper ones are centred at the lowest  $E_c$  and correspond to samples t-15 and t-30. As far as  $P_r$  is concerned, no trend is observed. A 5 min annealing already results in a high  $P_r$  value of 82  $\text{mC m}^{-2}$ , close to the maximum  $P_r$  obtained for t-15.

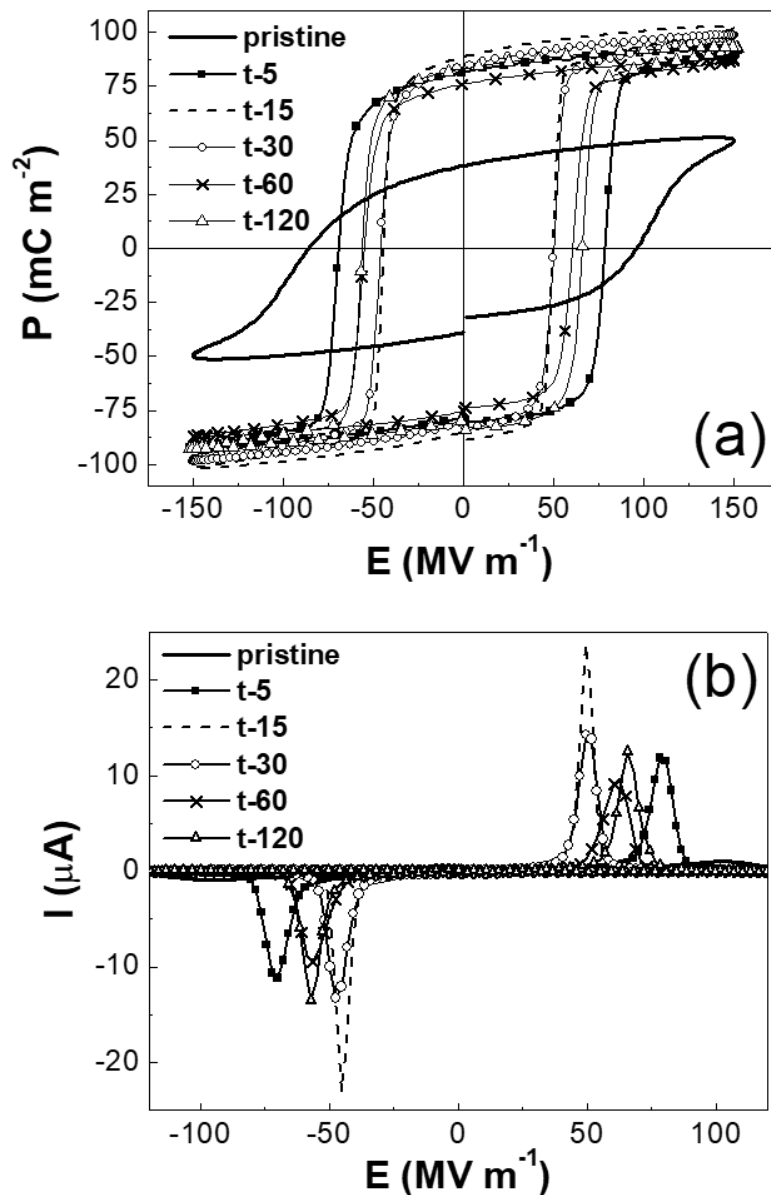


**Figure 2.3** (a) Polarisation vs electric field hysteresis loops for the pristine sample and for those annealed at 135 °C for 5 min, 15 min, 30 min, 60 min and 120 min. (b) the corresponding current vs electric field data. The height of the symbols on the polarisation curves corresponds to the error bar associated with the remnant polarisation.

Two main conclusions can be derived from these experiments. First, annealing temperature mostly affects remnant polarisation, while annealing time has more influence on coercive field. Figure 2.4a and Figure 2.4b respectively show the effect of temperature on  $P_r$  and the effect of time on  $E_c$ , as these were discussed above. This result already provides a tool for tuning ferroelectric properties through processing. When one seeks to increase the surface charge density – and thus the amount of information stored in a device – annealing temperature should be modulated. On the other hand, if promoting a fast ferroelectric switching is the objective, one should tune the annealing time.

The second conclusion concerns the processing conditions that should be applied for optimum ferroelectric performance. The shaded areas in Figure 2.4a and Figure 2.4b suggest that a maximum polarisation and a minimum coercive field are achieved when the isothermal cold-crystallisation step is performed in the temperature range between 133 °C and 137 °C for short annealing times of only 15 to 30 min. This processing conditions result not only in high  $P_r$  and low  $E_c$  but also in square hysteresis loops with minor polarisation losses when passing from the saturated polarisation  $P_s$  to the remnant value  $P_r$ , fast switching and, thus, very good bistability of the ferroelectric properties of the prepared devices.

In fact, the result that optimum ferroelectric response is achieved for only 15 min of annealing is particularly interesting for industrial applications where time-consuming and energy-consuming treatments are not desirable. Here it is demonstrated that long annealing treatments are not necessary since they do not lead to a functional improvement but rather deteriorate device performance. We can conclude that the 2 h annealing step has been mostly used so far <sup>23,26,27</sup> can be replaced by a shorter and more efficient thermal treatment such as that resulting from our study.

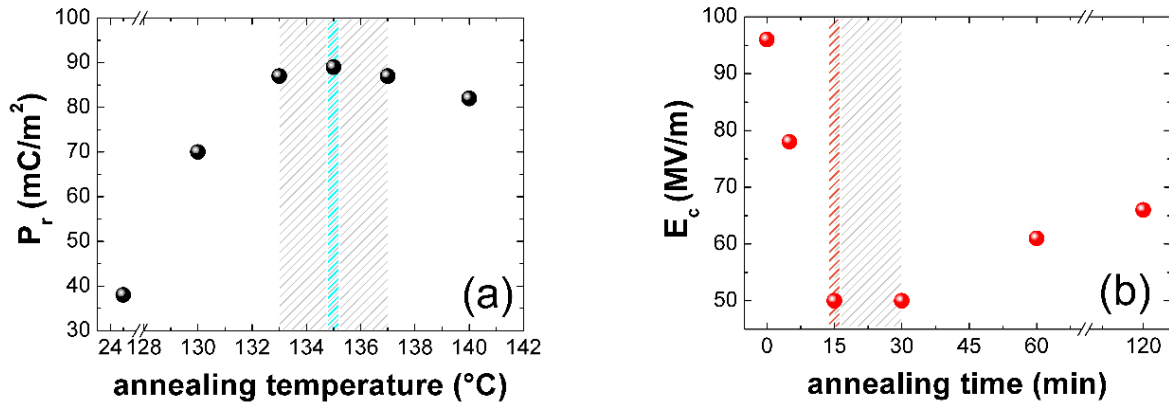


**Figure 2.4** (a) Effect of annealing temperature on  $P_r$  and, (b) effect of annealing time on  $E_c$ .

In order to explore the origin of this enhanced ferroelectric performance under certain processing conditions, grazing incidence wide-angle x-ray scattering (GIWAXS) experiments have been performed. This experiment allows to identify and quantify the crystalline phases present in P(VDF-co-TrFE) films. Films for GIWAXS have been deposited on Si substrates following the same processing conditions as those followed for the fabrication of the capacitors. Si has been chosen instead of Al because it scatters less than Al. This is important for a quantitative analysis as the one endeavoured below since all background contributions should be removed as precisely as possible. Nonetheless, we have cross-checked that the orientation of the crystallites is not affected by the choice of the substrate.

2D scattering patterns have been recorded at room temperature for all films processed using the same thermal protocols studied above (inset in Figure 2.5a, Figure 2.6 and Figure 2.7). All necessary corrections (listed in the Annex Section) have been applied to the raw GIWAXS patterns, including background scattering subtraction and wedge correction.<sup>29</sup> The corrected 2D images were radially integrated to extract the 1D scattered intensity vs scattering vector (*Intensity vs q*) patterns (such as the one presented in Figure 2.5a).

Figure 2.5a shows the *Intensity vs q* scattering pattern obtained for the film that was annealed at 135 °C for 15 min while the corresponding wedge-corrected 2D image is presented in the inset. This pattern includes the typical reflections that are assigned to the ferroelectric orthorhombic unit cell of P(VDF-co-TrFE).<sup>9,11,30,31</sup> The first peak at around  $1.5 \text{ \AA}^{-1}$  corresponds to a combination of the (200) and (110) reflections, the second peak at  $2.6 \text{ \AA}^{-1}$  to the superposition of (001), (310) and (020) planes, and the third one at  $3 \text{ \AA}^{-1}$  is assigned to the

(111) and (201) reflections, which spatially overlap with the second order reflections (220) and (400).

In the scattering image, the (110),(200) reflection appears more intense on the meridian, which is consistent with a preferential orientation of the *c*-axis (that corresponds to the chain backbone) parallel to the substrate.<sup>26</sup> This crystal orientation favours ferroelectricity, since in P(VDF-*co*-TrFE) the dipoles that induce the ferroelectric property are perpendicular to the backbone and therefore in this case they are oriented parallel to the external applied electric field. All films under study exhibit this orientation, as apparent in Figure 2.6 and Figure 2.7, except sample T-140 that will be discussed later on.

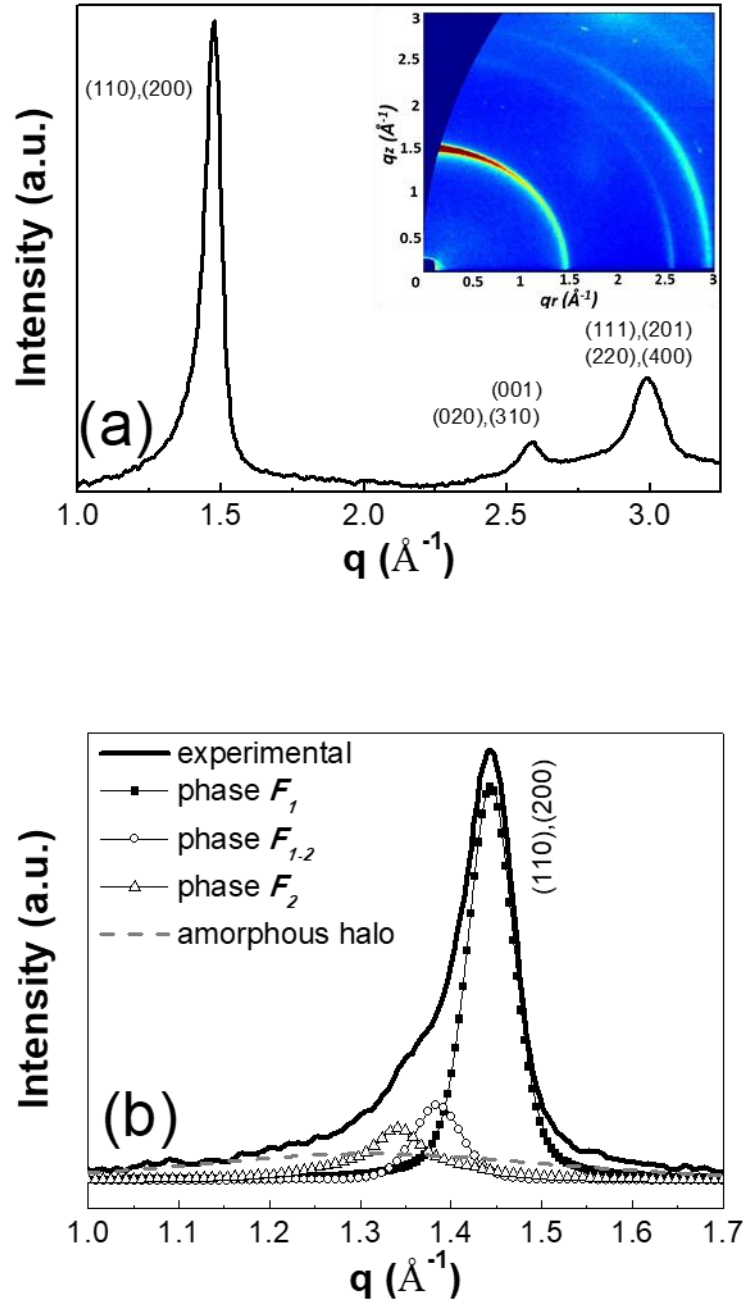


**Figure 2.5** a) The 1D GIWAXS pattern obtained for the films annealed at 135 °C for 15 min and the corresponding 2D wedge-corrected GIWAXS image (inset). b) A zoom at the (110),(200) peak, along with the fitted curves that were used to deconvolute this peak.

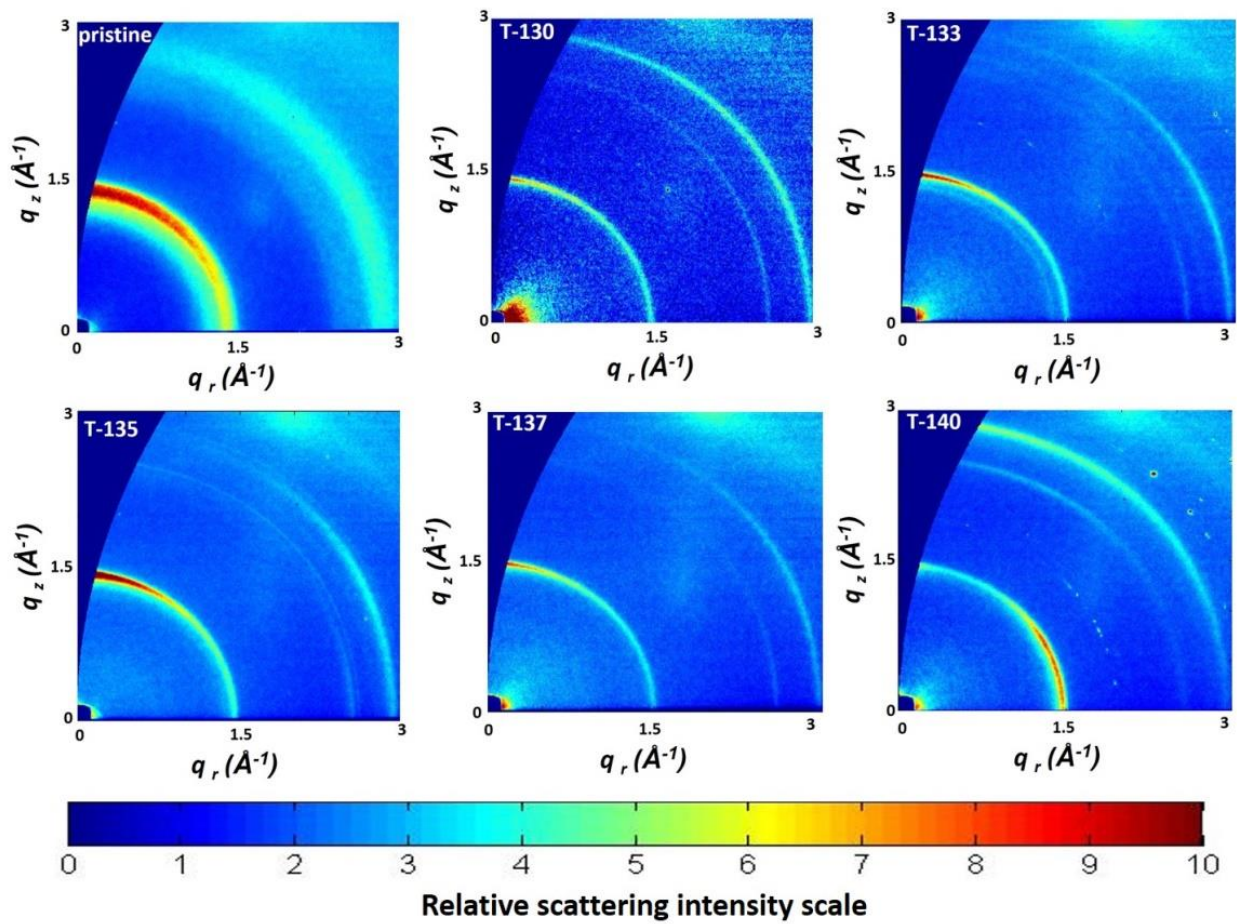


**Figure 2.6** Wedge-corrected GIWAXS images of the samples annealed for 15 min at different temperatures.

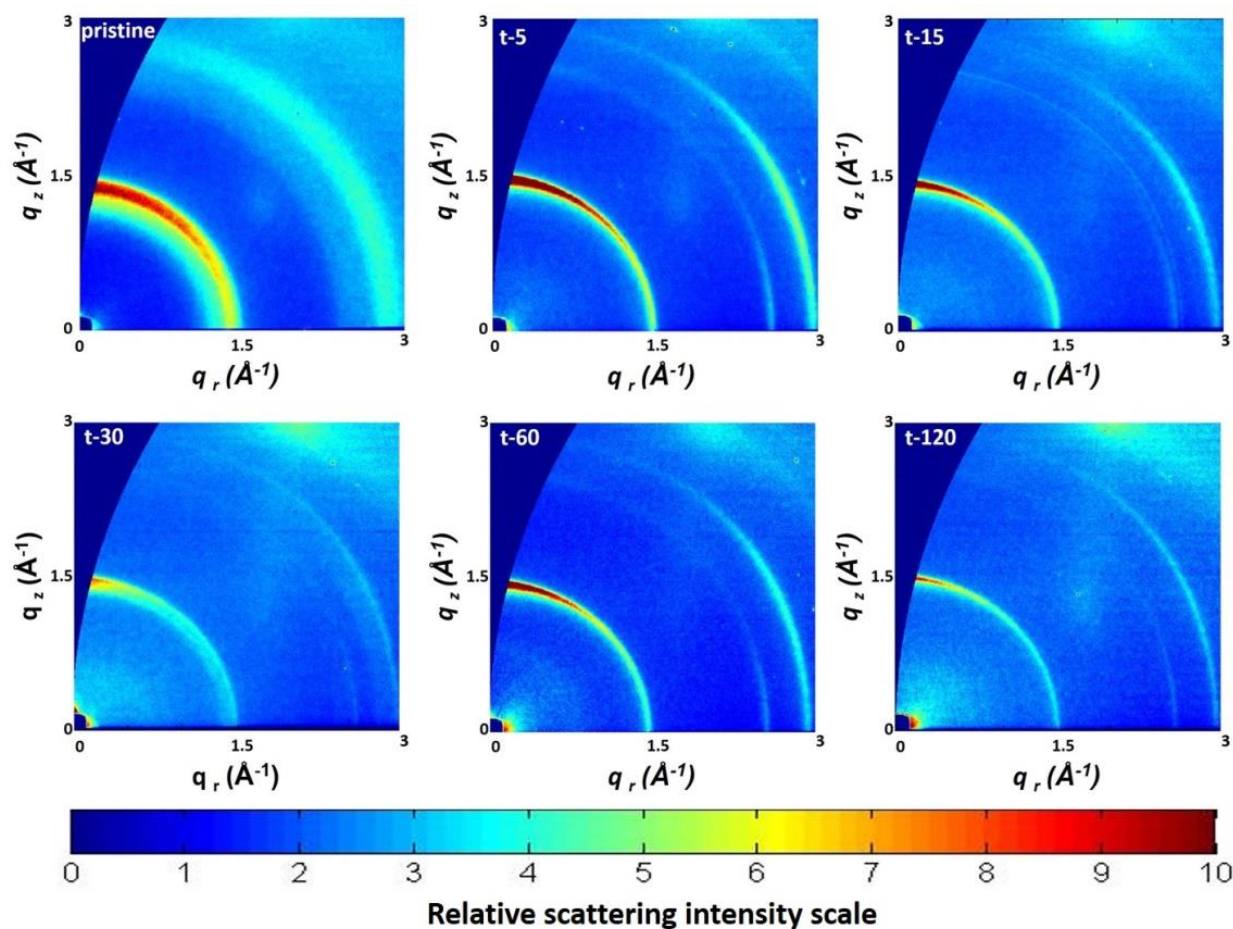


**Figure 2.7** Wedge-corrected GIWAXS images of the samples annealed at 135 °C for different times.

According to current understanding concerning the phase transitions in P(VDF-co-TrFE),<sup>3,7-10,32-34</sup> no paraelectric phase exists below the Curie temperature but only ferroelectric ones. In particular Kim *et al.*<sup>8,9</sup> and Gregorio *et al.*<sup>32</sup> examined the Curie transition mainly by DSC and concluded that several ferroelectric phases can co-exist at room temperature, having different amounts of conformational gauche defects and hence different thermodynamic stability.

Moreover, gauche defects are reported to induce lattice expansion, which shifts the Bragg peak to lower angles.<sup>8,9,11</sup> Indeed, the presence of defects is expected to induce a less compact packing of chains, which results in an increased  $d$ -spacing along the  $a$  and  $b$  axes and consequently in a Bragg reflection that appears at lower  $q$ -values in the reciprocal space with respect to a less- or non-defective phase. This suggests that at room temperature each ferroelectric phase – characterised by a different amount of defects – crystallises into an orthorhombic unit cell, with slightly different lattice parameters depending on the amount of

defects. Based on this, the peak at around  $1.5 \text{ \AA}^{-1}$  should be considered as the superposition of the (110),(200) reflections of different ferroelectric phases. For the analysis carried out below we deconvolute this peak into the sum of an intense, predominant peak that is assigned to a ferroelectric phase with a low degree of gauche defects, named  $F_1$ , and a second less intense peak that is centred between  $1.3 - 1.4 \text{ \AA}^{-1}$  and is assigned to a more defective ferroelectric phase, named  $F_2$ . Note that several names have appeared in literature in the past to describe ferroelectric phases with different amount of defects.<sup>11,32,34</sup> A detailed review of the existing theories on the crystalline polymorphs of P(VDF-co-TrFE) has been provided in the Chapter 1 of this Thesis.

For samples T-133, T-135 and t-30, an intermediate peak is present in our data, located between the peaks that are assigned to  $F_1$  and  $F_2$  phases. Deconvolution of these patterns absolutely necessitates the introduction of this third peak. We assign this peak to an additional ferroelectric phase, less ordered/more defective than  $F_1$  but more ordered/less defective than  $F_2$ . Therefore, we name this intermediate phase  $F_{1-2}$ . The position of this peak justifies the correlation made with the amount of defects.

The  $F_1$ ,  $F_2$  and  $F_{1-2}$  peaks have been described by pseudo-Voigt functions. Additionally, a broad peak which extends from  $0.7 \text{ \AA}^{-1}$  to  $1.6 \text{ \AA}^{-1}$  should be considered and it is assigned to the amorphous halo contribution. To limit any possible error, a statistical study has been carried out (for every sample the deconvolution has been performed several times) while some parameters, such as the  $F_1$  peak position (concerning the crystalline contribution) which is easily identified from the data, and the width of the amorphous halo (concerning the amorphous contribution), have been kept fixed. This latter is imposed by the shape of the halo measured for a molten film at  $165 \text{ }^\circ\text{C}$  and fitted with an asymmetric function. The parameters that are related to the width of this asymmetric function have been kept fixed for deconvolution in order to correctly consider the shape of the amorphous halo.<sup>35</sup> The parameters related to the amplitude and to the position of the halo were free to vary. The deconvolution performed on sample T-135 is presented in Figure 2.5b as an example. All the other deconvolutions are presented in Figure 2.8. Although only the  $q$ -range between 1 and  $1.7 \text{ \AA}^{-1}$  is presented in Figure 2.5b for clarity reasons, deconvolution has been performed between  $0.8 \text{ \AA}^{-1}$  and  $2 \text{ \AA}^{-1}$ .

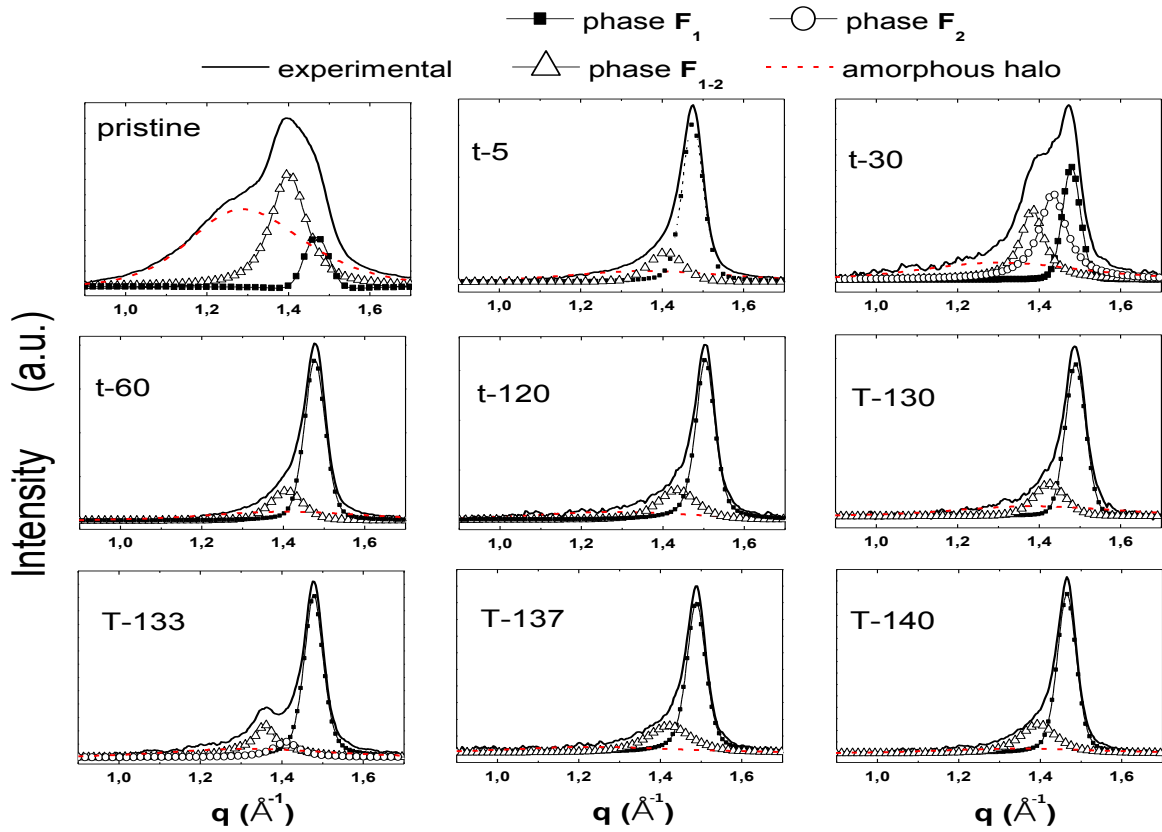


**Figure 2.8** The experimental (110),(200) peak of the differently thermally treated P(VDF-co-TrFE) films and the corresponding deconvoluted peaks. The  $F_1$ ,  $F_2$  and  $F_{1-2}$  phases have been described by pseudo-Voigt functions while the amorphous halo by an asymmetric function.

Based on the deconvolution of the (110),(200) peak we can evaluate the degree of crystallinity,  $\chi_{ferro}$ , and the amount of each ferroelectric phase in each sample. The degree of crystallinity we calculate is not the absolute one, but slightly lower than that, due to the missing scattered intensity for  $0^\circ < \chi < 5^\circ$  (at  $q \approx 1.5 \text{ \AA}^{-1}$ ),  $\chi$  being the polar angle, defined with respect to the out-of-plane direction. Thanks to the apparent amorphous halo contribution, the degree of crystallinity is calculated similarly to the case of WAXS, using Equation 2.1:

$$\chi_{ferro} = \frac{A_{F_1} + A_{F_2} + A_{F_{1-2}}}{A_{tot}} \quad (2.1)$$

Where  $A_{F_1}$ ,  $A_{F_2}$ , and  $A_{F_{1-2}}$  (when applicable) are the integrated areas of the respective fitted peak and  $A_{tot}$  is the total area of the (110),(200) peak, i.e. the sum of the areas of the ferroelectric peaks plus the amorphous halo contribution. It is highlighted that since the films

are studied below the Curie temperature, ferroelectric crystallinity corresponds to total crystallinity.<sup>32</sup>

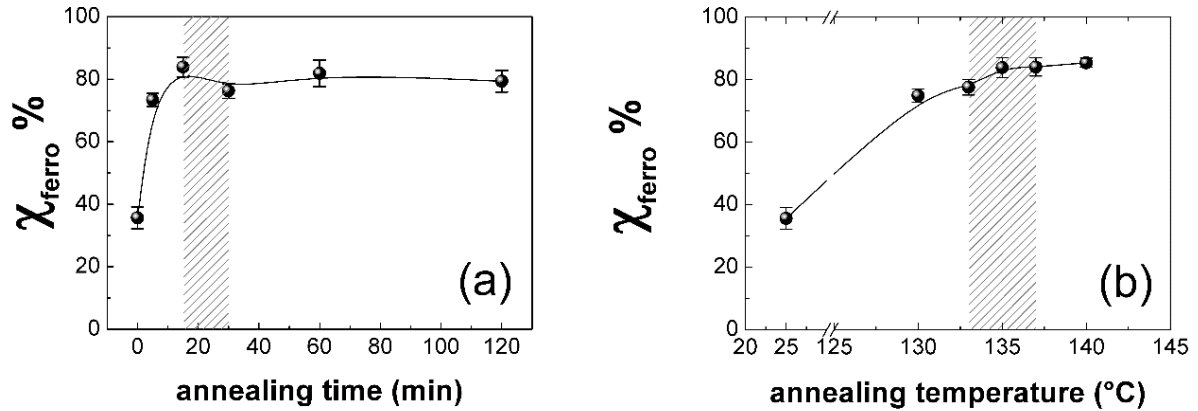


**Figure 2.9** Degree of ferroelectric crystallinity as a function of: (a) annealing time for a fixed annealing temperature 135 °C and (b) annealing temperature for a fixed annealing time 15 min. The lines that connect the data points serve as guides to the eye. The shady parts correspond to the annealing conditions that result in the optimum ferroelectric performance.

Figure 2.9a and Figure 2.9b show the evolution of the degree of crystallinity in these ferroelectric P(VDF-co-TrFE) films versus annealing time and annealing temperature respectively. The shady parts correspond to the annealing conditions that result in the optimum ferroelectric performance. Clearly, the pristine sample (that corresponds to 0 annealing time in Figure 2.9a and 25 °C in Figure 2.9b) exhibits the lowest crystallinity and contains the highest amount of amorphous phase (see also Figure 2.8). Moreover, the contribution of the defective crystalline phase  $F_2$  dominates over that of the more ordered  $F_1$  phase, as witnessed by its higher intensity and bigger area (Figure 2.8). For the annealed samples the situation is reversed, and  $F_1$  dominates over  $F_2$  and  $F_{1-2}$ . Note that the ferroelectric response of the pristine film is very poor as compared to that of the annealed films (Figures 2.2a and 2.3a). This result is expected, since annealing is known to increase the degree of crystallinity, which consequently increases polarisation,<sup>13,33</sup> given that the crystalline domains are the only regions involved in the ferroelectric switching process which is accomplished by the rotations of individual dipoles around the chain axes.<sup>13</sup>

Concerning the effect of annealing time Figure 2.9a suggests that crystallinity increases rapidly within the first 15 min of annealing and then reaches a plateau at which the fraction of ferroelectric phase is considerably high, around 80%. This result asserts that it is not necessary to perform a long thermal treatment of 2 hours in order to obtain a high degree of crystallinity, but only 15 or 30 minutes are enough, and, in fact, optimum device performance is achieved for these short times, as evidenced by the shady area.

Regarding the annealing temperature effect, we can assert that ferroelectric crystallinity increases with annealing temperature (Figure 2.9b), in consistence with previous reports,<sup>13</sup> and reaches its maximum value when annealing is performed at 140 °C. However, the GIWAXS image recorded for sample T-140 shows that an inversion of crystallite orientation has occurred at this temperature (Figure 2.6, T-140). The (110),(200) ring is now more pronounced at the equatorial than in the meridian, implying that the majority of polymer chains are oriented with their backbone perpendicular to the substrate, and, consequently, the dipoles are not aligned parallel to the electric field direction. This inverted orientation has a negative impact on the ferroelectric response and justifies the decreased  $P_r$ , despite the high degree of crystallinity in T-140.

On the other hand, the highly performing T-133, T-135 and t-30 samples exhibit a chain orientation parallel to the substrate, a high crystallinity and, moreover, the intermediate phase  $F_{1-2}$ . This intermediate state has some gauche defects, which are fewer than in case of phase  $F_2$ , and is considered to be a slightly unstable ferroelectric phase. We suggest that this phase is responsible for the superior ferroelectric performance of these films, given that the presence of some gauche defects in the ferroelectric crystal is reported to favour dipole rotation along the chain, by decreasing the respective potential energy barrier and thus facilitates polarisation switching.<sup>9</sup>

Finally, to further support the information derived by GIWAXS, DSC data recorded for self-standing films are presented below. Drop-casted films were prepared and underwent in the DSC crucible to heating/cooling sequences that mimic the preparation conditions used for the cold-crystallised films, i.e. heating from room temperature until the respective crystallisation temperature with a rate of 5 °C min<sup>-1</sup>, isothermal step at the crystallisation temperature for 15 min and cooling with a rate of 1.6 °C min<sup>-1</sup> to room temperature. The heating and cooling

rates correspond to those imposed by the hot plate. Right after, a second heating ramp has been performed from room temperature to 200 °C at a rate of 10 °C min<sup>-1</sup>. The DSC curves recorded during this last ramp are presented in Figure 2.10. A shift of the melting peak position towards higher temperatures is observed, which indeed indicates a better arrangement of the crystalline phase in bigger crystallites in case of semi-crystalline polymers.<sup>32</sup>  $T_m$  increases following the same trend obtained for the crystallinity (i.e. sample T-130 has a lower  $T_m$  with respect to T-133) and then  $T_m$  remains constant for samples T-133, T-135 and T-137, before increasing further for T-140. Conversely, the maximum of the Curie peak,  $T_{Curie}$ , slightly shifts towards lower temperatures when the annealing temperature is increased. This shift has already been correlated in literature with a larger amount of defects, since the generated ferroelectric phases require less energy in order to undergo the Curie transition.<sup>9</sup> Both the Curie transition peak and the melting peak correspond to a first order transition, but in case of the Curie transition the peak is broad indicating the participation of different ferroelectric phases to this transition.<sup>8,30</sup> Therefore the occurrence of the  $F_2$  and  $F_{1-2}$  ferroelectric phases, in addition to the less defective  $F_1$  phase is confirmed.

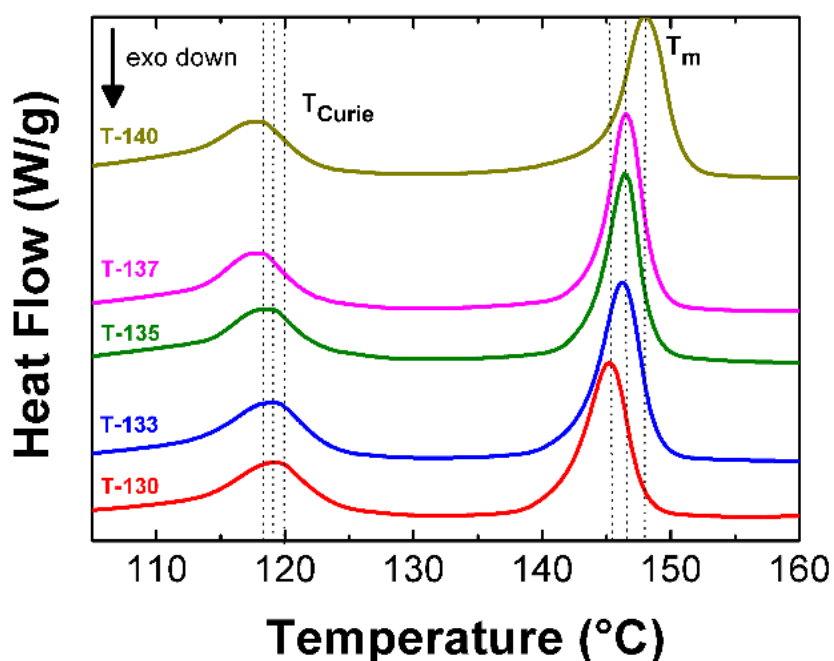


**Figure 2.10** DSC heat flow curves recorded for free standing P(VDF-co-TrFE) films upon the second heating cycle. The curves are presented shifted along the y-axis for clarity.

## 2.4 Conclusion

The effect of thermal processing on the ferroelectric properties of P(VDF-co-TrFE) films has been studied and the conditions that result in the best performing films have been identified. The annealing temperature was varied between 130 °C and 140 °C and the annealing time varied between 0 s (no annealing) and 2 h. It is underlined that to the best of our knowledge the effect of annealing time on the ferroelectric performance has not been studied so far and most usually annealing treatments as long as 2 h have been reported in literature. Our results suggest that only 15 min are enough to induce a high ferroelectric performance, proving that the 2 h-long annealing step that is traditionally applied is not necessary. In fact, optimal ferroelectric response, in terms of a high  $P_r$  and a low  $E_c$ , has been achieved when thermal processing takes place in the temperature range between 133 °C and 137 °C for 15 to 30 minutes. Thus, a  $P_r$  as high as 89 mC m<sup>-2</sup> and an  $E_c$  as low as 50 MV m<sup>-1</sup> have been obtained. Moreover, it is shown that annealing temperature affects mostly the remnant polarisation value, while annealing time has a severe effect on the coercive field value.

The enhanced performance achieved under these conditions has been rationalised through GIWAXS studies that revealed the crystalline phases apparent in these films and allowed the calculation of the degree of crystallinity. It is shown that a high degree of crystallinity is necessary for an improved performance, but this is not the only crucial parameter. An orientation of the crystallites with the  $c$ -axis parallel to the substrate is imperative. For all the films an orientation of the crystallite with their polymeric chain orientated parallel with respect to the substrate has been found apart from the sample annealed at 140 °C. This last finding justifies the decreased performance in spite of the considerable amount of ferroelectric crystallites. Moreover, a deconvolution study demonstrates the existence of a moderately unstable ferroelectric phase  $F_{1-2}$  that contains some gauche defects and that is designated to facilitate ferroelectric switching shown to improve the ferroelectric performance by facilitating the rotation of dipoles during the ferroelectric switching. The best performing structure exhibits a high degree of crystallinity, a preferential orientation of the crystallites with the polymer chains parallel to the substrate and the occurrence of three ferroelectric phases.

This study shines light on the processing-structure-function relationships that dictate the performance of cold-crystallised ferroelectric P(VDF-co-TrFE) films and provides the processing conditions that should be applied for the maximum exploitation of the ferroelectric functionality in organic electronic devices that incorporate this ferroelectric polymer.

## References

- 1 Lovinger, A. J. Ferroelectric polymers. *Science* **220**, 1115-1121 (1983).
- 2 Lovinger, A. J., Davis, G. T., Furukawa, T. & Broadhurst, M. G. Crystalline forms in a copolymer of vinylidene fluoride and trifluoroethylene (52/48 mol %). *Macromolecules* **15**, 323-328, doi:10.1021/ma00230a024 (1982).
- 3 Lovinger, A. J. Ferroelectric transition in a copolymer of vinylidene fluoride and tetrafluoroethylene. *Macromolecules* **16**, 1529-1534, doi:10.1021/ma00243a021 (1983).
- 4 Tashiro, K., Takano, K., Kobayashi, M., Chatani, Y. & Tadokoro, H. Structural study on ferroelectric phase transition of vinylidene fluoride-trifluoroethylene copolymers (III) dependence of transitional behavior on VDF molar content. *Ferroelectrics* **57**, 297-326, doi:10.1080/00150198408012770 (1984).
- 5 Tanaka, H., Yukawa, H. & Nishi, T. Effect of crystallization condition on the ferroelectric phase transition in vinylidene fluoride/trifluoroethylene (VF<sub>2</sub>/F<sub>3</sub>E) copolymers. *Macromolecules* **21**, 2469-2474, doi:10.1021/ma00186a028 (1988).
- 6 Legrand, J. F. Structure and ferroelectric properties of P(VDF-TrFE) copolymers. *Ferroelectrics* **91**, 303-317, doi:10.1080/00150198908015747 (1989).
- 7 Tashiro, K. & Kobayashi, M. Structural phase transition in ferroelectric fluorine polymers: X-ray diffraction and infrared/Raman spectroscopic study. *Phase Transit.* **18**, 213-246, doi:10.1080/01411598908206864 (1989).
- 8 Kim, K. J., Kim, G. B., Vanlencia, C. L. & Rabolt, J. F. Curie transition, ferroelectric crystal structure, and ferroelectricity of a VDF/TrFE(75/25) copolymer 1. The effect of the consecutive annealing in the ferroelectric state on curie transition and ferroelectric crystal structure. *Journal of Polymer Science Part B: Polymer Physics* **32**, 2435-2444, doi:10.1002/polb.1994.090321501 (1994).
- 9 Kim, K. J. & Kim, G. B. Curie transition, ferroelectric crystal structure and ferroelectricity of a VDF/TrFE (75/25) copolymer: 2. The effect of poling on curie transition and ferroelectric crystal structure. *Polymer* **38**, 4881-4889 (1997).
- 10 Bargain, F., Panine, P., Domingues Dos Santos, F. & Tencé-Girault, S. From solvent-cast to annealed and poled poly(VDF-co-TrFE) films: New insights on the defective

- ferroelectric phase. *Polymer* **105**, 144-156, doi:http://doi.org/10.1016/j.polymer.2016.10.010 (2016).
- 11 Bellet-Amalric, E. & Legrand, J. F. Crystalline structures and phase transition of the ferroelectric P(VDF-TrFE) copolymers, a neutron diffraction study. *Eur Phys J B* **3**, 225-236 (1998).
  - 12 Gowd, E. B., Shibayama, N. & Tashiro, K. Structural Correlation between Crystal Lattice and Lamellar Morphology in the Phase Transitions of Uniaxially Oriented Syndiotactic Polystyrene ( $\delta$  and  $\delta_e$  Forms) As Revealed by Simultaneous Measurements of Wide-Angle and Small-Angle X-ray Scatterings. *Macromolecules* **41**, 2541-2547, doi:10.1021/ma071759z (2008).
  - 13 Tajitsu, Y., Ogura, H., Chiba, A. & Furukawa, T. Investigation of switching characteristics of vinylidene fluoride/trifluoroethylene copolymers in relation to their structures. *Japanese Journal of Applied Physics* **26**, 554-560, doi:10.1143/jjap.26.554 (1987).
  - 14 Zeng, Z.-G., Zhu, G.-D., Zhang, L. & Yan, X.-J. Effect of crystallinity on polarization fatigue of ferroelectric P(VDF-TrFE) copolymer films. *Chinese J. Polym. Sci.* **27**, 479-485, doi:10.1142/s025676790900414x (2009).
  - 15 Mao, D., Quevedo-Lopez, M. A., Stiegler, H., Gnade, B. E. & Alshareef, H. N. Optimization of poly(vinylidene fluoride-trifluoroethylene) films as non-volatile memory for flexible electronics. *Org. Electron.* **11**, 925-932, doi:https://doi.org/10.1016/j.orgel.2010.02.012 (2010).
  - 16 Guo, D., Stolichnov, I. & Setter, N. Thermally induced cooperative molecular reorientation and nanoscale polarization switching behaviors of ultrathin poly(vinylidene fluoride-trifluoroethylene) films. *J Phys Chem B* **115**, 13455-13466, doi:10.1021/jp2061442 (2011).
  - 17 Mahdi, R., Gan, W. & Majid, W. Hot Plate Annealing at a Low Temperature of a Thin Ferroelectric P(VDF-TrFE) Film with an Improved Crystalline Structure for Sensors and Actuators. *Sensors* **14**, 19115 (2014).
  - 18 Aliane, A. *et al.* Impact of crystallization on ferro-, piezo- and pyro-electric characteristics in thin film P(VDF-TrFE). *Org. Electron.: phys. mater. appl.* **25**, 92-98, doi:10.1016/j.orgel.2015.06.007 (2015).

- 19 Kim, J. *et al.* High-Performance Piezoelectric, Pyroelectric, and Triboelectric Nanogenerators Based on P(VDF-TrFE) with Controlled Crystallinity and Dipole Alignment. *Adv. Funct. Mater.* **27**, 1700702, doi:10.1002/adfm.201700702 (2017).
- 20 Xia, W., Wang, Z., Xing, J., Cao, C. & Xu, Z. The Dependence of Dielectric and Ferroelectric Properties on Crystal Phase Structures of the Hydrogenized P(VDF-TrFE) Films With Different Thermal Processing. *IEEE Transactions on Ultrasonics, Ferroelectrics, and Frequency Control* **63**, 1674-1680, doi:10.1109/tuffc.2016.2594140 (2016).
- 21 Lovinger, A. J., Johnson, G. E., Bair, H. E. & Anderson, E. W. Structural, dielectric, and thermal investigation of the Curie transition in a tetrafluoroethylene copolymer of vinylidene fluoride. *Journal of Applied Physics* **56**, 2412-2418, doi:10.1063/1.334303 (1984).
- 22 Sharma, P., Reece, T. J., Ducharme, S. & Gruverman, A. High-Resolution Studies of Domain Switching Behavior in Nanostructured Ferroelectric Polymers. *Nano Letters* **11**, 1970-1975, doi:10.1021/nl200221z (2011).
- 23 Barique, M. A. & Ohigashi, H. Annealing effects on the Curie transition temperature and melting temperature of poly(vinylidene fluoride/trifluoroethylene) single crystalline films. *Polymer* **42**, 4981-4987, doi:10.1016/s0032-3861(00)00937-x (2001).
- 24 Zhao, D., Katsouras, I., Asadi, K., Blom, P. W. M. & De Leeuw, D. M. Switching dynamics in ferroelectric P(VDF-TrFE) thin films. *Phys. Rev. B Condens. Matter Mater. Phys.* **92**, 214115, doi:10.1103/PhysRevB.92.214115 (2015).
- 25 Koga, K. & Ohigashi, H. Piezoelectricity and related properties of vinylidene fluoride and trifluoroethylene copolymers. *Journal of Applied Physics* **59**, 2142-2150, doi:10.1063/1.336351 (1986).
- 26 Park, Y. J. *et al.* Irreversible extinction of ferroelectric polarization in P(VDF-TrFE) thin films upon melting and recrystallization. *Appl. Phys. Lett.* **88**, 242908, doi:10.1063/1.2207831 (2006).
- 27 Xia, F., Razavi, B., Xu, H., Cheng, Z.-Y. & Zhang, Q. M. Dependence of threshold thickness of crystallization and film morphology on film processing conditions in poly(vinylidene fluoride–trifluoroethylene) copolymer thin films. *J. Appl. Phys.* **92**, 3111-3115, doi:10.1063/1.1503395 (2002).

- 28 Fu, Z. *et al.* Improved Thermal Stability of Ferroelectric Phase in Epitaxially Grown P(VDF-TrFE) Thin Films. *Macromolecules* **49**, 3818-3825, doi:10.1021/acs.macromol.6b00532 (2016).
- 29 Müller-Buschbaum, P. The Active Layer Morphology of Organic Solar Cells Probed with Grazing Incidence Scattering Techniques. *Adv. Mater.* **26**, 7692-7709, doi:10.1002/adma.201304187 (2014).
- 30 Koga, K., Nakano, N., Hattori, T. & Ohigashi, H. Crystallization, field-induced phase transformation, thermally induced phase transition, and piezoelectric activity in P(vinylidene fluoride-TrFE) copolymers with high molar content of vinylidene fluoride. *Journal of Applied Physics* **67**, 965-974, doi:10.1063/1.345706 (1990).
- 31 Hasegawa, R., Takahashi, Y., Chatani, Y. & Tadokoro, H. Crystal Structures of Three Crystalline Forms of Poly(vinylidene fluoride). *Polym J* **3**, 600-610, doi:10.1295/polymj.3.600 (1972).
- 32 Gregorio, R. & Botta, M. M. Effect of crystallization temperature on the phase transitions of P(VDF/TrFE) copolymers. *J. Polym. Sci. B Polym. Phys.* **36**, 403-414, doi:10.1002/(sici)1099-0488(199802)36:3<403::aid-polb2>3.0.co;2-s (1998).
- 33 Furukawa, T. Ferroelectric properties of vinylidene fluoride copolymers. *Phase Transit.* **18**, 143-211, doi:10.1080/01411598908206863 (1989).
- 34 Tashiro, K. & Tanaka, R. Structural correlation between crystal lattice and lamellar morphology in the ferroelectric phase transition of vinylidene fluoride-trifluoroethylene copolymers as revealed by the simultaneous measurements of wide-angle and small-angle X-ray scatterings. *Polymer* **47**, 5433-5444, doi:https://doi.org/10.1016/j.polymer.2005.06.128 (2006).
- 35 Guo, Q. *Polymer Morphology: Principles, Characterization, and Processing*. (Wiley, 2016).

# Chapter 3

*Unravelling  
the P(VDF-co-TrFE)  
polymorphism  
by investigating its  
crystallisation from melt*



## 3 Unravelling the P(VDF-co-TrFE) polymorphism by investigating its crystallisation from the melt

### 3.1 Introduction

The advantage of using the copolymer P(VDF-co-TrFE) instead of the homopolymer PVDF is that the copolymer spontaneously crystallises into a highly polar ferroelectric phase. This is true for all compositions between  $54\% \leq \text{VDF} \leq 82\%$  that have been studied in literature.<sup>1,2</sup> Moreover copolymers having these molar compositions exhibit a clear ferroelectric-to-paraelectric Curie transition,  $T_{\text{Curie}}$ , at temperatures below the melting point  $T_m$ , which is not the case for PVDF.<sup>3-5</sup> In fact the Curie transition takes place at temperatures that increase with the increase of VDF content, until overtaking and exceeding the melting point in case of PVDF, whose  $T_{\text{Curie}}$  cannot be discerned from the  $T_m$ .<sup>6,7</sup>

The Curie transition is a solid-state reversible transformation: intramolecular dipoles rotations introduce gauche kinks that transform the polar all-trans conformation of pristine ferroelectric crystallites into nonpolar paraelectric crystallites, where the polymer chains adopt a partly disordered conformation consisting of irregular  $TG^+$ ,  $TG^-$  and TT sequences. The Curie transition of P(VDF-co-TrFE) does not occur at a specific temperature but it is extended in a wide range of temperatures, normally tens of degrees large. Such broad-range transitions are typical for polymers, since they normally involve more than one phase.

Similar to the PVDF homopolymer, the copolymer P(VDF-co-TrFE) exhibits a complex polymorphism which is considered to be molar ratio dependent. In literature many studies have investigated the crystalline structures of P(VDF-co-TrFE) with different molar ratios.<sup>1-3,6,8-10</sup> Lovinger's and Furukawa's works highlighted the crystalline difference between copolymers with a VDF content higher or equal to 54 mol%.<sup>1</sup> Copolymers with VDF content higher than 54% were found to co-crystallise directly into a ferroelectric phase analogous to the highly polar  $\beta$ -PVDF.<sup>1</sup> In the 80ies, Tashiro and Kobayashi,<sup>2,11</sup> by establishing a temperature vs VDF content phase diagram, found that for similar molar ratio copolymers (VDF  $\approx$  55 mol%) three crystal forms exist: a Low Temperature (LT) phase, a High Temperature (HT) and a CooLed (CL)

phase.<sup>2,11</sup> The LT is essentially the  $\beta$ -PVDF phase, the HT is characterised by the packing of statistical TT and TG<sup>+/-</sup> isomers in a non-polar hexagonal unit cell,<sup>2</sup> namely the paraelectric phase, and the CL phase is an individual disordered ferroelectric phase defined as a superlattice of long trans chains domains linked together at the boundaries with disordered trans-gauche bonds.<sup>2,11</sup> For copolymers with 70-80<sub>mol</sub>% of VDF, the LT crystalline phase was observed at room temperature. Upon heating, this LT phase undergoes a Curie transition and converts to the paraelectric HT phase. For copolymers with a VDF content lower than 70<sub>mol</sub>% when the HT phase is cooled down to room temperature the CL is generated.<sup>2,11</sup>

Besides this work, many other studies on P(VDF-co-TrFE) crystalline structure reported the existence of different ferroelectric phases for various VDF/TrFE compositions (from 50 to 80<sub>mol</sub>% VDF), elaborated by various processes and by various post treatments.<sup>1-3,6,8-10</sup> Koga *et al.* have proposed the existence of three different ferroelectric phases for copolymers with 60% $\leq$ VDF $\leq$ 90%, based on the multiple-shaped Curie transition peak recorded upon heating with DSC.<sup>3,8</sup> Kim *et al.* succeeded in separating these multiple Curie peaks into isolated ones and suggested that, upon heating, during the Curie transition, the peak at higher temperature corresponds to a transition of an “ordered” ferroelectric phase to the paraelectric phase, since this ordered phase would require higher thermal energy to be converted into the paraelectric phase.<sup>12</sup>

Numerous designations have been used so far for the polymorphs of P(VDF-co-TrFE) either in the ferroelectric or in the paraelectric state. The ferroelectric phase with all-trans conformations was named LT,<sup>2</sup> as said above, but also F $_{\beta 1}$ ,<sup>9</sup>  $\beta^8$ , or FE<sup>13</sup>; at high temperature, the paraelectric phase was designated as HT,<sup>2</sup>  $\gamma^8$  or PE<sup>13</sup> while the intermediate phase was named CL,<sup>2</sup> LTD (Low Temperature Disordered) or F $_{\beta 2}$ .<sup>3,8,9</sup> The related literature review has been provided in Chapter 1. Regardless the terms used to describe the polymorphs of P(VDF-co-TrFE), a common element is the consensus that these polymorphs originate from defects in the highly polar all-trans structure. So, before moving on, we will discuss the concept of “defective phase”.

A defective, or disordered, ferroelectric phase differs from a well-ordered, nearly perfect all-trans (TTT) phase due to the appearance of gauche defects (G<sup>+/-</sup>) within all-trans domains. Those conformational defects enable an easier rotation along the chain-axis, with a resulting decrease of the ferroelectric-to-paraelectric transition activation energy. Consequently, those

defective ferroelectric phases upon heating are expected to evolve into the paraelectric state at lower temperature than the ordered ones.<sup>3</sup> The amount of conformational gauche defects along the chain dictates the structural characteristics of P(VDF-co-TrFE), giving rise to a more or less defective, and thus more or less stable, ferroelectric phase.<sup>12</sup>

These G<sup>+/-</sup> conformations have been considered arising from chemical defects like the head-to-head, HH, or tail-to-tail, TT, formed in expense of the correct head-to-tail, HT, configuration where the head is the unit (CH<sub>2</sub>) and the tail is (CF<sub>2</sub>).<sup>14</sup> Lovinger *et al.* have studied the defective crystalline structure of the homopolymer PVDF, by synthesising PVDF samples with various amounts of HH and TT defects.<sup>15</sup> Increasing the amount of configurational defects leads to a switch from a perfect PVDF  $\beta$ -phase to an intermediately defective (for an intermediate amount of HH or TT defects,  $\approx 13\%$ ) until achieving a paraelectric-like phase at  $\approx 17\%$  of HH or TT defects. A continuous evolution of the cell parameters was observed while increasing the amount of defects. However, they concluded that the Curie transition did not occur because the conversion of the low temperature phase into the PE phase occurs mainly at the expense of the antipolar  $\alpha$ -phase, rather than the polar  $\beta$ -phase and therefore this should not be considered as a Curie transition.<sup>15</sup> In any case, HH and TT are chemical defects, created during polymerisation so in theory they are not affected by processing since they already exist in pristine samples. Even though, so far, the defective phase has been reported only for not annealed copolymers with a very low VDF content ( $\leq 54\%$ )<sup>6</sup> or for high VDF content copolymers after they undergo thermal annealing.<sup>2,3</sup>

Besides the HH and TT chemical defects one should keep in mind that the TrFE units can be also seen as chemical defects in the copolymer chain and, thus, the complexity of the system is increased.

Recently, Bargain *et al.* documented the structural changes of isotropic films by means of simultaneous SAXS/WAXS and DSC experiments during heating and cooling.<sup>14</sup> They concluded that an orthorhombic defective ferroelectric phase, that they call *DFE*, is formed upon cooling of a hexagonal paraelectric phase that contains defective segments. They reported that gauche defects are irreversibly incorporated within the paraelectric crystallites during the first heating above the Curie transition. These defects have been called by the authors “chemical gauche conformational defects”, meaning that they are *gauche conformations* that have been generated by the presence of *chemical defects*, as HH, TT or by different distributions of TrFE groups along the chains. Yet, such defects should appear during polymerisation and therefore,

annealing should not be required in order to induce them. Nevertheless, Bargain *et al.* reported the appearance of the DFE just after annealing above the  $T_{\text{Curie}}$ .<sup>14</sup>

It arises that, despite the huge amount of studies on P(VDF-*co*-TrFE) crystalline structure, even the origin of defective phases seems still to be not very clear. As already said, a convergent theory on the polymorphism of P(VDF-*co*-TrFE) is still lacking. Herein stems the aim of this work: understand the structural behaviour of P(VDF-*co*-TrFE) and unravel the phase transitions that take place during thermal heating or cooling, in particular across the Curie transition. For this, a DSC study complemented with time resolved WAXS experiments have been conducted and will be presented in this Chapter, following the crystallisation of P(VDF-*co*-TrFE) from the melt.

Melt crystallisation is chosen because it allows us to study crystallisation in a controlled way, starting from the same molten state where no crystallites pre-exist. We will study the effect of different crystallisation temperatures,  $T_c$ , on the formed paraelectric phases and see the dependence of the FE polymorphs on the mother PE phase. In particular, we would like to unveil the origins of the defective phases and their role on ferroelectric functionality. Some studies on the melt crystallisation of P(VDF-*co*-TrFE) have already appeared in literature. The main advantage of the work presented herein with respect to published work is that we follow the crystallization and the Curie transitions with two complementary techniques in real-time, with an unprecedented time resolution coupled with high quality scattering data provided by synchrotron radiation. The main outcomes of the previous works are listed below.

Based on DSC studies, it was demonstrated that, when crystallising from the molten state, higher isothermal crystallisation temperatures result in paraelectric crystallites with greater thermodynamic stability (i.e. lower free energy,  $G$ ) and greater structural order, implied by the increased  $T_m$ .<sup>9,16</sup> It was suggested that these paraelectric crystallites of greater stability must be cooled to lower temperatures before undergoing the PE-to-FE transition, and analogously they reform sooner (i.e. at lower temperatures) on subsequent heating.<sup>16</sup> Moreover, it was suggested that the conformational defects enable an easier rotation along the chain axis, with a resulting decrease of the ferroelectric-to-paraelectric transition activation energy. Consequently, upon heating, a defective ferroelectric phase is expected to evolve into the paraelectric state at lower temperatures than the ordered one.<sup>3</sup> The amount of conformational gauche defects along the chain dictates the structural characteristics of

P(VDF-*co*-TrFE), giving rise to different ferroelectric phases with more or less defects, and thus, more or less stability.<sup>12</sup> Based on that, Kim *et al.* suggested that, upon heating, during the Curie transition, the DSC peak at higher temperatures corresponds to a transition of a well-ordered ferroelectric phase to a paraelectric one, since this transition would require higher thermal energy.<sup>12</sup>

As demonstrated in Chapter 2, altering the final crystalline structure of P(VDF-*co*-TrFE) induces variations of the ferroelectric properties.<sup>17,18</sup> To complement this work and in order to make the link between the structural modifications induced by melt crystallisation and ferroelectric properties, at the end of this Chapter we discuss the device performance of melt crystallised thin films incorporated in capacitors.

## 3.2 Sample preparation

The P(VDF-*co*-TrFE) copolymer investigated herein has a VDF/TrFE molar ratio of 70-30.

The P(VDF-*co*-TFE) powder was first heated from RT until 165 °C (above the  $T_m$ ) with a rate of 5 °C min<sup>-1</sup>. An isothermal step is performed for 5 minutes in order to ensure the complete melting of all crystallites. Then a fast cooling is performed with a rate of 40 °C min<sup>-1</sup> until the crystallisation temperature of choice ( $T_c$ : 129 °C, 131 °C, 133 °C, 135 °C, 137 °C, 140 °C) at which an isothermal crystallisation step takes place for 1 hour. Then a slow cooling rate of 2 °C min<sup>-1</sup> is applied until room temperature. A second heating and cooling ramp with both heating and cooling rates of 10 °C min<sup>-1</sup> have been finally performed. Both these cycles have been monitored by DSC and time resolved WAXS.

Capacitor devices have been fabricated by evaporating a bottom Al electrode onto clean glass substrates, then by spin-coating P(VDF-*co*-TrFE) films of a thickness of around 1.5 μm on top, and finally by evaporating through a shadow mask the Al top electrodes. These devices underwent the thermal treatment described above for the first heating and cooling cycles. The fast cooling from 165 °C to the  $T_c$  of choice has been realized by rapidly moving the sample from the hotplate where the melting step has been performed onto another hotplate already

set at the crystallisation temperature of choice. Then the films were cooled down to room temperature on the same hotplate, the cooling rate being  $2\text{ }^{\circ}\text{C min}^{-1}$ .

### 3.3 Results and discussion

DSC has been performed to follow the phase transitions in P(VDF-co-TrFE). As described above an atypical DSC analysis was programmed (Figure 3.1). The initial heating and cooling ramps, normally executed to delete the thermal history of the sample, are substituted by heating and cooling ramps that mimic the thermal treatment of films using the hotplate employed for device fabrications as described in the previous sample preparation session.

In particular, we performed a first heating ramp, ①, from RT to  $165\text{ }^{\circ}\text{C}$  with a rate of  $5\text{ }^{\circ}\text{C min}^{-1}$ , followed by an isothermal step at  $165\text{ }^{\circ}\text{C}$  for 5 minutes to assure melting of all crystallites. Then a first cooling ramp, ②, is performed that comprises cooling from  $165\text{ }^{\circ}\text{C}$ , with a fast cooling rate of  $40\text{ }^{\circ}\text{C min}^{-1}$ , until the chosen crystallisation temperature,  $T_c$ , then an isothermal crystallisation step at  $T_c$  during 1 hour, and finally a slow cooling down to RT with a cooling rate of  $2\text{ }^{\circ}\text{C min}^{-1}$ . Next, a second heating ramp ③ is performed from RT to  $180\text{ }^{\circ}\text{C}$  with a heating rate of  $10\text{ }^{\circ}\text{C min}^{-1}$ . Finally, a cooling ramp ④ from  $180\text{ }^{\circ}\text{C}$  to RT is performed with the same cooling rate  $10\text{ }^{\circ}\text{C min}^{-1}$ .

The above-described DSC thermal protocol is represented in Figure 3.1, while in Figure 3.2 the corresponding DSC cycles are shown. For sake of clarity, just one  $T_c$  is presented as an example, (the one recorded for a  $T_c$  of  $129\text{ }^{\circ}\text{C}$ , which corresponds to sample S-m129). Red line corresponds to ramp ①, green line to ramp ②, blue line to ramp ③ and the grey line to ramp ④.

The crystallisation temperatures,  $T_c$ , herein investigated are  $129\text{ }^{\circ}\text{C}$ ,  $131\text{ }^{\circ}\text{C}$ ,  $133\text{ }^{\circ}\text{C}$ ,  $135\text{ }^{\circ}\text{C}$ ,  $137\text{ }^{\circ}\text{C}$ ,  $140\text{ }^{\circ}\text{C}$ . Therefore, the samples will be hereinafter called S-m129, S-m131, S-m133, S-m135, S-m137, S-m140 respectively. The letter “m” before the  $T_c$  indicates that the samples underwent *melt* crystallisation, differently from Chapter 2 where cold-crystallisation was studied.

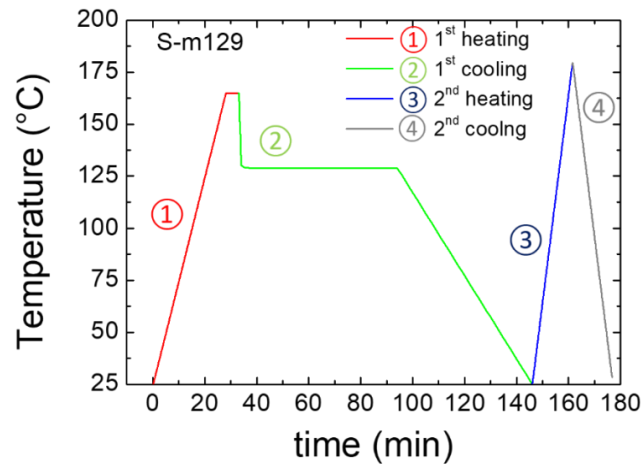


**Figure 3.1** The four thermal ramps performed by DSC in the case of a  $T_c$  of 129 °C. (1) Red line: 1<sup>st</sup> heating from RT to 165 °C with a rate of 5 °C min<sup>-1</sup>, followed by an isothermal step at 165 °C for 5 minutes. (2) Green line: 1<sup>st</sup> cooling ramp from 165 °C to 129 °C ( $T_c$ ) with a cooling rate of 40 °C min<sup>-1</sup>, followed by an isothermal step at 129 °C of 1 hour; then from 129 °C to RT the cooling steps continues with a rate of 2 °C min<sup>-1</sup>. (3) Blue line: 2<sup>nd</sup> heating from RT to 180°C with a rate of 10 °C min<sup>-1</sup>. (4) Grey line: 2<sup>nd</sup> cooling from 180 °C to RT with a rate of 10 °C min<sup>-1</sup>.

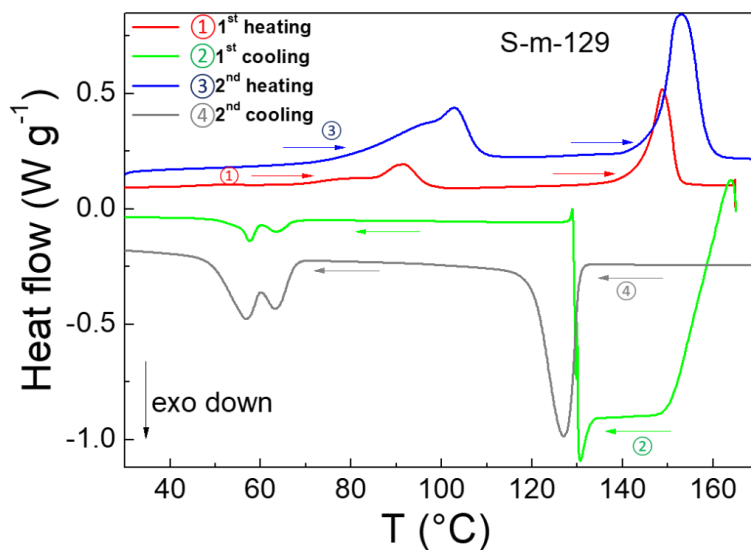


**Figure 3.2** The DSC curves recorded for the sample crystallised at  $T_c = 129$  °C.

### 3.3.1 ① First heating ramp: Curie transition and melting

Figure 3.3 displays the Curie transition upon the first heating,  $T_{Curie, 1^{st} h}$  (red line). The Curie FE-to-PE transition does not occur at a distinct temperature but takes place over a broad temperatures range between 45 °C and 100 °C.

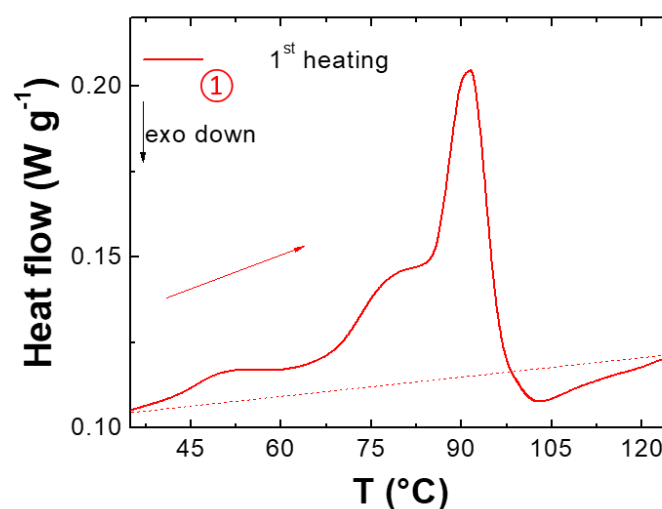


**Figure 3.3** Zoom at the Curie transition peak of the first heating DSC ramp: different FE-to-PE transition shoulders indicate that different FE phases are participating to the transition. The dash line is the DSC baseline and serves to indicate the cold crystallisation exothermic peak at  $\approx 105$  °C.

The Curie transition exhibits a main peak at 90 °C with a shoulder at 80 °C and a less intense shoulder at 52 °C. The appearance of these distinct shoulders and the diffuse character of this first order transition has been largely reported in literature and explained by the participation of many ferroelectric phases with different stability.<sup>12</sup> Since the Curie transition is a crystalline phase transition, its behaviour is highly dependent on the thermodynamic stability of each crystalline phase. In particular, the shoulders of the Curie peak at low temperatures were assigned to FE-to-PE transitions involving defective ferroelectric phases.<sup>3,12,17</sup>

We here highlight that in our study the appearance of defective ferroelectric phases is found *ab initio* before any thermal treatment. So far defective ferroelectric phases have been reported for not annealed copolymers with a low VDF content ( $\leq 54\%$ ), or for copolymers with high VDF content (like the one studied herein) that have been already thermally annealed.<sup>14</sup> A first explanation of the origin of these defective faces has been provided by Lovinger that considered that  $G^{+/-}$  defects can arise from chemical conformational defects HH and TT.<sup>15</sup> These chemical defects are created during polymerisation, so they are already apparent in pristine samples. The reason why they were not apparent in previous studies may be related to heating rates; herein low heating rate are applied making possible the discrimination of the two shoulders.

The Curie transition is followed by a small exothermic peak (Figure 3.3) that is attributed to the ongoing cold crystallisation.<sup>14,19,20</sup> This peak is considered as a proof that the sample has never been heated above the Curie temperature before this first heating.<sup>14,19,20</sup> The drawn dash line is in fact the DSC baseline and serves to visualise clearly this small exothermic peak.

Finally, the endothermic peak recorded above 130 °C corresponds to the melting peak. Figure 3.4 shows the first heating DSC ramps ① for all the  $T_c$  studied herein. No significant differences arise: the Curie transition and the melting endotherms are almost identical in shape and temperature range at which they occur. All the samples exhibit the same behaviour during the first heating ramp since they all undergo the same thermal treatment, starting from the same initial state.

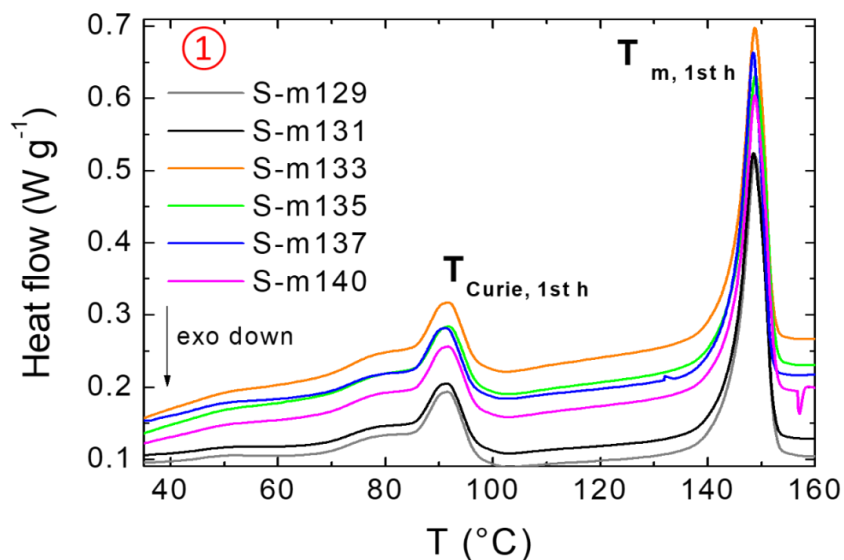


**Figure 3.4** 1<sup>st</sup> heating cycles recorded for the different  $T_c$ s under study. From 60°C to 100°C the Curie transition is encountered followed by the melting at around 150°C.

### 3.3.2 ② First cooling ramp: isothermal crystallisation and Curie transition

From the molten state, P(VDF-co-TrFE) was cooled down to different  $T_c$  with a fast rate of 40 °C min<sup>-1</sup> and let to isothermally crystallise for 1 hour.

In Figure 3.5 the *heat flow* (W g<sup>-1</sup>) vs *time* (min) plots recorded during the isothermal step are displayed for each  $T_c$ . A very sharp variation of the heat flow as a function of time is found for the low  $T_c$ s. As expected, going from a low  $T_c$  to a high  $T_c$  results in a shift of the

crystallisation peak towards longer times, along with a peak broadening (Figure 3.5). For S-m129 (grey curve) and S-m131 (black curve) the crystallisation takes place within the first 2 minutes after the  $T_c$  is reached. S-m133 (orange curve) is slightly shifted, the crystallisation starts around 30 seconds after the  $T_c$  is reached. S-m135 (green curve) is slightly shifted, the crystallisation starts around 30 seconds after the  $T_c$  is reached. For higher  $T_c$  a shift of the isothermal peaks is more evident together with a broadening of the peak: S-m135 (green line) exhibits slower kinetics of crystallisation, which starts 1 minute after the  $T_c$  is reached and lasts for 5 minutes. For S-m137 (blue line) crystallisation starts 2.5 minutes after the  $T_c$  is reached and lasts for almost  $\approx 10$  minutes. An even more evident time shift and broadening occur for S-m140 peak (pink line, shown cut by a break in the time axis between 21 and 38 minutes, just for better visualising the lower  $T_c$  isothermal crystallisation peaks).

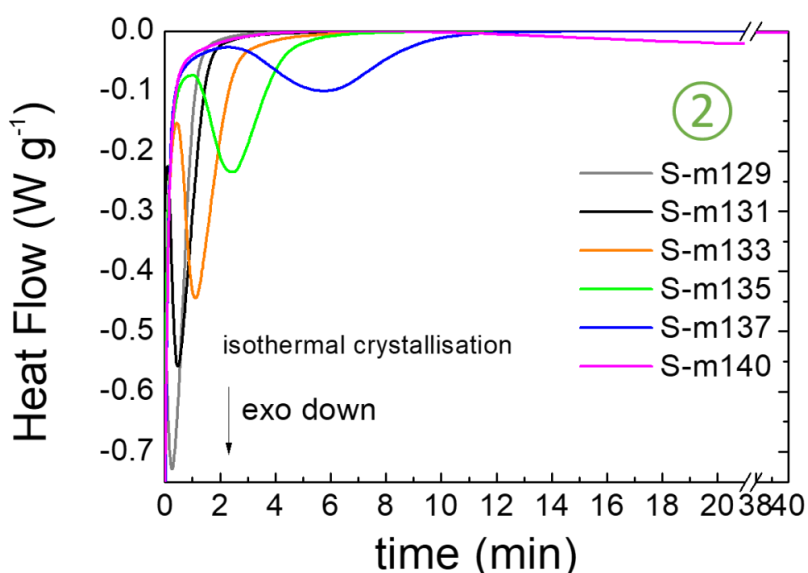


**Figure 3.5** Heat flow ( $W g^{-1}$ ) vs time (min) curves recorded during isothermal crystallisation for the various  $T_c$  studied.

It has to be said that, for low  $T_c$ s, an exothermic peak is detected in the *heat flow vs time* plots before the  $T_c$  is reached, as shown in Figure 3.6a for S-m129. In fact, the sample starts to crystallise during the fast cooling, before reaching the  $T_c$ . This non-isothermal crystallisation will be called hereinafter pre-isothermal crystallisation,  $T_{c, pre-iso}$ . Actually, every sample herein investigated exhibits this pre-isothermal crystallisation as shown in Figure 3.6b where the *heat flow vs T* plot shows the appearance of an exothermic peak just before the respective  $T_c$  (i.e

at higher temperatures), whose contribution decreases with the increase of  $T_c$ . The  $\Delta H$  of this crystallisation is calculated by integrating the area of the peaks shown in Figure 3.6b.

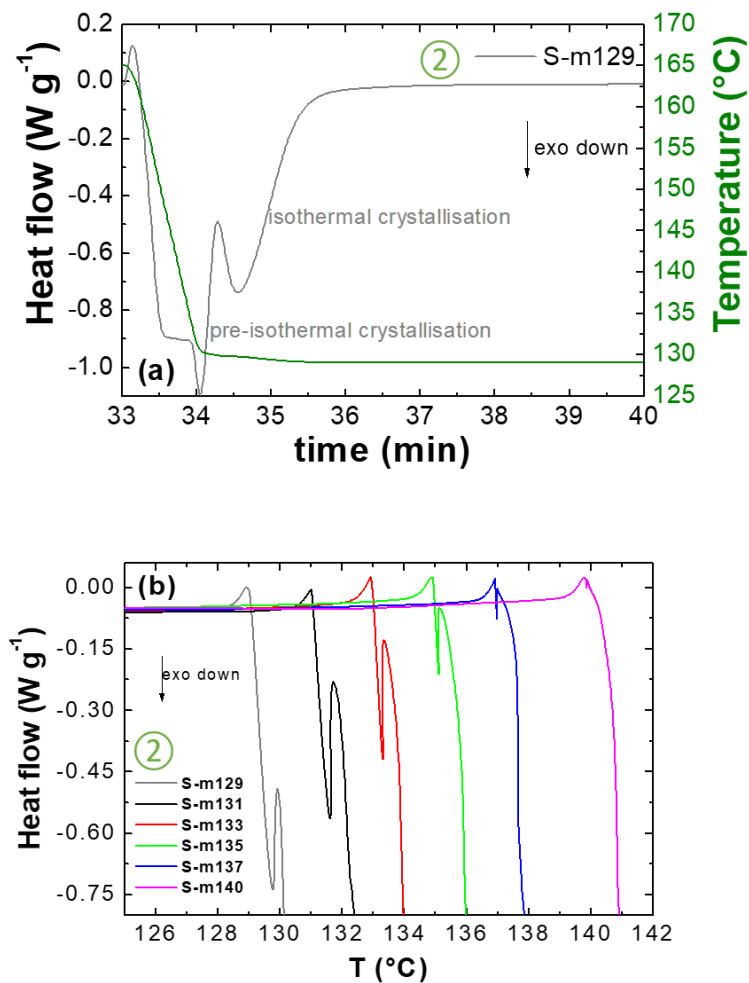


**Figure 3.6** (a) The recorded heat flow along with the corresponding DSC temperature variations as a function of time for the sample S-m129. It clearly shows that the crystallisation has already started before the  $T_c$  is reached. The peak centred at 34 min corresponds to the non-isothermal crystallisation occurring before the isothermal one. (b) Heat flow vs  $T$  curves that show the pre-isothermal crystallisation for the various  $T_c$ .

Additionally, we observe a third, non-isothermal crystallisation peak, after each isothermal step, which will be called post-isothermal crystallisation:  $T_{c, \text{post-iso}}$ . Figure 3.7 displays the  $T_{c, \text{post-iso}}$  for S-m140 which exhibits the most evident peak for this post-isothermal crystallisation among all samples.

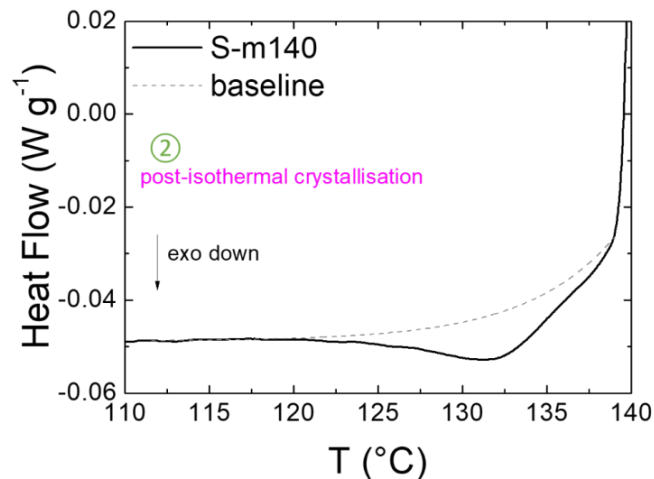


**Figure 3.7** Heat flow ( $W g^{-1}$ ) vs temperature ( $^{\circ}C$ ) after the isothermal step for the S-m140. The dashed curve corresponds to the DSC baseline used to calculate the area of this post-isothermal crystallisation peak. An exponential fit has been performed to derive the baseline.

The isothermal and the non-isothermal crystallisation enthalpies are calculated by integrating the corresponding exothermic peaks and by considering the cooling rate when necessary. An exponential baseline is fitted and subtracted before integration (as the one shown in Figure 3.7, dotted grey line).

In Figure 3.8a the pre-isothermal crystallisation enthalpy,  $\Delta H_{pre-iso}$ , (blue spheres) calculated by integrating the exothermic peaks of Figure 3.6b, the isothermal crystallisation enthalpy,  $\Delta H_{iso}$ , (grey spheres) calculated by integrating the exothermic peaks of Figure 3.5, and the post-isothermal crystallization enthalpy,  $\Delta H_{post-iso}$ , (cyan spheres) calculated by integrating the exothermic peaks shown in Figure 3.7, are plotted as a function of  $T_c$ .

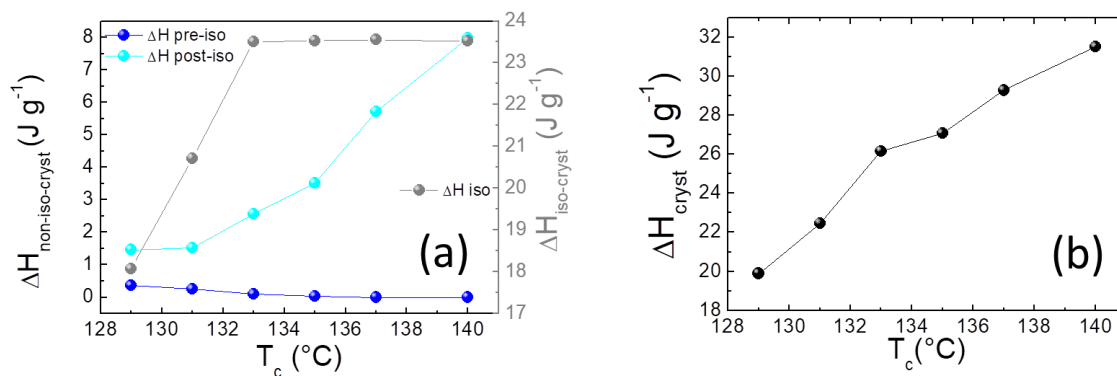


**Figure 3.8** (a)  $\Delta H_{pre-iso}$  (blue spheres and line),  $\Delta H_{iso}$  (grey spheres and line), and  $\Delta H_{post-iso}$  (cyan spheres and line), vs  $T_c$ ; (b);  $\Delta H_{cryst}$  given by the sum of the three  $\Delta H$ , as function of  $T_c$ .

The  $\Delta H_{pre-iso}$  is small compared to the others and decreases with the increase of  $T_c$  till becoming negligible for S-m140. Indeed, the bigger is the super-cooling  $\Delta T = T_m - T_c$ , the larger is the area of the pre-isothermal crystallisation peak (Figure 3.6b).  $\Delta H_{iso}$  increases with  $T_c$  until 133 °C, at which a plateau is reached. In the same way,  $\Delta H_{post-iso}$  increases with  $T_c$ . Indeed, for this third crystallisation we have found an opposite behaviour with respect to the first one ( $T_c, pre-iso$ ): the higher the  $T_c$  the bigger the contribution of the post-isothermal crystallisation.

Considering the difficulties in the evaluation of the crystallisation enthalpies we should be careful in building our theory on the absolute  $\Delta H$  calculated values but we still can trust on the trends as a function of  $T_c$ . As expected, the highest crystallisation enthalpy is achieved for the highest  $T_c = 140^\circ\text{C}$ , as can be derived from Figure 3.8b where the total crystallisation enthalpy  $\Delta H_{cryst}$  given by the sum of the three crystallisation enthalpies is plotted as a function of the crystallisation temperature,  $T_c$ . This finding suggests that the degree of crystallinity increases with  $T_c$ , in consistence with what is expected for the melt crystallisation of common polymers.

Time-resolved WAXS experiments have been performed for the melt-crystallised samples following the thermal protocols applied for the DSC experiments. These experiments have been conducted at DUBBLE at the ESRF by Dr. G. Portale from the University of Groningen, NL.

In Figure 3.9 the time resolved WAXS patterns are presented for three representative samples at the different crystallisation steps: at the onset of the isothermal crystallisation, i.e.

the first  $I$  vs  $q$  plot recorded when the temperature reaches the  $T_c$  (Figure 3.9a), at the end of the isothermal crystallisation, i.e. the last  $I$  vs  $q$  plot recorded at  $T=T_c$  (Figure 3.9b), and at 30 °C below each  $T_c$ , i.e. 99 °C for S-m129, 103 °C for S-m133 and at 110 °C for S-m140 (Figure 3.9c), when all crystallisations should have ended according to DSC. The S-m129 annealed at the lowest  $T_c$  is shown in grey, the S-m133 annealed at an intermediate  $T_c$  is shown in orange and the S-m140, annealed at the highest  $T_c$ , is shown in pink.

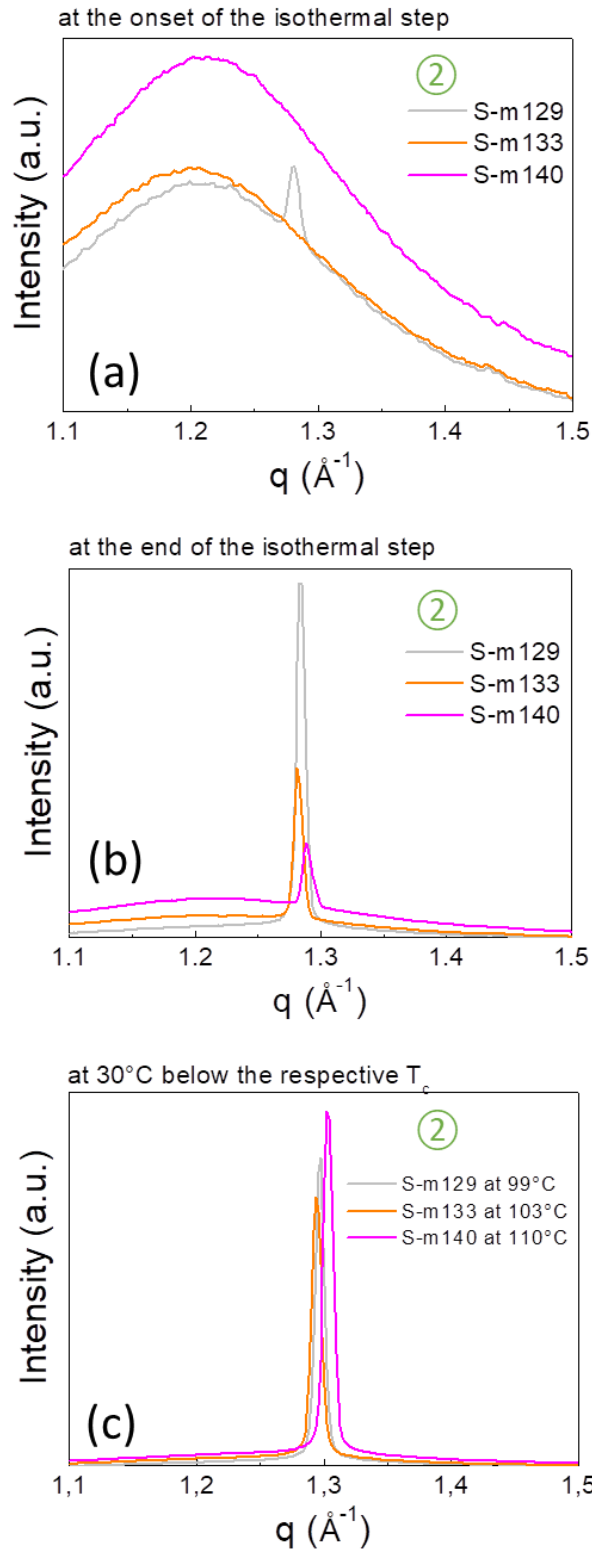


**Figure 3.9**  $I$  vs  $q$  patterns for samples S-m129 (grey line), S-m133 (orange line) and S-m140 (pink line) (a) at the onset of the isothermal crystallisation (at which just the pre-isothermal crystallisation has occurred), (b) at the end of the isothermal crystallisation and (c) at 30 °C below the  $T_c$  at which all three crystallisations (pre-isothermal, isothermal and post-isothermal) have already finished.

Figure 3.9a shows the scattering patterns for the three samples at the onset of the isothermal crystallisation. As expected, for S-m133 and S-140 it is not recorded any crystalline peak, but just an amorphous halo. This means that at 140 °C and at 133 °C the state is still the molten state: the crystallisation has not yet started. However, for sample S-m129 a peak is apparent at  $\approx 1.28 \text{ \AA}^{-1}$  and is assigned to the paraelectric crystalline phase.<sup>10,14</sup> This peak is attributed to the crystallites formed during the pre-isothermal crystallisation as just discussed above based on our DSC results. The pre-isothermal crystallisation contribution is so small for the other two samples S-m133 and S-140 that it is not recorded any scattering peak in WAXS for those samples (Figure 3.9a).

Figure 3.9b presents the scattering patterns of the three samples at the end of their isothermal crystallisation steps. The paraelectric peak of S-m129 (grey line) did not shift along the  $q$ -axis during the isothermal step (the two grey peaks in Figure 3.9a and Figure 3.9b are centred at the same  $q=1.28 \text{ \AA}^{-1}$ ) meaning that, along the progression of the isothermal crystallisation, the crystalline phase that is formed is the same. However, the pattern of S-m129 at the end of the isothermal step (Figure 3.9b) exhibits a much sharper and of higher intensity peak with respect to that recorded at the onset of  $T_c$  (Figure 3.9a) suggesting that the amount of crystallites has much increased during this step.

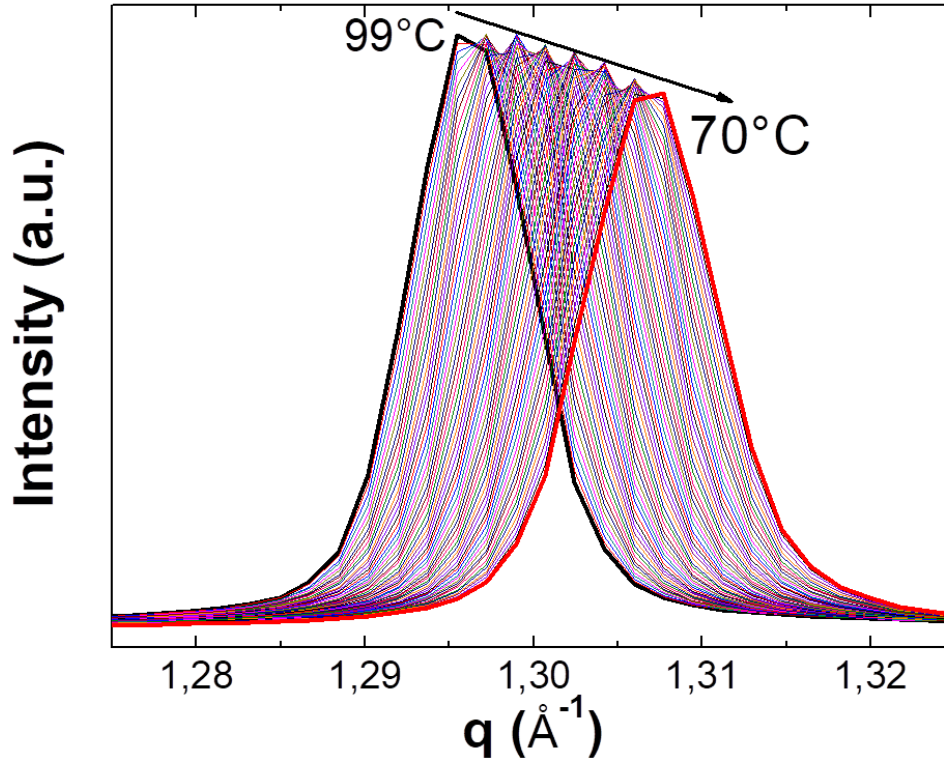
Concerning S-m133 (orange line in Figure 3.9b) at the end of the isothermal step a paraelectric peak is recorded at a  $q$  position very close to that of S-m129 ( $q \approx 1.28 \text{ \AA}^{-1}$ ). Besides the lower crystallisation kinetics of S-m133, the two samples S-m129 and S-m133 seem to behave in the same way, giving rise to a similar paraelectric phase. On the other hand, S-m140 (pink line) presents a crystallisation peak at around  $1.29 \text{ \AA}^{-1}$  at the end of the isothermal step (Figure 3.9b). Between S-m140 and S-m129 (or S-m133) there is a small  $\Delta q$  of  $0.1 \text{ \AA}^{-1}$ . This shift towards higher  $q$  values indicates that the paraelectric crystallites formed at 140 °C are better packed and therefore possess a higher amount of trans conformations with respect to the crystallites formed at  $T_c$  129 °C or at 133 °C. It is reminded that the higher the  $q$ , the smaller the interplanar spacing,  $d$ , and thus the better the chain packing. When gauche conformations are converted into trans, a better packing of chains is achieved and with it a reduction of the  $d$  ( $d = 2\pi/q$ ) that in this case is from  $4.91 \text{ \AA}$  ( $q=1.28 \text{ \AA}^{-1}$ ) to  $4.87 \text{ \AA}$  ( $q=1.29 \text{ \AA}^{-1}$ ).

Figure 3.9c presents the scattering patterns recorded at 30 °C below each  $T_c$ , when all the isothermal and non-isothermal crystallisation processes that were recorded with DSC are completed. For all three samples a slight shift of the paraelectric peak position towards higher  $q$ 's is observed. The S-m129 peak shifts from 1.28 Å<sup>-1</sup> to 1.30 Å<sup>-1</sup>, for S-m133 the peak shifts from 1.28 Å<sup>-1</sup> to 1.29 Å<sup>-1</sup> and for S-m140 the peak shifts from 1.29 Å<sup>-1</sup> to 1.31 Å<sup>-1</sup>. These shifts result from a re-arrangement of the polymer chains that occurs during cooling via intramolecular rotation: gauche defects have the thermal energy to convert into trans conformations through rotational movements. Already, concerning the origin of defects, this suggests that these defects are not chemical ones but physical ones that are generated by thermal processing.

Additionally, during cooling, an increase of peak intensity is observed for all samples, meaning that, along with the increased order, an increase of the crystallinity degree occurs. This is consistent with the decrease of the background intensity, which represents the scattering contribution of the amorphous phase which meaning that, as expected, some amorphous regions are turning crystalline.

It can be concluded that by increasing the crystallisation temperature better crystalline packing, less defects, and higher crystallinity of the paraelectric phase (in accordance with DSC analysis) are achieved, yielding to a greater thermodynamic stability (lower free energy  $G$ ) of the paraelectric phase. According to literature,<sup>16</sup> this is expected to result in a shift of the Curie transition towards lower temperatures during cooling, and in an increase of the melting temperature during heating (due to the low  $G$  of the paraelectric state) that will be discussed later.

Next, the evolution of the paraelectric peak upon cooling between the  $T_c$  and the Curie transition is followed. Figure 3.10 shows the patterns recorded for S-m129, the behaviour of S-m133 and S-m140 being qualitatively the same. A shift of the PE peak towards higher  $q$  and a concomitant decrease of its intensity is detected. This shift means that the paraelectric phase continues to improve its intrinsic order: intermolecular rotations take place during cooling, inducing an inversion of gauche,  $G^{+/-}$ , into trans,  $T$ , conformations, resulting in a gradual shift of the crystalline peak towards higher  $q$  values, due to better chain packing. Note that no significant heat flow variation can be detected by DSC at this temperature range.



**Figure 3.10** *I* vs *q* detected at different *T*, under cooling from 99 °C (black thick line) until 70 °C (red thick line) for S-m129.

Upon further cooling the Curie transition is encountered. In Figure 3.11 the DSC curves at the Curie transition under the first cooling are displayed, after the base line subtraction, to allow a clear evaluation of differences between the samples annealed at different  $T_c$ . As anticipated and in consistence with literature, a global shift of the PE-to-FE transition towards lower temperatures with the increase of the isothermal  $T_c$  occurs. This shift is due to the increased ordering and stability of the paraelectric phase, just proven by time resolved WAXS results. As it can be noticed in Figure 3.11, the solid-state PE-to-FE transition recorded by DSC exhibits multiple exothermic peaks. According to literature, this feature is due to the formations of different ferroelectric phases, more or less ordered, with different amounts of defects.<sup>3,9,12,17</sup> Based on that, one could suggest that three ferroelectric polymorphs are formed for each sample.

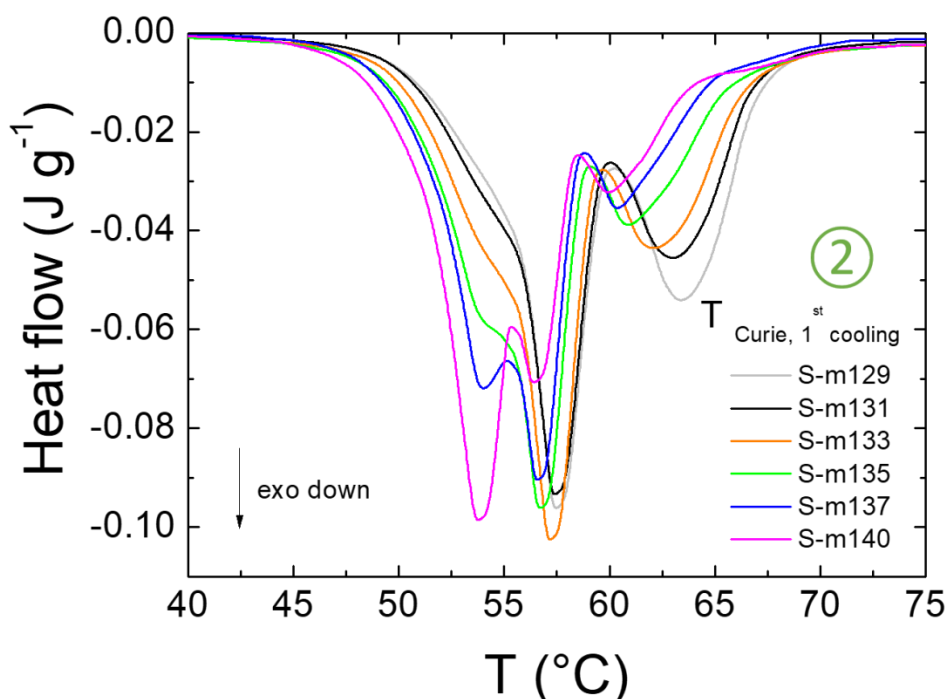


**Figure 3.11** The Curie transition under cooling  $T_{Curie,1st c}$  detected for all the different  $T_c$  after background subtraction.

In order to define these ferroelectric polymorphs and assign each peak of the Curie transition to a certain ferroelectric phase, the WAXS patterns recorded under cooling while crossing the Curie transition are discussed below.

In Figure 3.12 are presented the scattering patterns recorded at different temperatures under cooling, for the three representative samples separately, in order to simplify the understanding of the occurring transitions. Figure 3.12a displays the results for S-m129, Figure 3.12b for S-m133 and Figure 3.12c for S-m140. On the left side of Figure 3.12 the  $q$ -range from  $1.2 \text{ \AA}^{-1}$  to  $1.5 \text{ \AA}^{-1}$  is shown, while on the right side a zoom at low intensities for almost the same  $q$ -range is displayed in order to clearly see the appearance of the peak at  $1.41 \text{ \AA}^{-1}$ .

For each sample it is followed the structural transition from the paraelectric state, recorded at  $70 \text{ }^\circ\text{C}$ , before the beginning of the transition, until the ferroelectric state at  $29 \text{ }^\circ\text{C}$ . In order to describe how this solid-state transition occurs the scattering pattern at  $70 \text{ }^\circ\text{C}$  (black line) is plotted together with the patterns recorded at  $\approx 60 \text{ }^\circ\text{C}$  (red line) at which the “first”  $T_{Curie, 1st c}$  has its maximum, at  $\approx 57 \text{ }^\circ\text{C}$  (blue line) at which the maximum of the “second”  $T_{Curie, 1st c}$  occurs,

at  $\approx 54^\circ\text{C}$  (dark cyan) for the “third”  $T_{\text{Curie, 1st c}}$  (for low  $T_{\text{c}}$  it appears as a shoulder of the second Curie peak), and at  $29^\circ\text{C}$  (wine line). The plots represent also the scattering pattern at  $50^\circ\text{C}$  and  $40^\circ\text{C}$  (pink and orange lines respectively), which are below the Curie transition, as this is detected by DSC.

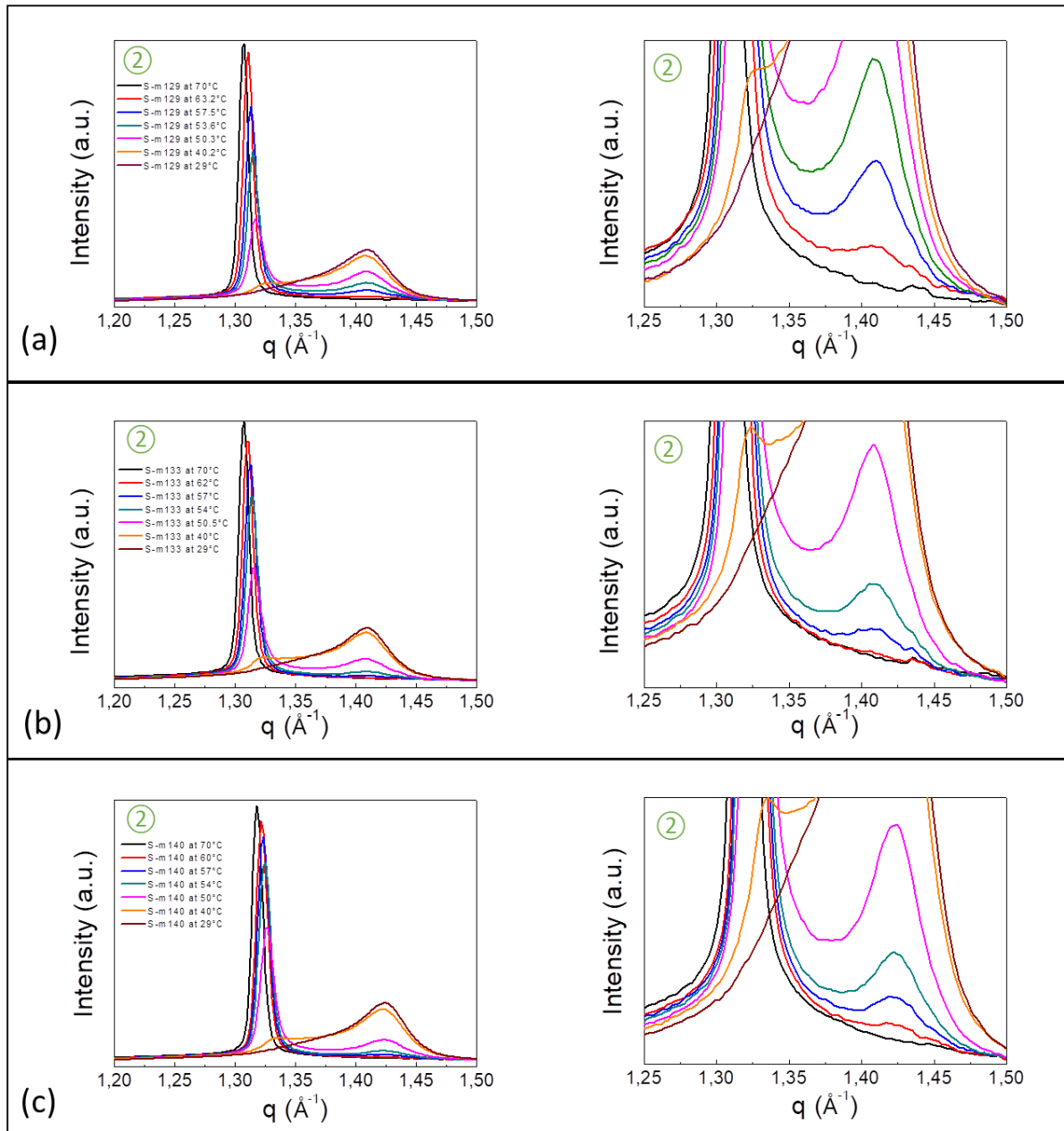


**Figure 3.12**  $I$  vs  $q$  scattering patterns for (a) S-m129, (b) S-m133 and (c) S-m140, recorded during cooling for the temperature range  $70^\circ\text{C} - 29^\circ\text{C}$ . The evolution of the PE-to-FE transition is demonstrated.

At 70 °C, before the PE-to-FE transition starts, just one peak is visible at 1.31 Å<sup>-1</sup> for S-m129 and S-m133 and at 1.32 Å<sup>-1</sup> for S-m140. This peak corresponds to the paraelectric phase that, at 100 °C, was found at q=1.29 Å<sup>-1</sup> for S-m129 and S-m133 and for S-m140 at q=1.31 Å<sup>-1</sup> (Figure 3.9) and now, after ordering through increase of trans segments, has shifted towards higher q's (see also Figure 3.10 and related discussion).

Following the changes under cooling of WAXS patterns (Figure 3.12) it can be noticed that concurrently to the shift of the PE phase towards higher q's and the decrease of its intensity, a ferroelectric peak starts to appear at around 1.4 Å<sup>-1</sup> at T ≈ 60 °C. The intensity of this FE peak increases with the decrease of the temperature. Going from ≈ 60 °C (red lines in Figures 3.12a, 3.12b, 3.12c respectively) to 57 °C (blue lines) and then to ≈ 54 °C (dark cyan line) it can be noticed an initial weak increase of the intensity at q= 1.4 Å<sup>-1</sup> that then turns into a real peak centred at 1.41 Å<sup>-1</sup> for both S-m129 and S-m133 and at 1.42 Å<sup>-1</sup> for S-140. This peak is centred at the higher q end of the PE-to-FE doublet and its position remains constant during the whole transition. We then propose that the PE phase at ~ 60 °C starts to convert into a well-ordered ferroelectric phase that corresponds to the ferroelectric phase called **F<sub>1</sub>** in Chapter 2.

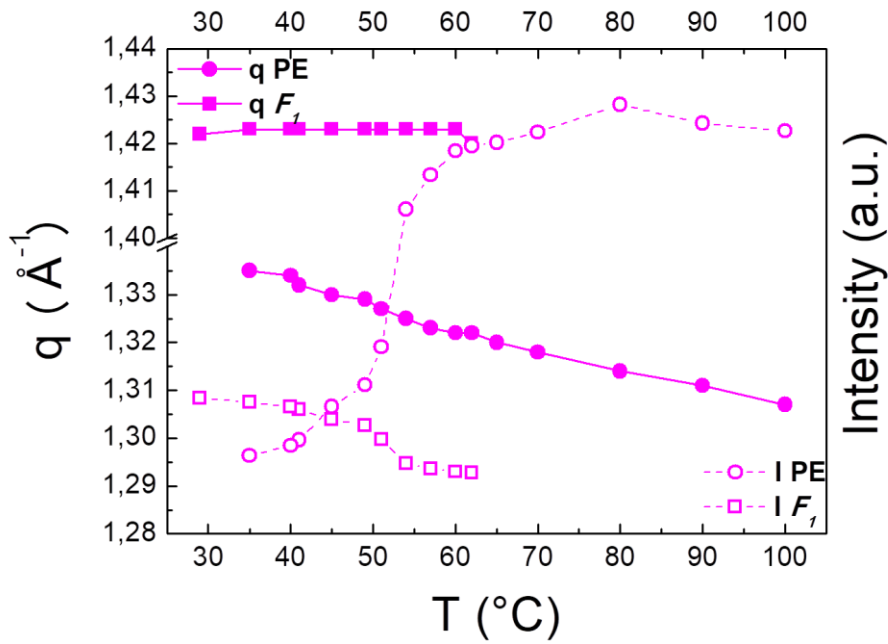
As far as the shift of the PE peak towards higher q's is concerned, this peak finally arrives close to the FE peak. Comparing the scattering patterns at 40 °C and at 29 °C it can be noticed that the small PE peaks at around 1,33 Å<sup>-1</sup> for S-m129 and S-m133 (Figure 3.12a, b right side) and at 1.33 Å<sup>-1</sup> (Figure 3.12c right side) still discernible at 40 °C, are the incorporated into the peak at q=1,4 Å<sup>-1</sup> at 29 °C, this additionally explains why the P(VDF-co-TrFE) peaks has this asymmetric shape.

It seems that intermolecular rotations in the PE phase continue until this peak being incorporated in the large FE peak centred at 1,4 Å<sup>-1</sup>, i.e. until all PE crystallites turn into ferroelectric ones. The asymmetric shape of the peak at 1.4 Å<sup>-1</sup>, that has been assigned to the **F<sub>1</sub>** phase, actually suggests that more than one ferroelectric phase (probably both **F<sub>1</sub>** and **F<sub>1-2</sub>**) is formed and they exhibit scattering peak at around 1.4 Å<sup>-1</sup>.

We can propose that by increasing its amount of T conformations through ordering, the remaining PE phase finally fully converts into the **F<sub>2</sub>** defective phase. Globally between 40 °C and 29 °C the PE phase converts into more than one different ferroelectric phases. This is supported by the asymmetric shape of the peak at 1.4 Å<sup>-1</sup> which suggests that more than one ferroelectric phases are formed and their scattering peaks are centred between 1,32 Å<sup>-1</sup> and

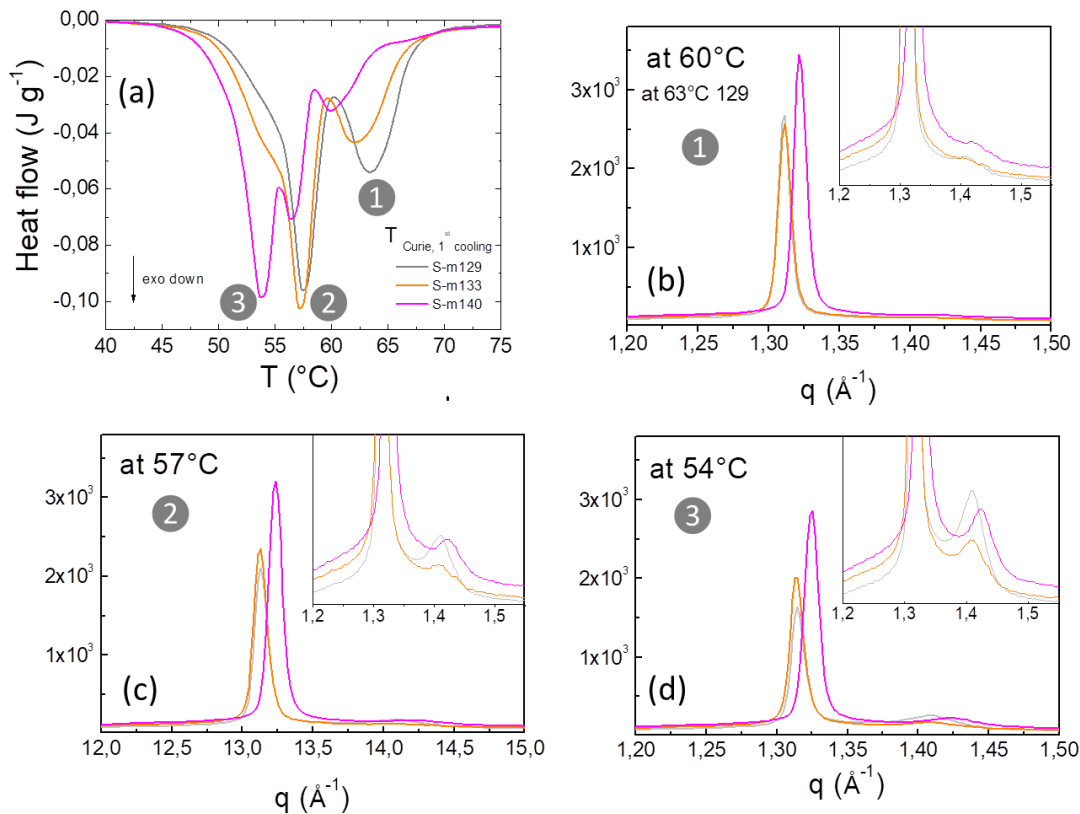
1,42 Å<sup>-1</sup>. In conclusion the scattered intensity at the lower q will be assigned to the most defective ferroelectric phase **F<sub>2</sub>** (already defined in Chapter 2) and can be considered as a residue of the PE phase. Moreover, besides the PE->**F<sub>2</sub>** and the PE->**F<sub>1</sub>** conversion, again based on the asymmetric broad shape of the ferroelectric peak, we can foresee the existence of a third crystalline peak between the peaks that correspond to the **F<sub>1</sub>** and **F<sub>2</sub>** phases and that will be assigned to an intermediately defective phase, **F<sub>1-2</sub>**, as this was defined and observed in Chapter 2.

Figure 3.13 allows visualising the PE-to-FE transition under cooling through the variations of the q position and intensity of the PE and **F<sub>1</sub>** phases. Those variations under cooling are reported just for S-m140 for sake of clarity, since all the three samples exhibit the same trends. Starting from 100 °C and moving towards lower temperatures we assist to an ordering of the paraelectric phase: the q position of the PE phase of S-m140 (pink scattering full circle and full lines) shifts towards higher q positions, from 1,31 Å<sup>-1</sup> at 100 °C to 1,33 Å<sup>-1</sup> at 40 °C. At 64,2 °C appears the **F<sub>1</sub>** phase at 1,42 Å<sup>-1</sup> (pink scattering full squares and full lines), when still the PE peak is present. The **F<sub>1</sub>** phase peak does not shift along the q-axis during cooling to 29 °C keeping its position at 1,42 Å<sup>-1</sup>. The intensity of the PE peak (pink scattering open circle and dashed lines) is almost constant between 100 °C and 70 °C, but starts to significantly decrease below 60 °C, reaching a minimum at 40 °C and then disappearing. This decrease of intensity occurs simultaneously with the appearance at around 60 °C of the **F<sub>1</sub>** phase whose peak intensity increases continuously during cooling from 60 °C to 29 °C (pink scattering open squares and dashed lines).



**Figure 3.13** *I* and *q* position variations of the PE and  $F_1$  ferroelectric peaks of S-m140 During the Curie transition upon cooling.

In Figure 3.14 we compare the DSC curves during the Curie transition with the time resolved WAXS patterns recorded at the three maxima of the DSC Curie transition (i.e.  $\approx 60$  °C,  $57$  °C and  $54$  °C) for the samples S-m129, S-m133, and S-m140. We do this comparison in order to check if we can assign the three DSC peaks to the formation of the three FE phases. As we can see in Figure 3.14b, the peak of the  $F_1$  phase (at  $1.4 \text{ \AA}^{-1}$ ) has just appeared at  $\approx 60$  °C in the WAXS patterns while the solid-state transition that corresponds to the high T DSC peak has largely occurred for S-m129 and S-m133. Moreover, from Figures 3.14 c and 3.14d there is no feature that suggests that the PE  $\rightarrow F_1$ , PE  $\rightarrow F_2$  and PE  $\rightarrow F_{1-2}$  transitions are discrete and take place individually, at specific temperature ranges, as the three discrete DSC peaks would suggest. In fact, WAXS suggest that the structural transitions in all these three samples seem to be gradual. Therefore, assign each Curie transition peak to either  $F_1$  or  $F_{1-2}$  or  $F_2$  cannot be supported by WAXS experiments.



**Figure 3.14** (a) Heat flow vs  $T$  variations at the Curie transitions recorded by means of DSC for S-m129 (grey lines), S-m133 (orange lines) and S-m140 (pink lines), and the  $I$  vs  $q$  patterns recorded at (b) 60 °C (c) 57 °C and (d) 54 °C.

### 3.3.3 ③ Second heating ramp: Curie transition of the melt-crystallised samples

Following cooling down to room temperature, we performed a second heating ramp from RT to 180 °C, with a heating rate of 10 °C min<sup>-1</sup>. The recorded DSC curves that comprise the Curie transition,  $T_{\text{Curie, 2nd h}}$ , and the melting,  $T_m$ , for all the samples isothermally crystallised at different  $T_c$  are shown in Figure 3.15.

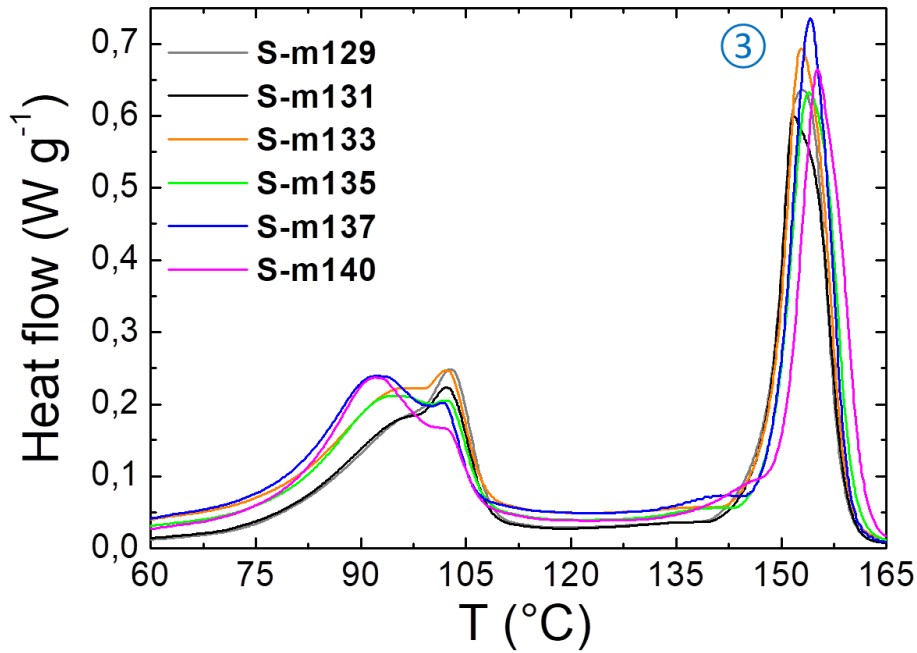


**Figure 3.15** 2<sup>nd</sup> heating ramps recorded by DSC for all samples that have been isothermally crystallised from the melt at different  $T_c$ . The Curie transition is encountered between 75 °C and 105 °C while the melting peak is around 155 °C.

The  $T_{\text{Curie, 2nd h}}$  comprises 2 peaks, a broad shoulder at lower temperatures and a sharp peak at higher temperatures, centred at around 102 °C. According to literature<sup>3,8</sup> the shoulder should be assigned to the transition of the defective ferroelectric phases, the  $F_2$ , into a paraelectric phase, while the sharper peak should be attributed to the transition of the well-ordered ferroelectric phase, the  $F_1$ , into the paraelectric phase. Assuming that, one can conclude that the area of the shoulder that corresponds to the defective phases increases with the increase of  $T_c$  in the expense of the ordered ferroelectric phase transition peak. In fact, with the increase of  $T_c$  the shoulder at lower  $T$  becomes predominant. This would suggest that the sample S-m140 would contain more defective ferroelectric crystallites at room temperature than S-m129. The intermediate  $F_{1-2}$  ferroelectric phase will convert as well into a paraelectric phases at temperature that depends on the level of defects. We do not distinguish anymore three peaks because now the heating rate is much larger than the cooling rate used after isothermal crystallisation. As it can be noticed the transitions occur within the same range of temperatures without a shift between the various samples, we could address this to the convergence of the different FE formed for the different  $T_c$  to the same ordered or

disordered ferroelectric phases. What changes is the amount of each ferroelectric phase. The defective broad peak area seems to increase with the increase of  $T_c$  in spite of the ordered ferroelectric phase transition peak. With the increase of  $T_c$  the shoulder at lower  $T$  becomes predominant. A deconvolution study of the GIWAXS peaks is in perspectives since it will provide the amount of defective  $F_2$ , intermediately defective  $F_{1-2}$  and ordered  $F_1$  phases and eventually confirm or reject what it has been proposed so far.

Before moving to the consideration of the melting peak we would like to go backwards to the first Curie transition encountered upon the first heating. In Figure 3.16 both  $T_{\text{Curie, 1st h}}$  and  $T_{\text{Curie, 2nd h}}$  are displayed.

First it should be noticed that the red curve reproducing the first heating shows three main Curie transitions, which is in line with our description of three ferroelectric phases.<sup>18</sup> The second heating blue curve does not show three distinct peaks. This phenomenon is attributable to the heating rate that in the case of the first heating is low and in the case of the second heating high. In literature, this has been largely documented showing how the shape of the Curie transition is affected by the heating/cooling rate.

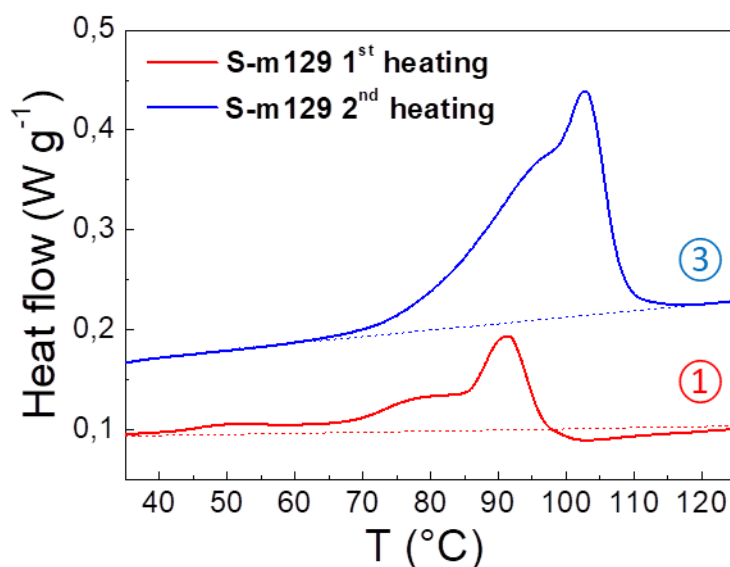


**Figure 3.16** Zoom at 35 °C-125 °C of the 1<sup>st</sup> heating and 2<sup>nd</sup> heating DSC ramp that shows the Curie transition peak shape. The dashed baseline clearly shows the cold crystallisation exothermic peak at ~105 °C just for the 1<sup>st</sup> heating cycle.

We can assume that initially upon the first heating (red curve) the majority of ferroelectric crystallites are  $F_1$ , since the sharper peak at higher temperatures (centred at 90 °C) is predominant with respect to the less intense shoulder at low temperature (at around 80 °C). After annealing (blue curve), insertion of  $G^{+/-}$  defects has occurred as evidenced by the enhanced contribution of the broader peak at lower temperatures  $\sim 95$  °C, assigned to the  $F_2$  (and  $F_{1-2}$ ), with respect to the one at 102-3 °C, which is attributed to the  $F_1$ .

Even though after annealing the  $F_1$  is still predominant, an increase of the defective phases, likely at the expense of pristine ordered, has occurred after thermal treatment. This is in agreement with previous studies where it has been demonstrated that, if on the one hand, an annealing at temperature below the Curie transition improves the order of the already existing ferroelectric phase, on the other hand, an annealing performed in the paraelectric state, so at temperature above the  $T_{Curie}$  (as performed here) produces bigger crystallites but defective.<sup>12</sup>

Upon further heating the melting peak is detected (Figure 3.15). In Figure 3.17 we plot the onset (grey symbols) and the gravitational maxima (black symbols) of the melting peak and the  $\Delta H_m$  calculated (red symbols) by integrating the melting peak after background subtraction. An increase of the crystallite sizes occurs:  $T_m$  position (i.e. its gravitational centre) shifts at higher temperatures with the increase of  $T_c$ , as shown in Figure 3.17.  $\Delta H_m$  follows the same trend which suggests that higher  $T_c$  results in a higher degree of crystallinity, in consistence with the results obtained during crystallisation (Figures 3.8 and relative discussion).

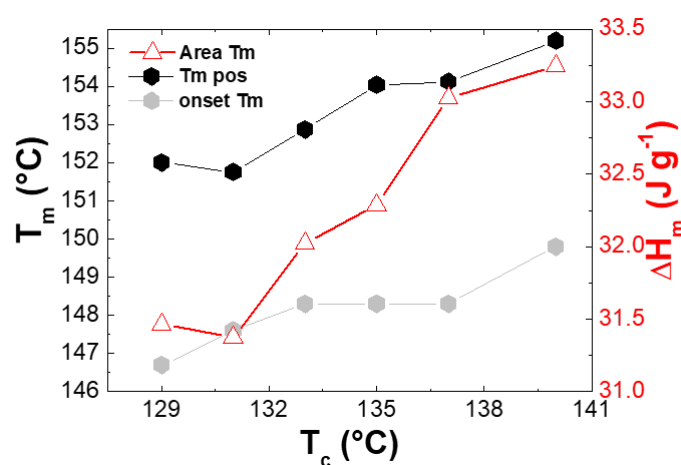


**Figure 3.17** The gravitational centre (black hexagons) and onset (grey hexagons) of the melting peak, as well as the melting peak area (red open triangles), as a function of  $T_c$ .

To complete this discussion, the data recorded during the second cooling are not herein reported since after the second melting the thermal history for all samples is deleted and they all undergo the same crystallization and Curie transition.

### 3.3.4 Impact on the ferroelectric properties

Having completed the structural characterisation of the isothermally melt-crystallised P(VDF-co-TrFE) we proceed now with the ferroelectric characterisation. The effect of melt-crystallisation and of the  $T_c$  used on the ferroelectric properties has been studied by fabricating capacitor devices applying the same thermal protocols used for the structural characterisations.

Polarisation hysteresis loops have been recorded at room temperature (Figure 3.18a) applying a continuous sinusoidal voltage at 10 Hz frequency until the electric field of  $150 \text{ MV m}^{-1}$  to ensure that saturation of the polarisation is reached. From a qualitative evaluation of the ferroelectric loops in Figure 3.18a we can distinguish two groups of samples: S-m129, S-131, S-m133 and S-m135 exhibit hysteresis loops that tend to overlap. In particular, for these first 4 samples almost the same value of remnant polarisation,  $P_r$ , is found at around  $70 \text{ mC m}^{-2}$  and the same coercive field,  $E_c$ , at around  $67 \text{ MV m}^{-1}$ . For the second group of samples, S-m137 and S-m140, a lower  $P_r$  of around  $59 \text{ mC m}^{-2}$  and a higher  $E_c$  ( $71 \text{ MV m}^{-1}$  for S-m135 and  $75 \text{ MV m}^{-1}$  for S-m140) are recorded. In Figure 3.18b the respective  $I$  vs  $E$  current switching peaks are shown: a similar behaviour for the first four samples in terms of similar shape, position and FWHM of the peaks is found. While for S-m137 and S-m140 an enlargement of the width, simultaneously with a decrease of the intensity, and a shift of the switching peaks at higher electric fields are recorded.

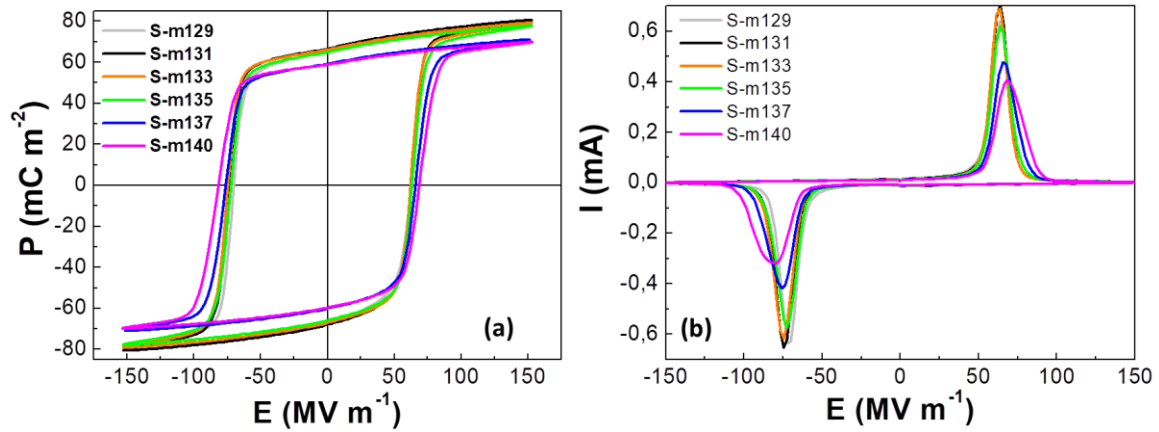


**Figure 3.18** (a) Ferroelectric hysteresis loops where the polarisation  $P$  is measured as a function of the electric field  $E$  and (b) the corresponding  $I$  vs  $E$  switching current peaks for the samples annealed at a  $T_c$  of 129 °C, 131 °C, 133 °C, 135 °C, 137 °C and 140 °C.

The evolution of these ferroelectric parameters with respect to the applied  $T_c$  is displayed in Figure 3.19a for  $P_r$  and  $E_c$  and in Figure 3.19b for the FWHM of the switching current peaks. The plots clearly show that two main groups can be discerned as said above: the first 4 samples having high  $P_r$ , low  $E_c$  and small FWHM and the other two samples having lower  $P_r$  and increasing  $E_c$  and FWHM.

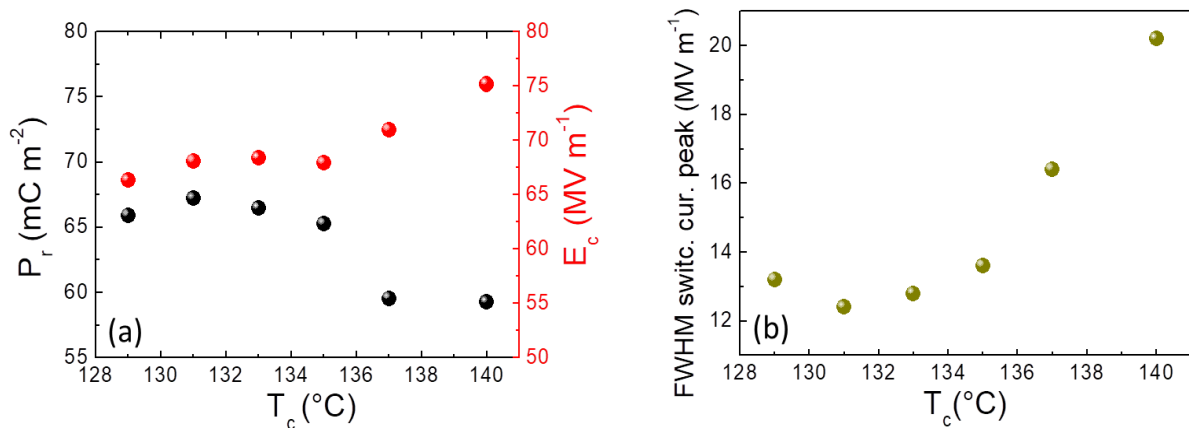


**Figure 3.19** (a)  $P_r$  and  $E_c$ , (b) FWHM of the switching current peaks as a function of the different  $T_c$ .

Considering a high  $P_r$  and a low  $E_c$  as the desired ferroelectric properties we can conclude that by crystallising the films between 129 °C and 135 °C we obtain good, and similar between them, performances. When  $T_c$  is increased to 137 °C or 140 °C a slight deterioration of the performance occurs leading to a decrease of  $P_r$  ( $\approx 59 \text{ mC m}^{-2}$ ) and an increase of  $E_c$ .

According to the structural investigations presented above, an increase of the crystallinity degree has been derived when the crystallisation temperature is increased and, thus, the performance of S-m137 and S-m140 should be expected to be superior with respect to the samples annealed at lower  $T_c$ . However, we should highlight that the analysis of the WAXS data is not completed yet and the volume fractions of the different ferroelectric phases that exist at room temperature have not yet been calculated. Moreover, no information on the orientation of the P(VDF-co-TrFE) crystallites with respect to the substrate has been evaluated yet. Therefore, an integrated analysis of the scattering data (similar to that performed in Chapter 2) should precede the final correlation between  $T_c$  and the ferroelectric properties. Still, one can derive the conclusion that the crystallinity degree is not the only structural parameter that dictates ferroelectric performance.

It is worth now to emphasise that the shown ferroelectric hysteresis loops and so their derivatives (switching current peaks) are obtained after the saturation is reached. During poling a rearrangement of the chain is induced for orientating the dipoles. It has been reported that in the case of the existence of defective ferroelectric phases, those are converted, through poling, into a single ordered phase. Analogously a too perfect  $F_1$  phase can generate gauche defects during poling.<sup>9</sup> In Chapter 2 we have discussed the appearance of an intermediate ferroelectric, slightly defective phase, the  $F_{1-2}$  which we proposed to have the role of facilitating dipoles rotation along the chain through gauche kinks rotation.<sup>9</sup> In this Chapter we also learned that the highly defective  $F_2$  is the result of a gradual transition of the paraelectric phase (made by a random conformation of T and  $G^{+/-}$  segments) which then is expected to be highly defective. Indeed, even though both  $F_{1-2}$  and  $F_2$  are defective phases, we described that the  $F_2$  phase can be seen as a kind of PE residue that turns into disordered ferroelectric crystallites, while  $F_{1-2}$  could be generated with the ordered  $F_1$ , since the asymmetric shape of the peak appearing at peak at  $1.4 \text{ \AA}^{-1}$  could be attributed to both  $F_1$  and  $F_{1-2}$  phases. Considering this potential different structural origin, the phases  $F_2$  and  $F_{1-2}$  are expected to reveal different functional properties with respect to the  $F_2$ . If in the case of an

intermediately defective ferroelectric phase, as  $F_{1-2}$ , few gauche defects can help the rotation, an extreme level/contribution of  $G^{+/-}$  defects, as the one of  $F_2$ , will block the rotation or in any case considerably hinder the dipoles switching.

For the samples S-m137 and S-m140 we have derived from DSC (Figure 3.15) a high contribution of the  $F_2$  where many gauche defects hinder the chain rotation and so cause an enlargement of the switching current peak width or equally a less steep slope of the hysteresis loop. The electric field to apply in order to achieve saturation is higher and the  $P_r$  reached is in any case lower because of the loss of the contribution of the ordered  $F_1$  and slightly defective  $F_{1-2}$ .

We can conclude that while the high content of  $F_{1-2}$  seems to be desirable to get a highly ordered  $F_1$  after pooling, contrarily the  $F_2$  is hindering the switching and indeed is found to be very predominant for the samples S-137 and S-140, which have shown worse ferroelectric properties.

### 3.4 Conclusions

By means of time resolved WAXS and DSC analysis, the isothermal crystallisation of P(VDF-co-TrFE) from the melt and the solid-state transitions its crystallites undergo during cooling or heating have been followed and its polymorphs have been investigated.

For the first time we observe the appearance of defective phases in pristine samples, before any annealing above the  $T_{Curie}$  is performed. Even though previous studies have described that the gauche kinks originate from chemical defects (HH and TT),<sup>15</sup> so they should be apparent ab initio in the samples, so far the appearance of defective ferroelectric phases have been documented only for not annealed P(VDF-co-TrFE) with a very low content of PVDF or for high content VDF copolymers after thermal annealing above the Curie.<sup>2,3</sup>

By following the cooling ramp of the melt-crystallisation protocol it has been found that three crystallisations occur: the pre-isothermal crystallisation during cooling from the molten state to the  $T_c$  (before the  $T_c$  is reached) which generates paraelectric crystallites having a definite unit cell, the isothermal crystallisation where crystallinity degree of the paraelectric

phase decreases significantly, and the post-isothermal crystallisation immediately after the isothermal step. The contribution of the pre-isothermal and the post-isothermal crystallisations to overall crystallinity is lower with respect to that of the isothermal crystallisation. An overall increase of the crystallinity degree arises when  $T_c$  increases.

One paraelectric phase has been observed above the Curie transition. Its unit cell decreases continuously during cooling suggesting the ongoing increase of ordering through increase of trans segments. Before the Curie transition, the paraelectric phase was found to be more ordered for the samples crystallized at higher  $T_c$ .

Upon the Curie transition, the paraelectric P(VDF-co-TrFE) crystallites were found to convert into a well-ordered ferroelectric  $F_1$  phase, its scattering peak being located at a constant  $q$ -value throughout crystallisation, as well as in one or more disordered ferroelectric phases as suggested by the asymmetry of the peak at  $1,4 \text{ \AA}^{-1}$  assigned to the appearance of  $F_1$ .  $F_2$  intermediately ordered phase as found in Chapter 2. In any case from the WAXS data we do not have any evidence of how this intermediate phase originates because of its vicinity in  $q$  position to the  $F_1$  phase. A deconvolution study of this peak should be performed in order to derive with accuracy the position and the volume fraction of each ferroelectric phase apparent in the samples. During the transition the paraelectric peak continuous to shift towards high  $q$ 's and its intensity decreases while the intensity of the  $F_1$  peak increases, until vanishing. The data suggest that the defective  $F_2$  phase is a residual of the paraelectric phase.

Considering the ferroelectric properties of the melt-crystallised samples, we have distinguished two main groups between the samples herein investigated: from  $129 \text{ }^\circ\text{C}$  to  $135 \text{ }^\circ\text{C}$  high  $P_r$  and low  $E_c$  values, together with a small FWHM of the switching current peaks are achieved; while for samples S-m137 and S-m140 a decrease of the devices performance has been found. We attribute this decrease of the performances of the second group to a possible high content of the highly defective  $F_2$ , (from DSC experiments) which undermines the ferroelectric switching. Despite the crystallinity degree increases with the increase of  $T_c$  and is higher among all samples for the S-m140, our data show that its ferroelectric performance is not optimal. Once more, a deconvolution studies on the WAXS data is necessary and is in perspectives.

We proposed that the correlations between structural phases and performance need to be searched in the intramolecular rotational during poling. Indeed, when we do apply an electric field to a P(VDF-co-TrFE) copolymer we are inducing rotation along the chains for aligning the dipoles. It has been already proposed in Chapter 2 that an intermediate phase, the  $F_{1-2}$ , would even favour more than a very perfect ferroelectric phase, the intramolecular rotation thanks to the presence of few gauche defects that acts as activation site for the rotation to begin. In the other hand a too defective phase  $F_2$  is expected to show some dipoles orientation, which in any case will not reach the degree of that of the  $F_1$  and  $F_{1-2}$  leading to a decrease in the performances.

## References

- 1 Lovinger, A. J., Furukawa, T., Davis, G. T. & Broadhurst, M. G. Crystallographic changes characterizing the Curie transition in three ferroelectric copolymers of vinylidene fluoride and trifluoroethylene: 1. As-crystallized samples. *Polymer* **24**, 1225-1232, doi:http://dx.doi.org/10.1016/0032-3861(83)90050-2 (1983).
- 2 Tashiro, K. & Kobayashi, M. Structural phase transition in ferroelectric fluorine polymers: X-ray diffraction and infrared/Raman spectroscopic study. *Phase Transit.* **18**, 213-246, doi:10.1080/01411598908206864 (1989).
- 3 Koga, K. & Ohigashi, H. Piezoelectricity and related properties of vinylidene fluoride and trifluoroethylene copolymers. *Journal of Applied Physics* **59**, 2142-2150, doi:10.1063/1.336351 (1986).
- 4 Lovinger, A. J., Johnson, G. E., Bair, H. E. & Anderson, E. W. Structural, dielectric, and thermal investigation of the Curie transition in a tetrafluoroethylene copolymer of vinylidene fluoride. *J. Appl. Phys.* **56**, 2412-2418, doi:10.1063/1.334303 (1984).
- 5 Kepler, R. G. & Anderson, R. A. Ferroelectric polymers. *Advances in Physics* **41**, 1-57, doi:10.1080/00018739200101463 (1992).
- 6 Lovinger, A. J., Davis, G. T., Furukawa, T. & Broadhurst, M. G. Crystalline forms in a copolymer of vinylidene fluoride and trifluoroethylene (52/48 mol %). *Macromolecules* **15**, 323-328, doi:10.1021/ma00230a024 (1982).
- 7 Lovinger, A. J. Ferroelectric polymers. *Science* **220**, 1115-1121 (1983).
- 8 Koga, K., Nakano, N., Hattori, T. & Ohigashi, H. Crystallization, field-induced phase transformation, thermally induced phase transition, and piezoelectric activity in P(vinylidene fluoride-TrFE) copolymers with high molar content of vinylidene fluoride. *Journal of Applied Physics* **67**, 965-974, doi:10.1063/1.345706 (1990).
- 9 Gregorio, R. & Botta, M. M. Effect of crystallization temperature on the phase transitions of P(VDF/TrFE) copolymers. *Journal of Polymer Science Part B: Polymer Physics* **36**, 403-414, doi:10.1002/(sici)1099-0488(199802)36:3<403::aid-polb2>3.0.co;2-s (1998).

- 10 Bellet-Amalric, E. & Legrand, J. F. Crystalline structures and phase transition of the ferroelectric P(VDF-TrFE) copolymers, a neutron diffraction study. *Eur Phys J B* **3**, 225-236 (1998).
- 11 Tashiro, K., Takano, K., Kobayashi, M., Chatani, Y. & Tadokoro, H. Structural study on ferroelectric phase transition of vinylidene fluoride-trifluoroethylene copolymers (III) dependence of transitional behavior on VDF molar content. *Ferroelectrics* **57**, 297-326, doi:10.1080/00150198408012770 (1984).
- 12 Kim, K. J., Kim, G. B., Vanlencia, C. L. & Rabolt, J. F. Curie transition, ferroelectric crystal structure, and ferroelectricity of a VDF/TrFE(75/25) copolymer 1. The effect of the consecutive annealing in the ferroelectric state on curie transition and ferroelectric crystal structure. *Journal of Polymer Science Part B: Polymer Physics* **32**, 2435-2444, doi:10.1002/polb.1994.090321501 (1994).
- 13 Su, R. *et al.* Ferroelectric behavior in the high temperature paraelectric phase in a poly(vinylidene fluoride-co-trifluoroethylene) random copolymer. *Polymer* **53**, 728-739, doi:https://doi.org/10.1016/j.polymer.2012.01.001 (2012).
- 14 Bargain, F., Panine, P., Domingues Dos Santos, F. & Tencé-Girault, S. From solvent-cast to annealed and poled poly(VDF-co-TrFE) films: New insights on the defective ferroelectric phase. *Polymer* **105**, 144-156, doi:http://doi.org/10.1016/j.polymer.2016.10.010 (2016).
- 15 Lovinger, A. J., Davis, D. D., Cais, R. E. & Kometani, J. M. The role of molecular defects on the structure and phase transitions of poly(vinylidene fluoride). *Polymer* **28**, 617-626, doi:https://doi.org/10.1016/0032-3861(87)90478-2 (1987).
- 16 Stack, G. M. & Ting, R. Y. Thermodynamic and morphological studies of the solid-state transition in copolymers of vinylidene fluoride and trifluoroethylene. *J. Polym. Sci. B Polym. Phys.* **26**, 55-64, doi:10.1002/polb.1988.090260102 (1988).
- 17 Kim, K. J. & Kim, G. B. Curie transition, ferroelectric crystal structure and ferroelectricity of a VDF/TrFE (75/25) copolymer: 2. The effect of poling on curie transition and ferroelectric crystal structure. *Polymer* **38**, 4881-4889 (1997).
- 18 Spampinato, N. *et al.* Enhancing the ferroelectric performance of P(VDF-co-TrFE) through modulation of crystallinity and polymorphism. *Polymer*, doi:10.1016/j.polymer.2018.06.072 (2018).

- 19 Oliveira, F. *et al.* Process influences on the structure, piezoelectric, and gas-barrier properties of PVDF-TrFE copolymer. *Journal of Polymer Science Part B: Polymer Physics* **52**, 496-506, doi:10.1002/polb.23443 (2014).
- 20 Alves, N., Plepis, A. M. G., Giacometti, J. A. & Oliveira, O. N. Influence of preparation methods and thermal treatment in melt-solidified and cast films of poly(vinylidene fluoride-trifluoroethylene)copolymers. *Ferroelectrics Letters Section* **23**, 99-105, doi:10.1080/07315179808204185 (1998).

# Chapter 4

*The effect of crystallites  
orientation on the  
ferroelectric performance of  
P(VDF-co-TrFE)*



## 4 The effect of crystallites orientation on the ferroelectric performance of P(VDF-co-TrFE)

### 4.1 Introduction

After having studied the effect of the cold- and melt- isothermal crystallisation on structural and ferroelectric properties of P(VDF-co-TrFE), in this Chapter 4 we investigate the effect of crystallites orientation. From Chapter 2 we have comprehended that the orientation of the crystallites plays a crucial role in the final device performance. Despite the high degree of crystallinity of sample S-140, we recorded a decreased ferroelectric performance for this sample, due to an altered crystallites orientation with respect to the substrate, compared to the samples annealed at lower crystallisation temperatures or the pristine one.<sup>1</sup>

P(VDF-co-TrFE) is known to commonly crystallise into needle-like shaped crystallites which are composed by stacks of lamellae as represented in Figure 4.1a, reported from reference <sup>2</sup>.

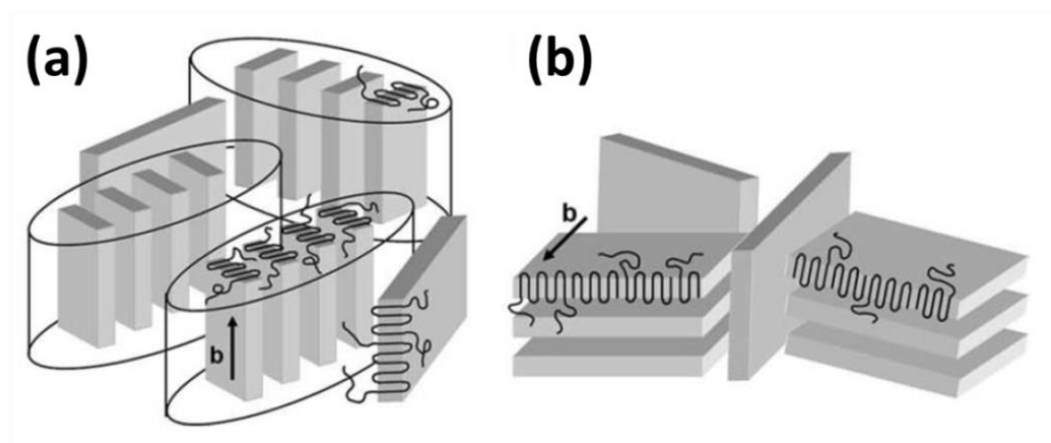


**Figure 4.1** A schematic representation of the microstructure for (a) an edge-on orientation, where the polar b-axis is perpendicular to the substrate and (b) for a face-on orientation, where the polar b-axis is parallel to the substrate. Reproduced from <sup>2</sup>.

Normally in P(VDF-*co*-TrFE) films obtained by spin-coating, the strong centrifugal force of the deposition technique induces a preferred “edge-on” orientation of these crystalline lamellae.<sup>2</sup> In the edge-on orientation, as can be seen from Figure 4.1a, the polymeric chains lie parallel to the substrate and consequently the dipoles, orthogonal to the chain axis, are perpendicular to the substrate (the b-arrow represents the unit cell b-axis that corresponds to the directions of the dipoles),<sup>2</sup> and thus perpendicular to the applied electric field. As shown in Figure 4.1b, in a “face-on” orientation, the lamellae lie on the substrate and consequently the molecular chain c-axis and the polar b-axis are respectively perpendicular and parallel to the substrate.

Several authors<sup>2-4</sup> have documented the occurrence of an inversion from the preferred “edge-on” orientation to a “face-on” orientation either induced by thermal annealing, either induced by film thickness variation. Park *et al.* proved that this inversion is induced when a heat treatment upon the melting point is performed.<sup>2</sup> Guo *et al.*,<sup>5</sup> studying P(VDF-*co*-TrFE) ultrathin films, reported that the abrupt stand-up of the polymer backbone, formerly lying on the substrate, actually occurs at a critical temperature, around 140 °C, with a simultaneous reorientation of the polarisation axis. Figure 4.2 (reproduced from reference<sup>5</sup>) clearly shows this inversion of orientation at different length scales: (a) the back-bone orientation, (b) the b-axis orientation within the unit cell, where the c-axis comes out of the page, and (c) the overall lattice cell orientation with respect to the substrate, where the blue arrows represent the dipoles orientation.

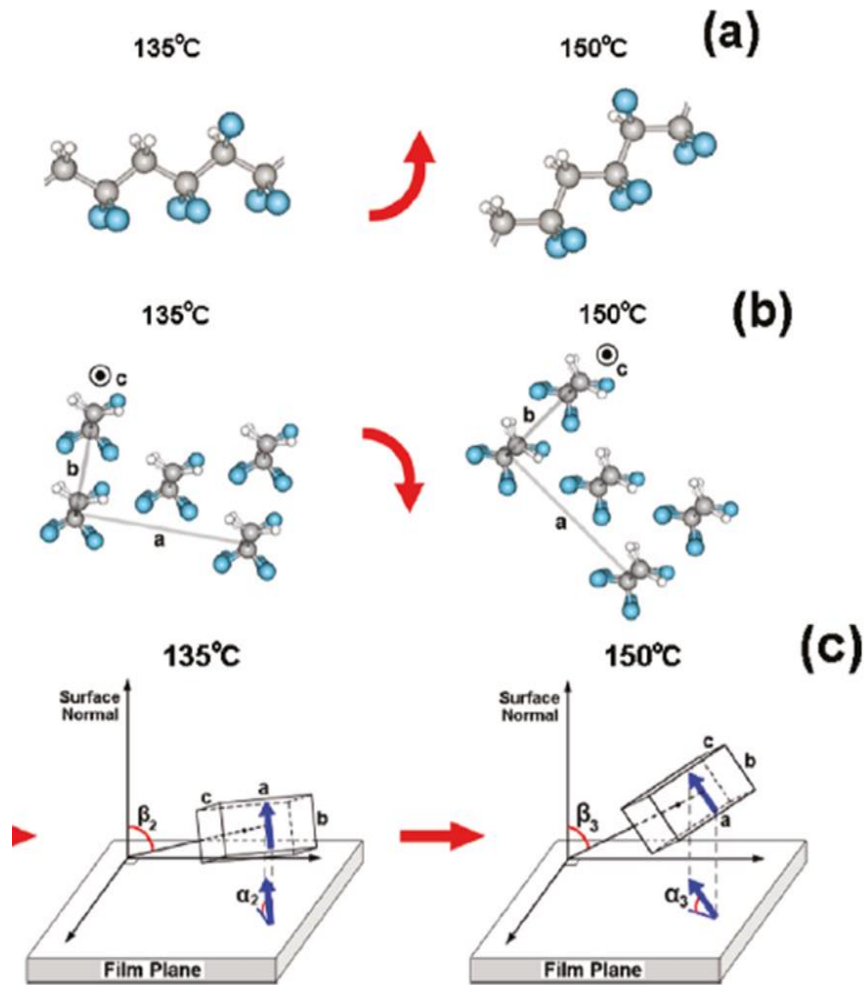


**Figure 4.2** Schematic illustration of the (PVDF-co-TrFE) molecular orientation (left side) after an annealing at 135 °C and (right side) at 150 °C. From the top to the bottom are represented (a) the backbone orientation, (b) the b-axis orientation and (c) lattice orientation (a unit lattice cell is used for clarity), where the blue arrows represent the dipoles orientation. Reproduced from reference <sup>5</sup>.

When the inversion occurs, a reduction or an extinction of the ferroelectric response to the applied electric field is detected. The decreased ferroelectric properties need to be ascribed to the direction of the b-axis, which is the direction of the dipoles. As it can be seen from Figure 4.1a or 4.2c left side, in the case of an “edge-on” orientation, the polar b-axis is already aligned towards the direction of the electric field applied, if we consider the capacitor geometry, where bottom and top electrodes are parallel to the plane of the P(VDF-co-TrFE) film. While when a “face-on” orientation is induced, an inversion of  $\approx 90^\circ$  of the chains occurs (Figure 4.1b and Figure 4.2c right side): polymer crystals have now the c-axis and b-axis

respectively perpendicular and parallel to the substrate, and consequently to the electrodes plane.<sup>2</sup>

This is the reason why “edge-on” crystallites are preferred for a high ferroelectric performance, since the externally applied electric field will easier align the dipoles.

While in case of Park,<sup>2</sup> the face-on orientation induced by annealing above the melting point, leads to the extinction of the ferroelectric polarisation i.e. to an almost zero coercive electric field  $E_c$  and a negligible  $P_r$ , in our case<sup>1</sup> and in the case investigated by Guo,<sup>5</sup> a ferroelectric response is detected despite the absence of the preferred “edge-on” orientation. The discrepancy between the final ferroelectric behaviours could be attributed either to the presence of residual crystallites that are still in the preferred edge-on orientation, or to partial crystallite rotation (i.e. not a complete 90 ° rotation).

Therefore, we can summarise that adjusting thermal annealing or the thickness of the films, a variation of the orientation of P(VDF-co-TrFE) crystals can be induced with a simultaneous reduction or, in some cases extinction, of the ferroelectric properties.<sup>6,7</sup>

In this Chapter 4 we describe how different crystals orientations are generated when considerably different thermal protocols are applied. In particular, we first discuss how melting, quenching and annealing processes affect chain orientation and the whole crystalline structure of P(VDF-co-TrFE) films, and then move to the investigation of ferroelectric and dielectric properties of films with different crystals orientations. A quantitative study of the effect of crystallites orientation on the final performance is endeavoured.

## 4.2 Sample preparation

A solution of P(VDF-co-TrFE), with a VDF-TrFE molar ratio of 75-25, has been spin coated onto Si (for GIWAXS experiments) and onto Al/glass substrates (for capacitor fabrication). For the capacitors fabrication, after spin-coating, thermal depositions of the top electrodes have been performed before applying the film processing thermal protocols. Four samples were prepared using four different thermal treatments that consist in:

- (1) Isothermal cold crystallisation,
- (2) isothermal crystallisation from the melt,
- (3) non isothermal crystallisation from the melt,
- (4) melt-quench-isothermal crystallisation method.

The sample prepared by protocol (1) corresponds to the best performing sample of Chapter 2, which has been heated from RT to 135 °C, isothermally annealed for 15 min, and then slowly cooled down to RT.<sup>1</sup> This sample is called S-135.

The annealing treatment (2) is representative of the thermal protocols applied in Chapter 3: a heating from RT to 165 °C (above the  $T_m$ ), where an isothermal step of 15 min is performed, is followed by a fast cooling to 135 °C, where an isothermal crystallisation is carried for 15 min, followed by a slow cooling to RT. This sample is called S-165-135.

The sample that follows the protocol (3) is heated from RT to 165 °C, isothermally melted for 15 min and then slowly cooled to RT. Thus a non-isothermal crystallisation from the melt occurs. This sample is called S-165.

The sample that follows the protocol (4) was heated onto a hotplate from RT to 165 °C then isothermally melted for 15min, then quenched by immersing it in liquid nitrogen ( $N_{2,liq}$ ). After this step the sample is quickly transferred onto a hot stage already set at the crystallisation temperature of 135 °C, and is isothermally cold-crystallised at 135 °C for 15 min, then it was slowly cooled down to RT. The sample is called S-165- $N_2$ -135.

## 4.3 Results and discussion

### 4.3.1 Structural characterisation: crystallites orientation distribution

In order to identify the crystallites orientation of the four samples S-135, S-165, S-165-135 and S-165- $N_2$ -135 and quantify their crystallinity degree, GIWAXS experiments have been performed at RT. As already explained in Chapter 2, the choice of the substrate is very important when GIWAXS experiments are carried out. In fact, we avoided the use of Al/glass substrates, employed for the preparation of the capacitor devices, because of the high scattering contribution coming from the aluminium that overwhelms the scattered

information of the P(VDF-co-TrFE) crystallites. Therefore, silicon was chosen as substrate for GIWAXS experiments since it scatters less than Al and thus is more suitable for a quantitative analysis that requires a background subtraction as precise as possible. All necessary corrections (listed in the Annex Section) have been applied to the raw GIWAXS patterns, including background scattering subtraction and wedge correction.<sup>8</sup>

The 2D wedge-corrected images give us the information about the preferred orientation of the crystallites. Indeed, we can define an azimuthal angle  $\chi$  with respect to the  $q_z$ -axis: at the intersection with the  $q_z$ -axis, i.e. the “out-of-plane” axis,  $\chi = 0^\circ$ , while at the intersection with the  $q_r$ -axis, that is the “in-plane” axis,  $\chi = 90^\circ$ .<sup>9</sup> When the scattering intensity at a certain  $q$  is higher along certain angle  $\chi$  range, a preferred orientation of the crystallites is revealed. When higher intensity is revealed close to the out-of-plane axis, named also “meridian”, the preferred orientation is the edge-on, while, when the intensity is higher along the in-plane axis, also named “equator”, the preferred orientation is the face-on as shown in Figure 4.3 reproduced from reference<sup>10</sup>.

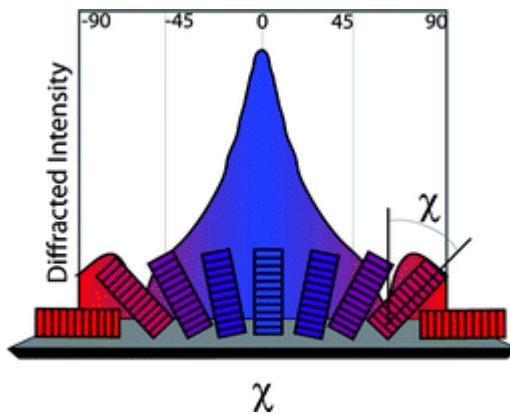


**Figure 4.3** Schematic representation of the variation of  $I$  vs  $\chi$  and the corresponding crystalline lamellae orientations with respect to the substrate plane. Reproduced from reference<sup>10</sup>.

Therefore, by qualitatively evaluating the variation of the scattering intensity at the peak position we can define the preferred crystals orientation of each differently processed sample.<sup>2</sup> The 2D-wedge corrected images of the four samples are displayed in Figure 4.4. All the four patterns display the arced strong reflection at  $q \approx 1.4 \text{ \AA}^{-1}$  which corresponds to both (110) and (200) reflections of P(VDF-co-TrFE) crystalline unit cell. The P(VDF-co-TrFE)

crystalline phase has an orthorhombic lattice that is characterised by a ratio of its  $a$  and  $b$  axes equal to  $\sqrt{3/2}$  ( $=1.225$ ) and in turns results in a nearly equal (110) and (200) spacing ( $\sim 0.45$  nm).<sup>26</sup>

We herein display and describe the four samples in a sequence that follows the gradual variation of the intensity along the ring at  $q \approx 1.4 \text{ \AA}^{-1}$ , from an accentuated intensity along the meridian to one accentuated along the equator. Therefore, in Figure 4.4a is shown the S-135, in Figure 4.4b the S-165-N<sub>2</sub>-135, in Figure 4.4c the S-165 and in Figure 4.4d the S-165-135.

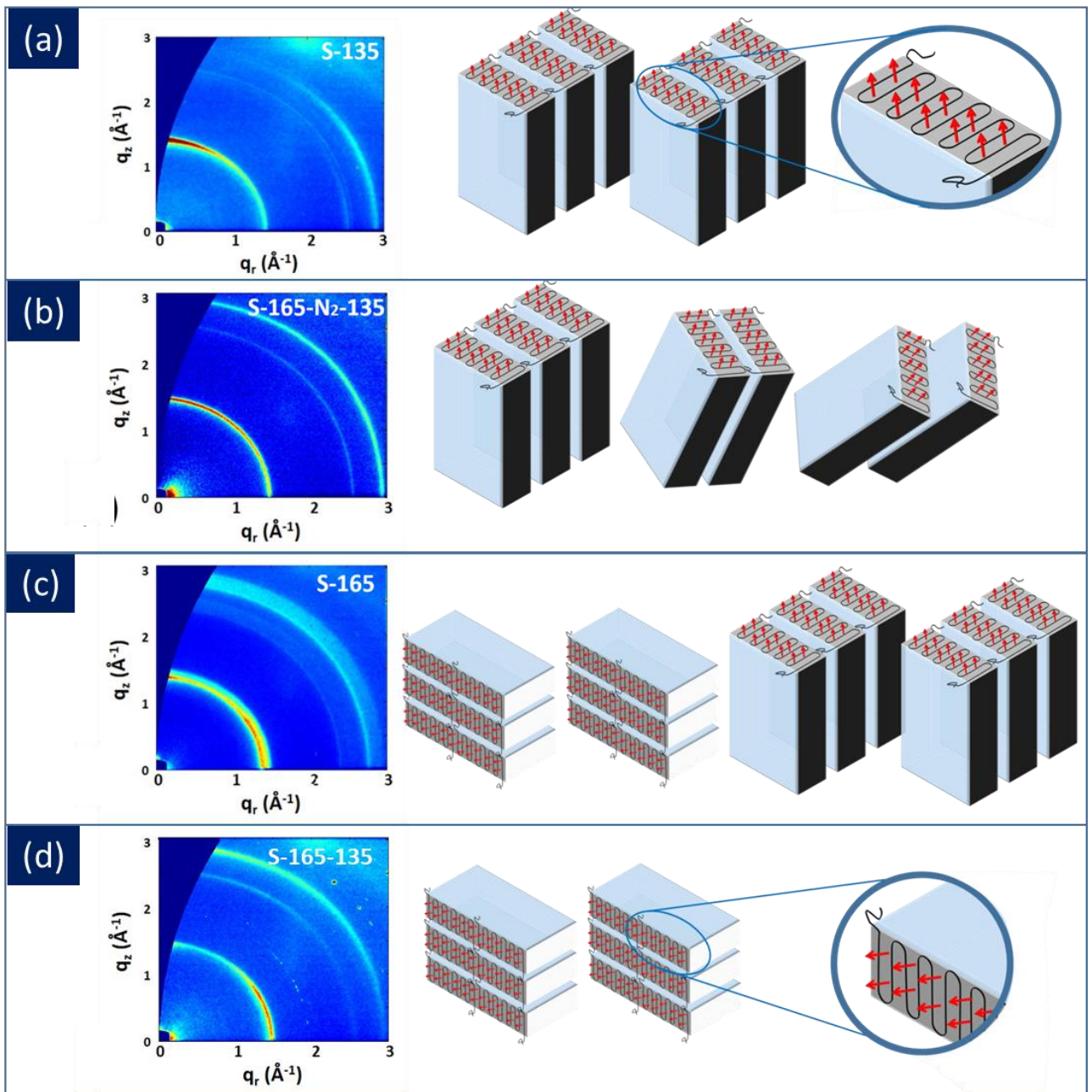


**Figure 4.4** 2D wedge-corrected GIWAXS images (on the left side) and the corresponding microstructure schematic representation (on the right side) for (a) S-135, (b) S-165-N<sub>2</sub>-135, (c) S-165 and (d) S-165-135.

In Figure 4.4a S-135 exhibits a broadly arced (110),(200) reflection whose intensity is higher at the meridian.<sup>6</sup> This intensity distribution declares a preferential orientation of crystals with their chain c-axis dominantly lying parallel to the substrate. For this orientation it has been described that both a- and b- axes can rotate around the c-axis randomly.<sup>2</sup>

In Figure 4.4b the 2D wedge corrected image of S-165-N<sub>2</sub>-135 shows a scattering peak at  $q \approx 1.4 \text{ \AA}^{-1}$  with high intensity from the meridian ( $\chi = 0^\circ$ ) up to  $\approx 60^\circ$ -  $70^\circ$  off meridian. The fact that a high scattering intensity is detected almost all along the entire ring, suggests that the S-165-N<sub>2</sub>-135 crystallites are oriented in a nearly isotropic way, with a slight preference towards the out-of-plane/edge-on orientation. We do not record high scattering intensity along  $q_r$ , meaning that there are no face-on crystals. Through “melt-quench-isothermal” crystallisation, a quasi-random orientation of the crystallites seems to be induced: in S-165-N<sub>2</sub>-135 not just edge-on oriented crystallites exist, as found for S-135, but also crystallites tilted with respect to the substrate plane.

In Figure 4.4c the (110),(200) arced reflection of S-165 reveals a scattering intensity that is high at both the meridian and the equator, meaning that there are crystallites whose c-axis is parallel to the substrates (high intensity at the meridian) and others with a preferential orientation of the c-axis perpendicular to the substrate (high intensity near the equator). It can be concluded then that the sample S-165 has crystallites with two main preferred orientations: “edge-on” and “face-on”.

For the sample S-165-135 displayed in Figure 4.4d, a pronounced scattering intensity is found at the equator, implying that the majority of polymer chains are aligned with their c-axis (i.e. their backbone) perpendicular to the substrate, with both a- and b-axis parallel to the substrate.<sup>2</sup> Consequently, the preferred orientation of the crystallites is considered to be “face-on” mainly. However, high intensity is also detected at the meridional, implying that a residue of the preferred edge-on orientation seems to be persistent.

This first qualitative evaluation of the 2D-wedge corrected images let us conclude that samples crystallised after melting tend to have crystallites that have rotated, giving rise to a microstructure that is or a mixture of edge-on and face-on lamellae, as in the case of S-165, or, as in the other case of S-165-135, to an almost complete inversion of the lamellae towards the face-on orientation.

It should be said that the preferred face-on orientation was found by Park *et al.*<sup>2</sup> when either a slow or a fast cooling from melt is carried out.<sup>2</sup> This is consistent with our observations on samples S-165 and S-165-135. For sample S-165-N<sub>2</sub>-135 (Figure 4.4b) the quenching step freezes the crystallites into a random, nearly isotropic orientation, inhibiting rotation. In other

words, the cooling (rapid or slow) from the molten state seems to be the step that induces rotation of the lamellae towards a face-on orientation, and this rotation seems not to be completely accomplished when quenching of the molten state is performed.

So far, the 2D-wedge corrected images in Figure 4.4 have been just qualitatively described. Going one-step further, we now seek to quantify the relative amount of crystallites oriented towards a certain direction. In order to carry out this analysis the orientation distribution  $I(\chi)$  vs  $\chi$  plots need to be evaluated as well as the crystallinity of each samples.

First the  $I(\chi)$  vs  $\chi$  plots that correspond to a cut that follows the  $\chi$ -arc of the (200)(110) peak (at  $q=1.4 \text{ \AA}^{-1}$ ) are shown for the four samples in Figure 4.5. Before continuing with the analysis, it is brought the attention to the fact that the intensity in these plots is corrected by multiplying with  $\sin(\chi)$  (Figure 4.5). Considering the detected scattering intensity “ $I$ ” as representing the “amount of material” would result in an error since just a “cut” of the Ewald sphere in the 3D reciprocal-space is detected by the 2D GIWAXS detector. In order to take into account this error the samples symmetry should be considered. In this case that “in-plane powder” approximation,<sup>11</sup> which assumes an isotropic in-plane orientation of the crystallites can be adopted. The observed scattering intensity near  $q_r$  is due to a whole scattering ring in the 3D reciprocal-space, this ring is smaller at larger  $\chi$ ; multiplying by the  $\sin(\chi)$  factor we account for this variation,<sup>9</sup> and we obtain a corrected intensity which now is proportional to the amount of material oriented at that  $\chi$  angle.

In Figure 4.5 the corrected scattering intensity of the (110)(200) diffraction ring as a function of the polar angle  $\chi$  is shown for the four samples. In Figure 4.5a the S-135 sample exhibits a maximum intensity at  $\approx 20^\circ$ , indicative of a preferred edge-on orientation ( $\chi < 45^\circ$ ). In Figure 4.5b the S-165-N<sub>2</sub>-135 sample has a broad maximum between  $25^\circ$  and  $40^\circ$ , which decreases smoothly at higher  $\chi$  angles compared to S-135. Many orientations seem to co-exist, rendering the overall orientation almost isotropic. In Figures 4.5c and 4.5d S-165 and S-165-135 exhibit both a preferred face-on orientation, since the intensity is higher at high  $\chi$  angle ( $\chi > 45^\circ$ ). The fact that a plateau is apparent at  $\chi > 60^\circ$  shows that crystallites are predominantly tilted or lying on the substrate.

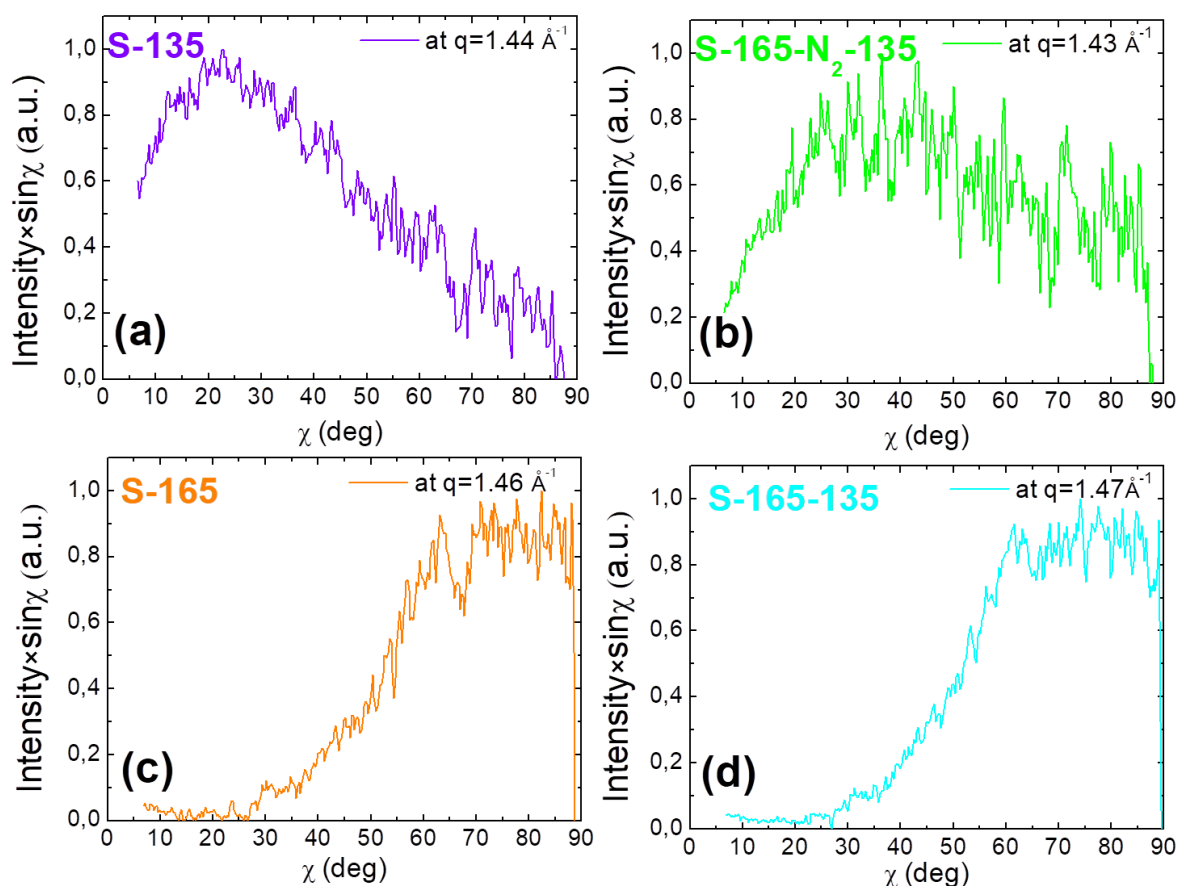


**Figure 4.5**  $I$  vs  $\chi$  at the maximum intensity  $q$  position of the (a) S-135, (b) S-165-N<sub>2</sub>-135, (c) S165 and (d) S-165-135.

In Figure 4.6 the  $I(\chi) \times \sin(\chi)$  vs  $\chi$  plots of Figure 4.5 are merged together in order to better visualise the gradual variation of crystallites orientation for the four samples. S-135 has mainly edge-on lamellae, S-165-N<sub>2</sub>-135 crystallites are more tilted and obtain quite an isotropic orientation, while this tilt further increases and a preferred stand-up chain orientation (namely face-on) occurs for S-165 and S-165-135.

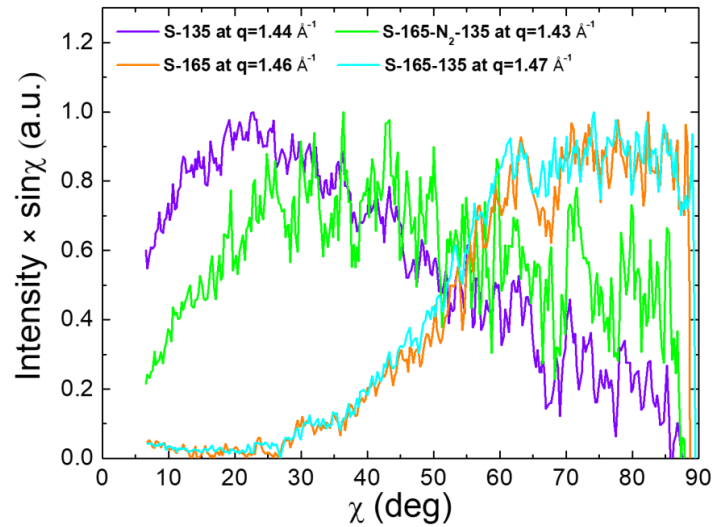


**Figure 4.6**  $I(\chi) \times \sin(\chi)$  vs  $\chi$  plots at the maximum intensity  $q$  position of the S-135 (violet line), S-165-N<sub>2</sub>-135 (green line) S165 (orange) and S-165-135 (cyan line).

Quantitative information on the crystallite orientation can be extracted from the  $I(\chi) \times \sin(\chi)$  vs  $\chi$  plots. In particular, the fraction of edge-on oriented crystallites can be estimated from the ratio between the  $I(\chi) \times \sin(\chi)$  vs  $\chi$  integral from 0° to 45° and the one from 0° to 90°. Similarly, the volume fraction of face-on oriented crystallites is calculated from the ratio between the  $I(\chi) \times \sin(\chi)$  vs  $\chi$  integral from 45° to 90° and the one from 0° to 90°. The results obtained for these four samples are presented in Figure 4.7. In accordance with the qualitative data description provided above, the maximum edge-on volume fraction (72%) is obtained for S-135 and the lower (9%) for S-165 and S-165-135.

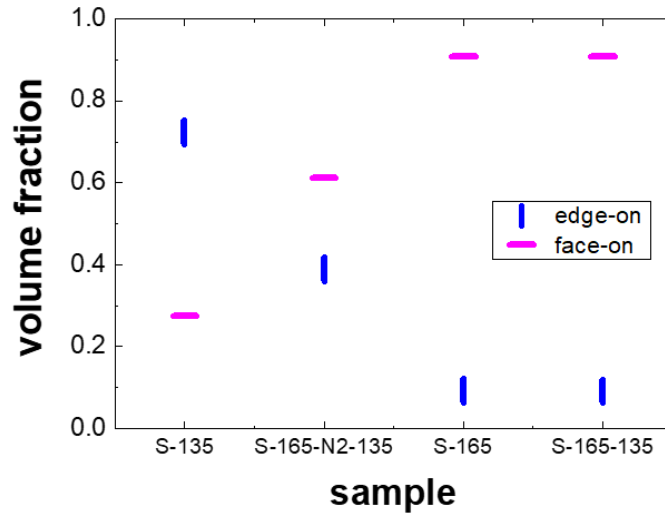


**Figure 4.7** The volume fraction of edge on (blue) and of the face-on (pink) oriented crystallites for these four samples.

Next, we calculate the crystallinity degree of the four samples. The 2D wedge corrected images (Figure 4.4 left side) were radially integrated to extract the 1D-scattered intensity vs scattering vector (*Intensity vs q*) patterns of the four samples, which are shown below in Figure 4.8.

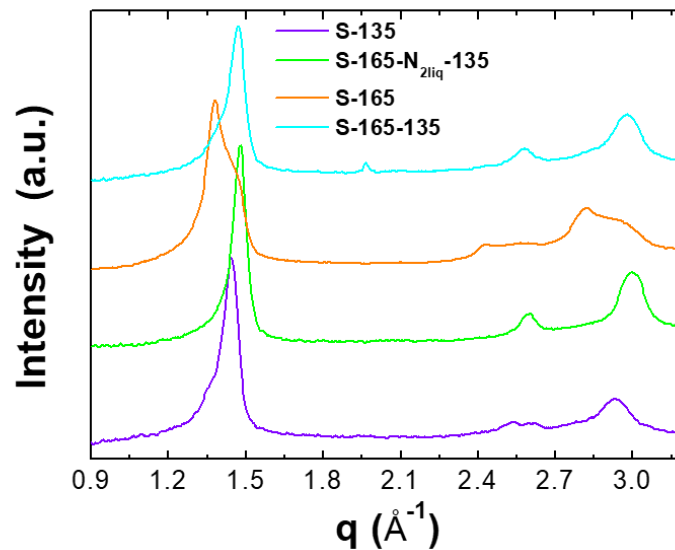


**Figure 4.8** 1D GIWAXS pattern obtained for S-135 (violet line), S-165-N<sub>2</sub>-135 (green line), S-165 (orange line) and S-165-135 (cyan line).

All the 4 samples show the typical reflections of the ferroelectric orthorhombic unit cell of P(VDF-co-TrFE)<sup>12-15</sup>. The first peak at around  $1.4 \text{ \AA}^{-1}$  arises from the overlap of the (200) and (110) reflections as said above. (For the assignment of the others scattering peaks at higher  $q$  positions see Chapter 2).

It can be noticed that the 1D-scattering pattern of S-165 presents some differences compared to the other three samples that can be discussed focusing on the comparison of their first main peaks (Figure 4.8). The main peak centred at  $\approx 1.4 \text{ \AA}^{-1}$  has the “classical”<sup>12-15</sup> shape characterised by a high intensity at high  $q$  positions (at  $1.44 \text{ \AA}^{-1}$  for S-135 (violet line), at  $1.47 \text{ \AA}^{-1}$  for 165-N<sub>2</sub>-135 and S-165-135 (green line and cyan lines respectively) with a shoulder at lower  $q$  positions. Contrarily S-165 shows a more pronounced peak at lower  $q$  position (at  $q=1.38 \text{ \AA}^{-1}$ ) that we have previously assigned to a defective phase peak **F<sub>2</sub>**. For S-165 a peak at higher  $q$  positions, assigned to the most ordered phase **F<sub>1</sub>**, is still apparent at around  $q=1.47 \text{ \AA}^{-1}$  but it is less pronounced with respect to the **F<sub>2</sub>**.

The crystallinity degree has been calculated through the deconvolution of the first peak at around  $1.4 \text{ \AA}^{-1}$  as already discussed in Chapter 2, where it has been said that this peak should be considered as the superposition of the (110),(200) reflections of different ferroelectric phases. In Figure 4.9 an example of the fitting obtained from the deconvolution study is shown for all the four samples. Pseudo-Voigt functions were used to describe the crystalline peaks, while an asymmetric function was used for the amorphous halo. Based on the  $q$  position at which their maxima occur, the fitted peaks were assigned to the ordered ferroelectric phase **F<sub>1</sub>**, at higher relative  $q$  positions (at  $1.44 \text{ \AA}^{-1}$  for the S-135, at  $1.47 \text{ \AA}^{-1}$  for the S-165-N<sub>2</sub>-135 and the S-165-135 and at  $1.45 \text{ \AA}^{-1}$  for the S-165), to the very defective ferroelectric phase **F<sub>2</sub>** at lower relative  $q$  positions (at  $1.34 \text{ \AA}^{-1}$  for the S-135, at  $1.32 \text{ \AA}^{-1}$  for the S-165, at  $1.36 \text{ \AA}^{-1}$  for the S-165-135) and to a mildly defective ferroelectric phase, the **F<sub>1-2</sub>**, located at an intermediate  $q$  position between the **F<sub>1</sub>** and **F<sub>2</sub>** peaks (at  $1.38 \text{ \AA}^{-1}$  for the S-135 and the S-165, at  $1.42 \text{ \AA}^{-1}$  for the S-165-N<sub>2</sub>-135, and at  $1.41 \text{ \AA}^{-1}$  for the S-165-135). To limit any possible error, the deconvolutions have been performed several times for every sample and some parameters as the width of the amorphous halo were kept fix. As described in Chapter 2, for the amorphous contribution the width of the asymmetric function was imposed by the shape the scattering halo recorded for a molten film, whose scattering is generated obviously only by the amorphous regions.<sup>16</sup>

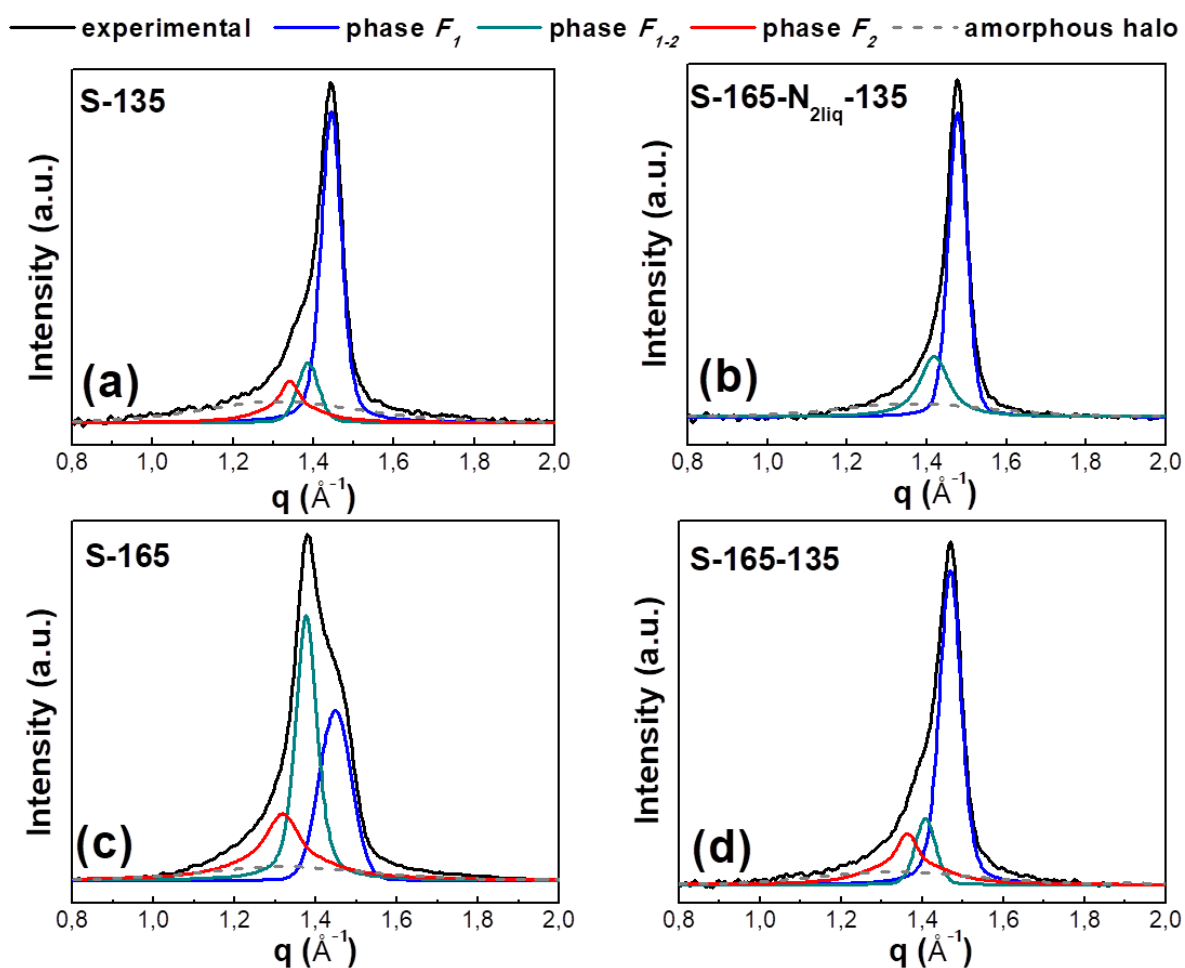


**Figure 4.9** Example of fitting obtained from a statistical deconvolution study of (a) S-135, (b) S-165-N<sub>2</sub>-135, (c) S-165 and (d) S-165-135. The crystalline fitted peaks are assigned to the  $F_1$  phase (blue line), the  $F_{1-2}$  phase (dark cyan line) and  $F_2$  phase (red line); the amorphous contribution is the fit described by the grey dotted line.

For sample S-165-N<sub>2</sub>-135 (Figure 4.9b) only two crystalline peaks were needed for a correct cumulative fit. According to the  $q$  positions of their maxima we attributed the two peaks to the phases  $F_1$  (blue line) at higher  $q$  and  $F_{1-2}$  (dark cyan line) at lower  $q$  position. For all the other three samples S-135, S-165 and S-165-135 three peak functions were required and assigned to the phases  $F_1$  (blue line),  $F_{1-2}$  (dark cyan line) and  $F_2$  (red line).

The calculated volume fractions  $F_1$ ,  $F_{1-2}$  and  $F_2$  % for the four samples are shown in Figure 4.10a.

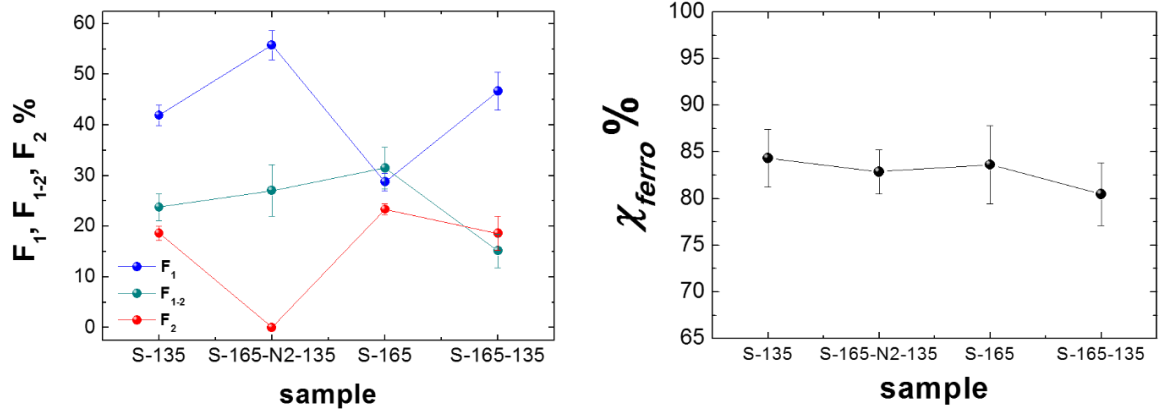


**Figure 4.10** (a) Volume fractions for the three ferroelectric phases  $F_1$  (blue line),  $F_{1-2}$  (dark cyan line) and  $F_2$  (red line) and (b) total ferroelectric crystallinity degree (black line) for the four samples.

Based on the deconvolution of the (110),(200) peak, the degree of the ferroelectric crystallinity  $\chi_{ferro}$ <sup>17</sup> has been calculated (similarly to the case of WAXS, thanks to the apparent amorphous halo contribution) from the Equation 2.1:

$$\chi_{ferro} = \frac{A_{F1} + A_{F2} + A_{F1-2}}{A_{tot}} \quad (2.1)$$

Where  $A_{F1}$ ,  $A_{F2}$  and  $A_{F1-2}$  are the integrated area underneath the GIWAXS deconvoluted crystalline peaks respectively assigned to the phases  $F_1$ ,  $F_2$  and  $F_{1-2}$  and  $A_{tot}$  is the total area of the (110),(200) peak given by the sum of all the three contributions, plus the integrated area of the amorphous halo. We herein remind, as we did in Chapter 2, that the calculated  $\chi_{ferro}$  is not the absolute crystallinity but slightly lower due to the missed scattered intensity for  $0^\circ < \chi < 5^\circ$  (at  $q \approx 1.5 \text{ \AA}^{-1}$ ) (see the 2D-reshaped images in Figure 4.4 where the dark curved triangle represents the Ewald-sphere correction).<sup>11</sup> The calculated degree of crystallinity is plotted in Figure 4.10b. Apparently, no big differences between the four samples have been detected since  $\chi_{ferro}$  varies between 80 and 84%. In Chapter 2 we had correlated the ferroelectric performance with crystallinity. Herein, the crystallinity being the almost constant, we expect that any differences observed in ferroelectric performance of the four samples will originate to the crystallites orientation.

### 4.3.2 Ferroelectric properties

In order to study how the attained crystallites orientations affect the ferroelectric properties, capacitors have been fabricated and thermally annealed by following the four different thermal protocols. Figure 4.11a shows the polarisation vs electric field ( $P$  vs  $E$ ) hysteresis loops recorded by applying an external oscillating electric field of amplitude  $150 \text{ MV m}^{-1}$  under a frequency of  $0.1 \text{ Hz}$  at room temperature for the four samples S-135 (violet line), S-165- $\text{N}_2$ -135 (green line), S-165 (orange line) and S-165-135 (cyan line). In Figure 4.11b the respective switching current peaks are shown as a function of the electric field. Depending on thermal processing conditions, the ferroelectric properties of P(VDF-co-TrFE) films change significantly.

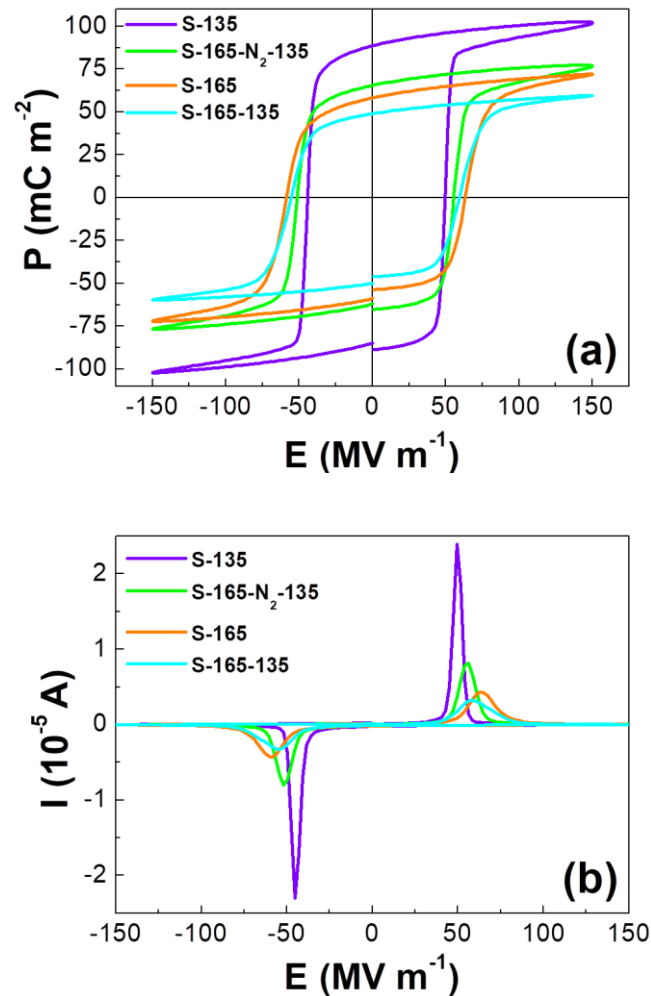


**Figure 4.11** (a) Polarisation hysteresis loops and (b) switching current peaks measured at RT for the S-135 (violet line), S-165- $\text{N}_2$ -135 (green line), S-165 (orange line) and S-165-135 (cyan line).

The S-135 exhibits the highest  $P_r$  of  $89 \text{ mC m}^{-2}$ , it follows the S-165-N<sub>2</sub>-135 with a  $P_r$  of  $65 \text{ mC m}^{-2}$ , then the S-165 with a  $P_r$  of  $58 \text{ mC m}^{-2}$  and finally the S-165-135 with a  $P_r$  of  $49 \text{ mC m}^{-2}$ . The lowest  $E_c$  of  $50 \text{ MV m}^{-1}$  is recorded for S-135, while S-165-N<sub>2</sub>-135 has an  $E_c$  of  $55 \text{ MV m}^{-1}$ , S-165 of  $63 \text{ MV m}^{-1}$  and S-165-135 of  $59 \text{ MV m}^{-1}$  (Figure 4.11a). Moreover, Figure 4.11b suggests that broader switching current peaks are apparent for the molten samples. As discussed in the previous Chapters, low  $P_r$ , high  $E_c$  and broad switching current peaks are indicative of a decreased ferroelectric performance. Comparing with Figure 4.7 and the edge-on/face-on volume fractions we see that this decreased performance follows the evolution (namely, the decrease) of the edge-on volume fraction. This result corroborates others authors' findings<sup>1,3,5,16</sup>: the edge-on orientation is necessary to achieve good ferroelectric performance, since it favours ferroelectricity, while a random or a face-on orientation has negative impact on the ferroelectric response. During polarisation measurements, the applied external electric field is expected to induce irreversibly a preferential orientation of the polar b-axis towards the electric fields direction. In the case of an edge-on orientation where the b-axis is already more or less aligned with the electric field, a high permanent polarisation ( $89 \text{ mC m}^{-2}$ ) is reached, whereas in the case where in-plane crystalline lamellae exist a lower  $P_r$  ( $49 \text{ mC m}^{-2}$ ) is detected.

The advantage of our study with respect to previous studies is that the GIWAXS analysis performed above allow us to quantitatively estimate the edge-on volume fraction. In the last section of this Chapter, based on this volume fraction we will endeavour to quantitatively correlate the ferroelectric to the structural properties.

### 4.3.3 Dielectric properties

The same kind of capacitor devices, annealed as above described, have been characterised by means of dielectric spectroscopy, that allows to obtain information about the dipoles relaxation. An AC voltage of  $0.1 \text{ V}$  is applied sweeping the frequency from  $0.1 \text{ Hz}$  to  $1 \text{ MHz}$  and the dielectric permittivity, real,  $\epsilon'$ , and imaginary,  $\epsilon''$ , as well as the  $\tan\delta$  (i.e. the  $\epsilon''/\epsilon'$ ) are recorded. In Figure 4.12 the  $\epsilon'$  (a) and the  $\epsilon''$  (b) as function of frequency have been

measured at RT for the four devices S-135 (violet data), S-165-N<sub>2</sub>-135 (green data), S-165 (orange data) and S-165-135 (cyan data).

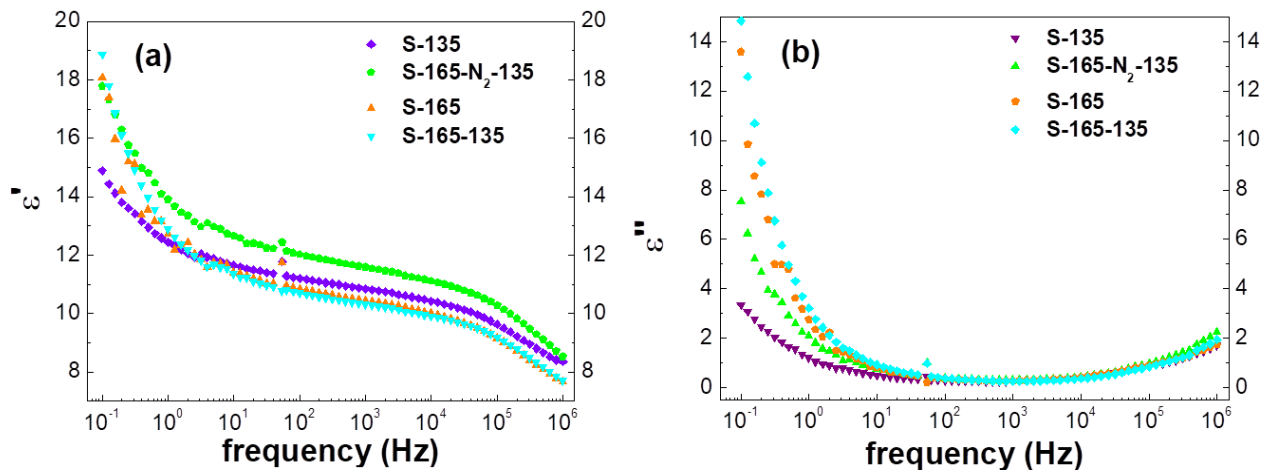


**Figure 4.12** (a)  $\epsilon'$  and (b)  $\epsilon''$  of S-135 (violet data), S-165-N<sub>2</sub>-135 (green data), S-165 (orange data), S-165-135 (cyan data) measured as functions of frequency at RT.

In Figure 4.12a it can be noticed that the  $\epsilon'$  of three samples are nearly overlapped at least at intermediate frequencies range, all samples exhibit a  $\epsilon' = 11$ , apart from sample S-165-N<sub>2</sub>-135 whose  $\epsilon'$  is slightly higher:  $\epsilon' = 12$ . These values are in accordance with literature.<sup>18</sup> An increased  $\epsilon'$  has been attributed to a higher amount of “ $\beta$ ” phase, our  $F_1$ , which is in accordance with our results (see Figure 4.10).

As it arises from Figure 4.12, at RT not many information about the relaxations of the four samples can be derived, since the energy given by the small electric field is not enough to induce dipoles relaxation.<sup>19</sup> At low frequencies an increase of both real,  $\epsilon'$ , and imaginary,  $\epsilon''$ , part is detected. This high increase of the dielectric parameters is known to be caused by the ionic DC conductions due to polarisation of interfacial or spatial charges.<sup>19,20</sup>

At high frequencies the variation of dielectric properties, i.e. decrease of  $\epsilon'$  and increase of  $\epsilon''$ , is due to the so called  $\beta$  or  $\alpha_a$  relaxation (glass transition relaxation<sup>19</sup>), ascribed to the micro-Brownian motion of non-crystalline chain segments<sup>20</sup> associated to cooperative orientation movement of the amorphous-crystalline interface. Indeed, it is herein reminded that the glass transition of P(VDF-co-TrFE) is -50 °C, then the molecular chain at RT have already enough mobility to relax under the application of the electric field. At frequencies higher than 1 MHz it would be possible to detect this dipoles relaxation peak even at RT.

The same experiment (dielectric properties measured as function of the frequency) have been carried out at increasing temperatures, going from RT to 140 °C before the melting. In particular, starting from RT the devices were annealed at the chosen temperature, for example 40 °C, then, before starting the dielectric spectroscopy measurements, 3 minutes were accorded to give the time to the sample to reach the thermal equilibrium, and after the dielectric measurement is carried out, we heat to the next temperature and we repeat the protocol of waiting-measuring-heating. After 40 °C we then heat to 60 °C, then to 80 °C, to 100 °C, then to 120 °C, 130 °C and finally to 140 °C.

We opted to present herein the  $\tan\delta$  vs  $f$  plots instead of the  $\epsilon''$  just for sake of clarity. Indeed, it is easier to follow the relaxation peak described by the  $\tan\delta$  for our range of frequencies investigated. The  $\tan\delta$  vs  $f$  measured at different temperatures is shown for the device S-135 in Figure 4.13a, for the S-165-N<sub>2</sub>-135 in Figure 4.13b, for the S-165 in Figure 4.13c and for the device S-165-135 in Figure 4.13d. At 80 °C a peak starts to appear for all the four samples. This relaxation occurring at temperature close to the Curie transition is associated to the  $\alpha$  or  $\alpha_c$  relaxation ascribed to the crystalline motion of the FE-to-PE transition<sup>18</sup>. The same authors<sup>18,20</sup> have found that this peak it as to be ascribed to both amorphous and crystalline relaxations since the  $\beta$  and  $\alpha$  relaxation are inseparable in a frequency domain because both relaxation times  $\tau$  are identical or very close.

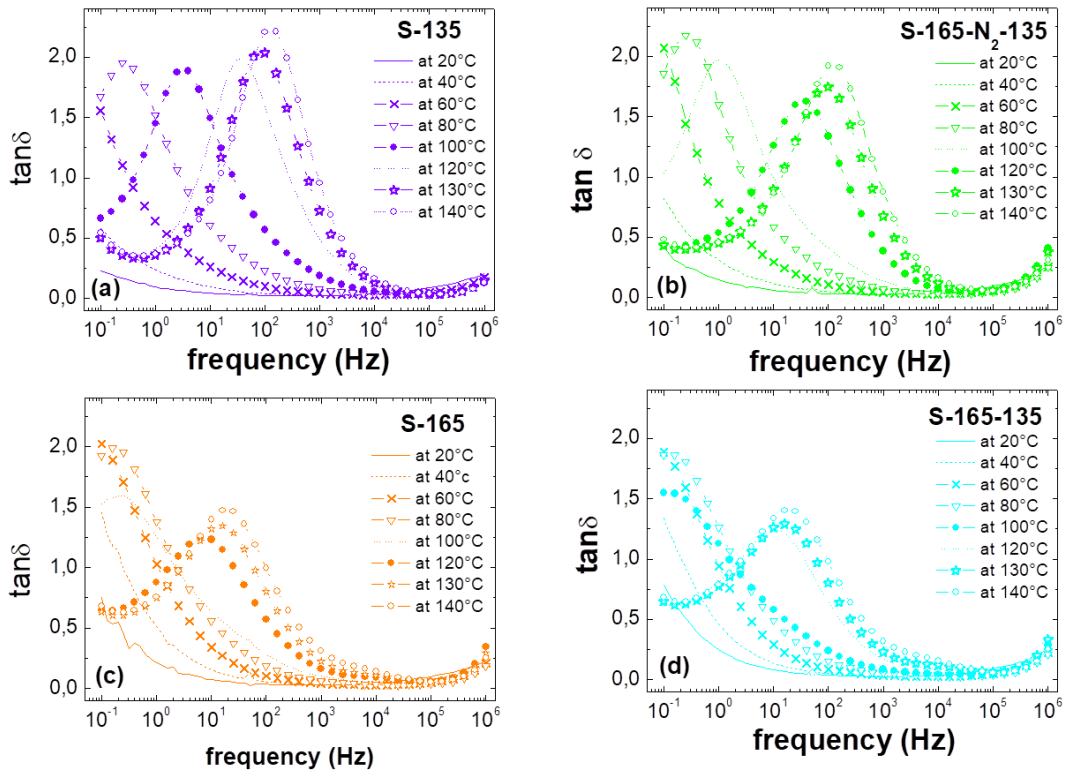


**Figure 4.13**  $\tan \delta$  vs  $f$  measured at different temperatures for the (a) S-135, (b) S-165-N<sub>2</sub>-135, (c) S-165 and (d) for the S-165-135 devices.

The maximum frequency,  $f_m$ , of the  $\tan \delta$  peak shifts towards higher temperatures when the temperature increases. In order to evaluate the activation energy,  $E_a$ , of this relaxation we first calculated the relative relaxation times,  $\tau$ , at which the maxima occur, according to the Equation 4.1:

$$\tau = \frac{1}{2\pi f_m} \quad (4.1)$$

Then we plotted the  $\ln(\tau)$  against the reciprocal of absolute temperatures multiplied for a 1000 factor ( $1/T \cdot 1000$ ) in Figure 4.14. The axis on the top is just nearly indicative of the temperature in Celsius. It seems that different relaxation contributions are apparent for this  $\tan \delta$  peak. But actually it has to be specified that, the plateau that we see for all the samples apart from S-135 at low temperatures (first point at 80 °C) is probably an artefact due to the fact that with our frequency range the evaluation of the first  $f_m$  at 80 °C is not exact for all the

samples, therefore this point should be discarded. The shoulder at higher temperatures, between 130 °C and 140 °C, which exists for all the four samples, has been documented in literature and it is assigned to a critical slowing-down phenomenon of crystalline dipole motion associated to the segmental motions of the amorphous regions.<sup>18</sup>

In order to evaluate the activation energy  $E_a$  of this *FE-to-PE* relaxation process, a linear fit has been done for the S-135 between 80 °C and 130 °C, while for the others between 100 °C and 130 °C. These ranges of temperatures where the linear fitting is performed, are highlighted with shadows in Figure 4.14a. We calculate the  $E_a$  according to Equation 4.2:

$$\ln \tau_m = \ln \tau_0 + \frac{E_a}{RT} \quad (4.2)$$

Where  $\tau_0$  is the intercept to the y-axis and  $E_a/R$  is the slope of the linear fit, where  $R$  is the gas constant ( $R=1.987 \cdot 10^{-3} \text{ kcal mol}^{-1} \text{ K}^{-1}$ ). The relaxation activation energy, of orders of tens of  $\text{kcal mol}^{-1}$  (in accordance with previous results<sup>20</sup>), is lower for S-135 and increase for the others as shown in Figure 4.14b.

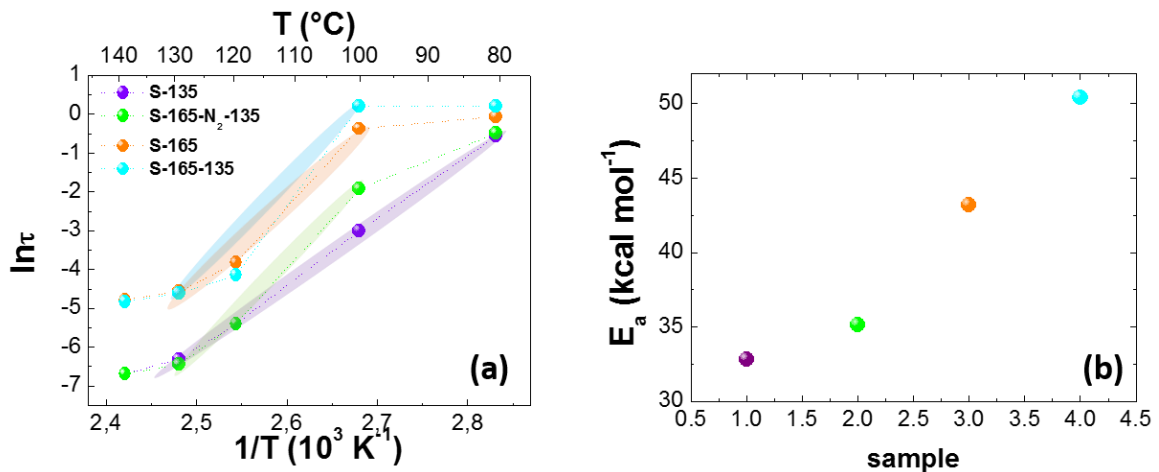


**Figure 4.14** (a)  $\ln \tau$  vs  $1000/T$  where the shaded curves correspond to the range at which the linear fitting has been carried out. (b)  $E_a$  plotted for the different samples.

It can also be noticed that the relaxation frequency increases going from S-135 to S-165-135. In Figure 4.15a the maximum frequency  $f_m$  for the different experiment temperature are shown. Two groups can be distinguished in terms of high  $f_m$  (S-135 and S-165-N<sub>2</sub>-135) and lower  $f_m$  (S-165 and S-165-135). Moreover, a decrease of the intensity of  $\tan \delta$  follows the

same trend: from a highest value for the sample S-135 to the lowest value for S-165-135 (Figure 4.15b).

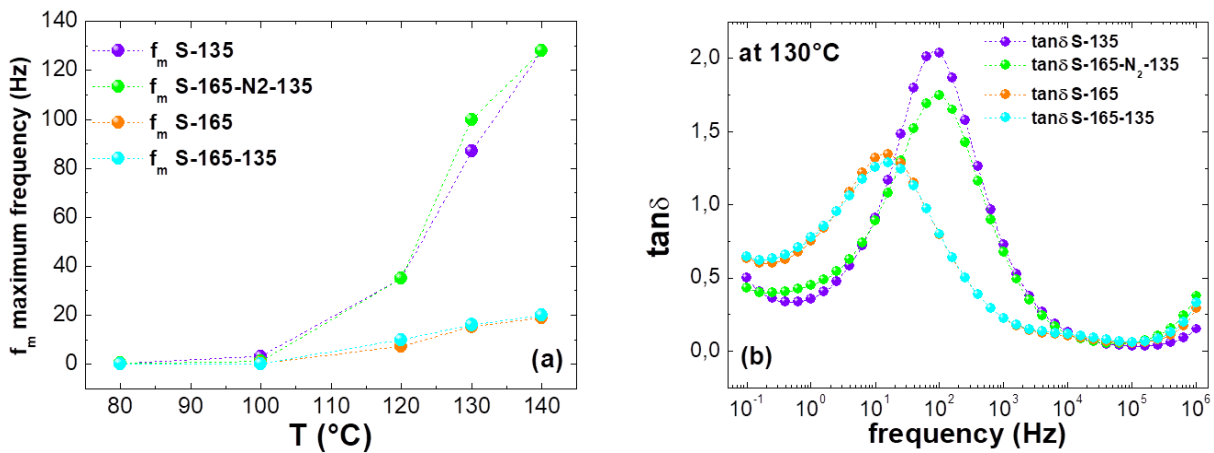


**Figure 4.15** (a)  $f_m$  vs experiment temperature and (b)  $\tan \delta$  vs  $f$  at a fixed experiment temperature for all the different samples.

Lower frequency and higher  $E_a$  of the relaxation between the two steady states of the dipoles could be ascribed to an increase of disorder, of defects. We can conclude that the different orientations probably behave as defects in our system. If we consider a schematic double well potential energy diagram, the two equilibrium states of a permanent dipole that is fluctuating (because thermally activated), will be energetically equal in the case of an ordered state (blue double well potential of Figure 4.16). In the case of a disordered or defective system, one of the two polarisation state would be favoured (red double well potential of Figure 4.16) therefore  $E_a$  will increase.

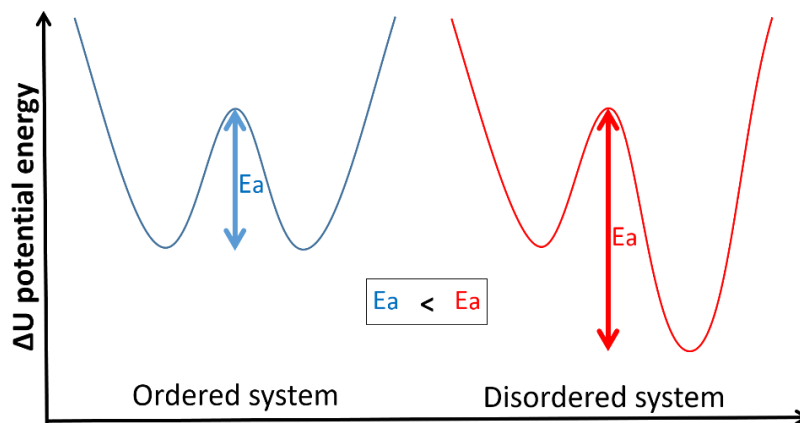


**Figure 4.16** Schematic of double well potential diagram for an ordered or a disordered system.

The difference in energy of the two polarisation states causes an increase of the relaxation energy  $E_a$ . As shown in Figure 4.16 in a case of an ordered system the  $E_a$  of the relaxation would be lower than in the case of a defective system.

#### 4.3.4 Structure – Function relationships in ferroelectric polymers

In order to go one step further towards the understanding of the laws that relate structural with functional properties, we have searched for any existing dependence between the resulted ferroelectric parameters and the structural characteristics (as the crystallinity degree, the amount of defective phases, the edge-on amount,  $L_{\text{coherence}}$  size, etc...).

So far we have discussed about the edge-on volume fraction that has been calculated by integrating the  $I(\chi)$  vs  $\chi$  between  $0^\circ$  and  $45^\circ$ , but now in order to evaluate the exact amount of crystallites edge-on and face-on oriented in the four samples, we have multiplied the calculated total crystallinity by the edge-on and face-on fractions.<sup>21</sup> As expected, we have found a dependence of the ferroelectric parameters as a function of the edge-on amount, as shown in Figure 4.13. In Figure 4.13a we can clearly see that both the  $P_r$  and the slope of the hysteresis loop (i.e. index of the speed of the switching from a positive polarisation state to a negative one) increase when the edge-on amount increases, meaning that the preferential edge on orientation leads not just to a higher amount of charges per surface, (i.e. high  $P_r$ ) but helps for the switching transition from a polarisation direction to the opposite one. In Figure 4.13 b other two ferroelectric parameters, the  $E_c$  and the FWHM of the switching current peaks are plotted as function of to the edge-on amount: the  $E_c$  decreases and the FWHM increases (index of a less abrupt switching) when the edge-on amount increases. Considering the  $E_c$  trend we can conclude that, when the face-on is the preferred orientation, a higher electric field is required to induce the polarisation switching. With the increase of the edge-on amount, the FWHM which is related to the hysteresis slope increases as well as found for the hysteresis slope.

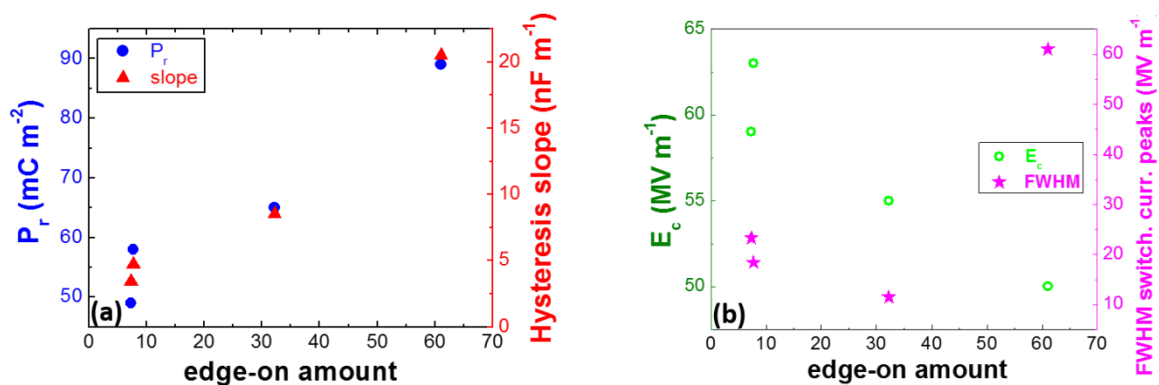


**Figure 4.17** (a)  $P_r$  and hysteresis loop slope and (b)  $E_c$  and FWHM of the switching current peaks as function of the edge-on crystalline amount.

Moreover, as described in Figure 4.18 we found that the  $E_a$  of the dielectric relaxation is smaller when the amount of edge on crystallites is high; and that the slope of the hysteresis loop is itself affected by this  $E_a$ : the lower the  $E_a$  the easier the polarisation switching indeed the higher (i.e. steeper) the slope.

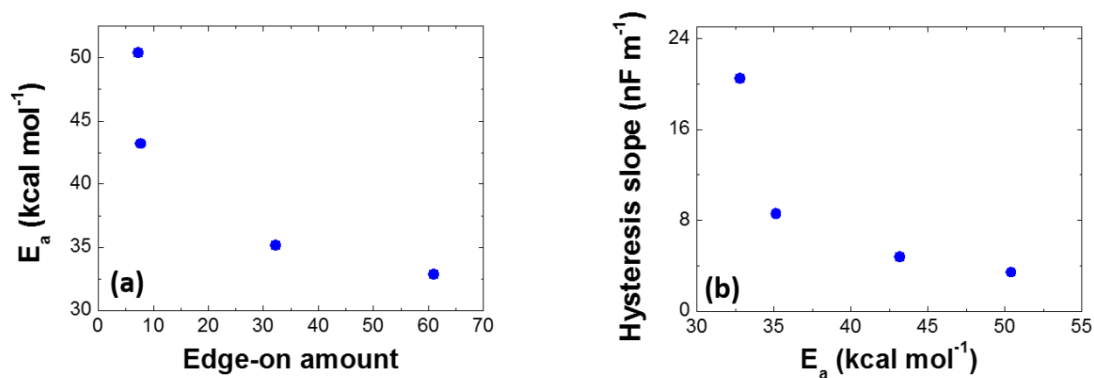


**Figure 4.18** (a)  $E_a$  as function of the edge-on crystalline amount and (b) hysteresis loop slope as function of  $E_a$ .

Another interesting dependence between structural and functional parameters was found and concerns the dependence of the  $E_c$  to the coherence length size of the crystallites,  $L_{\text{coherence}}$ . In particular, we herein present the dependence of the  $E_c$  as function of the  $L_{\text{coherence}}$  of the  $F_1$  (Figure 4.19), thanks to the fact that, from our deconvolution study we have information about each single phase. The data plotted in Figure 4.19 have been fitted with an

exponential law that furnishes the dependence of the  $E_c$  from the coherence length size of the crystallites.

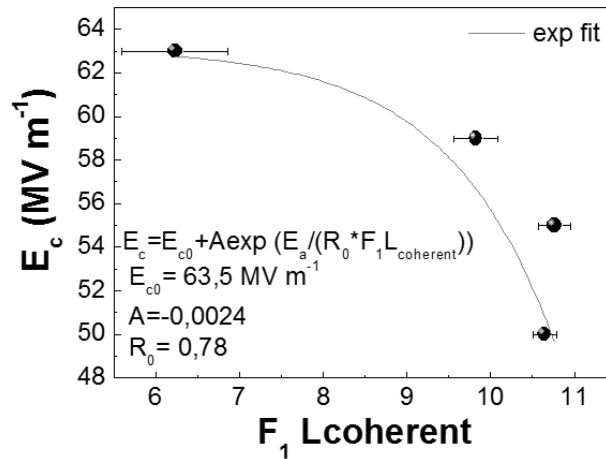


**Figure 4.19**  $E_c$  dependence to the coherence length size of the ordered ferroelectric phase  $F_1$ .

We can conclude that the face-on crystal orientation should be avoided for realising devices of P(VDF-co-TrFE) such as non-volatile memory where a high  $P_r$  and a low  $E_c$  are desired. Edge-on amount orientation seems to favour the dipoles relaxations, which indeed affects the speed of the switching between the two polarisation states described by the ferroelectric hysteresis loop slope. Moreover, a lowered coercive field is found in the case of smaller  $F_1$  crystallites mean size.

## 4.4 Conclusions

Different orientations have been induced by drastically varying the thermal annealing processing. We found that trough melt-crystallisation, randomly oriented crystallites, or preferentially face-on oriented are formed. In particular, we found that S-135 has mainly edge-on lamellae, S-165-N2-135 exhibits edge-on tilted towards the substrate, nearly isotropic orientation while a preferred stand-up chain orientation occurs for S-165 and S-165-135.

The S-135 which exhibits the highest amount of edge-on crystallites (~75%) among all exhibited the better ferroelectric response in terms of high  $P_r$  and low  $E_c$ . The ferroelectric parameters indeed were found to strongly depend on the orientation of the crystallites: not just a higher  $P_r$  and lower  $E_c$  are found for a high edge-on amount distribution but also the polarisation switching was shown to be faster. An interestingly dependence of the coercive field with the mean size of  $F_1$  crystallites was found, dictating that when the crystallites  $L_{coherence}$  increases, the  $E_c$  decays exponentially.

From dielectric spectroscopy investigations at different temperatures we have found that going from S-135 to S-165-N<sub>2</sub>-135 to S-165 and then S-165 an increased activation energy simultaneously with a decreased  $f_m$  of the FE-to-PE relaxation occurs, indicating that the face-on orientation can be seen as a defective parameter, that hinder dipoles relaxations and therefore a faster switching between the two polarisation states.

## References

- 1 Spampinato, N. et al. Enhancing the ferroelectric performance of P(VDF-co-TrFE) through modulation of crystallinity and polymorphism. *Polymer* **149**, 66-72, doi:<https://doi.org/10.1016/j.polymer.2018.06.072> (2018).
- 2 Park, Y. J. et al. Irreversible extinction of ferroelectric polarization in P(VDF-TrFE) thin films upon melting and recrystallization. *Appl. Phys. Lett.* **88**, 242908, doi:[10.1063/1.2207831](https://doi.org/10.1063/1.2207831) (2006).
- 3 Xia, F. et al. High electromechanical responses in a poly(vinylidene fluoride-trifluoroethylene-chlorofluoroethylene) terpolymer. *Advanced Materials* **14**, 1574-1577, doi:[10.1002/1521-4095\(20021104\)14:21<1574::aid-adma1574>3.0.co;2-#](https://doi.org/10.1002/1521-4095(20021104)14:21<1574::aid-adma1574>3.0.co;2-#) (2002).
- 4 Guo, D. & Setter, N. Impact of confinement-induced cooperative molecular orientation change on the ferroelectric size effect in ultrathin P(VDF-TrFE) films. *Macromolecules* **46**, 1883-1889, doi:[10.1021/ma302377q](https://doi.org/10.1021/ma302377q) (2013).
- 5 Guo, D., Stolichnov, I. & Setter, N. Thermally Induced Cooperative Molecular Reorientation and Nanoscale Polarization Switching Behaviors of Ultrathin Poly(vinylidene fluoride-trifluoroethylene) Films. *J. Phys. Chem. B* **115**, 13455-13466, doi:[10.1021/jp2061442](https://doi.org/10.1021/jp2061442) (2011).
- 6 Park, Y. J. et al. Molecular and Crystalline Microstructure of Ferroelectric Poly(vinylidene fluoride-co-trifluoroethylene) Ultrathin Films on Bare and Self-Assembled Monolayer-Modified Au Substrates. *Macromolecules* **41**, 109-119, doi:[10.1021/ma0718705](https://doi.org/10.1021/ma0718705) (2008).
- 7 Jung, H. J. et al. Shear-induced ordering of ferroelectric crystals in spin-coated thin poly(vinylidene fluoride-co-trifluoroethylene) films. *Macromolecules* **42**, 4148-4154, doi:[10.1021/ma900422n](https://doi.org/10.1021/ma900422n) (2009).
- 8 Müller-Buschbaum, P. The Active Layer Morphology of Organic Solar Cells Probed with Grazing Incidence Scattering Techniques. *Adv. Mater.* **26**, 7692-7709, doi:[10.1002/adma.201304187](https://doi.org/10.1002/adma.201304187) (2014).
- 9 Rivnay, J., Mannsfeld, S. C. B., Miller, C. E., Salleo, A. & Toney, M. F. Quantitative Determination of Organic Semiconductor Microstructure from the Molecular to Device Scale. *Chemical Reviews* **112**, 5488-5519, doi:[10.1021/cr3001109](https://doi.org/10.1021/cr3001109) (2012).

- 10 Baker, J. L. et al. Quantification of Thin Film Crystallographic Orientation Using X-ray Diffraction with an Area Detector. *Langmuir* **26**, 9146-9151, doi:10.1021/la904840q (2010).
- 11 Website, G. C. Example:P3HT orientation analysis, <[http://gisaxs.com/index.php/Example:P3HT\\_orientation\\_analysis](http://gisaxs.com/index.php/Example:P3HT_orientation_analysis)> (2015).
- 12 Kim, K. J. & Kim, G. B. Curie transition, ferroelectric crystal structure and ferroelectricity of a VDF/TrFE (75/25) copolymer: 2. The effect of poling on curie transition and ferroelectric crystal structure. *Polymer* **38**, 4881-4889 (1997).
- 13 Bellet-Amalric, E. & Legrand, J. F. Crystalline structures and phase transition of the ferroelectric P(VDF-TrFE) copolymers, a neutron diffraction study. *Eur Phys J B* **3**, 225-236 (1998).
- 14 Koga, K., Nakano, N., Hattori, T. & Ohigashi, H. Crystallization, field-induced phase transformation, thermally induced phase transition, and piezoelectric activity in P(vinylidene fluoride-TrFE) copolymers with high molar content of vinylidene fluoride. *Journal of Applied Physics* **67**, 965-974, doi:10.1063/1.345706 (1990).
- 15 Hasegawa, R., Takahashi, Y., Chatani, Y. & Tadokoro, H. Crystal Structures of Three Crystalline Forms of Poly(vinylidene fluoride). *Polym J* **3**, 600-610, doi:10.1295/polymj.3.600 (1972).
- 16 Guo, Q. *Polymer Morphology: Principles, Characterization, and Processing*. (Wiley, 2016).
- 17 Gregorio, R. & Botta, M. M. Effect of crystallization temperature on the phase transitions of P(VDF/TrFE) copolymers. *J. Polym. Sci. B Polym. Phys.* **36**, 403-414, doi:10.1002/(sici)1099-0488(199802)36:3<403::aid-polb2>3.0.co;2-s (1998).
- 18 Furukawa, T., Ohuchi, M., Chiba, A. & Date, M. Dielectric relaxations and molecular motions in homopolymers and copolymers of vinylidene fluoride and trifluoroethylene. *Macromolecules* **17**, 1384-1390, doi:10.1021/ma00137a015 (1984).
- 19 Gregorio, R. & Ueno, E. M. Effect of crystalline phase, orientation and temperature on the dielectric properties of poly (vinylidene fluoride) (PVDF). *Journal of Materials Science* **34**, 4489-4500, doi:10.1023/a:1004689205706 (1999).
- 20 Furukawa, T. & Johnson, G. E. Dielectric relaxations in a copolymer of vinylidene fluoride and trifluoroethylene. *Journal of Applied Physics* **52**, 940-943, doi:10.1063/1.328781 (1981).

- 21 *Petsagkourakis, I. et al. Structurally-driven Enhancement of Thermoelectric Properties within Poly(3,4-ethylenedioxythiophene) thin Films. Scientific Reports 6, 30501, doi:10.1038/srep30501 <https://www.nature.com/articles/srep30501#supplementary-information> (2016).*

# Chapter 5

*P(VDF-co-TrFE) a sensor for  
ventricular laparoscopic surgery  
simulation*



## 5 P(VDF-co-TrFE) a sensor for ventricular laparoscopic surgery simulation

### 5.1 P(VDF-co-TrFE) for biomedical sensing

In this Chapter we explore the implementation of the ferroelectric polymer P(VDF-co-TrFE) for a specific organic electronic application in the field of medical pressure-sensors<sup>1</sup>. In this case we are interested in exploiting the piezoelectric properties of P(VDF-co-TrFE).

We all know that a ferroelectric material is also a piezoelectric material. When a piezoelectric material is stressed by an external mechanical force, a strain of the material is induced and with it the generation of an electrical potential that is proportional to the applied stress.<sup>2</sup> This is called “direct piezoelectric effect”. Inversely, when an electric oscillating field is applied to the piezoelectric material, a mechanical deformation is generated and it is translated into a vibrational mode. This is called “reverse piezoelectric effect”.

Piezoelectric catheters have found their medical application in measuring the cardiac functions and in detecting eventual cardiac diseases for example arrhythmia. As reported by Langberg *et al.*<sup>3</sup> “*Arrhythmia surgery and catheter ablative techniques have become important alternatives to the pharmacologic treatment of patient with ventricular tachycardia but these methods require the localisation of the arrhythmia focus within the ventricle*”. It arises the importance of having an exact mapping of the localised cardiac functions. In this general context is placed the aim of the work that will be presented in this Chapter.

Herein the results obtained in the LCPO within the chair of a project called “Sweet Heart” in collaboration with the IHU (Institut Hospitalo-Universitaire) LiryC research institute (based in Pessac) will be presented. The institute acronym “LiryC” stands for “*l’insitut de rythmologie et modélisation cardiaque*” that emphasises the specialisation of this institute in cardiac diseases. The aim of the project is indeed the development of flexible piezoresponsive P(VDF-co-TrFE) matrix sensor for laparoscopic simulation. The goal is to obtain a piezoelectric matrix that allows mapping different regions of a 3D plastic heart (Figure 5.1a) which, having similar

mechanical characteristic of a human heart, is used in training sessions by students to simulate surgery investigation by means of a catheter technique. In medical surgery, ventricular arrhythmia can be revealed if an abnormal (very low current) output electrical signal is recorded as consequence to the pressure applied by a catheter.

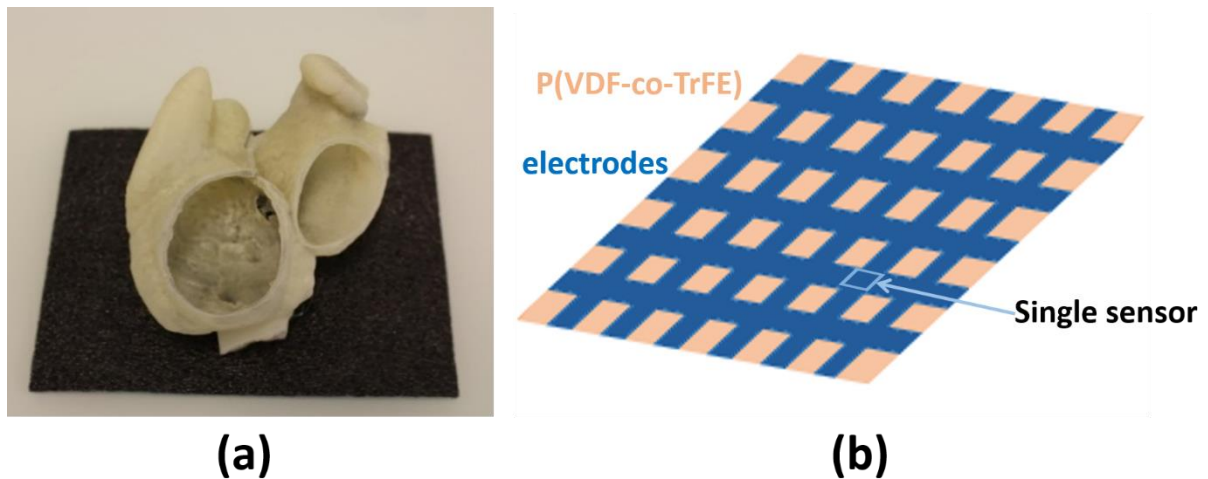


**Figure 5.1** on the left side the 3D-printed plastic heart at the inside of which the sensor should be deposited. On the right schematic of the grid of bottom (horizontal blue lines) and top (vertical blue lines) electrodes at the surfaces of a piezoelectric layer made of P(VDF-co-TrFE) pink backgrounds.

In this chapter, will be described some remarkable results that have been obtained from the cooperative work of a big team where I and my colleagues Alizée Glasser, Konstantinos Kallitsis, Cindy Gomes Correia and Lauriane Giraud worked together for the development of the piezoelectric device. This project is actually still on-going. Therefore, we reveal in advance that the finalised device will not be herein presented, but the progressive steps that have brought to outstanding amelioration of the sensor device will be discussed.

The piezoelectric material used is the P(VDF-co-TrFE) provided by Piezotech, while as semiconducting material the PEDOT:PSTFSI, poly(3,4-ethylene dioxythiophene):poly(4-styrene trifluoromethyl (bissulfonylimide)), ink formulated and synthesised in our laboratory by Alizée Glasser, and silver and gold have been used as electrodes.

Since, as mentioned above, our objective is to map the ventricle, we do need to fabricate a device network as the one shown in Figure 5.1b. The blue horizontal lines and the vertical lines correspond respectively to the bottom and the top electrodes and, each intersection between horizontal and vertical blue lines represents a single device.

The network of sensors has to perfectly adhere to the model of the 3D-printed heart. Therefore, our first attempt was to directly spray onto the 3D printed heart both PEDOT and P(VDF-*co*-TrFE) polymers, but in both cases a deterioration of the heart substrate was induced due to the high temperatures required by spray coating technique (around 100 °C). We therefore opted to change approach and to start with the fabrication of independent devices, to try then to adapt and encapsulate them onto the model heart. The main advancements achieved in the device fabrication and characterisation will be discussed chronologically. In particular, the different developed systems will be described, firstly in terms of the materials and fabrication process and secondly in terms of the obtained device characterisation.

### 5.1.1 First system: organic device on Polyethylene terephthalate (PET)

Polyethylene terephthalate was used as substrate on top of which by means of spray-coating deposition technique squared patterned PEDOT, bottom electrodes have been deposited through a shadow mask. A layer of P(VDF-*co*-TrFE) was then spray-coated, by shielding with a mask the bottom electrodes terminals that need to be available for contacting. The top PEDOT patterned electrodes were spray-coated, as said before for the bottom electrodes, but the shadow mask has been rotated of 90 ° in order to avoid overlap between the electrodes arms. The schematic of the fabricated device is shown below in Figure 5.2.

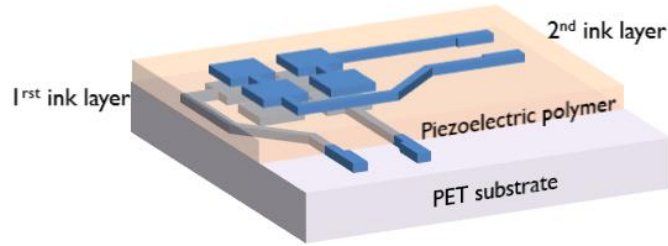


**Figure 5.2** A schematic of the device where the blue patterns called 1<sup>st</sup> ink layer and 2<sup>nd</sup> ink layer represent the bottom and the top electrodes respectively. The embedded active layer is the piezoelectric P(VDF-co-TrFE) and the substrate is PET.

The spray coating technique was chosen in order to fabricate the piezoelectric sensor directly onto the inner surface of the 3D-heart. Unfortunately, this technique turned out to be unsuitable for fabricating sensor devices for our purpose, since it leads to a not homogenous deposition: thicker PEDOT regions appear as darker drops clearly visible by eye on a clear blue PEDOT surface. Moreover, a non-perfect adhesion between the PET substrate and the shadow mask caused a non-perfect patterning of the PEDOT, which has the tendency to spread below the shadow mask.

Indeed, herein, we do not show any electrical characterization of these devices, because it was not possible to record any hysteresis loop due to the high leakage current and to the occurring short circuit when increasing voltages were applied.

Nevertheless, we were able to perform PFM Piezo Force Microscopy on this system as shown in Figure 5.3. PFM is an atomic force microscopy, AFM, contact mode imaging technique that allows recording the electromechanical response of piezoelectric materials when an AC voltage is applied between the conductive probing tip (which represents the top electrode) and the sample that is grounded through its bottom electrode. Expansions and contractions are detected as amplitude of the mechanical displacement vertically to the sample plane. In Figure 5.3a a schematic of the experiment conduct with PFM is shown and the recorded PFM vertical amplitude is displayed for an area of 25  $\mu\text{m}^2$  in Figure 5.3b.

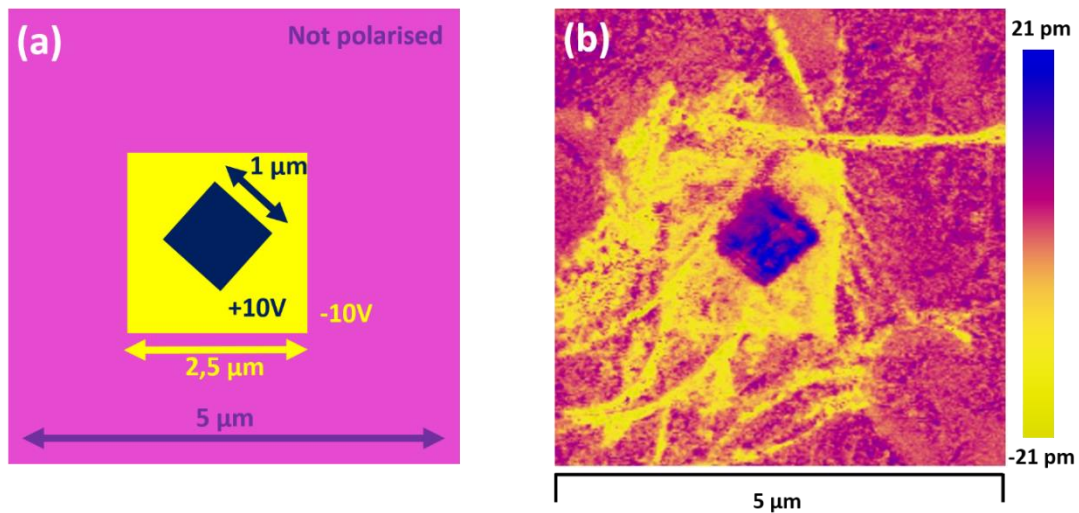


**Figure 5.3** (a) Schematic of the PFM image on the right. Pink colour indicates absence of induced polarisation, yellow colour represents a square that have been polarised with a positive voltage and the blue colour a smaller rhombus polarised with a positive voltage. (b) VPFM image of an area of  $25 \mu\text{m}^2$ . The yellow square has shown a negative vertical displacement and the blue rhomb a displacement into the opposite direction. The two different colour demonstrate that the larger square exhibits negative displacement (shrinking) while the inner rhomb a positive vertical displacement (elongation).

In Figure 5.3a the yellow square with a dimension of  $2.5 \mu\text{m} \times 2.5 \mu\text{m}$  and the circumscribed blue  $1 \mu\text{m} \times 1 \mu\text{m}$  rhombus correspond to two region polarised with two opposite voltages, which causes different directions of the displacement recorded along the z-axis, as shown in Figure 5.3b. The yellow region in Figure 5.3b corresponds to a decrease of the VPFM amplitude, while the blue colour to an increase of the VPFM amplitude. One is obtained by applying a negative voltage, the other by applying a positive voltage.

In Figure 5.3b yellow lines are visible out from the yellow square. We attribute this effect to the fact that when we perform a scan, applying a certain voltage into a certain area, the polarisation is induced on the entire hit crystallite. Due to the large thickness of the P(VDF-co-TrFE) film herein studied, the morphology at the surface exhibits crystalline fibres that, in this case, exceed in broadness the squared area. Therefore, by polarising a fibre that exists within the scanned square, we are polarising also the part of the fibre that continues outside the scanned square.

When PFM measurements are performed, the film under study needs to be deposited on top of a bottom electrode since the bottom electrode of the system needs to be grounded in order to apply a voltage onto the film surface through the AFM tip. As just described in Figure 5.3, we were able to polarise the piezoelectric film deposited onto of PEDOT bottom electrodes. In this way we have proven that our PEDOT:PSTFSI is suitable to be used as electrode for this system. Moreover, from this first result, we then conclude that the spray-coating deposition technique needs to be discarded if we want to obtain homogenous layers.

### 5.1.2 Second system: organic flexible device on PDMS

After having proven that our PEDOT can be used as electrode on flexible substrate (as the PET) we now move to a more flexible substrate, the poly-dimethylsiloxane, PDMS. We now deposit the patterned PEDOT electrodes by means of doctor-blading technique below a shadow mask. The P(VDF-co-TrFE) is deposited by means of doctor-blade technique too. With this deposition technique, we are able to control the processing parameters, and then better smoothness is achieved. In Figure 5.4a a picture and, Figure 5.4b, a schematic of the fabricated device is displayed.

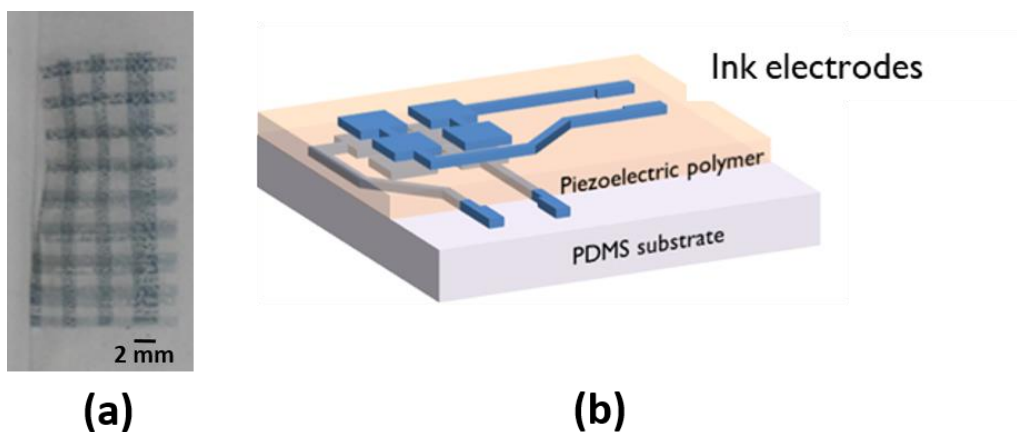


**Figure 5.4** (a) Picture and (b) a schematic of the PEDOT/P(VDF-co-TrFE)/PEDOT/PDMS device. In (a) the first two lines on the left delimit devices with an area of  $1 \text{ mm}^2$  while the third line on the right delimits devices with an active area of  $2 \text{ mm}^2$ .

The first drawback encountered for this fabrication is associated to the patterning of the bottom electrodes: as found for the previous case, due to a non-perfect adhesion between the PDMS substrate and shadow mask, the PEDOT passes below the mask rendering impossible a good control of the patterning. Another issue encountered for this system is related to the poor affinity between PDMS and PEDOT that causes de-wetting as sequence of this incompatibility.

In order to solve the issue, we decided to avoid the use of doctor blading for the deposition of the patterned PEDOT electrodes on PDMS. We opted to use inkjet-printing technique. Inkjet printing is a non-contact technique where a nozzle does the deposition of droplets; it allows obtaining a pattern without requiring the use of any shadow mask. Improving its compatibility with PEDOT through an UV-O<sub>3</sub> treatment of 20 minutes has optimised the printing conditions. The PEDOT deposition by means of inkjet printing was performed keeping the substrate at 50 °C, this strategy allows a better wettability of the PDMS substrate and enhance homogeneity of the PEDOT layer. Then a drying step has been performed for 5 min at 100 °C. The P(VDF-co-TrFE) was deposited by doctor blade obtaining thick films of ~ 15µm that have been isothermally annealed at 135 °C during 30 min.

Polarisation vs electric field curves have been recorded at 100 Hz and are shown for different increasing applied voltages in Figure 5.5. Due to their shape the curves below cannot be considered ferroelectric hysteresis loops.

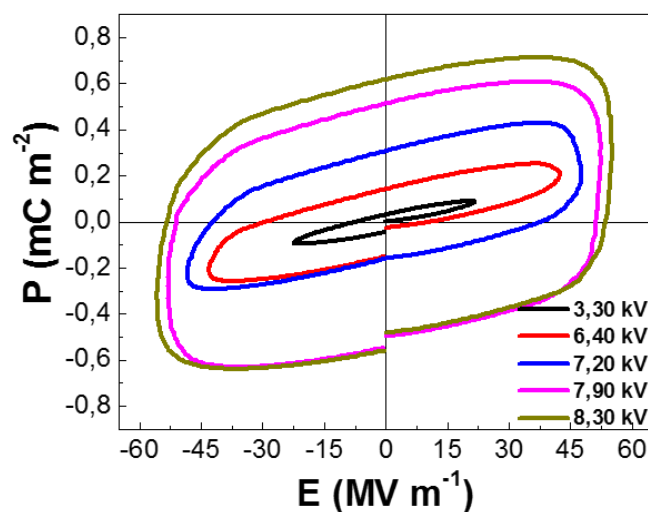


**Figure 5.5** Polarisation vs electric field curves recorded increasing voltages for the PEDOT/P(VDF-co-TrFE)/PEDOT/PDMS device.

In order to improve the system, we prolonged the UV-O<sub>3</sub> treatment and we performed a pre-heating steps before PEDOT and P(VDF-co-TrFE) deposition. Even though better homogeneity and smoothness of PEDOT layers have been achieved and slightly less leaky polarisation loops have been recorded, this response was detected just for few devices onto the same sample. Because we did not obtain reproducible responses for this system, we decided to abandon this configuration and move to other systems.

### 5.1.3 Third system: free standing sensors

In order to avoid adhesion issues spotted when PDMS substrates are used we decided to fabricate freestanding sensors. First we obtained a 10 μm P(VDF-co-TrFE) free standing films by means of doctor-blading deposition on Teflon, from which the piezoelectric film can be easy peeled off. The deposition has been carried on Teflon sheet at 60 °C with a blade speed of 10 mm s<sup>-1</sup>. Then the patterned PEDOT bottom and top electrodes have been inkjet printed on both surfaces of the free standing film.

A picture (Figure 5.6a) and a schematic (Figure 5.6b) of the fabricated free standing organic system are displayed below.

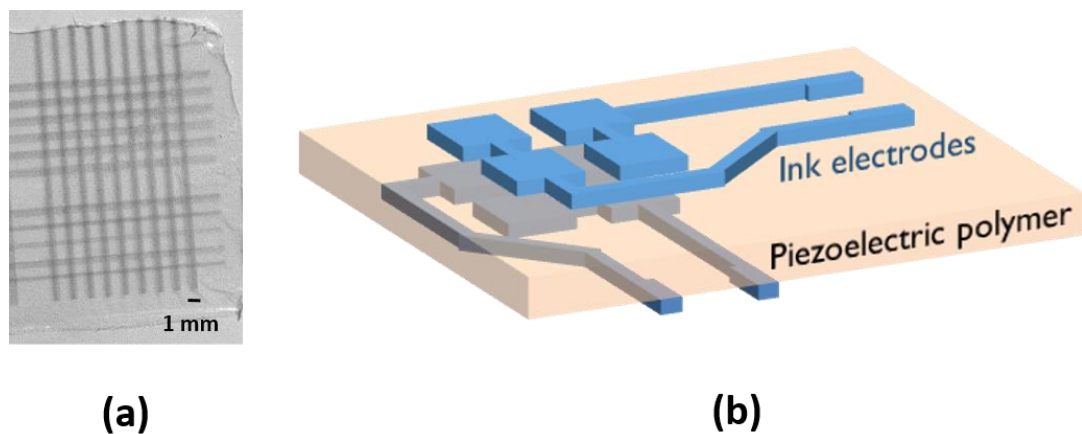


**Figure 5.6** (a) Picture and (b) Schematic of the fabricated free standing PEDOT/P(VDF-co-TrFE)/PEDOT device. In (a) the active area of the devices is of 1 mm<sup>2</sup>.

The system has been characterised by recording *polarisation vs electric field* hysteresis loops at a frequency of 100 Hz. The hysteresis loops obtained for this freestanding organic device at different increasing voltages are displayed in Figure 5.7a. A better ferroelectric response in terms of less leaky hysteresis loop and higher  $P_r$ , as compared to the one achieved with the former system (Figure 5.5), is recorded.  $P_r$  has increased of one order of magnitude (from  $P_r \approx 0.6 \text{ mC m}^{-2}$  recorded at  $\sim 8 \text{ kV}$ , for the previous system on PDMS, to  $\sim 6 \text{ mC m}^{-2}$  recorded at  $\sim 0.9 \text{ kV}$ ) but the direct comparison between the two systems should be avoided because of the different electric field used for the two systems.

Once that polarisation is achieved we record the mechanical displacement,  $D$ , as function of the electric field, shown in Figure 5.7b (red curve). A distorted  $D$  vs  $E$  hysteresis butterfly loop is recorded, showing the detection of the inverse piezoelectric effect (see Annex section).

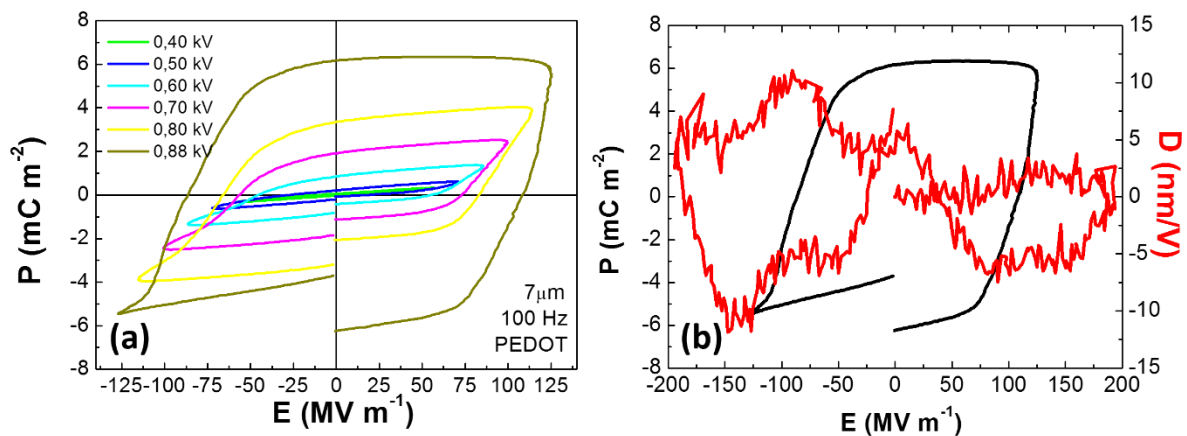


**Figure 5.7** (a) Polarisation vs electric field hysteresis loops recorded for a free standing PEDOT/P(VDF-co-TrFE)/PEDOT device at different increasing voltages. (b) The hysteresis loop recorded at 880 V (black line) is overlapped with the mechanical displacement vs electric field butterfly loop (red line).

Even though piezoelectric effect has been recorded, both polarisation hysteresis and butterfly loops are leaky and distorted respectively. We decided therefore to test the use of metallic electrodes instead. A hybrid system where the PEDOT has been substituted by patterned metallic electrodes of gold and silver (300 nm thick) that have been thermally evaporated on both surfaces of the freestanding piezoelectric film has been fabricated. The P(VDF-co-TrFE) free standing films were obtained once more by means of doctor-blading

technique (thickness of the piezoelectric layer  $\approx 10\mu\text{m}$ ). In Figure 5.8 a picture of the fabricated device and its schematic is represented.

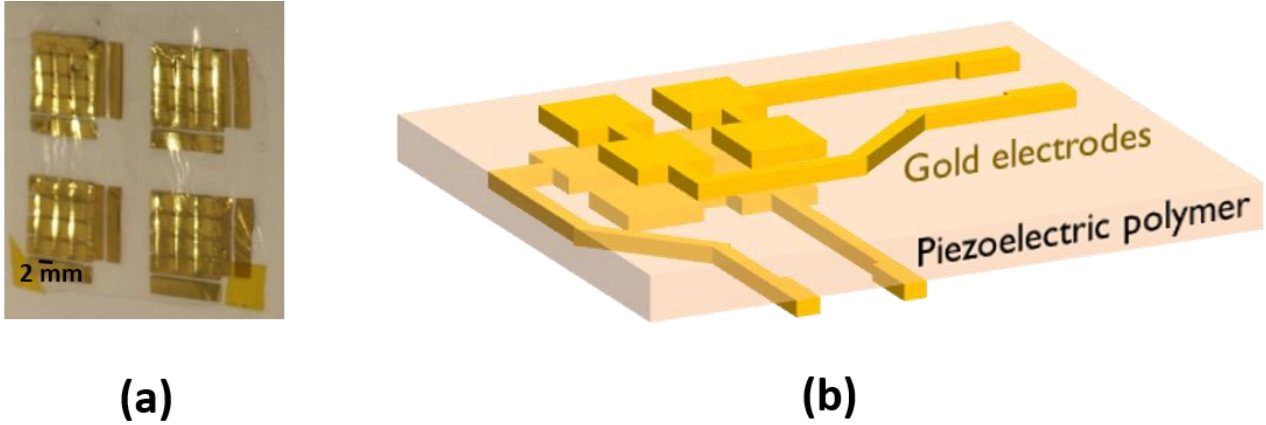


**Figure 5.8** (a) Picture and (b) Schematic of the fabricated free standing Au/P(VDF-co-TrFE)/Au device. In (a) the active area of the devices is of 4 mm<sup>2</sup>.

Ferroelectric hysteresis loops have been recorded for this kind of hybrid system as shown in Figure 5.9 where three ferroelectric loops recorded at 100 Hz at increasing voltages are shown. A clear improvement of the shape of the hysteresis loops is evident.

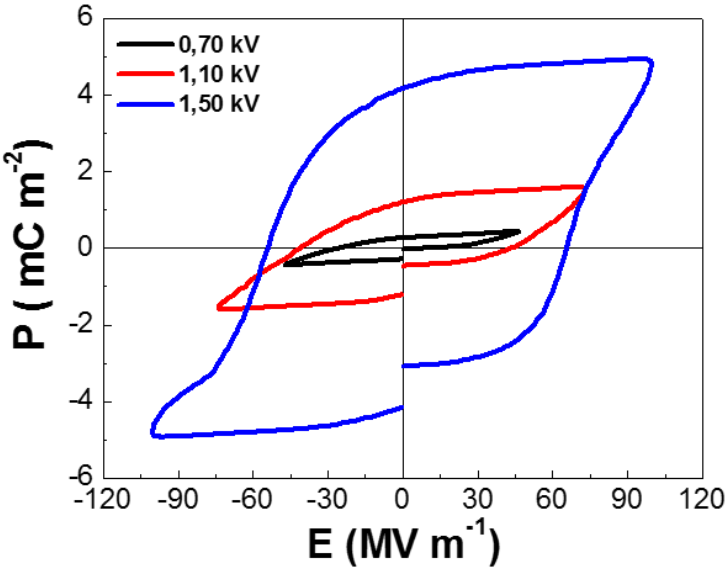


**Figure 5.9** P vs E hysteresis loops of free standing Au/P(VDF-co-TrFE)/Au device.

The current leakage is almost absent, demonstrating that by using metallic electrodes no current is passing through the piezoelectric layer.

Since this hybrid system has shown the best ferroelectric response so far, we decided to focus on this system and to work on the improvement of this kind of devices. Different parameters have been varied, such as different concentrations of P(VDF-co-TrFE) in cyclopentanone, different doctor blade “air gap”, different electrodes and different metals. What herein is not shown is also a huge work that has been done by Alizée in the realisation of shadow masks with differently sized patterns, which has allowed investigating different areas. In Figure 5.10 as examples, we report two free standing devices obtained with Au (on the left side) and Ag (on the right side) where Au has smaller active area of 2 mm x 2 mm than Ag, which has of device areas of 4 mm x 4 mm.

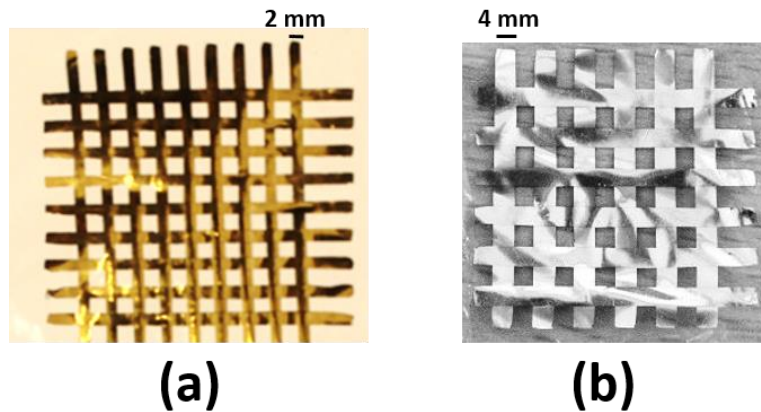


**Figure 5.10** (a) Picture of the free standing Au/P(VDF-co-TrFE)/Au device and (b) of the free standing Ag/P(VDF-co-TrFE)/Ag device. In (a) the active area of the devices is of 4 mm<sup>2</sup>, in (b) is of 16 mm<sup>2</sup>.

Herein we will show only the results obtained for the Ag electrode devices with an area of 4 mm<sup>2</sup> as the one showed in Figure 5.10b, since with gold we encounter problems of delamination. Below in Figure 5.11 are summarised the processing conditions that has led to the best performing device in terms of high  $P_r$ , low leakage and high dielectric displacements or in other words nice butterfly shaped curve as shown in Figure 5.12 where the hysteresis loops and butterfly loops obtained for such processed devices are shown.

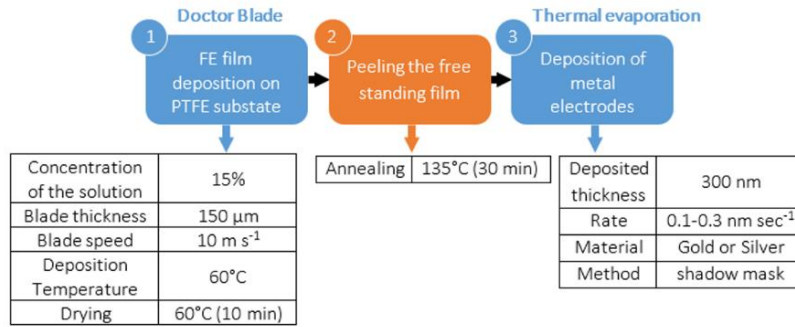


**Figure 5.11** The optimised processing parameters for the hybrid device.

In Figure 5.12 the hysteresis loops of this system clearly exhibits improved performance as compared with the organic device investigated above, in terms of less leaky hysteresis loops, higher  $P_r$ , and symmetric butterfly loop.

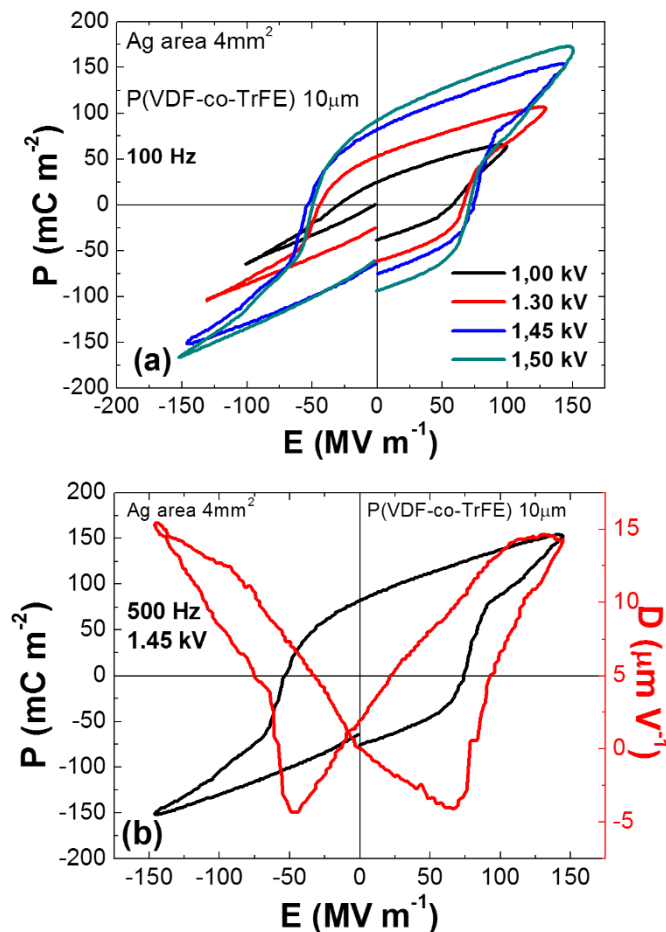


**Figure 5.12** (a)  $P$  vs  $E$  hysteresis loops at increasing voltages recorded for a Ag/P(VDF-co-TrFE)/Ag device and (b) the piezoelectric displacement recorded after saturated polarisation is reached. A perfect butterfly is shown.

So far, by recording the butterfly loops we have demonstrated the indirect piezoelectric effect, but our target is to fabricate a sensor that exploits the direct piezoelectric effect i.e. we need to be able to record the output voltage when pressure is applied. This can be done by means of oscilloscope.

Just for “a proof of concept”, we performed measurements with the oscilloscope on a very rough device where the bottom electrode was an aluminium foil on top of which there were two free standing piezoelectric films with different thicknesses, and on top of it two squared aluminium foil of 4 cm<sup>2</sup> and 16 cm<sup>2</sup> (Figure 5.13).

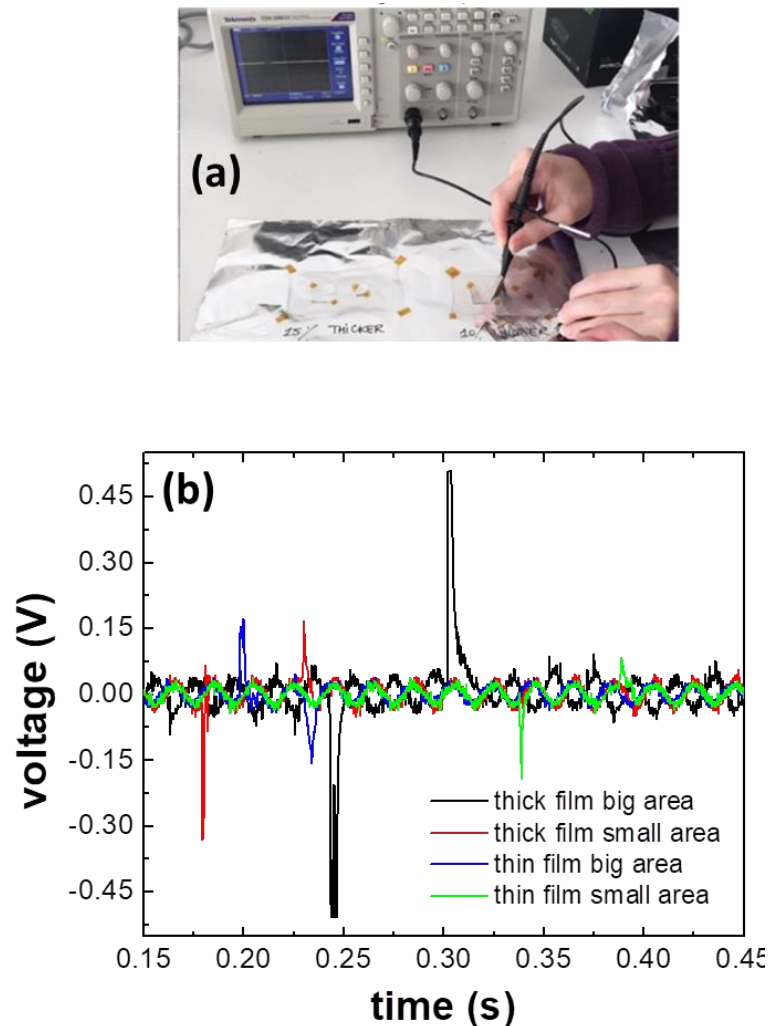


**Figure 5.13** (a) Picture of the measurement (top) and (b) output voltage V vs time (seconds) recorded for free standing films having two different thicknesses and two different active areas (bottom).

As we can see from Figure 5.13 the thicker the film and the larger the area, the higher the output voltage. Two peaks having opposite directions are visible. The first peak is generated during the direct pressure applied, and is indeed the direct consequence of the electrical displacement (whose electrical polarization induced by the applied stress generates surface charges because of the piezoelectric activity) induced into the film; while the second peak is due to the voltage released when the film relaxes back to its initial thickness.

For the freestanding devices above described (Figure 5.10), the output voltages detected by the oscilloscope were too low and often hidden by the intrinsic electric noise of the instrument. In any case, these devices with good performance missed the characteristic of a good flexibility since bending without cracking or damaging the device was nearly impossible.

Therefore, we proceeded with another route by thermally evaporating bottom and top electrodes on top of two separated films of PDMS and by using them to embed the piezoelectric freestanding layer (Figure 5.14a).

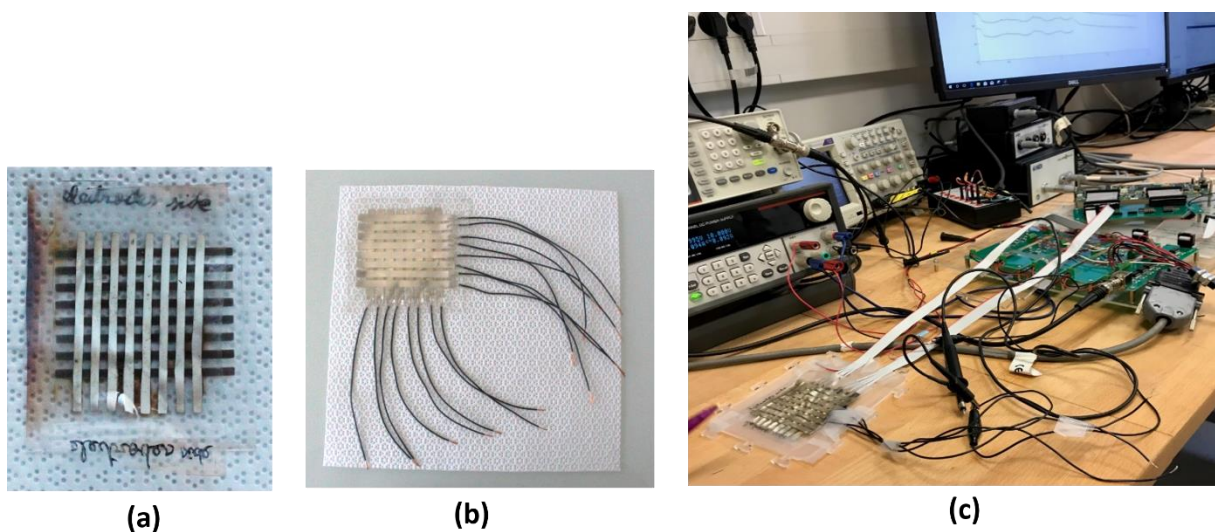


**Figure 5.14** (a) Device where the free standing P(VDF-co-TrFE) is encapsulated between two PDMS layers on top of which Ag electrodes were thermally evaporated; (b) (middle side) and finally the setup used by the team of the Liryc centre. The device area is of  $16 \text{ mm}^2$ .

In order to allow an easy contact of the electrodes arms we attached to the electrodes terminals metallic wires as shown in Figure 5.14b and we fixed them by means of silver

paste. This system showed quite good signals for the output voltage. This final device was evaluated by the Liryc institute.

In Liryc, the device has been connected to an electrical grid (as shown in Figure 5.14c) that allows the simultaneous recording of the output voltages generated pressure is applied. Unfortunately, at the time of the test problems were encountered due to the electronic grid: even if the pressure was applied on a certain device an output voltage was detected also for the others devices whose electrode terminals were connected to the grid, but on top of which not any pressure was exerted. We do think that the problem was assigned to the grid because for all the different device the same output signal appear with no any delay or difference in the intensity. The engineers of the Lyric are considering reviewing their electronic recording system. The devices are still on the evaluation at the moment of the submission of this manuscript.

## 5.2 Conclusion

In this Chapter we have shown the advancements that have been achieved within the project “sweet heart”. Since the goal was to obtain a flexible network of sensors that perfectly adhere to the model of a 3D-printed heart in order to map the localised output voltages generated by a mechanical stress our first attempt was to directly spray the conducting and the piezoelectric polymers in the inner of the heart. Deterioration of the heart substrate was induced by the high temperatures required so we opted fabricate independent devices to then let adhere onto the model heart.

The system firstly investigated was constituted of PET substrate, and spray-coated patterned PEDOT electrodes and spray-coated P(VDF-co-TrFE) film. PFM measurements demonstrate that the PEDOT:PSTFSI synthesised in our lab works well as electrode but the inhomogeneity of the systems suggest that other deposition techniques should be used.

We therefore chose to use doctor blade technique to deposit the piezoelectric film and inkjet printing for the patterned electrodes on top of a more flexible PDMS substrate. Hysteresis loops have been recorded but the current leakage was very evident.

The third approach was to fabricate freestanding devices. After several approaches we found a way to obtain highly flexible piezoelectric sensors by thermally evaporating the metallic silver electrodes on top of thick PDMS substrates and encapsulate a P(VDF-co-TrFE) film between them. Since the temperature at which we perform the thermal evaporation does not exceed 180°C, the degradation of PDMS is prevented, being the decomposition temperature of PDMS  $\approx$  500 °C. Even though for this most performing device the characterisation is herein not presented because their analysis is still ongoing we succeeded to furnish a good sensor to test. We think that the optimisation of this flexible piezoelectric network of sensors complemented with a resolution of the issues linked with the electronic conversion and amplifying system would give a proper sensor to allow the localisation of different electrical responses for laparoscopic medical simulation.

## References

- 1 Sharma, T., Je, S.-S., Gill, B. & Zhang, J. X. J. Patterning piezoelectric thin film PVDF–TrFE based pressure sensor for catheter application. *Sensors and Actuators A: Physical* **177**, 87-92, doi:<https://doi.org/10.1016/j.sna.2011.08.019> (2012).
- 2 Ferry, J. D. *Viscoelastic properties of polymers*. (Wiley, 1980).
- 3 Langberg, J. J. *et al.* The echo-transponder electrode catheter: A new method for mapping the left ventricle. *Journal of the American College of Cardiology* **12**, 218-223, doi:10.1016/0735-1097(88)90377-4 (1988).



# Chapter 6

*Phase separated  
P(VDF-co-TrFE):rr-P3HT blend:  
an alternative to organic  
photovoltaics?*



## 6 Phase separated P(VDF-co-TrFE):rr-P3HT blend: an alternative to organic photovoltaics?

### 6.1 An introduction to the P(VDF-co-TrFE):P3HT blend

Polymeric blends have been beneficially applied in organic electronics, for instance as active layers in photovoltaic devices,<sup>1</sup> light-emitting diodes,<sup>2</sup> field-effect transistors,<sup>3</sup> and memories.<sup>4,5</sup>

Among all the different types of blends in which the ferroelectric, *FE*, P(VDF-co-TrFE) has been employed, <sup>6-9</sup> its blends with semiconducting, *SC*, polymers are continuously grabbing attention.

Indeed, although the interesting electroactive nature of ferroelectric polymers, these materials are obviously dielectrics, acting as a barrier for the free charges flow. This aspect could be seen as a drawback for their application in organic electronic devices, which require charge transport and therefore the participation of semiconducting materials: hence the idea of blending *FE* with *SC* polymers.

In such blends normally the *FE* is P(VDF-co-TrFE) and the *SC* is the poly(3-hexylthiophene), P3HT. Other semiconducting polymers have been used as well, such as poly[3-(ethyl-5-pentanoate) thiophene-2,5-diyl] (P3EPT),<sup>10</sup> poly(9,9-dioctylfluorenyl-2,7-diyl) (PFO),<sup>7</sup> or Poly[(9,9-din-octylfluorenyl-2,7-diyl)-alt-(benzo[2,1,3]thiadiazol-4,8-diyl)](F8BT).<sup>11,12</sup>

All of these semiconducting polymers are conjugated polymers, which have alternating single, and double bonds, with  $sp^2$  hybridization, that allow the delocalization of  $\pi$ -electrons.

When  $sp^2$ -hybridization occurs between 2p and 2s orbitals in C atoms, three  $sp^2$  hybrid orbitals and one  $p_z$  orbital of two neighbouring carbons highly overlap to form planar  $\sigma$ -bonds, while the remaining  $p_z$  orbitals weakly overlap to form  $\pi$ - bonds, perpendicular to the molecular plane (Figure 6.1a). The splitting between the bonding  $\pi$  and the anti-bonding  $\pi^*$  orbitals is weaker than the one between the bonding and anti-bonding  $\sigma$ - and  $\sigma^*$ -orbitals as

shown in Figure 6.1b. Therefore, in typical organic materials with  $\pi$ - and  $\sigma$ -bonds, a  $\pi$ -orbital forms the Highest Occupied Molecular Orbital (HOMO) and a  $\pi^*$ -orbital the Lowest Unoccupied Molecular Orbital (LUMO) (see Figure 6.1b).<sup>13</sup> In the case of P3HT the HOMO is at -5.2 eV and the LUMO at -3 eV, with a resulting band gaps of  $\sim 2.2$  eV.

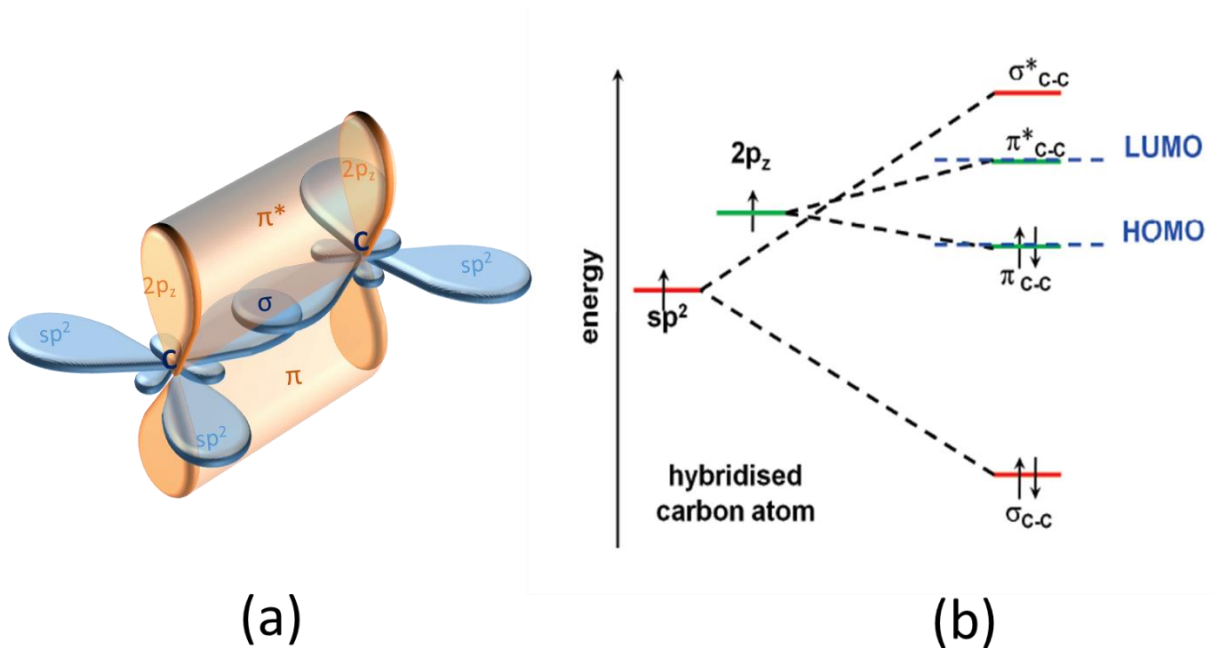


**Figure 6.1** (a) Schematic of the orbitals involved between two neighbour C atoms: two  $sp^2$  hybrid orbitals can merge to give  $\sigma$  molecular orbitals while two pure  $p$  orbitals can merge to form  $\pi$  molecular orbitals. (b) energy splitting between bonding and antibonding orbitals:  $sp^2$  orbitals highly overlap in comparison with the  $p$  orbitals, causing a smaller splitting between bonding  $\pi$  and anti-bonding  $\pi^*$  orbitals. Thus the  $\pi$ -orbital forms the HOMO and a  $\pi^*$ -orbital the LUMO of the molecule.

In general SC materials can be seen as electrical insulators with a low energy band gap that can be crossed by charge carriers at room temperature thanks to the thermal energy contribution  $k_B T$  (of the order of meV at RT), where  $k_B$  is the Boltzmann constant  $8.6 \cdot 10^{-5}$  eV  $K^{-1}$  and  $T$  is the temperature in Kelvin (298.15 K at RT).

After this short reminder about semiconducting polymers we come back to the FE-SC blends. The FE-SC blends found their main application in memories, which overpass the limits related to those based on single FE capacitor. Indeed, even though ferroelectric polymers,

thanks to their bistable reversible polarisation, are by themselves suitable for data storage, in simple ferroelectric capacitors the reading-out is destructive since it requires the application of an electric field that exceeds the coercive field,  $E_c$ .<sup>14</sup> These memories need then to be reprogrammed after reading-out.

A non-destructive reading-out device, named non-volatile memory, requires resistive switching. Bistable conduction has been demonstrated in ferroelectric Schottky diodes where inorganic ferroelectrics, considered as wide-band-gap semiconductors, conduct electricity owing to the presence of lattice defects (i.e. vacancies). The depletion width in ferroelectric Schottky diodes varies depending on the polarisation state of the ferroelectric.<sup>15,16</sup> A polarisation parallel to the built-in field leads to a small depletion width, that can be crossed by charge carriers (the diode has a low resistance); *vice versa* a polarisation antiparallel to the built-in field leads to a large depletion width and consequently to a high resistance. The attempts to increase the conductivity of inorganic ferroelectric Schottky diodes through doping, strongly reduces ferroelectric polarisation since the additional free charge carriers neutralise the polarisation charges.

Such obstacles in developing Schottky-based non-volatile memories have pushed research to develop new solutions, for instance separating the switching (ferroelectricity) from the reading-out (electric conductivity) functionalities<sup>17</sup> by means of the employment of two materials each bearing a different function. Thus, Asadi and co-workers with the development of *FE-SC* polymers blend based diodes achieved a breakthrough in non-volatile organic memories.<sup>4</sup> The extremely promising alternative of Asadi *et al.* overtook the drawbacks linked to the volatility of simple ferroelectric capacitor and to the difficulties in modulating two opposite properties borne by the same material. Organic non-volatile ferroelectric resistive memories were realised by using a phase-separated system where the two distinct functional polymers coexist. The advantage of using phase separated *FE-SC* blends is given by the phase separation itself. The fact that the two phases that bring the two divergent functionalities (the ferroelectric and the resistive one) are morphologically separated, permits the individual optimisation of each functionality independently. Therefore, on one side by acting on the ferroelectric material, the switching property can be varied, while on the other side, by modulating the semiconducting material the reading-out functionality can be adjusted.<sup>5</sup>

A simplified layout of the non-volatile memory device cross-section made of the ferroelectric P(VDF-co-TrFE) and of the semiconducting P3HT (whose chemical structures are depicted in Figure 6.2a and 6.2b) is shown in Figure 6.2c: two metal electrodes sandwich the thin active layer, which consists of SC polymeric paths embedded in the FE matrix.

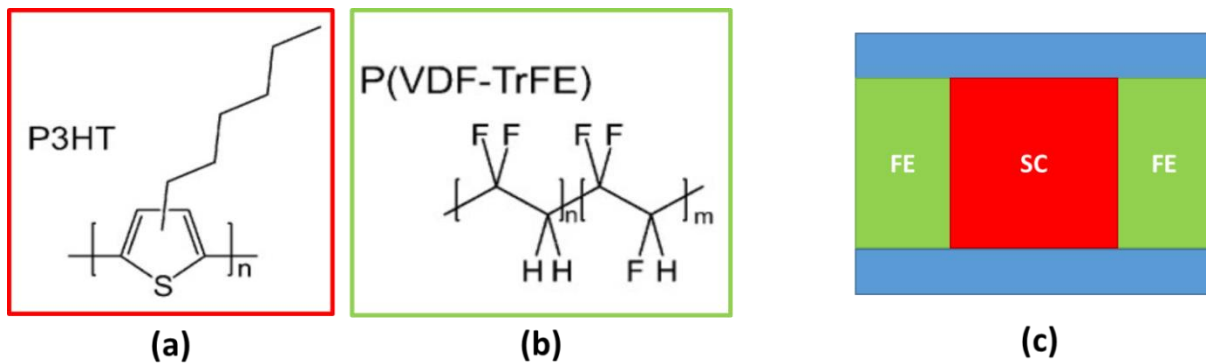


**Figure 6.2.** Chemical structures of (a) P3HT and of (b) P(VDF-co-TrFE). (c) Schematic layout of the FE (green squares)-SC (red squares) diode between two electrodes (blue bars).

Charge carriers flow is possible only via the SC phase that, as p-type semiconductor, conducts holes. The holes' injection barrier is the difference in energy between the work function of the electrode and the HOMO level of P3HT ( $\text{HOMO}_{\text{P3HT}} = -5.2 \text{ eV}$ ), that is 0.9 eV if we consider an Ag electrode ( $\Phi_{\text{Ag anode}} = -4.3 \text{ eV}$ ) as in the example shown in Figure 6.3a reported from reference <sup>4</sup>.

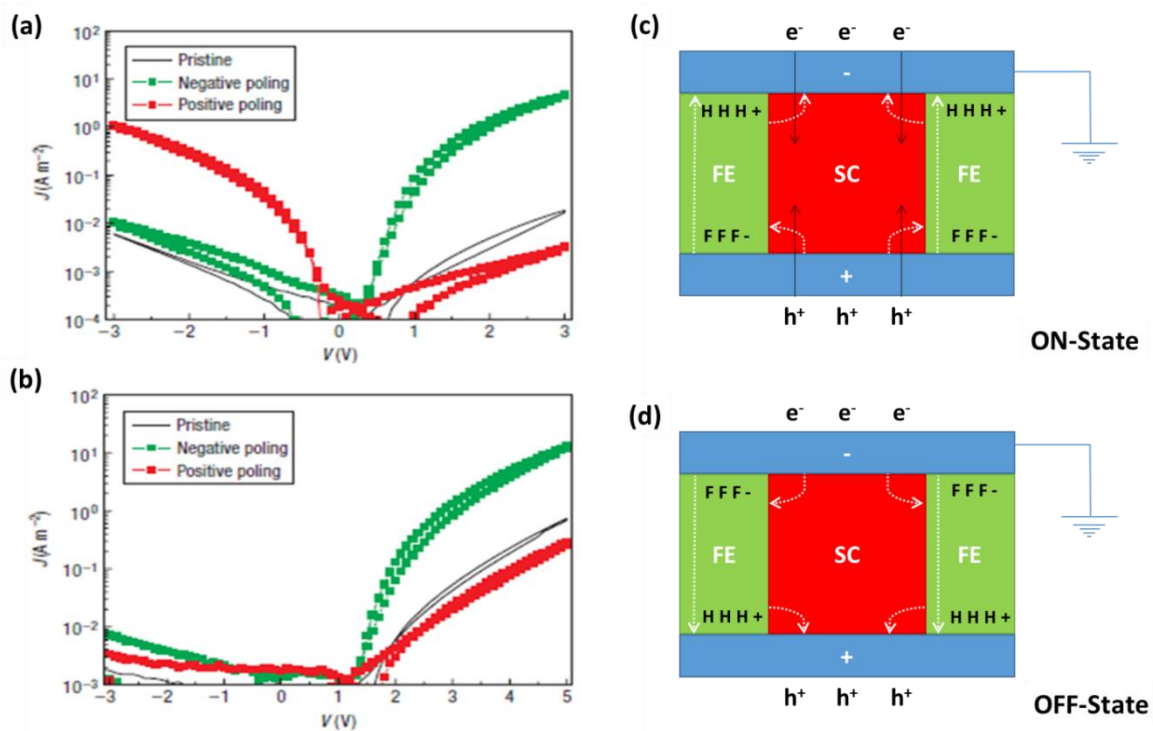


**Figure 6.3** *J-V characteristics of a P(VDF-co-TrFE):P3HT pristine film, and after positive and negative polarization in a diode configuration with (a) two Ag contacts, and with (b) an Ag bottom electrode and blocking LiF/Al top electrode. Reproduced from reference <sup>4</sup>. The device is in (c) the ON-state and in (d) the off-state of the devices. Black minus (-) and black plus (+) in the FE indicate its polarisation charges. White dashed arrows indicate the FE stray field, while the black full arrows indicate the path of the charges carriers. In the ON-state the polarisation is parallel to the built-in field, charges can cross easily the injection barriers that is lowered (black arrows are apparent). (d) In the OFF-state the polarisation reversal hinders the charges flow, the injection barrier has increased, blocking the current flow of the device (no black arrows are apparent).*

In the case of the symmetric configuration Ag/P3HT/Ag, silver acts as a poor injection contact as shown by the low current density for the pristine, unpoled junction in Figure 6.3a (black line). If the top Ag is grounded, when a positive voltage is applied to the bottom Ag anode, the holes' injection occurs from the bottom anode to the P3HT layer, contrarily when a negative voltage is applied to the anode, the holes' barrier slightly increases at the bottom Ag anode/P3HT interface: a slightly lower  $J$  is recorded at -3V compared to the  $J$  recorded at +3V in Figure 6.3a for the pristine blend device (black line).

When the ferroelectric matrix is poled, the induced polarisation field serves to control the injection barrier locally at the *SC*/metal interface.<sup>4</sup> Depending on the polarisation direction a lowering (or an increase) of the injection barrier at the *SC*/metal interface occurs and with it an increase (or a reduction) of the device current. Applying to the bottom anode an electric field that exceeds the negative  $E_c$  of P(VDF-*co*-TrFE) brings the device into the ON-state (Figure 6.3c), since the *FE* polarisation is parallel to the built-in field, and therefore the charges can cross easily the lowered injection barrier. On the other hand, exceeding the positive  $E_c$  leads to the OFF-state device (Figure 6.3d) at positive bias, indeed the injection is now improved at the top electrode (the poled junction is still a bistable resistive diode, but in the reverse direction<sup>4</sup>). Switching from the off-state to the on-state generates a bistable resistive switch whose driving force is controlled by the stray field of the ferroelectric.<sup>18</sup>

If a metal contacts with a small work function, for example the (LiF/Al) is used, an important injection barrier of 2 eV results at the P3HT/(LiF/Al) interface. This blocking contact makes the junction a *rectifying* bistable resistive switch (see Figure 6.3b reported from reference<sup>4</sup>).

The operation mechanism of this device relies on the formation of a phase-separated network with continuous semiconducting pathways that expand through the entire thickness, indispensable for charge carriers flow from the top to the bottom electrodes.<sup>19,20</sup> Indeed Asadi *et al.* asserted the formation of a phase-separated pillar-like network (i.e. P3HT pillars embedded in a FE matrix) with a lateral phase separation typically of 200 nm.<sup>21</sup> Due to these structural requirements, and driven by the need for further optimisation and device miniaturisation, many research groups have investigated the morphology of the P(VDF-*co*-TrFE):P3HT blend.

In 2010 McNeill, Asadi and co-workers<sup>19</sup> through AFM and Scanning Transmission X-ray Microscopy (STXM) showed that the two polymers form a phase-separated structure, where *SC* columns with a lateral size ranging from 100 nm to 500 nm depending on the molecular ratio, are extended through the entire thickness of P(VDF-*co*-TrFE):P3HT thin films.

Even though (STXM) allows investigating the bulk structure of thin-films of polymer blends<sup>10</sup> they underline that one needs to “be careful in reading too much the vertical information and the appearance of a wetting layer at the interface demanded further investigations with surface-sensitive techniques”.

Three years later, by means of Atomic force microscopy (AFM) Khikhlovskiy *et al.* have shown that the semiconducting polymer domains can form either convex protrusions at the film surface, or concave depressions, these latter being mainly responsible for the charge conduction in the device.<sup>11</sup> In particular, in order to reconstruct the 3D-morphology blend, selective dissolution of the different components was combined with AFM analysis, revealing the existence of various types of embedded semiconductor domains as well as a thin wetting layer at the bottom electrode (see Figure 6.4). Domains that go through the entire film thickness do exist (feature (1) in Figure 6.4), and thus would connect bottom and top electrodes, while others are electrically non-active, either protruding at the surface (feature (2) not connected with the bottom electrode) or laying on the substrate, reminiscent of a partial wetting layer buried by the matrix.<sup>12</sup> It is highlighted that these latter kind of domains are undesirable for device fabrication because they do not contribute to overall current and could even be detrimental to device performance by affecting either the potential charges injection at the electrode/semiconducting interface, or the charges collection to the other electrode.<sup>10</sup>

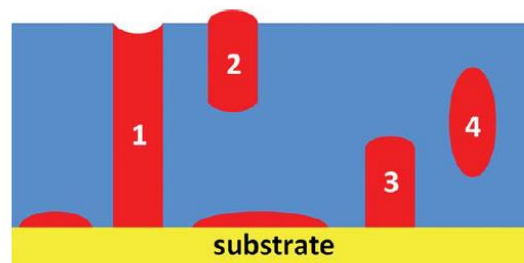


**Figure 6.4** Different semiconducting domains (red features) embedded into a ferroelectric matrix (blue), reproduced from <sup>12</sup>.

Even though a “pillar-like” morphology seems fundamental to collect charges that vertically travel through semiconducting pathways,<sup>4</sup> the results summarised above well document that in reality the semiconducting domains deviate from the simplified pillar-like morphology.

Differences in morphology between the surface and bulk could play an important role in charge carrier transport and overall device performance, for example if a homogeneous layer of semiconducting material stands at the metallic interface charge conduction is not possible. It arises that the device operation is intimately linked to the phase separated morphology.

Since the phase separation of the *FE-SC* blends cannot be easily controlled, perhaps one should resort to alternative strategies as the one proposed by Martinez-Tong *et al.* who succeeded in obtaining controlled periodic surface nanostructures by means of laser-induced patterning.<sup>22</sup>

A well-distributed nanostructure of vertical SC domains that connect the bottom to the top electrodes indeed seems to be required for efficient device operation, since the polarisation induced current density is reported to be higher in the perimeter of semiconducting domains<sup>11</sup>.

This last statement is based on the theoretical model proposed by Kemerink *et al.*<sup>18</sup> according to whom the driving force for the resistance switching of the *FE-SC* diode is the ferroelectric stray field of the polarized ferroelectric phase within the SC domains, which can modulate the charge injection from the electrode into the semiconductor. The stray field is localised in the regions where semiconductor and ferroelectric phases exist, and only the SC regions that are very close to the SC/FE interface are affected by the stray field. Therefore, the advantages coming from the *FE* material are lost if the poled *FE* material and metal-SC interface are too far away for the stray field to penetrate in the SC and modify the charge injection barrier.<sup>4</sup>

The structure of this *FE-SC* polymer blend system has also been investigated formerly in our lab by the PhD student Carine Lacroix whose Thesis was focused on the electric/photoelectric characterisation of such system for its application in memories and photovoltaic devices.<sup>23</sup> In this Chapter we will present complementary results obtained from the 3D-nanostructural analysis of the *FE-SC* blends and few results obtained focusing on their potential application in organic photovoltaics OPVs.

In particular in this Chapter we will present the investigation of the morphological nanostructure of P(VDF-*co*-TrFE):P3HT blends by a combination of Scanning Probe Microscopy techniques which allows to provide the 3D-reconstruction of this system. Most of the studies on such or similar systems normally use regio-irregular P3HT, *rir*-P3HT, which ensures to obtain amorphous SC domains within the semi-crystalline FE matrix. We here employ the regio-regular P3HT, *rr*-P3HT, in view of a potential application of the *FE-SC* blend in photovoltaics, since semi crystalline P3HT is known to allow a better charge conduction, which is needed in OPV devices. The use of *rr*-P3HT is indeed preferable with respect to *rir*-P3HT

since holes mobility is increased for rr-P3HT, assisted by the ordered  $\pi$ - $\pi$  stacking of the thiophene rings ( $\mu_{h+rr-P3HT} = 10^{-3} \text{ cm}^2 \text{ V}^{-1} \text{ s}^{-1} > \mu_{h+rr-P3HT} = 10^{-4} \text{ cm}^2 \text{ V}^{-1} \text{ s}^{-1}$ )<sup>24</sup>. After having characterised *FE-SC* blends with different weight ratio compositions of the *FE* and *SC* polymers, we will move to the device fabrication and to their electrical characterisation in order to test the potential application of such blends in OPVs.

## 6.2 Phase separated structure: a morphological characterisation

In this session we first focus on the 3D-morphological characterisation of P(VDF-*co*-TrFE):rr-P3HT blends having different compositions. Three different *FE:SC* compositions, i.e. 95:5<sub>wt/wt</sub>, 90:10<sub>wt/wt</sub> and 80:20<sub>wt/wt</sub>, have been investigated by means of a combination of multiple force microscopy techniques, namely Atomic Force Microscopy (AFM), Piezoresponse Force Microscopy (PFM), Kelvin Probe Force Microscopy (KPFM) and Conductive Atomic Force Microscopy (C-AFM).

### 6.2.1 Samples preparation

P(VDF-*co*-TrFE) with a VDF/TrFE molar ratio of 75/25 and rr-P3HT (with a  $M_w$  of 60 kDa) were co-dissolved in tetrahydrofuran, THF, at a total concentration of 25 mg ml<sup>-1</sup>. Three weight ratios of P(VDF-*co*-TrFE):rr-P3HT have been prepared, i.e. 95:5, 90:10 and 80:20 and spin-coated onto cleaned ITO substrates. Films with a thickness of  $\approx$  250 nm were obtained. The films have been annealed on a precision hot stage from RT to 135 °C and an isothermal step has been performed for 15 min in order to increase both polymers crystallinity and promote the phase separation. Then the films were let to cool down slowly until RT on the same hot stage.

## 6.2.2 Structural characterisation

Thin films of P(VDF-co-TrFE):rr-P3HT blend with different *FE:SC* weight ratios, i.e. 95:5, 90:10 and 80:20, are studied first by means of Piezoresponse Force Microscopy (PFM).

PFM is a contact mode imaging technique that allows recording the electromechanical response of a material, in our case of the piezoelectric P(VDF-co-TrFE). During scanning an alternating AC voltage is applied between the tip and the sample. The ITO, on top of which the film has been deposited, represents the ground contact, while the conductive probing tip of PFM represents the top electrode. If the electrically stimulated film is piezoelectric, expansions and contractions will be recorded as a vertical mechanical displacement.

In Figure 6.5 the PFM height (topography in Figure 6.5a) and the corresponding vertical PFM images (Figure 6.5b and Figure 6.5c) are shown for a sample having a weight ratio P(VDF-co-TrFE):P3HT of 90:10. For the other 95:5 and 80:20 blends similar images have been recorded. The amplitude of the mechanical displacement vertical to the substrate plane is shown in the VPFM amplitude image in Figure 6.5b, which gives information about the magnitude of the electromechanical polarisation displacement. The different orientations of the polarised piezoelectric domains are shown in the VPFM phase image in Figure 6.5c.

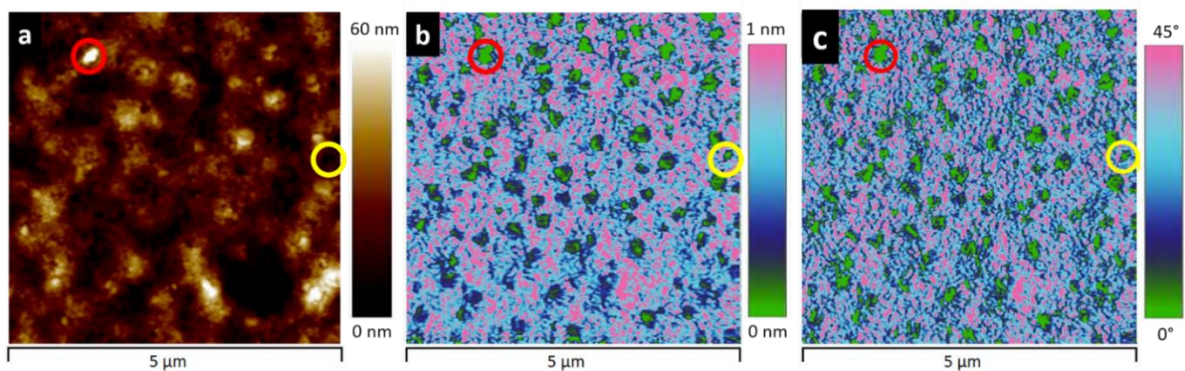


**Figure 6.5** a)  $5\ \mu\text{m} \times 5\ \mu\text{m}$  PFM height image, b) VPFM amplitude image and c) the VPFM phase image of 90:10<sub>wt/wt</sub> P(VDF-co-TrFE):rr-P3HT blend. All the three images are recorded simultaneously in the same sample region. The circles evidence the same features in the three images. Red and yellow rings highlight convex and concave P3HT domains respectively.

The PFM height, the VPFM amplitude and the VPFM phase images are recorded simultaneously during scanning, and correspond to the same sample area.

When the electrical stress is applied to the film throughout the piezo-tip a mechanical response is recorded only from the piezoelectric P(VDF-co-TrFE) matrix (pink and blue regions in Figure 6.5b and Figure 6.5c).<sup>23,24</sup> The P3HT domains do not respond to the applied voltage as shown by the green regions indicating absence of displacement. Indeed, P3HT is not piezoelectric: the ferroelectric (piezoelectric) and semiconducting phases can be discriminated. This PFM characterisation demonstrates that P(VDF-co-TrFE) maintains its functionality and does not suffer from its blending with the semiconducting P3HT. It also shows that irregular P3HT domains exist in the FE matrix.

In Figure 6.5 circles evidence the same morphological features on the different PFM images. By comparing Figure 6.5a with Figure 6.5b we see that both red and yellow circle correspond to P3HT. In Figure 6.5a the red circle surrounds a superficial convex protrusion, while the yellow circle corresponds to a superficial concave depression. Therefore, in agreement with previous works,<sup>4,19,20</sup> we conclude that the SC domains at the surface can be either convex or concave, appearing as protrusions or depressions.

The correlation between topographic and electronic properties for blends with different weight ratios have been investigated by means of Kelvin Probe Force Microscopy, KPFM. KPFM enables the evaluation of the electronic behaviour of the two polymers by providing the surface potential map of the sample under study at the nano-scale. The potential measured between the tip and surface of the film is called contact potential difference,  $V_{CPD}$ ,<sup>25</sup> and is defined by Equation 6.1:

$$V_{CPD} = \frac{\Phi_{tip} - \Phi_{sample}}{-e} \quad (6.1)$$

where  $\Phi_{sample}$  and  $\Phi_{tip}$  are the work functions of the sample and the tip respectively, and  $e$  is the electronic charge ( $e \approx 1.6 \cdot 10^{-19}$  C). When the tip is brought close to the film surface, an electrical force is generated between the tip and the surface, due to the differences in their Fermi energy levels.<sup>25</sup> Therefore, regions where a larger  $V_{CPD}$  is recorded indicate the existence of an electrical insulator material; *vice versa* when the measured  $V_{CPD}$  is low, a semiconducting

material is detected. In Figure 6.6 the topography images (top row) and the corresponding surface potential maps (bottom row) are reported for the blends with a *FE:SC* weight ratio of 95:5 (Figure 6.6a and Figure 6.6b respectively), of 90:10 (Figure 6.6c and Figure 6.6d) and of 80:20 (Figure 6.6e and Figure 6.6f).

The P3HT and the P(VDF-*co*-TrFE) can be unambiguously discriminated in  $V_{CPD}$  images that show the phase separation of the two components. The yellow features represent regions with low  $\Phi$ , namely semiconducting P3HT, while the pink regions correspond to high  $\Phi$ , that is the insulating P(VDF-*co*-TrFE) matrix. From this KPFM study, we can estimate how the rr-P3HT domain sizes scale with the rr-P3HT content. As the content of P3HT increases, the diameter of the semiconducting features increases going from about 100 nm for the 95:5 ratio (Figure 6.6b), to 200 nm for the 90:10 (Figure 6.6d) until reaching, for the 80:20 system, a mean diameter of 300 nm (Figure 6.6f). This result is in agreement with previous publications.<sup>20</sup>

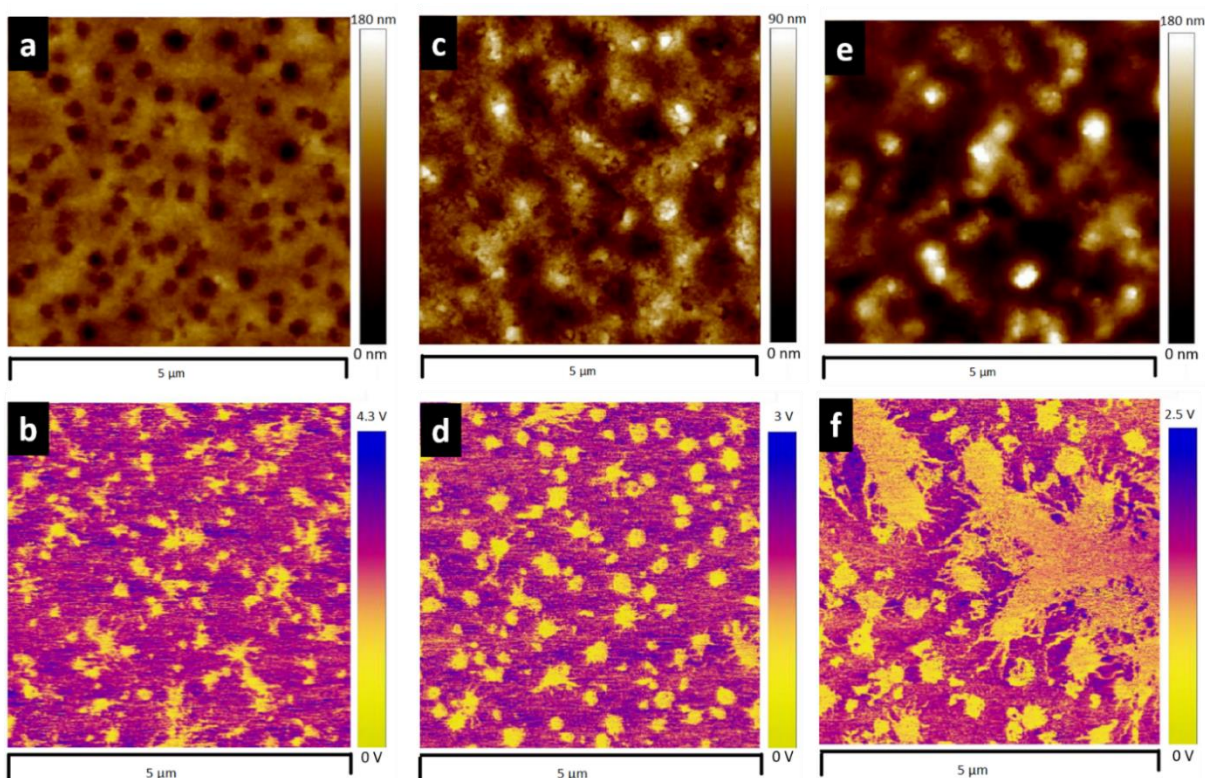


**Figure 6.6** KPFM topography images (top row) and the corresponding surface potential map (bottom row) for the weight ratios of 95:5 ((a) and (b)), 90:10 ((c) and (d)), and 80:20 ((e) and (f)) P(VDF-*co*-TrFE):P3HT blend.

It is worth to underline now that the KPFM is not a purely surface-sensitive technique,<sup>26</sup> but its sampling depth goes up to over 100 nm when semiconducting materials are investigated. We remind that the thickness of the investigated films is 250 nm, and then the PFM information is coming from almost half thickness of our system. This sort of “bulk sensitivity” of the technique means that the recorded “surface potential” map is not describing the composition at the *film-air* interface but gives us information about a thicker part of the layer.

By using the image processing software “*Image J*” we calculated the area occupied by P3HT on the  $V_{CPD}$  maps of  $25 \mu\text{m}^2$ . In Figure 6.7, the rr-P3HT fraction estimated by KPFM for the 95:5 film, the 90:10 film and the 80:20 film is plotted as a function of the P3HT content in the blend.

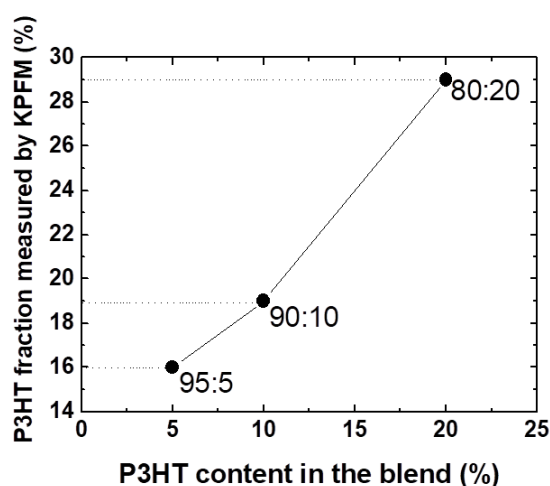


**Figure 6.7** P3HT fraction for the different FE:SC ratios evaluated from the KPFM VCPD images as a function of the respective P3HT % content in the blends.

Interestingly we find that the fraction of P3HT detected by KPFM is higher than the content of P3HT in the blend. This suggests a not controlled distribution along the entire film thickness of the P3HT, which probably segregates preferentially at the upper levels of the film, i.e. close to the film surface. In order to prove the possible origin of this surface segregation of P3HT, we have performed contact angle measurements on pure rr-P3HT and on pure P(VDF-co-TrFE) films with three different solvents: water, ethanol and isopropanol. We have calculated the respective surface tensions,  $\gamma$ , by using the OWRK model (Owens, Wendt, Rabel and Kaelble). The values that we have obtained are almost identical for both polymers:  $\gamma_{P3HT} = 31.85 \pm 0.3 \text{ mJ}$

$\text{m}^{-2}$  and  $\gamma_{\text{PVDF-co-TrFE}} = 33.02 \pm 0.7 \text{ mJ m}^{-2}$ , therefore no conclusion can be derived from the calculated surface tensions. Hence the fact that the P3HT domains, that appear with a very good contrast in the surface potential map, are hardly visible in AFM topography is probably due to a thin layer of P(VDF-co-TrFE) which covers the SC domains.

Moreover, from Figure 6.6 is evident that the rr-P3HT domains have the tendency to connect with each other, creating a network. This is deduced by the occurrence of connecting lines between the P3HT, at low P3HT weight ratios in the blend (Figure 6.6b and 6.6d), which turns into big domains for the 80:20 blend (Figure 6.6f). Hence, from the KPFM investigation it can be concluded that, in order to obtain the desirable phase-separated columnar structure the P3HT content in the blend should not exceeds the 10%, to avoid networking between the P3HT pathways.

Moving further, we investigated if the appearance of pillar-like semiconducting pathways that link the bottom to top surface can be confirmed. In order to reply to this question, we performed Conductive Atomic Force Microscopy, C-AFM that permits to map the variations of electrical conductivity across low-conducting and semiconducting materials. The samples are grounded through the ITO bottom electrode, while the AFM tip serves as the top electrode. If a current flow is passing between the bottom electrode and the AFM tip, it will be recorded. Topography images (top row of Figure 6.8) and high-resolution electric current flow maps (bottom row of Figure 6.8) are simultaneously measured in conductive AFM (Peak Force Tuna mode from Bruker).

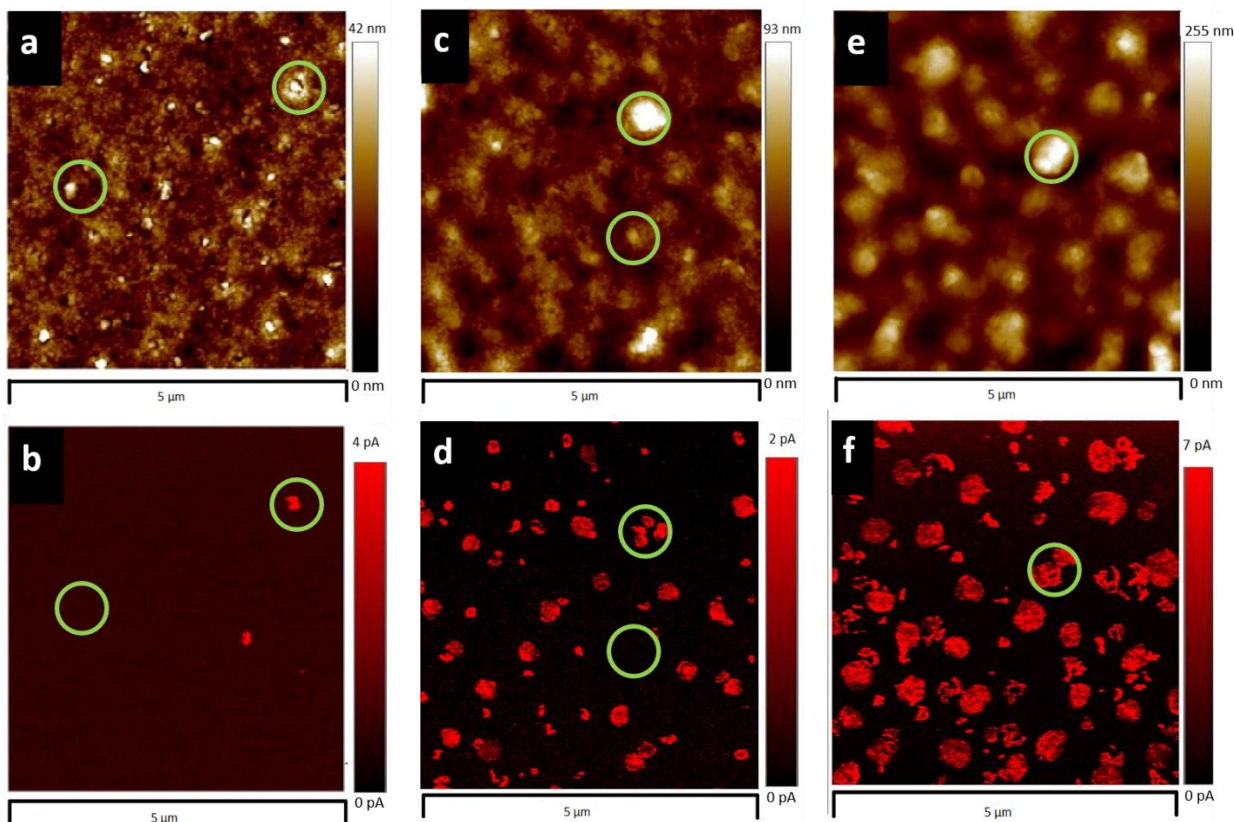


**Figure 6.8** C-AFM topography images (top row) and the corresponding current flow maps (bottom row) of  $25 \mu\text{m}^2$  of P(VDF-co-TrFE):P3HT 95:5 blend ((a) and (b) respectively), of the 90:10 blend ((c) and (d) respectively) and of the 80:20 ((e) and (f) respectively). The green circles evidence the same morphological features in the topography and current flow images.

In Figure 6.8a the green circle on the top right side circumscribes a P3HT spike which corresponds to a conducting pathway from the bottom to the top of the film, as shown by the red spot in Figure 6.8b. While for the green circle on the left-side of Figure 6.8a no any electric flow is recorded by the AFM tip in Figure 6.8b. This suggests that not all P3HT protrusions that exist at the surface are connected to the bottom interface by conductive channels. The same description can be done comparing Figure 6.8c with Figure 6.8d. It can be easily noted that by increasing the amount of P3HT in the blend, the number of conducting domains that connect the bottom and the top sides (sections of the P3HT network percolating across the film) increases. The size of these domains increases as well (Figure 6.8e and Figure 6.8f).

Note that in these current flow images the interconnecting network, that was obvious in the KPFM images, is missing. This suggests once more that the big P3HT interconnected domains that were apparent for the sample with a *FE:SC* weight ratio of 80:20 are localised not at the surface but they are rather buried by a P(VDF-co-TrFE) dielectric layer, which does not contribute to current flow.

Finally, from this complementary Scanning Probe Microscopy study we have found that various SC domains, convex protrusions or concave depressions, and structures deviating from the pillar-like morphology exist, as already anticipated by other authors.<sup>12</sup> In the case of the 80:20 blend, we have found that almost all SC pathways cross the entire thickness. Even though this is desirable for applications that demand for a high current density flow, the existence of a horizontal SC network at regions close to the surface, very pronounced for this 80:20 composition, could screen the effect of the ferroelectric stray field at the metal-SC interface. On the other hand, for the 95:5 *FE:SC* composition, SC pathways connecting the bottom to the top of the layer do exist, with a mean diameter of the SC domains of 100 nm that belongs to the optimum lateral semiconductor domain size range (that was found to be between 50–100 nm<sup>18</sup> for high performance memory diodes). However, we found that the number of connecting pathways per surface area for the 95:5 blend is very small compared to the other ratios. Therefore, we would suggest discarding the 95:5 composition because of the small current density expected, in view of a higher device performance and therefore to opt for a 90:10 *FE:SC* blend where is achieved a compromise between the number of SC pathways per surface area, the domain sizes and a lack of a horizontal SC network.

### 6.3 Application in organic photovoltaics

Normally, in blend-based devices like the above-mentioned diodes, as well as in the blend-based solar cells, controlling the phase-separated network is crucial in regulating the device operation and efficiency. For instance increased photovoltaic performances were obtained with the bulk heterojunction, BHJ, solar cells compared to the two-layer photovoltaic solar cell<sup>27</sup>, thanks to the increased number of interfaces between the n-type acceptor (e.g. the

[6,6]-phenyl-C<sub>61</sub>-butyric acid methyl ester, PCBM) and the p-type donor, (e.g. the P3HT) semiconductor materials.<sup>1,28</sup>

The main challenge in OPVs concerns the device efficiency improvement that is hindered by the significant energy loss caused by the recombination of electron-hole pairs and of free charges.<sup>29-32</sup> The ferroelectric materials, whose strong dipoles produce a permanent internal electric field, are able to assist the electron-hole separation and the extraction of free charges carriers in OPVs.<sup>33</sup> In particular, the polarisation electric field of the *FE* component favouring the holes-electrons,  $h^+e^-$ , separation at the FE-SC interface would prevent their recombination. Recently progresses have been achieved thanks to the integration of *FE* materials in OPV devices. The influence of ferroelectric materials in a *p-n* heterojunction has been studied through the insertion of a P(VDF-co-TrFE) layer either between P3HT and PCBM,<sup>31</sup> or between the active layer and the electrodes<sup>29</sup> (i.e. the cathode<sup>34</sup>) or by blending the ferroelectric polymer in the bulk heterojunction films.<sup>35</sup> All these configurations have been demonstrated to lead to an improvement of the energy conversion from 1-2% to 4-5%<sup>29,33</sup> (see Figure 6.9).

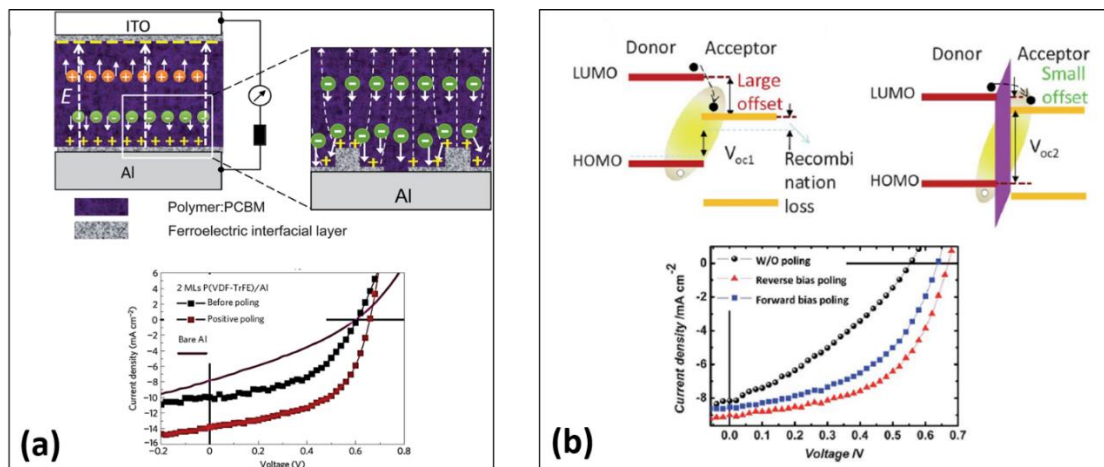


**Figure 6.9** (a) Schematics of ferroelectric-OPV where the active layer is inserted between the active layer and the electrodes and the photocurrent curves of *p-n* junction device without an *FE* layer (magenta line), with an *FE* layer before poling (black square line) and after poling (red squares).<sup>29</sup> (b) Energy level diagram of the semiconductor heterostructure without and with a dipole layer inserted at the *D/A* interface (violet panel) and the photocurrent curves for the as-made device (black balls), after poling the P(VDF-co-TrFE) layer with reverse (red triangles) and forward bias pulses (blue squares).<sup>34</sup> The two images are reproduced from reference<sup>32</sup>.

The OPVs mentioned above exploit the ferroelectric polarisation field in order to assist the transport of the dissociated charges to the electrodes or improve charge extraction. In this Chapter we propose to use the ferroelectric polarization field as the driving force for exciton dissociation. This approach circumvents the need for an external bias to dissociate the excitons formed in P3HT upon illumination. In fact, the n-type material is no more needed to provide – along with the p-type one – the driving force for exciton dissociation. In the event that the permanent ferroelectric polarisation field would act as a bias voltage to efficiently separate the electrons and holes, the P(VDF-*co*-TrFE):P3HT blend system could be arise as an alternative for organic photovoltaics.<sup>31</sup>

After having thoroughly characterised the nanostructure of this FE-SC, in the next session we will discuss few results obtained from the  $J$  vs  $V$  characterisation in dark and under light exposure of devices having as active layer a thin film of the P(VDF-*co*-TrFE):P3HT blend. We once more highlight that we herein use regio-regular P3HT, since crystalline semiconducting polymers can conduct higher current densities than amorphous ones, which is crucial for organic photovoltaics devices.

In view of a potential application of the FE-SC blends in photovoltaics, we had first studied a simple device geometry in which an active layer of P(VDF-*co*-TrFE):P3HT is sandwiched between a transparent bottom electrode, ITO and a gold top electrode. Then we moved to a more complex device Al/LiF/ P(VDF-*co*-TrFE):P3HT/PEDOT:PSS/ITO to obtain a device where the diode behaviour is more pronounced helped by the big difference in the energetic levels of the two electrodes.

### 6.3.1 Device fabrication

As above mentioned, devices have been prepared by using 2 configurations: 1) ITO and Au (100 nm) as the bottom and top electrodes respectively, and b) PEDOT:PSS/ITO and Al/LiF as the bottom and top electrodes respectively where LiF is 5 nm thick and Al 80 nm thick. PEDOT:PSS has been spin-coated as well as the blends layers. The metallic electrodes have been deposited by means of thermal evaporation.

### 6.3.2 J vs V characterisation

After having fabricated Au/blend/ITO devices we have recorded the  $J$  vs  $V$  curves and evaluated its photovoltaic potential. The ITO as bottom electrode is necessary for its transparency that allows the radiation to reach the active layer. The Au represents an almost Ohmic contact with the semiconducting P3HT, since the gold work function,  $\Phi$  ( $\Phi_{Au} \approx 5.1$  eV) is very close to the Highest Occupied Molecular Orbital, HOMO level of P3HT ( $\Phi_{HOMO\ P3HT} \approx 5.2$  eV), creating a very small injection barrier between Au and P3HT.<sup>36</sup> In this case so, by using ITO and Au as bottom and top electrodes respectively, we do not fabricate any rectifying devices since the holes blocking contact is missing. This nearly ohmic contact is expected to give almost symmetric contacts, as reported for devices in which the same bottom and top electrode used.<sup>37</sup> This kind of devices are called single-carrier diodes and are used to conduct only holes or electrons in both directions. The energy levels between rr-P3HT and the contacts of this first kind of fabricated device are depicted in Figure 6.10a.

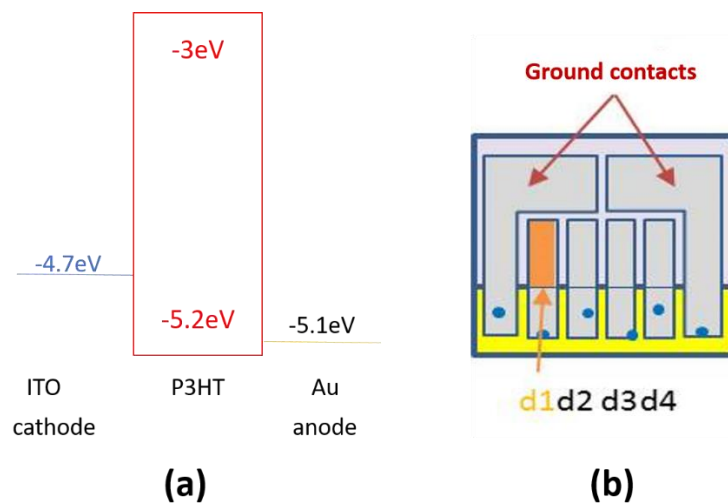


**Figure 6.10** Schematic of energy levels (on the left) and the device top view (on the right).

Thin films with the three different molar ratios blends have been incorporated between ITO and patterned Au top electrodes, obtaining 4 devices with an active area of  $10\text{ mm}^2$  as displayed in Figure 6.10b. The voltage applied is swept between -3V and +3V.

In Figure 6.11 the current density vs voltage,  $J$  vs  $V$ , responses of the 95:5, 90:10, 80:20 devices in dark and under illumination are presented. The measurements under illumination

are performed by means of a solar simulator whose lamp reproduces the solar spectrum. As expected, the samples exhibit high  $J$  because of the low contact resistance for charge extraction from the active layer. The blend having a  $FE:SC$  ratio of 95:5 exhibits lower current flows with respect to the others with higher P3HT content. At +3V, 30 mA cm<sup>-2</sup> are recorded for the 95:5 blend, 80 mA cm<sup>-2</sup> for the 90:10 and 600 mA cm<sup>-2</sup> for the 80:20. Note that the increase in current density is not linear with the fraction of the SC material in the blends. This electrical behaviour is in line with the morphological study discussed before where just few semiconducting pillars were found to connect the two electrodes for the 5% P3HT blends, which is expected to decrease the charge collected. Moreover, here we would like to underline that the lack of reproducibility is higher for this 95:5 weight ratio with respect to the 90:10 and the 80:20. In particular for the same sample with an active layer of 95:5 for just one or maximum two devices out of four it was possible to record  $J$  vs  $V$  curves. Moreover, for the 80:20 samples almost all P3HT domains are co-continuous therefore charge collection is expected to be maximised.

The  $J$ - $V$  curve of the 90:10 device exhibits a behaviour that varies more evidently when exposed to light. Also for the 80:20 we can see an effect of light irradiation, which is less evident than that for the 90:10. For the 95:5 the  $J$  measured in absence of light (dark current) seems to be mostly overlapped with the  $J$  measured under irradiation.

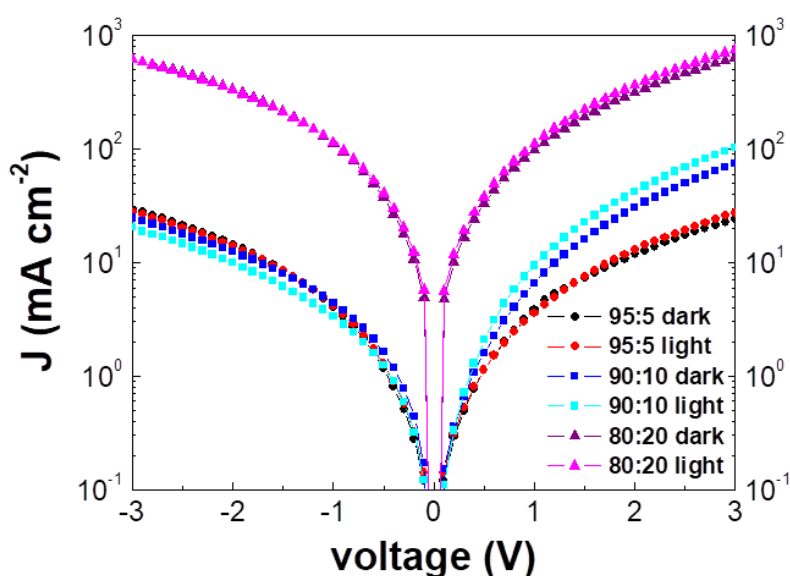


**Figure 6.11.** Density of current in logarithmic scale as function of the voltage applied in dark and under light for the samples 95:5, 90:10 and 80:20.

We opted to present herein the  $J$ - $V$  curves obtained after polarisation of the P(VDF-co-TrFE) just for the 90:10. Even though the high  $J$  found for the device 80:20 would be desirable for OPV applications, the optimum diameter of the semiconducting domains in a ferroelectric matrix has been estimated to be 50-100 nm,<sup>18</sup> therefore we prefer to avoid too large SC domains, that would decrease the area of  $FE$ - $SC$  interfaces. Once more remind that we found that the 90:10 blend has an average diameter of semiconducting domains that does not exceed largely the optimum sizes (90:10 has a mean SC diameter of 200 nm that is higher than the ideal 100 nm, but lower than the 300 nm found for the 80:20) and exhibits high current flow<sup>18</sup> (the number of SC pathways per area found for 90:10 is higher than the one found for the 95:5).

In Figure 6.12 we present a comparison between the  $J$  vs  $V$  behaviour of a not polarised 90:10 device, of positively “polarised” device and of a negatively “polarised” device.

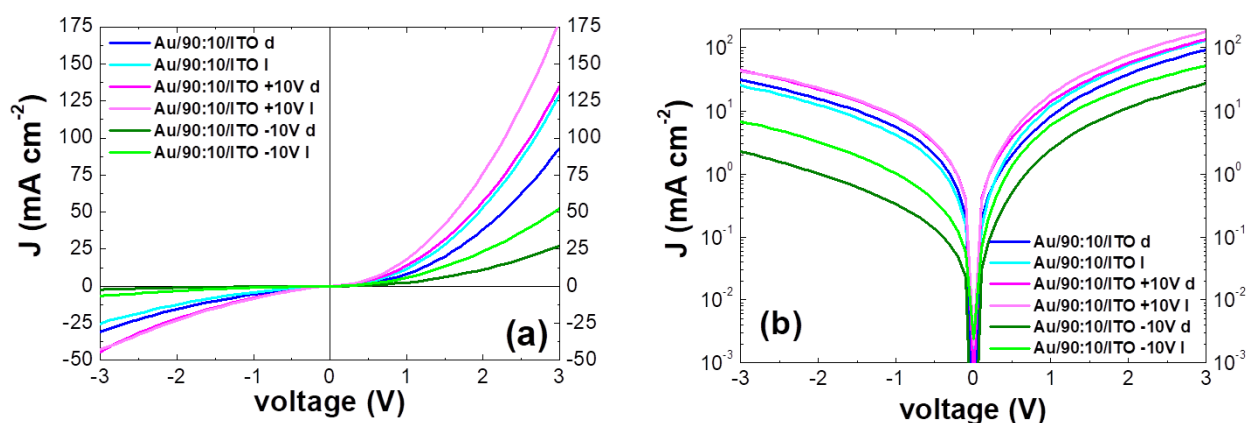


**Figure 6.12** (a)  $J$ - $V$  curves of the 90:10 pristine device, blue (dark current) and cyan (under light current) curves, compared with the  $J$ - $V$  curves of a positively poled 90:10 in dark (dark green) and under light (clear green) and compared with the  $J$ - $V$  curves of a negatively poled 90:10 in dark (dark pink) and under light (clear pink). (b) On the right the same graph with the  $y$  axis in log scale.

The positive and negative polarisation states have been achieved by applying, before the  $J$  vs  $V$  measurements, a DC bias of +10 V and of -10V respectively for a few minutes in order to drive the blend film into an “ON state” for a positively poled device, and to an “OFF-state” for a negatively poled device. Holes extraction occurs from the active layer to both electrodes. In this case, a positive polarisation will lead to a decreased injection barrier with Au and an

increased with ITO, while the negative one to an increased barrier with Au and increased with ITO. Considering a film thickness of 250 nm and knowing that approximately the  $E_c$  for P(VDF-co-TrFE) with a molar ratio of 75-25 is of  $50 \text{ MV m}^{-1}$  we can conclude that with 10 V we do not exceed the  $E_c$  in order to bring the *FE* film into a saturated forward or reversed polarisation state. We herein present this way to induce the preferred polarisation because we have tried different polarisation protocols by varying the voltages and it was found that exceeding 12.5V (voltage which corresponds to an  $E_c$  of  $50 \text{ MV m}^{-1}$  for a film of 250 nm) the device breaks down and short circuit occurs. This is expected, if we consider that we try to pole a sample that contains conducting pathways. In any case, we preferred to apply twice +10 V onto the same device and apply twice -10 V onto another device of the same sample, in order to induce different polarisation orientation and to compare their behaviour even though we do not reach a saturated polarisation. Indeed, even though not saturated polarisation is assured, we expect induce two different polarisation orientations.

A decrease of current density in the dark and under light is recorded after poling with a negative voltage (dark green and clear green in Figure 6.12) while for the device poled with a positive voltage an increase of dark J and light J is recorded (dark pink and clear pink in Figure 6.12) with respect to the not-poled device.

Defining the photocurrent,  $\Delta J$ , as the difference between the J measured under light and the J in the dark at a certain voltage:

$$\Delta J = \Delta(J_{light} - J_{dark}) \quad (6.2)$$

We have calculated  $\Delta J$  at +3V,  $\Delta J_{+3V}$ , and  $\Delta J$  at -3V  $\Delta J_{-3V}$ . The trends of  $\Delta J_{+3V}$  and  $\Delta J_{-3V}$  as a function of the device polarisation are shown in Figure 6.13. We can conclude that by positively poling the P(VDF-co-TrFE) the ferroelectric stray field increases the amount of current detected while, for a negative poling, J decreases. In any case, we do not detect any photovoltaic behaviour: the current is crossing at zero voltages, i.e the short circuit current density is zero.

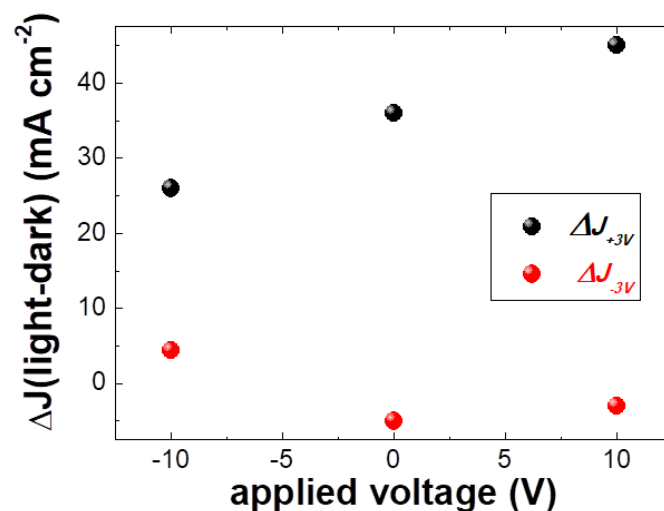


**Figure 6.13**  $\Delta(J_{light}-J_{dark})$  as a function of the negative poling (-10 V in the x-axis), positive poling (+10 V in the x-axis), and absence of poling (0 V in the x-axis).

In order to make a step further towards the photovoltaic application of this system we here present the results achieved for a more complex device configuration, that is a rectifying diode (Figure 6.14a). In particular we have deposited on top of ITO a thin film of PEDOT:PSS. After the spin coating of the blend film, a very thin layer of LiF (2nm) has been deposited before the Ag (80 nm) by means of thermal evaporation. In Figure 6.14a the schematic of the energy levels of the device are shown.

In Figure 6.14b the preliminary  $J$ - $V$  curves are presented. In Figure 6.14c the log scale clearly shows the asymmetry of the  $J$ - $V$  curves, i.e. the rectifying effect.

It is interesting to note that with this configuration the  $J$  recorded under illumination does not pass from zero and a  $J_{SC}$  can be recorded without need of polarising the  $FE$  polymer. A zoom of Figure 6.14c is shown in Figure 6.14d.

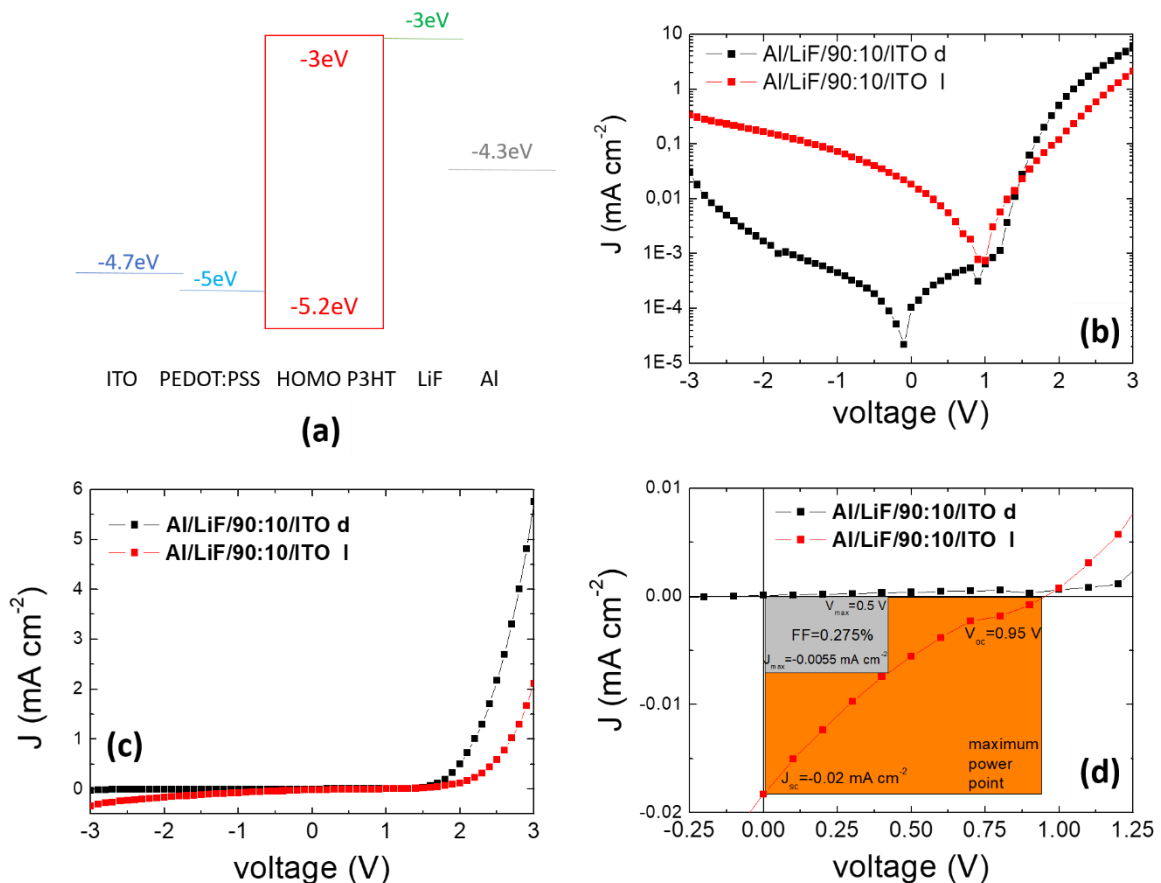


**Figure 6.14** (a) Schematic of the OPV device, J-V curves under dark and light of 90:10 blend films annealed at 135 °C for 15 min (black and red curves). (c) J-V graph with J in log scale, (d) zoom of the graph (b) with the  $J_{sc}$ ,  $V_{oc}$  and  $J_{max}$  and  $V_{max}$ .

As reminder in order to evaluate the performance of photovoltaic cells, current density vs voltage curves needs to be recorded during illumination. From this curve two parameters can be determined: the short-circuit current density,  $J_{sc}$ , i.e. the current at which the voltage across the “short-circuited” device is zero,<sup>13</sup> and the open circuit voltage,  $V_{oc}$ , i.e, the potential difference recorded at the terminals of the cell under illumination and in open circuit (for zero current). In Figure 6.14d the  $V_{oc}$  found is almost 1eV, which is quite high for a P3HT-based system (for P3HT:PCBM heterojunctions  $V_{oc}$  is around 0.6eV). The origin of this “un-expected good result” is unknown for the system.

The Fill Factor, FF, measures the device efficiency and is the power generated when JV is a maximum divided by  $J_{sc}V_{oc}$ .<sup>13</sup>

The equation 6.2 gives the power conversion efficiency  $\eta_p$  of an OPV device:

$$\eta_P = \frac{J_{SC}V_{OC}FF}{P_A} \quad (6.3)$$

Where  $P_A$  is the areal light power ( $\text{W m}^{-2}$ ) incident on the device.<sup>13</sup>

From the curve in Figure 6.14d we obtained a FF% of 0.275% and a power conversion efficiency  $\eta_P$  of 0.02%. The very low FF and the shape of the J vs V curve suggest that there are contact problems in the device that induce an important series resistance and a low parallel resistance. These problems normally are addressed by engineering the devices. However, the results we obtained give a proof of concept that such a phase separated FE-SC system could be employed for OPVs. Of course, it should be further investigated the correct way to induce polarisation on the FE matrix in such complex FE-SC system and it should be understood why a so high  $V_{OC}$  is detected. Furthermore, the J vs V shape further improved by eliminating the presence of the series resistances in the device. In any case these preliminary results could open the challenge of photovoltaic application of such a FE-SC blend.

## 6.4 Conclusions

The morphology of the FE-SC blend of P(VDF-co-TrFE) and rr-P3HT with different weight ratios, 95:5, 90:10 and 80:20 have been investigated by PFM, KPFM and C-AFM. We proved that the combinations of different SPM techniques are advantageous for a non-destructive reconstruction of 3D thin film morphology: an almost exhaustive comprehension of the phase-separated structure across the active layer thickness has been reached.

By means of PFM it has been confirmed that a phase separation occurs. The piezoelectric displacement recorded just for the matrix has proved that during phase separation the properties of each constituent are not affected. In particular P(VDF-co-TrFE) maintains its functional piezoelectric properties.

The SC phase was found to segregate as concave and convex semiconducting domains at the surface. By means of KPFM we conclude that, as already found for P(VDF-co-TrFE):rr-P3HT

blends, in P(VDF-co-TrFE):rr-P3HT blends, an increase of the size of the SC domains occurs with the increase of rr-P3HT content.

By means of CFM we were able to detect the SC pathways crossing the entire film thickness from the air-surface to the bottom interface. We noticed that the rr-P3HT percentage strongly influence the distribution of the SC pathways and that quite a lot of pathways are “blind”.

By means of KPFM we have described the presence of nearly superficial SC domains (at least until 100 nm below the air-film interface) for high P3HT contents, i.e. when the P3HT content exceeds 10%. Such networks were not detected with C-FM, which let us think that they are not involved in the current flow and therefore are buried under a dielectric layer. On the other hand, the 95:5 blend was found to generate a nanostructure where very few semiconducting pathways from the bottom to the top interfaces are formed. Then we conclude that the best ratio for organic electronic applications is the 90:10, in terms of SC domain size and number of SC pathways.

Next, devices with different weight ratio active layers have been fabricated and characterised by recording their respective  $J$  vs  $V$  curves in dark and under irradiation in order to evaluate their potential use as OPV devices. Our results show that such system could be promising for OPVs applications. Even though our results are just preliminary and very low values of efficiency have been found, they represent a proof of concept that such a system could be exploited as active layer in solar cells. Future studies on the way to achieve an ordered and controlled 3D-phase separated nanostructure along the entire thickness are requested for understanding the morphological influences to the performance in view of a device efficiency optimisation. Moreover, investigations on the appropriate way to induce polarisation of the FE matrix in presence of the semiconducting material is required. If the opened questions will be answered the P(VDF-co-TrFE):rrP3HT blend could represent itself the new active layer in OPVs.

## References

- 1 Yu, G., Gao, J., Hummelen, J. C., Wudl, F. & Heeger, A. J. Polymer Photovoltaic Cells: Enhanced Efficiencies via a Network of Internal Donor-Acceptor Heterojunctions. *Science* **270**, 1789-1791, doi:10.1126/science.270.5243.1789 (1995).
- 2 Pei, Q., Yu, G., Zhang, C., Yang, Y. & Heeger, A. J. Polymer Light-Emitting Electrochemical Cells. *Science* **269**, 1086-1088, doi:10.1126/science.269.5227.1086 (1995).
- 3 Arias, A. C., Endicott, F. & Street, R. A. Surface-Induced Self-Encapsulation of Polymer Thin-Film Transistors. *Advanced Materials* **18**, 2900-2904, doi:10.1002/adma.200600623 (2006).
- 4 Asadi, K., De Leeuw, D. M., De Boer, B. & Blom, P. W. M. Organic non-volatile memories from ferroelectric phase-separated blends. *Nat. Mater.* **7**, 547-550, doi:10.1038/nmat2207 (2008).
- 5 Asadi, K., de Boer, T. G., Blom, P. W. M. & de Leeuw, D. M. Tunable Injection Barrier in Organic Resistive Switches Based on Phase-Separated Ferroelectric–Semiconductor Blends. *Advanced Functional Materials* **19**, 3173-3178, doi:10.1002/adfm.200900383 (2009).
- 6 Kang, S. J. *et al.* Printable Ferroelectric PVDF/PMMA Blend Films with Ultralow Roughness for Low Voltage Non-Volatile Polymer Memory. *Advanced Functional Materials* **19**, 2812-2818, doi:10.1002/adfm.200900589 (2009).
- 7 Li, M. *et al.* Processing and Low Voltage Switching of Organic Ferroelectric Phase-Separated Bistable Diodes. *Advanced Functional Materials* **22**, 2750-2757, doi:10.1002/adfm.201102898 (2012).
- 8 Khan, M. A. *et al.* High-Performance Ferroelectric Memory Based on Phase-Separated Films of Polymer Blends. *Advanced Functional Materials* **24**, 1372-1381, doi:10.1002/adfm.201302056 (2014).
- 9 Costa, C. M. *et al.* Novel poly(vinylidene fluoride-trifluoroethylene)/poly(ethylene oxide) blends for battery separators in lithium-ion applications. *Electrochimica Acta* **88**, 473-476, doi:https://doi.org/10.1016/j.electacta.2012.10.098 (2013).

- 10 Su, G. M., Lim, E., Kramer, E. J. & Chabynyc, M. L. Phase Separated Morphology of Ferroelectric–Semiconductor Polymer Blends Probed by Synchrotron X-ray Methods. *Macromolecules* **48**, 5861-5867, doi:10.1021/acs.macromol.5b01354 (2015).
- 11 Khikhlovskiy, V. *et al.* Nanoscale Organic Ferroelectric Resistive Switches. *The Journal of Physical Chemistry C* **118**, 3305-3312, doi:10.1021/jp409757m (2014).
- 12 Khikhlovskiy, V. *et al.* 3D-morphology reconstruction of nanoscale phase-separation in polymer memory blends. *Journal of Polymer Science Part B: Polymer Physics* **53**, 1231-1237, doi:10.1002/polb.23769 (2015).
- 13 Geoghegan, M., & Hadziioannou, G. . Polymer electronics. *Oxford*, doi:10.1093/acprof:oso/9780199533824.001.0001 (2013).
- 14 Scott, J. F. Ferroelectric memories today. *Ferroelectrics* **236**, 247-258 (2000).
- 15 Blom, P. W. M., Wolf, R. M., Cillessen, J. F. M. & Krijn, M. P. C. M. Ferroelectric Schottky Diode. *Physical Review Letters* **73**, 2107-2110, doi:10.1103/PhysRevLett.73.2107 (1994).
- 16 Dawber, M., Rabe, K. M. & Scott, J. F. Physics of thin-film ferroelectric oxides. *Reviews of Modern Physics* **77**, 1083-1130, doi:10.1103/RevModPhys.77.1083 (2005).
- 17 Naber, R. C. G., Asadi, K., Blom, P. W. M., De Leeuw, D. M. & De Boer, B. Organic nonvolatile memory devices based on ferroelectricity. *Advanced Materials* **22**, 933-945, doi:10.1002/adma.200900759 (2010).
- 18 Kemerink, M., Asadi, K., Blom, P. W. M. & de Leeuw, D. M. The operational mechanism of ferroelectric-driven organic resistive switches. *Organic Electronics* **13**, 147-152, doi:https://doi.org/10.1016/j.orgel.2011.10.013 (2012).
- 19 McNeill, C. R., Asadi, K., Watts, B., Blom, P. W. M. & de Leeuw, D. M. Structure of Phase-Separated Ferroelectric/Semiconducting Polymer Blends for Organic Non-volatile Memories. *Small* **6**, 508-512, doi:10.1002/smll.200901719 (2010).
- 20 Asadi, K. *et al.* Spinodal Decomposition of Blends of Semiconducting and Ferroelectric Polymers. *Advanced Functional Materials* **21**, 1887-1894, doi:10.1002/adfm.201001505 (2011).
- 21 Asadi, K., De Leeuw, D. M., De Boer, B. & Blom, P. W. M. Organic non-volatile memories from ferroelectric phase-separated blends. *Nature Materials* **7**, 547-550, doi:10.1038/nmat2207 (2008).

- 22 Martínez-Tong, D. E. *et al.* Laser Fabrication of Polymer Ferroelectric Nanostructures for Nonvolatile Organic Memory Devices. *ACS Applied Materials & Interfaces* **7**, 19611-19618, doi:10.1021/acsami.5b05213 (2015).
- 23 Lacroix, C. *Etude des mélanges de polymères semi-conducteur / ferroélectrique en films minces : application en électronique organique.*, Université de Bordeaux, (2014).
- 24 Shyam S. Pandey *et al.* Regioregularity vs Regiorandomness: Effect on Photocarrier Transport in Poly(3-hexylthiophene). *Japanese Journal of Applied Physics* **39**, L94 (2000).
- 25 Melitz, W., Shen, J., Kummel, A. C. & Lee, S. Kelvin probe force microscopy and its application. *Surface Science Reports* **66**, 1-27, doi:https://doi.org/10.1016/j.surfrep.2010.10.001 (2011).
- 26 Liscio, A. *et al.* Local Surface Potential of  $\pi$ -Conjugated Nanostructures by Kelvin Probe Force Microscopy: Effect of the Sampling Depth. *Small* **7**, 634-639, doi:10.1002/sml.201001770 (2011).
- 27 Tang, C. W. Two-layer organic photovoltaic cell. *Applied Physics Letters* **48**, 183-185, doi:10.1063/1.96937 (1986).
- 28 Ma, W., Yang, C., Gong, X., Lee, K. & Heeger, A. J. Thermally Stable, Efficient Polymer Solar Cells with Nanoscale Control of the Interpenetrating Network Morphology. *Advanced Functional Materials* **15**, 1617-1622, doi:10.1002/adfm.200500211 (2005).
- 29 Yuan, Y. *et al.* Efficiency enhancement in organic solar cells with ferroelectric polymers. *Nature Materials* **10**, 296, doi:10.1038/nmat2951https://www.nature.com/articles/nmat2951#supplementary-information (2011).
- 30 Yuan, Y. *et al.* Understanding the effect of ferroelectric polarization on power conversion efficiency of organic photovoltaic devices. *Energy & Environmental Science* **5**, 8558-8563, doi:10.1039/c2ee22098a (2012).
- 31 Yang, B. *et al.* Tuning the Energy Level Offset between Donor and Acceptor with Ferroelectric Dipole Layers for Increased Efficiency in Bilayer Organic Photovoltaic Cells. *Advanced Materials* **24**, 1455-1460, doi:10.1002/adma.201104509 (2012).

- 32 Sun, K. *et al.* High-performance polymer solar cells with a conjugated zwitterion by solution processing or thermal deposition as the electron-collection interlayer. *Journal of Materials Chemistry* **22**, 24155-24165, doi:10.1039/c2jm35221d (2012).
- 33 Yuan, Y., Xiao, Z., Yang, B. & Huang, J. Arising applications of ferroelectric materials in photovoltaic devices. *Journal of Materials Chemistry A* **2**, 6027-6041, doi:10.1039/c3ta14188h (2014).
- 34 Yang, B. *et al.* Tuning the Energy Level Offset between Donor and Acceptor with Ferroelectric Dipole Layers for Increased Efficiency in Bilayer Organic Photovoltaic Cells. *Adv. Mater.* **24**, 1455-1460, doi:10.1002/adma.201104509 (2012).
- 35 Nalwa, K. S. *et al.* Enhanced charge separation in organic photovoltaic films doped with ferroelectric dipoles. *Energy Environ. Sci.* **5**, 7042-7049, doi:10.1039/c2ee03478f (2012).
- 36 Chua, L.-L. *et al.* General observation of n-type field-effect behaviour in organic semiconductors. *Nature* **434**, 194, doi:10.1038/nature03376 <https://www.nature.com/articles/nature03376#supplementary-information> (2005).
- 37 Sung, S. H. & Boudouris, B. W. Systematic Control of the Nanostructure of Semiconducting-Ferroelectric Polymer Composites in Thin Film Memory Devices. *ACS Macro Letters* **4**, 293-297, doi:10.1021/mz5007766 (2015).

# Chapter 7

*General conclusions*



## 7 General conclusions

In this Thesis the relations between structure and ferroelectric properties of P(VDF-co-TrFE) copolymers have been investigated with the aim of achieving a complete understanding of the properties necessary for existing applications and enabling new ones.

The first challenge of this Thesis was to define the “cold crystallisation” annealing conditions (normally used for organic electronic devices) that lead to best ferroelectric properties in terms of high remnant polarisation  $P_r$  and low coercive electric field  $E_c$  that was discussed in **Chapter 2**. Optimal ferroelectric response, in terms of a high  $P_r$  and a low  $E_c$ , has been achieved when thermal processing that takes place in the temperature range between 133 °C and 137 °C for 15 to 30 minutes annealing time. Our results proved that the 2 h-long annealing time step, traditionally applied is not necessary, but just 15 minutes are enough. Additionally, it arose that annealing temperature affects mostly the remnant polarisation value, while annealing time has a severe effect on the coercive field value. The enhanced performance achieved under these conditions has been rationalised through GIWAXS studies that revealed the crystalline phases apparent in these films and allowed the calculation of the degree of crystallinity. It is shown that a high degree of crystallinity is necessary as well as an edge-on orientation of the crystallites for an improved performance. Moreover, through a deconvolution study we discuss the existence of a moderately unstable ferroelectric phase  $F_{1-2}$  that facilitates ferroelectric switching through easier rotation of dipoles along the chain. The best performing structure exhibits a high degree of crystallinity, a preferential orientation of the crystallites with the polymer chains parallel to the substrate and the occurrence of three ferroelectric phases.

In **Chapter 3** we unravelled the polymorphism by following the structural transitions changes at which the ferroelectric polymer P(VDF-co-TrFE) undergoes by means of time-resolved WAXS and DSC employing an isothermal melt crystallisation protocol. Different isothermal crystallisation temperatures have been studied. With this study we were the first to describe the appearance of defective phases in pristine samples, before any annealing over the  $T_{Curie}$  is performed. By following the heating and cooling ramps of the melt-crystallisation

protocol three crystallisations were found to occur: before the isothermal crystallisation, during (obviously) the isothermal step, and immediately after the isothermal crystallisation. An overall increase of the crystallinity degree arises when  $T_c$  increases. Once, after crystallisation, the paraelectric crystallites are formed, during cooling at the Curie transition range they were found to convert into a  $F_1$  most ordered (directly formed with the lattice parameters typical of the ferroelectric phase), and the very disordered  $F_2$ . The asymmetry of the scattering peak assigned to the  $F_1$  phase, at  $1.4 \text{ \AA}^{-1}$  suggests the appearance of  $F_{1-2}$  intermediately ordered phase as found in Chapter 2, even though from the WAXS data we do not have any evidence of how this intermediate phase originates.

Nevertheless, the crystallinity degree has been proven to increase with the increase of  $T_c$  and consequently to be higher among all samples for the samples annealed at the higher  $T_c$  a non-optimal ferroelectric performance was detected. We attribute this decrease of the performances to a possible high content of the highly defective  $F_2$ , which undermines the ferroelectric switching. However, deconvolution studies of the GIWAXS peaks are in perspective work since are required for confirming the hypothesis herein proposed.

We conclude that the correlations between structural phases and performance need to be searched in the intramolecular rotational during poling. Indeed, when we do apply an electric field to a P(VDF-co-TrFE) copolymer we are inducing rotation along the chains for aligning the dipoles. As proposed in Chapter 2 the intermediate phase, the  $F_{1-2}$ , would favour more than a perfect ferroelectric phase the intramolecular rotation thanks to the presence of few gauche defects that acts as activation sites for the rotation to begin. On the other hand, a too defective phase  $F_2$  is expected to show some dipoles orientation, which in any case will not reach the degree of that of the  $F_1$  and  $F_{1-2}$  leading to a decrease in the performances.

In **Chapter 4** the effect of the crystallite orientation has been thoroughly investigated. Indeed, the link between polarisation and dipoles orientation within the crystallite points out that the crystallite orientation with respect to the applied electric field is fundamental to help the alignment and get after poling the maximum density of charges at the surface. In Chapter 4 we have quantified the impact of crystallite orientation on the ferroelectric properties by inducing various crystallite orientations through a variation of thermal protocol. We found that through melt-crystallisation, randomly oriented crystallites, or preferentially face-on oriented are formed. The sample that underwent to an isothermal cold crystallisation was

found to exhibit the highest amount of edge-on crystallites (~75%) among all and this was found to be related with the better ferroelectric response. The ferroelectric parameters indeed were found to strongly depend on the orientation of the crystallites: a higher  $P_r$ , lower  $E_c$  and a faster polarisation switching are found for a high edge-on amount. From dielectric spectroscopy investigations at different temperatures we have found that a cold crystallised sample exhibits lower dipoles relaxation activation energy with a decreased  $f_m$  of the FE-to-PE relaxation as compared to the melt-crystallised samples due to an edge on orientation. From dielectric spectroscopy investigations at different temperatures we have found that an increased activation energy of the dipoles relaxation, simultaneously with a decreased  $f_m$  of the FE-to-PE relaxation occurs when we go from a preferentially edge on oriented sample to a preferentially face-on sample. This suggests that the face-on orientation acts as defective parameter, hindering dipoles relaxations.

Finally, two applications of P(VDF-*co*-TrFE) in organic electronics have been explored in this Thesis. The first one concerns the implementation of P(VDF-*co*-TrFE) in medical piezoelectric sensors for laparoscopic training. The second concerns the use of P(VDF-*co*-TrFE) copolymers in photovoltaic devices.

In **Chapter 5** we discussed the advancement achieved within the chair of the project named “sweet heart” conducted in collaboration with the research centre *Liryc* (*L’Institut de Rythmologie et modélisation Cardiaque*). The objective is to fabricate a flexible matrix of piezoelectric sensors that could be encapsulated in the inner part of a 3D-printed heart for laparoscopic training. After having tried several approaches we succeeded in fabricating highly flexible piezoelectric sensors by thermally evaporating metallic silver electrodes on top of thick PDMS substrates and encapsulating a P(VDF-*co*-TrFE) film between them. The characterisation of this system is in a perspective work and concerns the resolution of the issues linked to the electronic conversion of the out-put voltage signals and their amplification. The above will furnish a proper sensor for laparoscopic medical simulation.

Finally, in **Chapter 6** we investigate a second application where a more complex structure than that of a simple capacitor was studied: devices in which P(VDF-*co*-TrFE) is blended with the semiconducting (SC) polymer P3HT. P(VDF-*co*-TrFE):P3HT blends form a phase separated active layer. Morphology at the nanoscale of different weight ratios (95:5, 90:10, 80:20) was thoroughly characterised by means of several scanning probe microscopy techniques such as

AFM, PFM, KPFM, CFM. By means of PFM was confirmed that a phase separation occurs without affecting the properties of each constituent component of the blend. In particular P(VDF-co-TrFE) maintains its functional piezoelectric properties. Moreover, semiconducting phase with the absence of piezoelectric response has been observed as concave and convex domains at the surface.

Combining KPFM and CFM we noticed that the rr-P3HT (a semiconductor polymer) percentage strongly influence the distribution of the SC paths. By means of KPFM we unravelled the appearance of nearly superficial SC networks (at least until 100 nm below the air-film interface) when the P3HT weight percentage exceeds the 10%. Such networks were not detected with CFM, therefore they do not act as semiconducting path. We concluded that the best ratio for organic electronic applications is the 90:10, in terms of SC domain size and reproducibility of the nanostructure. Photovoltaic devices have been fabricated and characterised by recording their respective  $J$ - $V$  curves in darkness and under light in order to evaluate the difference in their electrical behaviour. Even though our results are just preliminary they represent a “proof of concept” that such a system could be exploited in OPVs.

# Chapter 8

*Annex*



## 8 Annex

In this chapter we will first describe the materials, used in this Thesis. Then we will move to the thin films preparation and the devices fabrication details. The performed thermal treatments will be quickly summarised and finally the characterisation techniques will be described.

### 8.1 Materials

#### 8.1.1 P(VDF-co-TrFE)

The random copolymers P(VDF-co-TrFE) investigated in this thesis have been provided by courtesy of Piezotech® FC (France). We focused our study on P(VDF-co-TrFE) with VDF/TrFE molar ratios of 75/25 and 70/30 that have been largely studied due to their high remnant polarisation. The chemical structure of P(VDF-co-TrFE) copolymers is shown below (Figure 8.1).

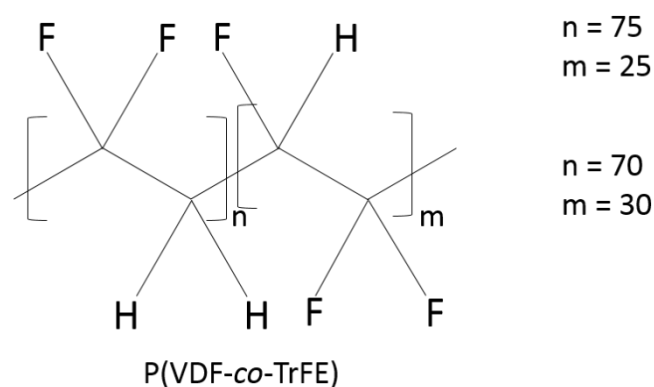


**Figure 8.1** P(VDF-co-TrFE) chemical structure.

Both P(VDF-co-TrFE) with the two VDF/TrFE molar ratios of 75/25 and of 70/30 used in this Thesis have a  $M_w \approx 400$  kDa.

### 8.1.2 P3HT

Regioregular rr-P3HT with a  $M_w$  of 610 kDa and a regioregularity of 96 %, was synthesised in our Laboratory by a former PhD student, Laurie Parrenin, according to Grignard metathesis method (GRIM)<sup>1,2</sup> polymerisation and then spin-coated and piled off in order to obtain films.

## 8.2 Thin films preparation

Every steps of the sample preparation as substrates cleaning, thin films deposition and thermal annealing were performed in a standard class 10.000 clean room with a relative humidity of 45 %.

Silicon, ITO and glass substrates (having a size of 15 mm x 15 mm) were thoroughly cleaned by successive sonication in acetone, ethanol and isopropanol for 20 minutes each and dried with compressed air.

### 8.2.1 P(VDF-co-TrFE) thin films

10<sub>wt%</sub> solutions of P(VDF-co-TrFE) with a 75/25 and a 70/30 VDF/TrFE molar ratios were obtained by dissolving the powders in cyclopentanone (SIGMA-Aldrich) which was used as received without any further purification. The solutions were then filtered with a 1  $\mu$ m PTFE filter.

150  $\mu$ L of solution were spin-coated on substrates of different nature in function of the forecast characterisation: Si substrates have been used for GIWAXS analysis, while Al/glass substrates for the fabrication of capacitors in view of the ferroelectric characterisation.

The spin-coating parameters were modulated in order to obtain P(VDF-co-TrFE) film with a thickness of 1  $\mu$ m and as measured by profilometry (BRUKER DEKTAK XT-A). In particular, this thickness was obtained for a 10<sub>wt%</sub> solution by using an rpm (rate per minutes) of 1000, with an acceleration of 500 rpm s<sup>-1</sup>, for 30 seconds.

Immediately after spin-coating deposition, a first thermal treatment at 40 °C to facilitate the solvent evaporation was carried out for 5 minutes.

### 8.2.2 P(VDF-*co*-TrFE):P3HT thin films

P(VDF-*co*-TrFE) with a VDF/TrFE molar ratio of 75/25 and rr-P3HT were co-dissolved in tetrahydrofuran, THF, at a total concentration in weight of 25 mg ml<sup>-1</sup>. Tetrahydrofuran THF (SIGMA-Aldrich) was used as received without any further purification. Three weight ratios of P(VDF-*co*-TrFE):rr-P3HT have been prepared: 95:5, 90:10 and 80:20 <sub>wt/wt</sub>. The dissolution was achieved by sonication at 55 °C for 3 hours. 200µL of each solution have been spin-coated onto cleaned glass and ITO substrates with an rpm (rate per minutes) of 3000 with a rpm s<sup>-1</sup> of 1000 for 90 seconds, obtaining a film thickness of ≈ 250 nm, as measured by profilometry (BRUKER DEKTAK XT-A).

## 8.3 Capacitor fabrication

Aluminium electrodes were thermally evaporated onto clean glass substrates to form 100 nm thick bottom electrodes (in inert atmosphere at 10<sup>-6</sup> mbar by means of ME400B PLASSYS evaporator) that were subsequently coated with the P(VDF-*co*-TrFE) films. 100 nm thick top Al electrodes were finally thermally evaporated. The temperature inside the evaporator was kept below 70 °C, i.e. below the Curie transition temperature, to avoid undergoing the ferroelectric-to-paraelectric transition. The thermal treatment of P(VDF-*co*-TrFE) has been conducted on the devices (i.e. after top electrode deposition) following the procedure described below.

## 8.4 Thermal treatment

The films were heated on a precision hot plate with a rate of  $5\text{ }^{\circ}\text{C min}^{-1}$  starting from room temperature until the temperature of choice. In particular, it has been performed:

- An isothermal steps of 15 minutes at  $130\text{ }^{\circ}\text{C}$ ,  $133\text{ }^{\circ}\text{C}$ ,  $135\text{ }^{\circ}\text{C}$ ,  $137\text{ }^{\circ}\text{C}$ ,  $140\text{ }^{\circ}\text{C}$ , or at  $135\text{ }^{\circ}\text{C}$  along 5, 15, 30, 60, 120 minutes, for the cold crystallisation study.
- An isothermal step at  $165\text{ }^{\circ}\text{C}$  for 5 minutes, followed by a fast cooling to the  $129\text{ }^{\circ}\text{C}$ ,  $131\text{ }^{\circ}\text{C}$ ,  $133\text{ }^{\circ}\text{C}$ ,  $135\text{ }^{\circ}\text{C}$ ,  $137\text{ }^{\circ}\text{C}$  and  $140\text{ }^{\circ}\text{C}$ . At each temperature an isothermal step of 15 minutes has been carried for the melt crystallisation study.
- An isothermal step at  $165\text{ }^{\circ}\text{C}$  for 15 minutes, followed by a quenching step through immersion of the sample in liquid nitrogen and an isothermal annealing at  $135\text{ }^{\circ}\text{C}$  for 15 minutes, for the melt quenched crystallised sample.

After every final isothermal steps the samples were cooled down to room temperature slowly, with a cooling rate of  $1.6\text{ }^{\circ}\text{C min}^{-1}$  on the same hot stage.

## 8.5 Techniques

### 8.5.1 Spin-coating deposition technique

Spin coating is one of the most common techniques for depositing polymer solutions into uniform thin films. The advantage of spin coating is its ability to quickly and easily produce very uniform films, ranging from a few nanometres to a few microns in thickness on solid, flat or slightly curved substrates.<sup>3</sup> The instrument is relatively simple, consisting of a small rotating support with a hole in the centre through which a vacuum depression allows to keep the substrate attached to the support during the spinning process (Figure 8.2).

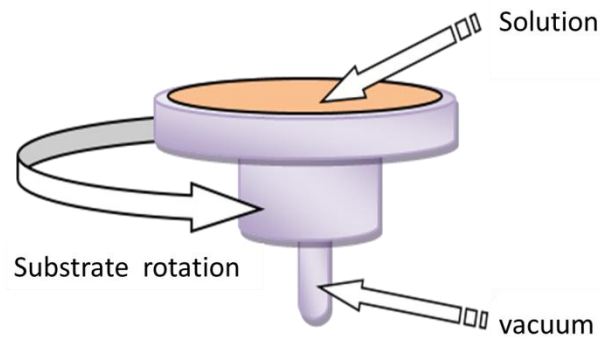


**Figure 8.2** Schematic of a spin coater.

A polymer, usually solubilised in a highly volatile solvent, is spread onto the substrate that is let to rapidly rotate at a constant acceleration rate until the desired rotation speed (Figure 8.3). The solution flows radially on the surface of the substrate and covers it uniformly thanks to the centrifugal force which pushes out the excess of solution and allows the thinning of the deposited film.

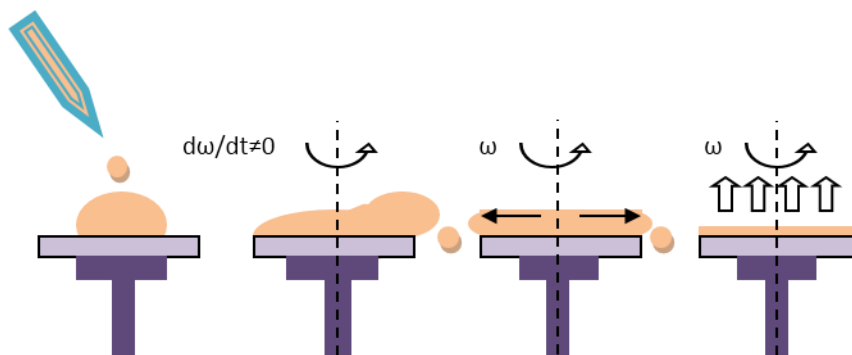


**Figure 8.3** Spin-coating steps: deposition, acceleration, rotation at a constant speed, rotation at a constant speed and evaporation of the solvent.  $d\omega/dt$  is the acceleration and  $\omega$  the rotational speed.

By varying parameters such as the rotation speed and/or the polymer solution concentration, it is possible to modulate the thickness of the film.

At the end of the process, only about 10% of solvent remains, which can be removed by a subsequent annealing phase.

### 8.5.2 Profilometer

The thickness of the thin films has been measured by means of a profilometer Bruker Dektak XT-A. A tip is let to scan the surface across a scratch previously created. The difference between the height of the film and the height of the substrate gives the thickness of the film. Several measurements are performed in order to decrease the error in the evaluation.

### 8.5.3 Differential Scanning Calorimetry (DSC)

The thermal analysis experiments were carried out by using a TA Instrument DSC Q100 RCS and LN2 with time/Temperature modulation, under the continuous flux of helium or azote. Tens of milligrams are used for DSC experiments. An aluminium capsule is filled with the sample to analyse, while an empty one is used as reference.

DSC curves were obtained for P(VDF-co-TrFE) powder having VDF/TrFE ratio of a) 75/25 (Chapter 2 and Chapter 4) and 70/30 (Chapter 3). DSC curves were recorded from RT to 180 °C-200 °C at a heating/cooling rate of 10 °C min<sup>-1</sup> and b) on free standing films of P(VDF-co-TrFE) having VDF/TrFE ratio of 75/25 prepared by drop-casting (Chapter 2).

Concerning the powder sample, a first heating ramp was used to erase thermal history; however, in the main text we presented the first cooling and the second heating ramps, in consistence with common practice.

Concerning the freestanding samples, they were heated in the DSC crucible from room temperature until the respective crystallisation temperature with a rate of 5 °C min<sup>-1</sup>. Then an isothermal step has been conducted at the crystallization temperature for 15 min, and then a cooling ramp has been performed with a rate of 2 °C min<sup>-1</sup>, until room temperature. This sequence mimics the preparation conditions used for the films under study. The heating and cooling rates correspond to those of the hot plate used for thermal processing. Right after, a second heating cycle has been performed from room temperature to 200 °C at a rate of 10 °C min<sup>-1</sup>. The DSC curves presented in Chapter 2 have been recorded during the second heating ramp.

The transition temperatures as the Curie point upon heating and the Curie point under cooling, the melting point and crystallisation temperature of the two molecular weight ratios 75/25 and 70/30 were evaluated for Figure 8.4.

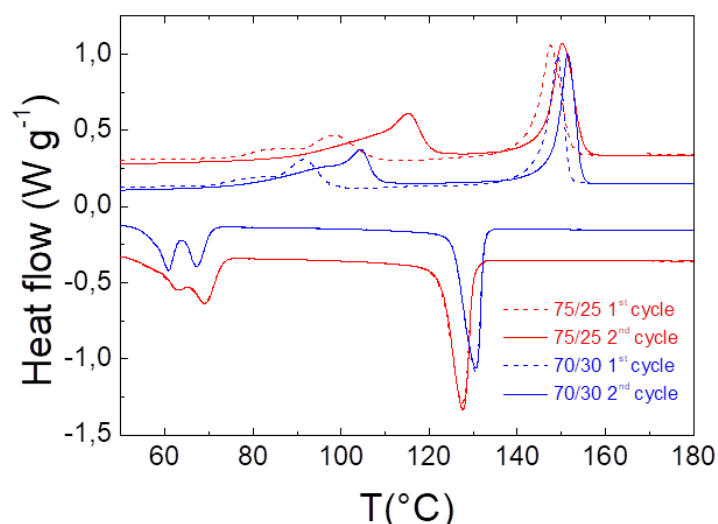


**Figure 8.4** 1<sup>st</sup> heating and 1<sup>st</sup> cooling (dashed lines) and 2<sup>nd</sup> heating and 2<sup>nd</sup> cooling (full lines) DSC curves for the P(VDF-co-TrFE) with VDF/TrFE molar ratio of 75/25 (red curves) and of 70/30 powder (blue curves).

#### 8.5.4 Grazing incidence Wide Angle X-ray scattering (GIWAXS)

Grazing incidence X-ray scattering (GIXS) provides information about the morphology of active materials and thin film layers. The X-ray beam impinges onto the sample surface with a shallow incident angle  $\alpha_i < 1^\circ$ .<sup>4</sup> The scattered intensity can be collected under a small exit angle  $\alpha_f$  (grazing incidence small angle X-ray scattering GISAXS) or as in the case of GIWAXS under a wide exit angle  $\alpha_f$  as shown in Figure 8.5.<sup>4</sup> Indeed the difference between GIWAXS and GISAXS stands in the sample-to-detector distance which is shorter in the case of GIWAXS and thus diffraction maxima at larger angles are observed. The beam interacts with the sample structure, giving rise to scattering features such as peaks and diffuse scattering. The scattering from the sample is then recorded with a 2D X-ray detector.<sup>4</sup> GIWAXS is sensitive to the crystalline parts and allows for the determination of the crystal structure and the orientation

of the crystalline regions with respect to the electrodes. Analysis of the 2D scattering pattern enables quantification of crystallinity degree of thin films as shown in this thesis.

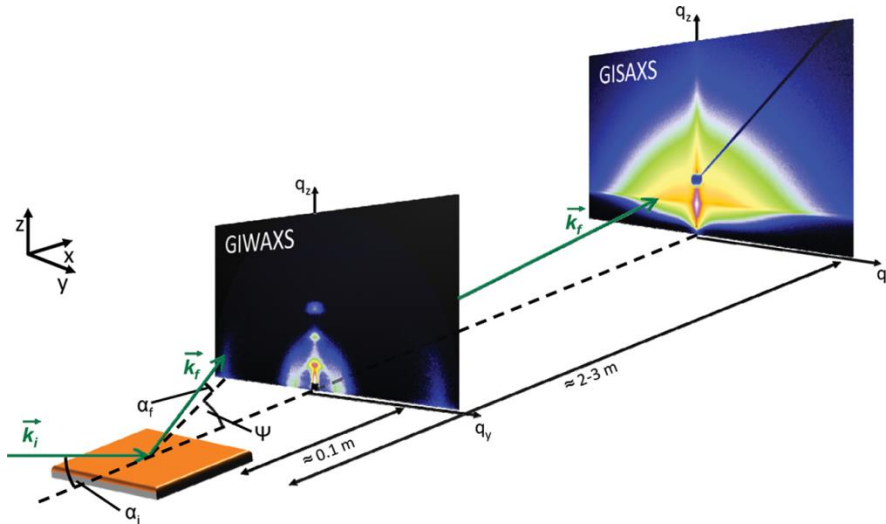


**Figure 8.5** GIXS experiment. The incident beam strikes the sample under a small angle  $\alpha_i$  close to the critical angle of total external X-ray reflection. The diffuse scattering with an angle  $\alpha_f$  and an out-of plane  $\psi$  angle from the sample is recorded with an area detector. Example of GISAXS and GIWAXS pattern for a thin film are shown. Reported from reference <sup>4</sup>

For GIWAXS measurements, the P(VDF-co-TrFE) films were spin-coated on silicon substrates. The GIWAXS experiments have been performed at the Dutch-Belgian beamline (DUBBLE CRG, station BM26B) of the European Synchrotron Radiation Facility (ESRF) in Grenoble, France.<sup>5</sup> X-rays photons with 12 keV energy were used and the sample-to-detector distance was set at 8 cm. The angle of incidence  $\alpha_i$  was set at  $0.15^\circ$ , slightly above the polymer critical angle to allow full penetration of the polymer film. The diffracted intensity was recorded by a Frelon CCD camera and was normalized by the incident photon flux and the acquisition time (30 s). Flat field, polarization, solid angle and efficiency corrections were subsequently applied to the 2D GIWAXS images.<sup>4</sup> The scattering vector  $q$  was defined with respect to the centre of the incident beam and has a magnitude of  $q = (4\pi/\lambda)\sin(\theta)$ , where  $2\theta$  is the scattering angle and  $\lambda$  is the wavelength of the x-ray beam (here  $\lambda=1.033 \text{ \AA}$ ). We opted to present the wedge-shaped corrected images where  $q_r$  and  $q_z$  are the in-plane and near out-of-plane scattering vectors, respectively. The scattering vectors are defined as follows:  $q_x =$

$(2\pi/\lambda)(\cos(2\theta_f)\cos(\alpha_f)-\cos(\alpha_i))$ ,  $q_y=(2\pi/\lambda)(\sin(2\theta_f)\cos(\alpha_f))$ ,  $q_z=(2\pi/\lambda)(\sin(\alpha_f)+\sin(\alpha_i))$ ,  $q^2=q_x^2+q_y^2$ , and  $q^2=q_r^2+q_z^2$ , where  $\alpha_f$  is the exit angle in the vertical direction and  $2\theta_f$  is the in-plane scattering angle, in agreement with standard GIWAXS notation.<sup>6</sup>

In addition, the crystallites structural coherence length  $L_{\text{coherence}}$  has been calculated by using a modified Scherrer's equation:  $L_{\text{coherence}}=(2\pi K)/\Delta q_{\text{hkl}}$ <sup>7</sup> where  $K$  is the Scherrer's constant ( $K\approx 0.93$ )<sup>7</sup> and  $\Delta q_{\text{hkl}}$  is the FWHM of the peak, in our case we have considered the deconvoluted peak.

### 8.5.5 Scanning Probe Microscopies: AFM, PFM, KPFM and CFM

Atomic force microscopy, AFM, Piezoresponse Force Microscopy, PFM, Kelvin Probe Force Microscopy, KPFM, and Conductive Force Microscopy, CFM, were performed with the Dimension FastScan, Bruker.

Atomic force microscopy is a high-resolution scanning probe microscopy technique for nanoscale imaging, measuring and manipulating surface features. The AFM principle is based on the interaction between a tip, mounted on a flexible cantilever, and the superficial atoms of the sample. The tip, usually in silicon nitride, and the reflective cantilever constitute the probe. This mechanical probe scans the surface generating attractive or repulsive forces between a tip and the sample surface. Since the cantilever obeys Hooke's law for small displacements, the strength of the interaction between the tip and the sample can be derived. The movement of the tip or of the sample is performed through an extremely precise position device obtained from piezoelectric ceramic materials that act as guides of the movement itself. A laser beam is focused on the reflective cantilever (Figure 8.6). While the tip scans the sample surface it deflects following the surface features and the laser beam focused on the cantilever is recoiled. Different interactions between the tip and the sample surface generate a difference in the intensity of the reflected light. A photodetector records such difference and the signal is sent off to the controller feedback loop which keeps the cantilever deflection constant by maintaining a constant distance between the cantilever and the sample. This is done by applying a voltage to the piezoelectric scanner which moves in the Z direction at each point.

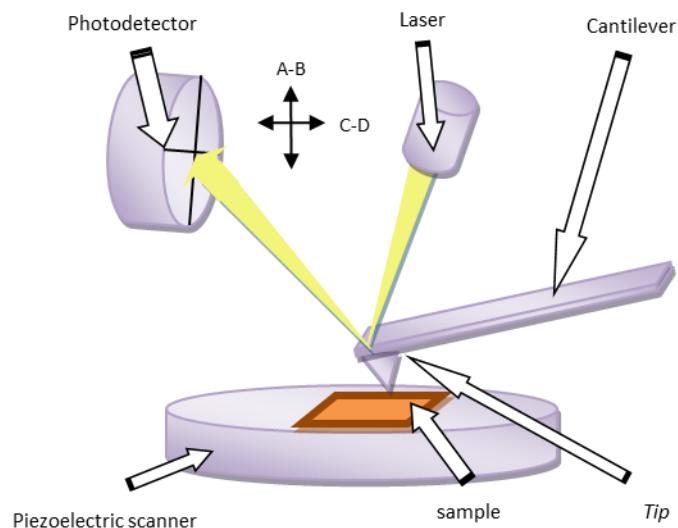


**Figure 8.6** Schematic illustration of the AFM cantilever work.

Depending on the type sample-tip interaction, there are three operation modes: contact mode, non-contact mode and tapping mode. In contact mode, the tip constantly touches the sample surface and scans across the surface. The contact mode microscopy gives an accurate image with high resolution, but both the sample and the tip may be damaged due to the direct contact. Such damage can be avoided by using non-contact mode; however, the resolution is decreased. Hence, the tapping mode, a combination of contact and non-contact mode, appears to be a good solution. In tapping mode, the tip is alternatively placed in contact with the surface to provide a high resolution and lifted above the surface to avoid dragging the tip across the surface. The cantilever oscillates close to its resonant frequency with an amplitude between 20 and 100 nm.

AFM was used in tapping mode to characterise the surface morphology of the films. Silicon cantilevers (Fastscan-A) with a typical tip radius of  $\approx 5$  nm, a spring constant of  $18 \text{ N m}^{-1}$  and a cantilever resonance frequency of about 1,4 MHz were used. Two responses are obtained one in phase and one in topography.

Piezoresponse force microscopy (PFM) allows to identify the presence of piezoelectric (hence ferroelectric in our case) domains. PFM is based on the principle of the inverse piezoelectric effect: an AC electric field applied through the AFM tip induces a local deformation on the sample that is measured along the xy plane (film plane) and along the z

axis (normal to the sample plane). PFM was performed in contact mode with a Platinum–iridium-coated probe (SCM-PIC, Bruker) with a spring constant of  $0.2 \text{ N m}^{-1}$  and resonant frequency of 15 kHz. An external AC bias ( $V_{ac} = 4 \text{ V}$ ,  $f = 60 \text{ kHz}$ ) is applied to the sample to detect its electromechanical response.

Kelvin probe force microscopy, KPFM, allows the evaluation of the surface potentials of the films. KPFM is a noncontact variant of AFM. KPFM measurements were performed in ambient atmosphere with a Dimension ICON (Bruker) in frequency–modulation mode (scan rate of 1 Hz, drive amplitude 4V). Highly doped Si probes (PFQNE-AL, Bruker) were used. For KPFM experiments, AC voltages of 5 V were applied to the sample. In FM-KPFM, the  $V_{CPD}$  (contact potential difference) is measured simultaneously to the surface imaging. The work function of the sample could be calculated as the tip work function is known. However, this was not possible in our case, since KPFM experiments were performed in ambient conditions and not in inert atmosphere.

Conducting Force Microscopy, CFM, permits the measurements of the conductivity of a sample. A tension is applied through the conducting tip and the current flow crossing the film thickness is measured. For C-AFM measurements, a DC bias of 5 V was applied between the bottom electrode (ITO) and the tip and the current flow is measured at each point of the image (current range between 2 pA and 1  $\mu\text{A}$ ). CFM measurements were performed in PeakForce mode with a Dimension ICON (Bruker) equipped with a TUNA module. Platinum–iridium-coated probes (SCM-PIT, Bruker) with a spring constant of  $2.8 \text{ N m}^{-1}$  and resonant frequency of 75 kHz were used.

AFM, PFM, KPFM and CFM images were analysed with NanoScope Analysis software, Bruker.<sup>13</sup>

### 8.5.6 Ferroelectric characterisation

Polarization hysteresis loops of the metal/ferroelectric/metal capacitors have been recorded at room temperature using the TF Analyzer 2000E of aixACCT Systems. A continuous sinusoidal wave with a 0.1 Hz frequency has been used and a  $150 \text{ MV m}^{-1}$  electric field was

applied to ensure that saturation is reached. Several devices have been measured per sample and a statistical study has been performed in order to corroborate the reproducibility of the polarization loops. (Chapter 2, Chapter 3, Chapter 4).

The polarisation is expressed in  $\text{mC m}^{-2}$  and is proportional to the amount of charges accumulated at the electrodes surfaces. The integration of the measured current in function of the time and of the electric field applied gives the dielectric polarisation  $P$ . The software aixPlover30 already gives the  $I$  vs  $E$  and the  $P$  vs  $E$  curves. The two maxima of  $I$  vs  $E$  observed in the two directions at the coercive fields (Figure 8.7a) corresponds to the charges displacement occurring to compensate the change in the polarisation state that follows the change of the applied electric field.<sup>8</sup> Moreover, the polarization switching by electric field in ferroelectric materials gives rise to a strain-electric field hysteresis, which resembles the shape of a butterfly and indeed is called “butterfly loop”<sup>8</sup> (Figure 8.7b).

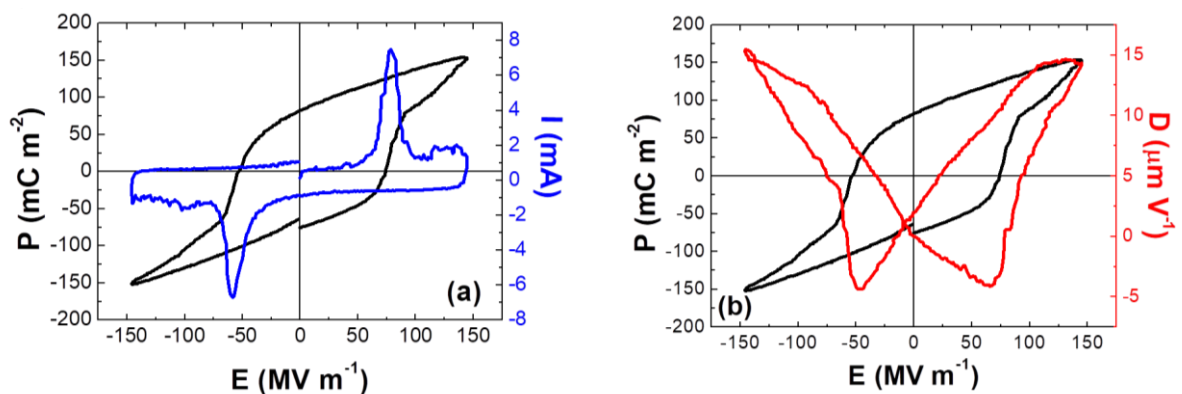


**Figure 8.7** Example of a ferroelectric hysteresis loop (black line) and the corresponding switching current peaks, (blue line) (a) and the respective mechanical displacement (red line) (b).

### 8.5.7 Dielectric spectroscopy

The dielectric characterisation has been realised with a Solartron (1296 dielectric interface, solartron analytical) and Impedance Analyzer (Solartron Analytical, SI 1260). These tools are interfaced with a computer whose command can be send by the software called “Smart”. For

the temperature experiment, a Linkam LTS 350 temperature controlled element has been used.

The dielectric permittivity describes the response of a medium to an applied electric field in function of the frequency of the electric field. Indeed the dielectric permittivity is a dynamic complex parameter,  $\epsilon_r^*(\omega)$  defined as:

$$\epsilon_r^*(\omega) = \epsilon_r'(\omega) - i \cdot \epsilon_r''(\omega) \quad (8.1)$$

Where the real part is  $\epsilon'$  (stored energy) and the imaginary part is  $\epsilon''$  (dissipated energy) that vary in function of  $\omega$  as shown in Figure 8.8. The ratio between imaginary  $\epsilon_r''$  and real part  $\epsilon_r'$  is defined as the charge losses  $\tan(\delta)$  that occurs if charges are passing through the material or are going out from the material. The magnitude of  $\epsilon'$  depends on the degree of polarisation that can occur. For air,  $\epsilon' = 1$ . For most ionic solids such as  $\text{Al}_2\text{O}_3$  and  $\text{NaCl}$ ,  $\epsilon' = 5-10$ . For inorganic ferroelectric materials such as  $\text{BaTiO}_3$ ,  $\epsilon' = 10^3-10^4$ , for polymeric ferroelectric as PVDF  $\epsilon' = 15$ . To increase  $\epsilon$  one should increase the density of electrical dipole moments. The applied electric field  $\vec{E}$  induces variation on both  $\epsilon'$  and  $\epsilon''$  functions as depicted in Figure 8.8 that describes the different relaxations involved as function of the frequency.

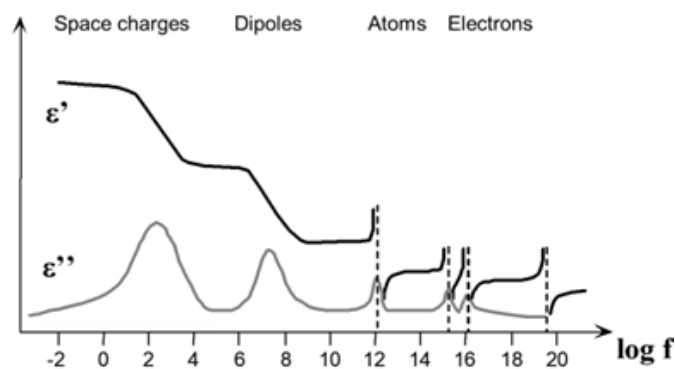


**Figure 8.8** Real and imaginary dielectric permittivity as function of the frequency.

The dielectric properties have been measured as function of the frequency that has been varied from 0.1 Hz to 1 MHz. Indeed, as shown in Figure 8.8 above different relaxations, occur

as function of the frequency analysed. At low frequency ( $f < 0.1$  Hz) charges relaxations due to impurity or to space charges dominate. At  $f > 1$  MHz, the vibration of elements of lighter dimension are detected, as the permanent dipoles of the materials.

### 8.5.8 Photovoltaic characterisation

The  $J$  vs  $V$  characteristics have been measured by means of a Keithley 4200 at atmospheric conditions in dark and under the illumination. The measurements under illumination have been performed by irradiating the sample with a solar simulator Sol2A, Oriel solartron analytical.

## References

- 1 Loewe, R. S., Khersonsky, S. M. & McCullough, R. D. A Simple Method to Prepare Head-to-Tail Coupled, Regioregular Poly(3-alkylthiophenes) Using Grignard Metathesis. *Advanced Materials* **11**, 250-253, doi:10.1002/(SICI)1521-4095(199903)11:3<250::AID-ADMA250>3.0.CO;2-J (1999).
- 2 Jeffries-EL, M., Sauv e, G. & McCullough, R. D. In-Situ End-Group Functionalization of Regioregular Poly(3-alkylthiophene) Using the Grignard Metathesis Polymerization Method. *Advanced Materials* **16**, 1017-1019, doi:10.1002/adma.200400137 (2004).
- 3 Hall, D. B., Underhill, P. & Torkelson, J. M. Spin coating of thin and ultrathin polymer films. *Polymer Engineering & Science* **38**, 2039-2045, doi:10.1002/pen.10373 (1998).
- 4 M uller-Buschbaum, P. The Active Layer Morphology of Organic Solar Cells Probed with Grazing Incidence Scattering Techniques. *Adv. Mater.* **26**, 7692-7709, doi:10.1002/adma.201304187 (2014).
- 5 Bras, W. *et al.* Recent experiments on a small-angle/wide-angle X-ray scattering beam line at the ESRF. *J. Appl. Crystallogr.* **36**, 791-794, doi:10.1107/S002188980300400X (2003).
- 6 Renaud, G., Lazzari, R. & Leroy, F. Probing surface and interface morphology with Grazing Incidence Small Angle X-Ray Scattering. *Surface Science Reports* **64**, 255-380, doi:http://dx.doi.org/10.1016/j.surfrep.2009.07.002 (2009).
- 7 Smilgies, D. M. Scherrer grain-size analysis adapted to grazing-incidence scattering with area detectors. *J. Appl. Crystallog.* **42**, 1030-1034, doi:10.1107/s0021889809040126 (2009).
- 8 Damjanovic, D. in *The Science of Hysteresis* (eds Giorgio Bertotti & Isaak D. Mayergoyz) 337-465 (Academic Press, 2006).



## Acknowledgments

This Thesis is to me not only the summary of the most interesting scientific results I have obtained during my PhD career, but additionally bears witness to my personal growth.

During these three years I have learned a lot about organic electronics, ferroelectric materials, how to face and organise a scientific project and how to deal with different problematics. I grew up as a small scientist willing to discover the physical motivation behind the data.

I am grateful to my supervisors Pr. Georges Hadziioannou, Dr. Mario Maglione and Dr. Eleni Pavlopoulou for giving me the opportunity to start this three years' fruitful experience in Bordeaux.

I would like to thank Georges for his interest in my research showed during all the discussions, meetings or fast exchanges at my desk. I appreciated his advices to improve posters and presentations. I should thank him for pushing me always a step further in doing more. Indeed, I hope I will continue enlarging my knowledge and skills through this brand-new opportunity of managing an industrial project.

I would like to thank Mario for the never ending discussions we had about my data, looking for their correct interpretation. I am grateful for the time he dedicated to me, from meetings at 18 h on Friday afternoon or at 4 h in the night for reading mails or revising my chapters...we struggled a lot, but eventually it was worth! It would have been great to have some more time to spend together for experiments and brain storming on dielectric spectroscopy.

I am glad to have worked with Dr. Eleni Pavlopoulou who has been not just a co-advisor but a family's member: I could count on her since my arrival in Bordeaux for everything, from finding me a place to live, until taking me to the hospital for an ankle sprain (to cite only two examples!) and of course for the good science we did together! During the infinite time spent together in her office I have learnt a lot from her: she has guided me from the preparation of devices and the way of studying them, to the scientific approach to GIWAXS technique and even if not with few difficulties, the way to write a paper! These are only few things I am mentioning now, since a lot of job has been done but the thesis has been already given! Nevertheless, it is also thanks to Eleni that I have strengthened self-consciousness about my skills.

There is a lot of people I would like to thank, who has accompanied me through all these three years. First I have to thank Dr. Jon Maiz who as Postdoc has guided me during my first year and has introduced me to the amazing world of the ferroelectric measurements with the TF analyser! I would like to thank Mickael and Gilles for all their help in device fabrication and

characterisation. I would like to thank Aude and Melanie for every single suggestion and comment they had for me, to help me solving my troubles as foreign or non-French speaker.

I would like to thank Giuseppe Portale who, with his Sicilian enthusiasm, has taught me some X-rays-measurements tips, thanks for all the skype (and non-) calls about science we had together and for the ones that will come!

I would like to thank Daniele, Aleksei and Michela from the beam line Dubble B26 in ESRF, Grenoble. I am going to miss a lot the beam time over there...it has been magic, being "caged" between those walls, apart from the beam cut!

I am grateful to the jury members Aurora Ruiz Nogales, Mark Geoghegan, Philippe Poulin, Bruno Ameduri and Giuseppe Portale for reading my manuscript and for the fruitful and interesting discussion we had during the Thesis defence. In particular, would like to thank Aurora and Mark for accepting the revision of my manuscript and Bruno for giving me his notes.

Of course I thank Amadeus for funding and the ELORPrintTec facility.

Moving to more personal thanks, I'd like to thank two friends of mine Ariana and Alberto with whom I started this adventure, we shared a lot of moments that we will never forget. You were always there for me and I thank you for all the nice times together and the support and complains we shared. I want to thank every B8ers...I believe I was really lucky to meet all of you people; we are an amazing crazy bunch of friends! A special thanks for having supported me and my improvised songs to my office mates: you're the best!

I have to thank one of the most amazing women of the world: my sister Valentina. She is not just a scientist, not just a beautiful and of character woman, she is not just the most generous sister I could always dreamed of, but for me she is an idol. I have to say that for me the idea to leave my hometown and "face" foreign people and languages had scared the hell out of me (just to cite the Muse) but thanks to her example I overcame this fear. She is of inspiration and I thank her for being as she is and also for being always there for me whatever the call is about!

Je voudrais même remercier Bertrand qui m'a donné beaucoup des conseils et m'a supportée toujours ! Merci !!

I need to thank Bruno who surprisingly still supports me and this is kind of miracle since I can be unpleasant for myself as well with my ups and downs. Thank you for being always there for me.

For the next paragraph I need to switch to Italian sorry!

Oggi sono la persona che sono grazie alla mia famiglia. Ogni giorno mi rendo conto di essere stata veramente fortunata ad avere i miei genitori Santa e Salvatore. Gli sono grata per come mi abbiano cresciuta ed é grazie al loro sostegno sono potuta arrivare fino a qui.

Siete una famiglia fantastica che mi supporta in ogni dove e sa consigliarmi alla meglio maniera, spero che siate fieri di me come io lo sono di voi.



# Résumé

*L'électronique organique représente une alternative réaliste aux technologies conventionnelles à base de silicium par le design, la synthèse et la mise en œuvre des matériaux organiques fonctionnels dans des dispositifs légers et flexibles. Les matériaux organiques, tels que les petites molécules ou les polymères organiques, sont avantageux pour leur faible coût, leur flexibilité et leur facilité de dépôt. Grâce aux avantages liés à l'utilisation de matériaux organiques, en termes économiques et de gain de temps, l'électronique organique est devenue un domaine innovant qui s'applique aux technologies de l'énergie, de l'environnement, de la santé, de l'information et de la communication.*

*L'électronique organique est issue de la découverte de polymères dotés de fonctionnalités semi-conductrices. Cependant, il ne faut pas négliger une autre classe de polymères exceptionnels, les polymères ferroélectriques. La nature électroactive des polymères ferroélectriques, qui sont également pyroélectriques et piézoélectriques, combinés aux avantages intrinsèques des polymères, les a désignés comme éléments constitutifs d'une gamme étendue de dispositifs électroniques organiques.*

*La famille de polymères ferroélectriques la plus connue est celle du poly (fluorure de vinylidène) P(VDF) et de son copolymère avec le trifluoroéthylène, P(VDF-co-TrFE). La récupération d'énergie, le stockage et la détection de données, principales applications de l'électronique organique, peuvent potentiellement tous être réalisés avec ces matériaux fonctionnels exceptionnels.*

*La ferroélectricité étant une propriété dépendant de la structure, il est indispensable de mieux comprendre les relations réciproques entre la structure et les propriétés ferroélectriques finales afin d'améliorer les applications existantes des polymères ferroélectriques en électronique organique et de promouvoir l'introduction du P(VDF-co-TrFE) dans de nouvelles applications.*

*P(VDF-co-TrFE) en tant que polymère semi-cristallin possède des propriétés cristallines sensibles au traitement thermique. Puisque seules les régions cristallines contribuent à la commutation électronique de la polarisation et non les amorphes, le degré de cristallinité est un facteur clé pour moduler les propriétés ferroélectriques. En outre, l'orientation des cristallites ainsi*

que la présence de défauts dans les cristallites sont des paramètres cruciaux qui jouent un rôle important dans la définition des performances finales des dispositifs dans lesquels P(VDF-co-TrFE) est incorporé. Tel est l'objectif de cette thèse : atteindre une compréhension exhaustive des relations traitement-structure-fonction qui serviront d'outil pour moduler les performances des dispositifs ferroélectriques.

Le premier challenge de cette thèse était de définir les conditions de recuit de « cristallisation à froid » (normalement utilisées pour les dispositifs électroniques organiques) qui conduisent aux meilleures propriétés ferroélectriques en termes de haute polarisation  $P_r$  et de bas champ électrique coercitif  $E_c$ . Une réponse ferroélectrique optimale, en termes de  $P_r$  élevé et de faible  $E_c$ , a été obtenue lorsque le traitement thermique a lieu dans des températures comprises entre 133 °C et 137 °C pendant 15 à 30 minutes de temps de recuit. Nos résultats ont prouvé que le pas de temps de recuit de 2 h, traditionnellement appliqué, n'est pas nécessaire, mais que seulement 15 minutes suffisent. De plus, il est apparu que la température de recuit affectait principalement la valeur de polarisation restante, alors que le temps de recuit avait un effet important sur la valeur du champ coercitif. Les performances accrues obtenues dans ces conditions ont été rationalisées grâce aux études GIWAXS qui ont révélé les phases cristallines apparentes dans ces films et ont permis de calculer le degré de cristallinité. Il est démontré qu'un degré élevé de cristallinité est nécessaire ainsi qu'une orientation des cristallites « edge-on » pour une performance améliorée. De plus, à travers une étude de déconvolution, il est discutée l'existence d'une phase ferroélectrique  $F_{1-2}$  modérément instable qui facilite la rotation des dipôles le long de la chaîne. La structure la plus performante présente un degré élevé de cristallinité, une orientation préférentielle des cristallites avec les chaînes polymères parallèles au substrat et la présence de trois phases ferroélectriques.

Ensuite, le polymorphisme a été étudié en suivant les transitions structurelles auxquelles le polymère ferroélectrique P(VDF-co-TrFE) est soumis au moyen de WAXS et DSC résolus en temps utilisant un protocole de « cristallisation isotherme à l'état fondu ». Différentes températures de cristallisation isothermiques ont été étudiées. Avec cette étude, nous avons été les premiers à décrire l'apparition de phases défectueuses dans des échantillons non traités (c'est-à-dire sans

recuit au-dessus de la  $T_{Curie}$ ). En suivant les étapes de chauffage et de refroidissement du protocole de « cristallisation à l'état fondu », il a été constaté que trois cristallisations se produisaient : une avant la cristallisation isotherme, une pendant l'étape isotherme et une immédiatement après la cristallisation isotherme. Une augmentation globale du degré de cristallinité se produit lorsque  $T_c$  augmente. Après la cristallisation, les cristallites paraélectriques se forment puis, lors du refroidissement dans la plage de transition de Curie, ils se transforment en une phase  $F_1$  plus ordonné (formé directement avec les paramètres de maille typiques de la phase ferroélectrique) et en  $F_2$  très désordonné. L'asymétrie du pic de diffusion attribuée à la phase  $F_1$  suggère l'apparition d'une phase  $F_{1-2}$  ordonnée de manière intermédiaire.

Néanmoins, bien qu'il ait été prouvé que le degré de cristallinité augmentait avec l'augmentation de  $T_c$ , nous avons détecté une performance ferroélectrique non optimale pour les échantillons recuits à  $T_c$  très élevée. Nous attribuons cette diminution des performances à une possible forte teneur en  $F_2$  hautement défectueux, ce qui ralentit la rotation ferroélectrique. Cependant, les études de déconvolution des pics GIWAXS sont un travail en perspective car elles sont nécessaires pour confirmer l'hypothèse proposée.

Les corrélations entre les phases structurales et les performances doivent être recherchées dans la rotation intramoléculaire lors de la polarisation. En effet, lorsque nous appliquons un champ électrique à un copolymère P(VDF-co-TrFE), nous induisons une rotation le long des chaînes pour aligner les dipôles. La phase intermédiaire  $F_{1-2}$  favoriserait plus la rotation intramoléculaire grâce à la présence de quelques défauts gauches servant de sites d'activation pour le début de la rotation contrairement à la phase ferroélectrique parfaite. D'autre part, une phase  $F_2$  trop défectueuse devrait montrer une certaine orientation des dipôles, qui dans tous les cas n'atteindra pas le degré de celui des  $F_1$  et  $F_{1-2}$ , entraînant une baisse des performances.

Ensuite, l'effet de l'orientation des cristallites est étudié en détail. En effet, le lien entre la polarisation et l'orientation des dipôles au sein de la cristallite indique que l'orientation de la cristallite par rapport au champ électrique appliqué est fondamentale pour faciliter l'alignement et obtenir, après polarisation, la densité maximale de charges à la surface. Nous avons quantifié l'impact de l'orientation des cristallites sur les propriétés ferroélectriques en induisant diverses orientations des cristallites au moyen d'une variation du protocole thermique. Nous avons

découvert que lors d'une « cristallisation en état fondu », il se forme des cristallites orientées de manière aléatoire ou préférentiellement orientées « face-on ». Il a été constaté que l'échantillon ayant subi une « cristallisation isotherme à froid » présentait la plus grande quantité de cristallites « edge-on » (environ 75%), ce qui était lié à la meilleure réponse ferroélectrique. Les paramètres ferroélectriques ont en effet été fortement dépendants de l'orientation des cristallites : un  $P_r$  plus élevé, un  $E_c$  plus faible, et une inversion de la direction de polarisation plus rapide sont trouvés pour une valeur de « edge-on » élevée. Des études de spectroscopie diélectrique à différentes températures nous ont permis de constater qu'un échantillon cristallisé à froid présente une énergie d'activation de la relaxation dipolaire inférieure avec une diminution de la relaxation FE-PE par rapport aux échantillons cristallisés à l'état fondu en raison de l'orientation « edge-on ». Ces études de spectroscopie nous ont également permis de constater qu'une énergie d'activation accrue de la relaxation dipolaire, ainsi qu'une diminution de la fréquence de relaxation FE-PE, se produisaient lorsque l'on passait d'un échantillon « edge-on » à un échantillon orienté de manière préférentiellement « face-on ». Cela suggère que l'orientation « face-on » agit comme un paramètre défectueux qui empêche la relaxation des dipôles.

De plus, des applications potentielles de P(VDF-co-TrFE) en électronique organique sont explorées dans cette thèse. Le premier concerne la mise en œuvre de P (VDF-co-TrFE) dans des capteurs médicaux piézoélectriques pour l'entraînement d'étudiants en laparoscopie. La seconde concerne l'utilisation de copolymères P (VDF-co-TrFE) dans des dispositifs photovoltaïques.

En regardant l'application des capteurs médicaux piézoélectriques les résultats obtenus dans le cadre du projet "sweet heart" conduit en collaboration avec le centre de recherche Liryc (L'Institut de Rythmologie et modélisation Cardiaque) sont discutés. L'objectif était de fabriquer une matrice flexible de capteurs piézoélectriques qui pouvant être encapsulés à l'intérieur d'un cœur imprimé en 3D. Après avoir essayé plusieurs approches, nous avons réussi à fabriquer des capteurs piézoélectriques très flexibles en évaporant thermiquement des électrodes en argent métallique sur des substrats PDMS épais et en encapsulant un film P (VDF-co-TrFE) entre eux.

Pour le dernier challenge de cette thèse, une étude des dispositifs électroniques dans lesquels P(VDF-co-TrFE) est mélangé avec le polymère semi-conducteur P3HT, poly(3-hexylthiophène), a

été effectuée. Ce mélange P(VDF-co-TrFE) : P3HT a déjà été appliqué dans les diodes à mémoire ferroélectrique non volatile et nous avons explorée son utilisation potentielle dans le champ de l'organique photovoltaïque.

Le mélange P(VDF-co-TrFE) : P3HT forme une couche active à séparation de phase. La morphologie à l'échelle nanométrique des différents rapports pondéraux (95 : 5, 90 : 10, 80 : 20) a été minutieusement caractérisée à l'aide de plusieurs techniques de microscopie à sonde à balayage telles que l'AFM, le PFM, le KPFM, et le CFM. Au moyen du PFM, il a été confirmé qu'une séparation de phase se produit sans affecter les propriétés de chaque composant du mélange. En particulier, P(VDF-co-TrFE) conserve ses propriétés piézoélectriques fonctionnelles. De plus, une phase semi-conductrice avec absence de réponse piézoélectrique a été observée sous forme de domaines concaves et convexes à la surface.

En combinant le KPFM et le CFM, nous avons constaté que le pourcentage de rr-P3HT influe fortement sur la distribution des chemins semi-conducteurs. Au moyen du KPFM, nous avons dévoilé l'apparition de réseaux semi-conducteurs quasi superficiels (au moins jusqu'à 100 nm au-dessous de l'interface air-film) lorsque le pourcentage en poids de P3HT dépasse 10%. Ces réseaux n'ayant pas été détectés avec le CFM, ils n'agissent donc pas comme un chemin semi-conducteur. Nous avons conclu que le meilleur rapport pour les applications électroniques organiques est le rapport 90 : 10, en termes de taille de domaine semi-conducteurs et de reproductibilité de la nanostructure. Les dispositifs photovoltaïques ont été fabriqués et caractérisés en enregistrant leurs courbes J-V respectives dans l'obscurité et à la lumière afin d'évaluer la différence de comportement électrique. Même si nos résultats ne sont que préliminaires, ils représentent une preuve de concept selon laquelle un tel système pourrait être exploité en photovoltaïque organique.